MODELLING OF UNIDIRECTIONAL THERMAL DIFFUSERS IN SHALLOW WATER

Joseph H. Lee
Gerhard H. Jirka
Donald R. F. Harleman

Energy Laboratory
Report No. MIT-EL 77-016

July 1977

MODELLING OF UNIDIRECTIONAL THERMAL DIFFUSERS IN SHALLOW WATER

by

Joseph H. Lee

Gerhard H. Jirka

and

Donald R. F. Harleman

Energy Laboratory

and

Ralph M. Parsons Laboratory
for
Water Resources and Hydrodynamics,
Department of Civil Engineering

Massachusetts Institute of Technology
Cambridge, Massachusetts 02139

sponsored by

New England Electric System
Westboro, Massachusetts

and

Northeast Utilities Service Company
Hartford, Connecticut

under the

MIT Energy Laboratory Electric Power Program

Energy Laboratory Report No. MIT-EL 77-016

July 1977

ABSTRACT

This study is an experimental and theoretical investigation of the temperature field and velocity field induced by a unidirectional thermal diffuser in shallow water.

A multiport thermal diffuser is essentially a pipe laid along the bottom of the water body and discharging heated water in the form of turbulent jets through a series of ports spaced along the pipe. A unidirectional diffuser inputs large momentum in one direction; it can achieve rapid mixing within relatively small areas, and has the advantage of directing the thermal effluent away from the shoreline.

The theory considers a unidirectional diffuser discharging into shallow water of constant depth in the presence of a coflowing ambient current. A fully mixed condition is hypothesized downstream of the diffuser. A two dimensional potential flow model is formulated and solved in the near field, where flow is governed by a dominant balance of pressure and inertia. A control volume analysis gives the total induced flow, which is used as an integral boundary condition in the potential flow solution. The shape of the slip streamline is solved using Kirchoff's method; the velocity and pressure field are then computed by a finite difference method. The correct boundary conditions along the diffuser are deduced. Knowledge of the flow field defines the extent of the near field mixing zone. The near field solution is coupled into an intermediate field theory. In this region turbulent lateral entrainment, inertia and bottom friction are the governing mechanisms of the flow, and the mixed flow behaves like a two dimensional friction jet. An integral model is formulated and solved numerically. The model predictions of induced temperature rises, velocities, plume widths enable comparisons of the overall effectiveness of different heat dissipation schemes.

A model for calculating the near field dilution and plume trajectory of a unidirectional diffuser discharging into a perpendicular crossflow is formulated and solved. The phenomenon of heat recirculation from the far field is ascertained in the laboratory and a semi-empirical theory is developed to evaluate the potential temperature buildup due to far field recirculation.

A comprehensive set of laboratory experiments have been carried out for a wide range of diffuser and ambient design conditions. The model is validated against the experimental results of this study as well as those of hydraulic scale model studies by other investigators.

The analytical and experimental insights gained in this study will aid future numerical modelling efforts and in better design of physical scale models. The principal results are applied to establish general design guidelines for diffusers operating in coastal regions. The ecological implications of the model predictions are discussed.

ACKNOWLEDGEMENTS

This study is funded by New England Electric System, Westboro Massachusetts and Northeast Utility Service Company, Hartford, Connecticut through the Electric Power Program of the M.I.T. Energy Laboratory. The co-operation of Dr. William Renfro of Northeast Utilities and Mr. Bradley Schrader of New England Electric is appreciated.

The material in this study was submitted by Joseph H. Lee, Research Assistant, to the Department of Civil Engineering in partial fulfillment of the requirements for the degree of Doctor of Philosophy. The research work was carried out under the technical supervision of Professor Donald R.F. Harleman, Professor of Civil Engineering and Director of the Ralph M. Parsons Laboratory for Water Resources and Hydrodynamics, M.I.T. and Dr. Gerhard H. Jirka, Research Engineer in the Energy Laboratory and Lecturer in the Department of Civil Engineering, M.I.T.

Several discussions with Dr. E. Eric Adams, Research Engineer and Professors Chiang C. Mei and Keith D. Stolzenbach have been very helpful. Mr. Roy G. Milley, machinist, and students Richard Trubiano, Jeff Diercks, Charles Almquist, and David Fry have provided assistance in the experimental program of this study. Computational work was carried out at the Civil Engineering-Mechanical Engineering Joint Computer Facility at M.I.T.

This manuscript was capably typed by Ms. Josephine Mettuchio.

TABLE OF CONTENTS

CHAPTER I

INTRODUCTION

1.1 Background

Technological advances in recent decades have led to man's increasing consumption of electricity. A by-product of this activity is the large quantities of waste heat resulting from steam-electric power production. At present the thermal efficiency of this mode of energy production is about 40% for a fossil fueled plant, and 33% for a nuclear fueled plant. Thus for every kilowatt of electrical energy produced, an equivalent of 1.5 to 2 kilowatts of energy is rejected to the environment as waste heat. The heat rejection rate is about 7×10^9 BTU/Hr. for a standard 1000 MWe fossil plant. As power plants are usually located far from populated areas, the present state of technology has not found it economical to make beneficial use of the low grade waste heat.

In many instances a "once through" condenser cooling water system is employed. Cooling water is withdrawn from an adjacent water body, circulated through the plant once, and discharged back into the water environment at 20 to 30 F higher than the ambient water temperature. The increase in water temperature changes our environment: the chemical composition and physical properties of the water-dissolved oxygen levels, viscosity, nutrient concentrations, etc. may be altered; the life processes of many aquatic organisms may be encouraged or hampered. The

waste heat input affects the ecological system. Although our knowledge of interactions of the essential components of an eco-system is admittedly meagre, it is important to provide a sound basis on which the impact of thermal discharges on our environment can be assessed. It is of interest to understand the various heat mixing mechanisms and induced fluid motion that govern the ultimate distribution of heat in the water body. For additional purposes of avoiding heat recirculation through the plant, it is desirable to predict the various temperature configurations associated with different thermal outfall designs. This is the point of departure of this study.

Different standards have been set up in the United States to regulate thermal discharges from power plants. Prior to the issuance of a thermal discharge permit the applicant must perform detailed engineering and ecological investigations to demonstrate that the thermal standards will not be violated. Depending on the aquatic environment and a multitude of factors, the regulatory standards are rather site specific, and vary from state to state. A common type of standards dictates that a certain temperature rise above the natural background water temperature is not to be exceeded beyond a relatively small mixing zone; a high rate of mixing is thus required close to the thermal outfall. Other standards may restrict the warm effluent to an upper layer of the receiving water for protection of benthic organisms. Important considerations that are of interest to biologists include the maximum temperature

rise near the discharge, the exposure time to elevated temperatues of organisms entrained in the cooling water flow, the location and extent of the plume. In recent years there has been a tendency to make thermal impact assessments on a case to case basis, allowing more inter-disciplinary interaction involving engineers, biologists and ecologists. This also furthers the need for a more complete picture of the induced temperature and velocity field.

For once through cooling systems there are basically two types of waste heat discharge schemes; surface schemes discharge heated cooling water at the free surface through a canal or a number of pipes located near the shoreline. This method usually results in a relatively large surface area of elevated temperatures, but has the advantage that the heated water forms a stably stratified surface layer and the effect on the bottom of the receiving water is reduced. Submerged discharge schemes consist of single port or multiports located near the bottom of the water body. The first type of thermal standards usually precludes the use of surface discharge or submerged single port discharges. A submerged multiport diffuser discharging the heated water in the form of high velocity turbulent jets has proved to be an efficient device to achieve rapid temperature reduction within a relatively small area.

Condenser cooling water systems require large quantities of cooling water. A typical condenser flow for a standard 1000 MWe plant is in the order of 1000 cfs. The projected daily

condenser cooling water requirement for steam-electric power generation for 1970 and 1980 was 113 and 193 billion gallons, as compared to the nation's average runoff of 1200 billion gallons/day (National Water Commision, 1971). Thus for once through systems, there has been a trend to build plants adjacent to coastal areas (great lakes or oceans) where there is an ample supply of water, the mixing capacity of thermal discharges in rivers being limited by the ratio of the river flow to the condenser flow.

1.2 Multiport Diffusers

A multiport diffuser is essentially a pipe laid along the bottom of the water body and discharging waste water in the form of turbulent jets through a series of ports spaced along the pipe. The ports can be oriented to give optimal mixing performance, and are usually closely spaced so that there is sufficient interaction among the jets to approximate a line source of pollutant, flow, and momentum.

Historically, submerged multiport diffusers have been used for sewage disposal in the marine environment. Recently they have been used in thermal discharge applications. There is, however, a marked difference in the mixing mechanisms of the two cases: Submerged sewage diffusers are characterised by high buoyancy of the discharge under deep water conditions. The relative density difference between the discharge and receiving water is about 0.025, and the typical water depth

about 100 ft. Thus the discharge can be represented as an equivalent two dimensional slot jet in an infinite field, and classical theories of buoyant jet analysis are applicable to predict diffuser performance. Submerged thermal diffusers, on the other hand, are characterised by low buoyancy of the discharge under shallow water conditions. The relative density difference is about 0.003 and the typical water depth 20 ft. For thermal discharge applications the buoyant jet patterns predicted by classical theories cannot be maintained and fully mixed conditions occur downstream of the diffuser (Fig. 1-1). In almost all practical situations, three dimensional thermal diffusers produce fully mixed conditions downstream; the nature of the flow field is altered considerably, and traditional methods of predicting diffuser performance for sewage applications cannot be carried over.

Fig. 1-2 shows three basic types of multiport diffusers. A unidirectional diffuser consists of ports all pointing in one direction and discharging perpendicular to the diffuser axis. A unidirectional diffuser inputs large momentum in one direction; it can achieve rapid mixing within a relatively small area, and has the advantage of directing the thermal effluent away from the shoreline. The ports in an alternating diffuser discharge alternately in opposite directions. The net momentum input is zero; the plume extends in both directions and flow is driven by buoyancy beyond a near field mixing zone.

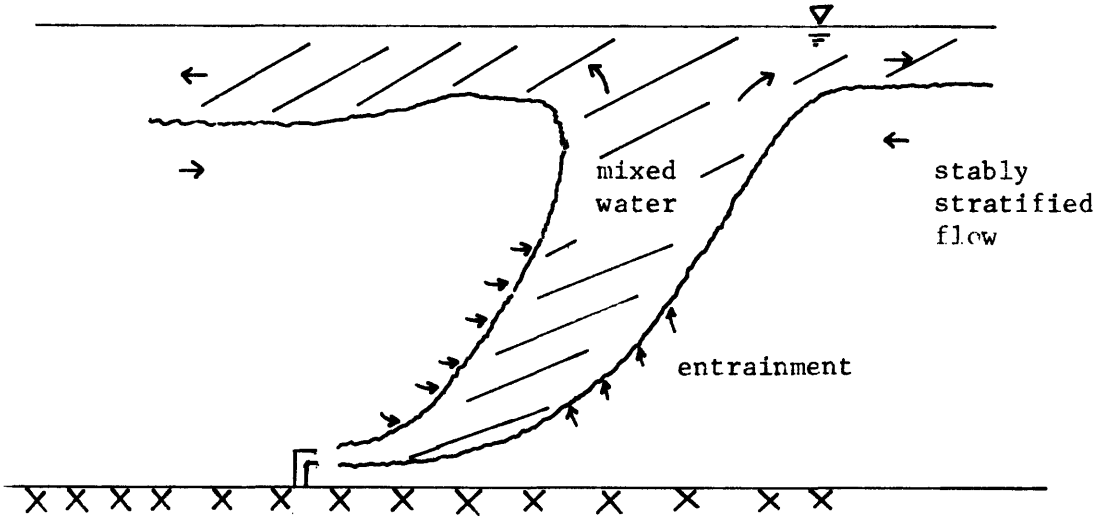

Fig. 1-1 a) Multiport diffuser discharge in deep water: Stable buoyant jet

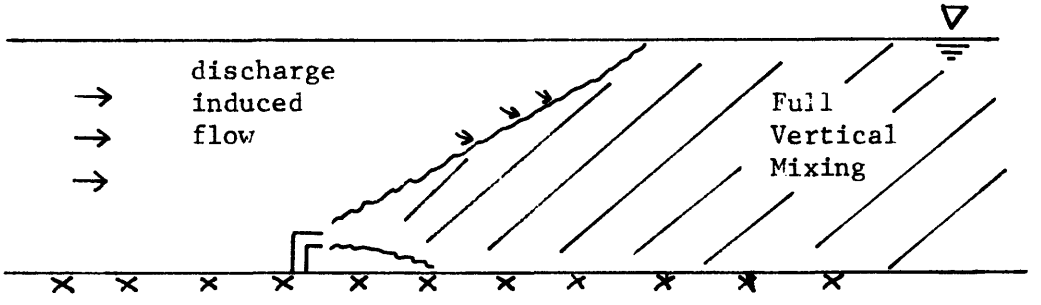

Fig. 1-1 b) Multiport diffuser discharge in shallow water: Unstable flow situation

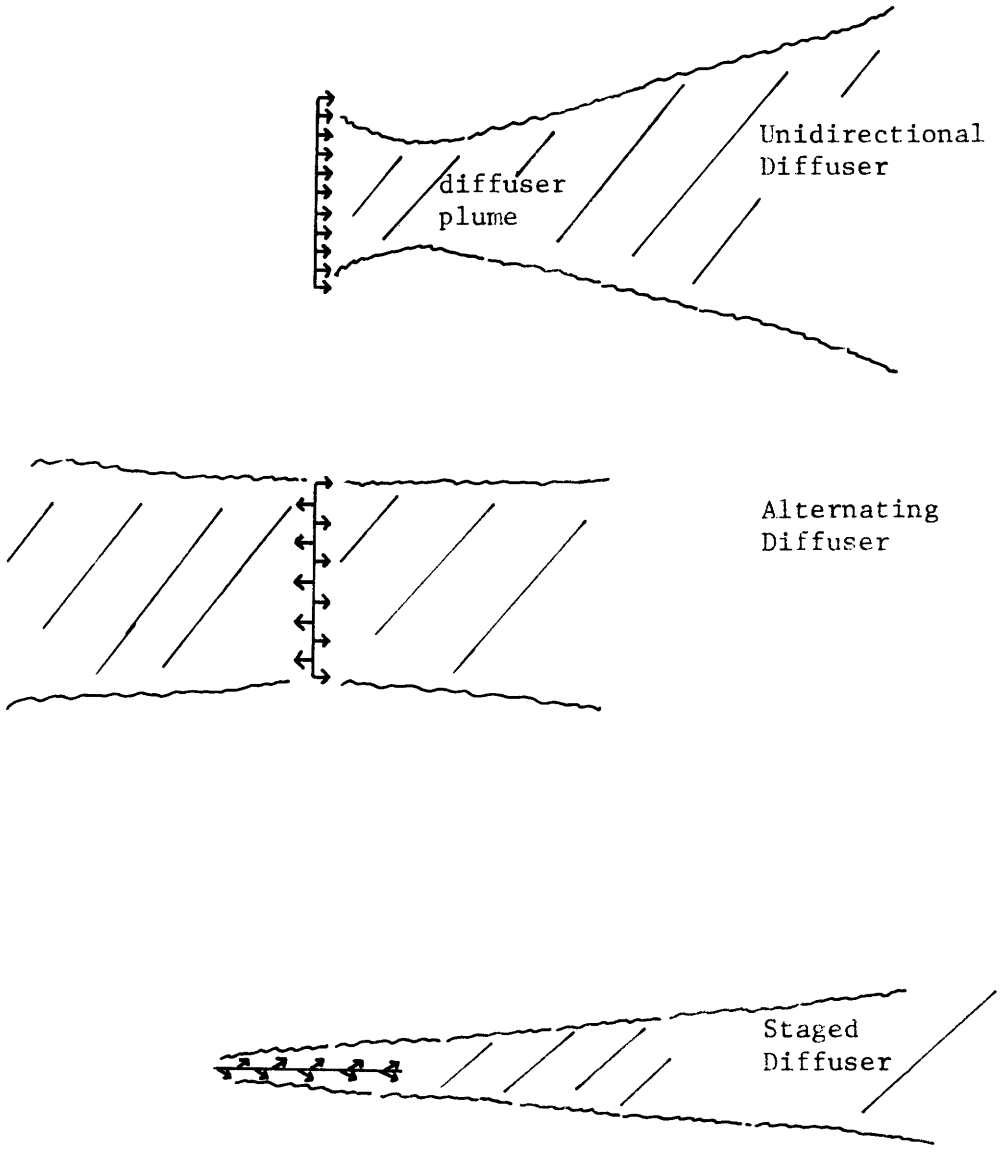

Fig. 1-2 Basic types of multiport diffuser configurations

As the induced flow has no preferred direction, this type of diffuser is suitable for use in a tidal situation with reversing currents. In a staged diffuser the ports are oriented in a tandom fashion: this type of arrangment is characterised by a narrow plume and distributed momentum input along the diffuser axis. For a given heat rejection rate and under stagnant conditions, the diffuser length required to achieve a specified degree of initial mixing is shortest for the unidirectional design (Harleman, Jirka, Stolzenbach, 1977).

The impact of a multiport diffuser operating in shallow water can be illustrated as follows: Consider a hypothetical plant with a condenser flow of 2000 cfs and having a dilution of 10, the total induced flow of 20,000 cfs approaches the low flow of the Mississippi River in Illinois! For a typical discharge nozzle velocity of 20 fps, the induced velocity around the diffuser is of the order of 2 fps-larger than current speeds frequently found in coastal regions. The high initial mixing also means the diffuser has to be placed some distance offshore so as to ensure a sufficient entrainment flow from behind.

Fig. 1-3 shows an example of induced temperature rise at the James A. Fitzpatrick Nuclear Power Plant on Lake Ontario. The site is characterised by a relatively small condenser flow, ambient stratification, and a strong offshore slope of 1/50.

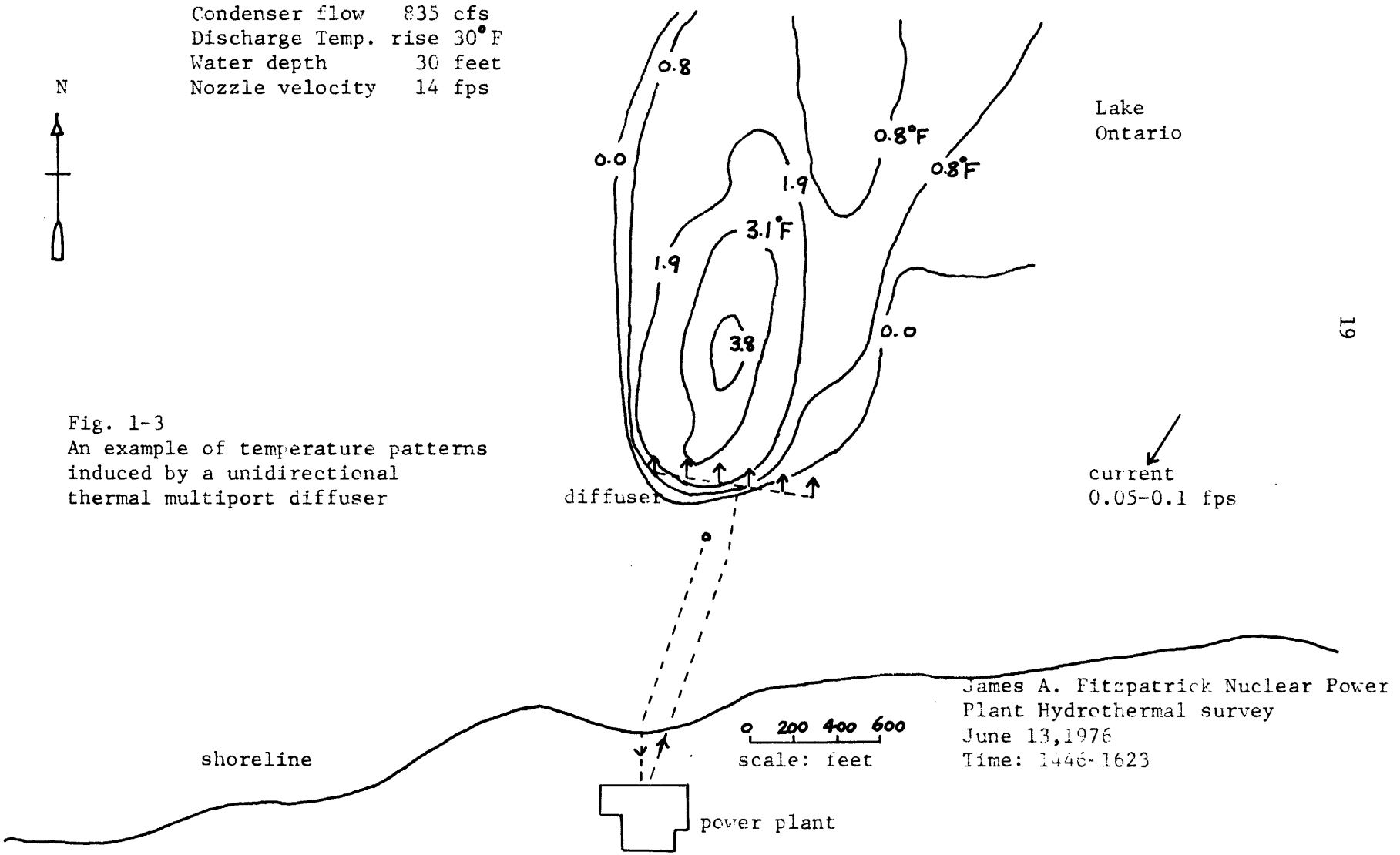

Fig. 1-3
An example of temperature patterns induced by a unidirectional thermal multiport diffuser

The isotherms are inferred from measurements of dye concentration taken in a hydrothermal field survey (Hydrothermal field studies, Stone and Webster, 1977).

For unidirectional diffusers the travel time in the discharge dominated flow regimes is of the order of an hour; for such time scales surface heat loss to the atmosphere is negligible, and the temperature reduction is governed by turbulent mixing with the ambient water.

1.3 Objectives and Summary of this study

This study is an analytical and experimental investigation of the temperature field and velocity field induced by a unidirectional thermal diffuser in shallow water. This type of design provides an effective source of horizontal momentum and is capable of meeting stringent thermal standards as regards allowable mixing zones and temperature rises.

This study considers a unidirectional diffuser discharging into shallow water of constant depth in the presence of an ambient unidirectional current. A fully mixed condition is hypothesized downstream of the diffuser. The objective is to develop a theory that predicts quantities of environmental interest; velocities, temperature rises, areas of surface isotherms. Surface temperature patterns are crucial for a comparison of the overall effectiveness of different heat dissipation schemes. Based on an understanding of the diffuser induced flow field, the effect of the heat return

from the far field on potential temperature build up in the near field can be evaluated. The analytical insights gained in this study will aid future numerical modelling efforts and in better design of physical scale models. The principal results are applied to establish general design guidelines for diffusers in coastal zones.

In Chapter II a summary of previous work on submerged multiport diffusers is presented and the conceptual basis underlying the present analytical and experimental modelling efforts is discussed.

Chapter III presents a two dimensional potential flow model for the near field of a unidirectional diffuser in a coflowing current. In this region flow is governed by a dominant balance of pressure and inertia. A control volume analysis gives the total induced flow, which is used as an integral boundary condition in the potential flow solution. The shape of the slip streamline is solved using Kirchoff's method; the velocity and pressure field are then computed by a finite difference method. The correct boundary conditions along the diffuser are deduced. Knowledge of the flow field defines the extent of the near field mixing zone. This is important in the prediction of surface temperature configuration and in future numerically modelling for a variety of ambient conditions.

In Chapter IV the near field solution is coupled into an intermediate field theory. In this region turbulent lateral entrainment and bottom friction are the driving mechanisms of the flow, and the mixed flow behaves like a two dimensional friction jet. An integral model is formulated and solved numerically. Considerable insight can be gained for the case of no current, when an analytical solution can be obtained. The model is capable of predicting velocity,plume width, temperature rises, and area of surface isotherms.

In Chapter V the experimental apparatus and run procedure employed in this study is described. The motivation for the design of each set of experiments is discussed. The run parameters are tabulated and the experimental results presented.

In Chapter VI the predictions of the model are compared with laboratory experiments conducted in this study as well as results of hydraulic scale model studies carried out by other investigators.

In Chapter VII the effect of diffuser orientation with respect to current is discussed and experimental results are interpreted in light of the theoretical insights set forth in the simpler situations.

In Chapter VIII the phenomenon of heat recirculation from the far field is ascertained in the laboratory and a semi-empirical theory is developed to evaluate the potential temperature build up due to far field recirculation.

In Chapter IX the theoretical and experimental results in this study are interpreted from the view-point of practical design of thermal diffusers for once through cooling systems. An ecological interpretation of the model predictions is advanced.

In Chapter X the findings in this study are summarised. General conclusions are drawn and recommendations are made in areas requiring further research.

CHAPTER II

REVIEW OF PREVIOUS WORK

A multiport diffuser can be characterised by a line of equally spaced incompressible turbulent jets issuing into a receiving water body of depth H.

2.1 The free turbulent jet

The mechanics of a two dimensional or three dimensional free turbulent jet in an infinite fluid has been studied extensively (Abramovich, 1963). Fig. 2-1 shows a turbulent jet from a finite source. Near the source the sharp discontinuity in velocity produces a region of high shear. This unstable situation gives rise to eddies, resulting in the less turbulent ambient fluid being entrained into the turbulent fluid. The jet, or the region of high turbulent intensity, thus grows in width as it entrains more ambient fluid. The mechanism of turbulent entrainment dilutes the concentration of any tracer material that may be introduced at the source.

For this type of free shear flow experiments have shown that pressure is approximately constant throughout the jet and that the jet width is small compared with the longitudinal length scale. A boundary layer type approximation is then legitimate. Based on different hypothesis of relating the turbulent shear terms $-\overline{u'v'}$ to the mean flow quantities, exact similarity solutions have been obtained by Prandtl, Taylor,

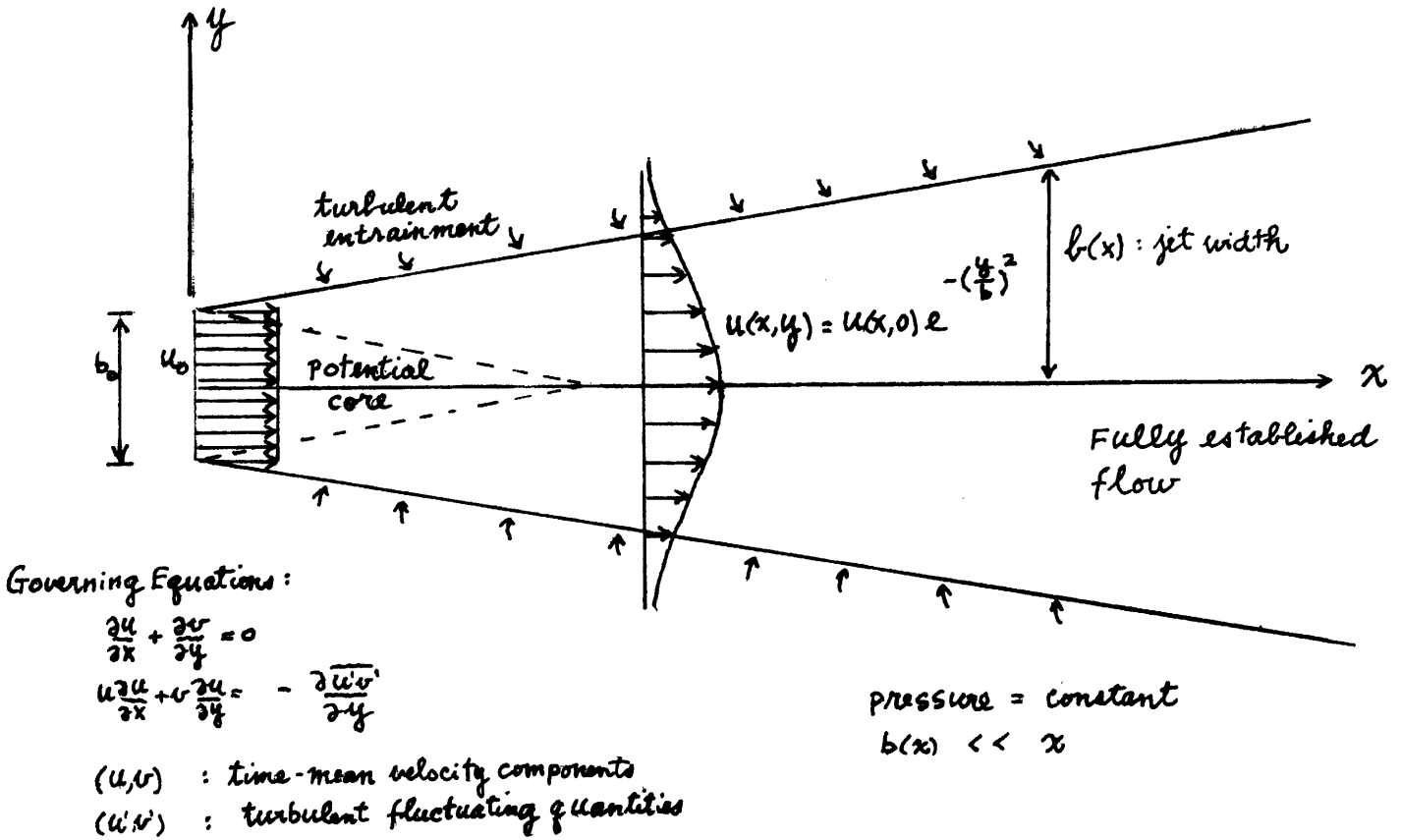

Fig. 2-1 The two-dimensional free turbulent jet

Reichardt (Abramovich). True similarity also exists for a pure source of buoyancy or a plume; this case was treated by Rouse, Yih and Humphreys (1952), and Morton, Taylor, and Turner (1956).

The similarity of velocity profiles and concentration (or buoyancy) profiles has been confirmed experimentally. The profiles can also be well approximated by Gaussian functions (Albertson et al, 1950)

$$u(x,y) = u(x,0)\ e^{-(\frac{y}{b})^2}$$

$$c(x,y) = c(x,0)\ e^{-(\frac{y}{\lambda b})^2}$$

where c : concentration of tracer

λ : empirical constant

2.2 Turbulent buoyant jets

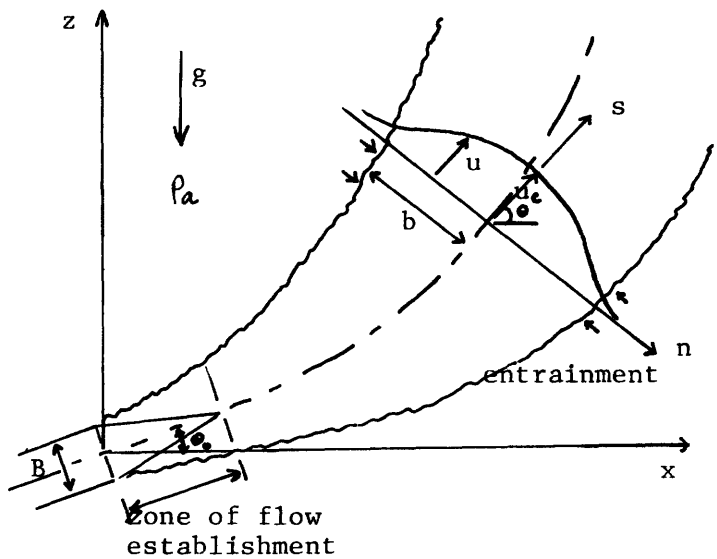

Fig. 2-2 Schematics of a slot buoyant jet

s,n: axial co-ordinates
u: axial velocity
u_c : centerline axial velocity
θ_o: angle of discharge
ρ_a: ambient density
B: slot jet width

The free jet theories have been extended by many investigators to study the behavior of turbulent buoyant jets in a variety of situations (Abraham, 1963; Fan, 1967; Stolzenbach and Harleman, 1971). The turbulent buoyant jet possesses both initial momentum and buoyancy, and as such it is neither a pure source of momentum nor a pure source of buoyancy. (Fig. 2-2) A review of previous work on turbulent buoyant jets as related to multiport diffusers has been given by Jirka and Harleman (1973).

For purposes of predicting gross quantities of interest in many practical applications it has been found convenient to assume a priori cross-sectional profiles for the velocity and concentration (buoyancy). The equations of motion are then integrated across the jet to yield a set of ordinary differential equations for the jet characteristics-plume position, centerline velocity, jet width, centerline concentration. This so called 'integral technique' has been successfully extended to other buoyant jet flows where true similarity does not exist (Abraham, 1963; Fan, 1967; Hoult et al, 1969).

2.3 Interaction of round jets from the multiport diffuser

The round jets issuing from the diffuser will gradually merge into one another as they spread by turbulent entrainment (Fig. 2-3). Knystautas (1963) studied the interaction of turbulent jets from a series of holes in line and discharging into a still fluid at incompressible speeds. Longitudinal

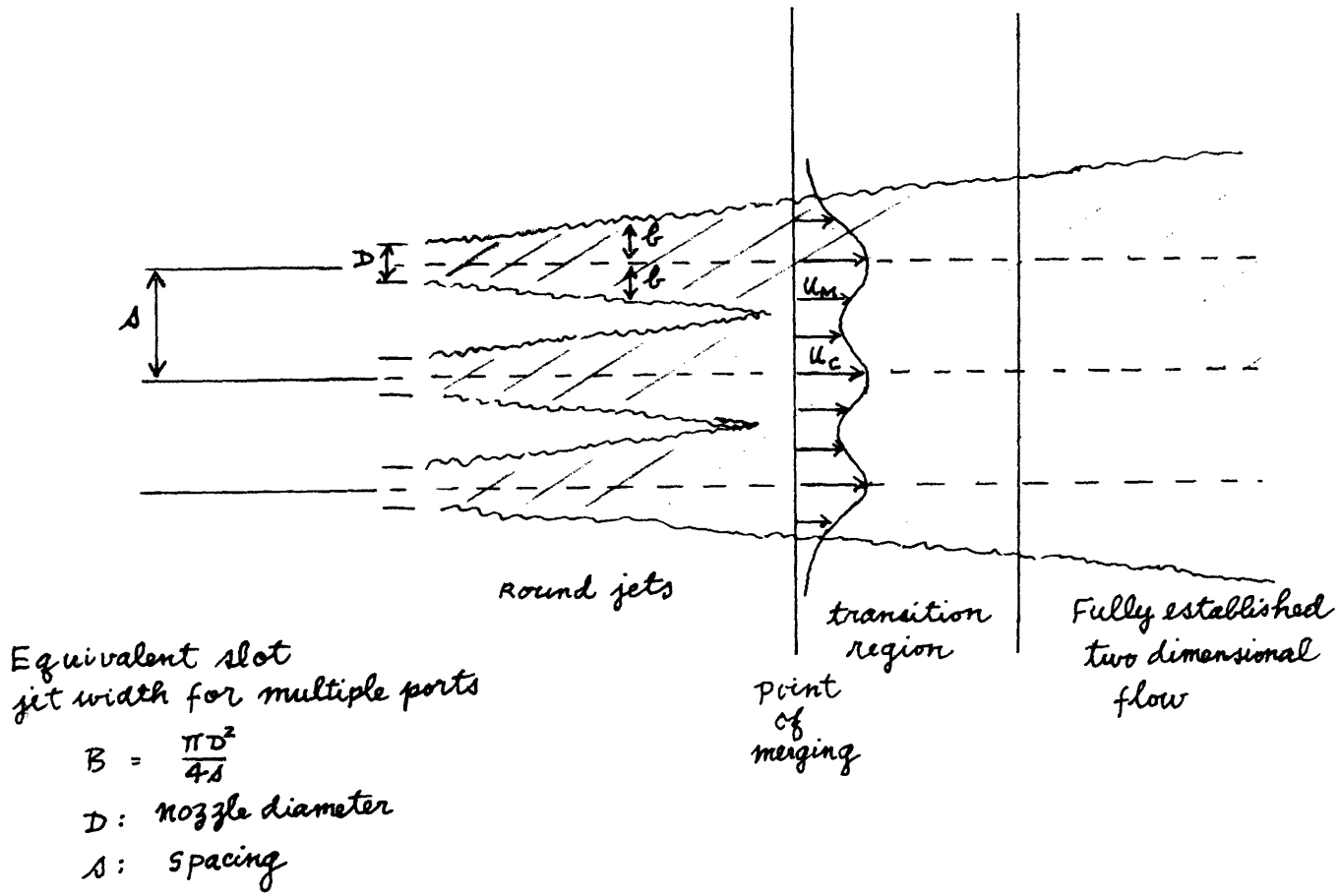

Fig. 2-3 Interference of round jets from a multiport diffuser

variations in static pressure are assumed to be negligible and thus the jet momentum is conserved. By extending Reichardt's hypothesis for the turbulent shear stress in a free jet which linearises the equation for the square of the mean velocity downstream, the momentum fluxes at each point of the interfering jet group may be found by superposition. The theory predicts that fully merged two-dimensional flow occurs at approximately 12 hole spacings downstream of the source.

Cederwall (1971) examined the same problem for a multiport diffuser used in sewage and thermal outfalls. By conserving momentum and volume fluxes per unit width, the width of an equivalent slot jet for a seriesof momentum jets can be shown to be $B = \frac{\pi D^2}{4s}$. Defining b as the nominal jet half-width, the radius at the point where the local jet velocity equals 1/e of the centerline velocity, and assuming interaction occurs when $2b \simeq s$, it can be shown that the jets merge at $x \simeq 4.4s$. The same line of reasoning can be worked through for a series of round plumes, in which case interaction occurs at $x \simeq 5.1s$. At the point of merging, the velocity at the edge of the jet is $u_M \simeq \frac{\sqrt{2}}{e} u_c = 0.52\ u_c$ (obtained by summing the momentum contributions from the individual jets); thus flow is far from fully two dimensional. Fully two dimensional flow is established over a transitional region beyond the point of merging.

Cederwall compared the mixing efficiency of a row of round momentum jets with that of an equivalent slot jet. An index of comparison, E is defined as

$$E = \frac{\text{Dilution for multiple ports}}{\text{Dilution for equivalent slot jet}}$$

At the point of merging, using well established relationships for free jets E was shown to be $\simeq 0.95$. For the case of a row of round plumes $E \simeq 0.78$.

2.4 Application of buoyant jet models for hydrothermal prediction

The considerations in the preceding sections are applicable to multiport diffusers under deep water conditions, such as the case for sewage applications, when the static or piezometric head can be regarded as constant in the flow field. The diffuser flow can then be modelled as an equivalent buoyant slot jet. Predictions of dilutions of sewage pollutant or temperature reduction of thermal discharges can then be estimated using buoyant jet models based on integral techniques (Brooks, 1972).

Under shallow water conditions, however, the presence of the free surface and the bottom boundary changes the nature of the flow field drastically; pressure can no longer be regarded as constant, and the momentum flux is not conserved. Multiport diffusers designed for use as thermal outfalls usually fall into this category. (Jirka, Abraham, Harleman, 1975).

2.4.1 Unidirectional multiport diffusers in a laterally confined environment

Cederwall (1971) carried out an experimental classification of the different types of flow regimes that can occur downstream of a buoyant slot jet in a confined, uniformly flowing environment

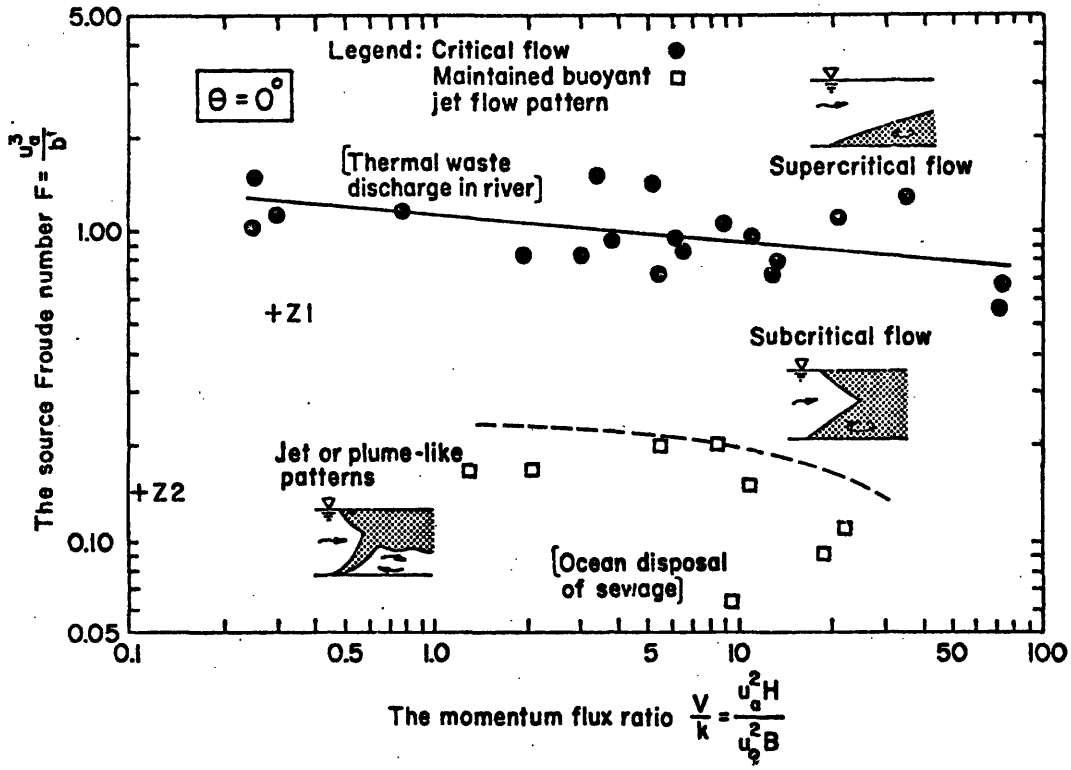

Observed flow regimes for a horizontal buoyant slot jet in a co-flowing stream. Critical flow defined as the situation when the formation of a surface wedge is incipient at the reference section.

Fig. 2-4 Downstream flow regimes for a horizontal buoyant slot jet in a coflowing stream (from Cederwall, 1971)

u_o jet velocity
B jet width
u_a ambient current velocity
$\Delta\rho_o$ initial density difference
b' buoyancy flux
$= g\frac{\Delta\rho_o}{\rho_a} u_o B$

(Fig. 2-4). This simulates a unidirectional thermal diffuser operating in a river situation. For a horizontal jet the downstream flow condition is primarily governed by a source Froude number defined by $F = u_a^3/g \frac{\Delta\rho_o}{\rho_a} u_o B$, a measure of the strength of the current relative to the buoyancy flux at the source. When $F \leq 1$ a subcritical flow with a surface wedge penetrating upstream of the diffuser is observed. When $F \geq 1$ a super-critical flow occurs with the jet flow swept downstream when reaching the surface; this represents the situation when the buoyant jet cannot entrain all the oncoming flow while maintaining the free buoyant jet flow pattern. The jet then breaks up and efficient mixing takes place close to the source.

Hydraulic scale model studies and field tests done for the thermal outfall into the Mississippi River from the Quad Cities Nuclear Plant, Illinois, also indicate complete vertical mixing of condenser water with the river flow downstream of the diffuser (Jain, Sayre, 1971; Parr, D., 1975). Similar conclusions were also reached by Harleman, Hall, Curtis (1968) in a study of thermal diffusion of condenser water in a river with application to the T.V.A. Browns Ferry Nuclear Power Plant.

Harleman, Jirka, Stolzenbach (1971) investigated the mixing downstream of three jets placed in a channel. Temperature measurements demonstrate that full horizontal and vertical mixing are obtained in the downstream region. Typical temperature profiles are shown in Fig. 2-5.

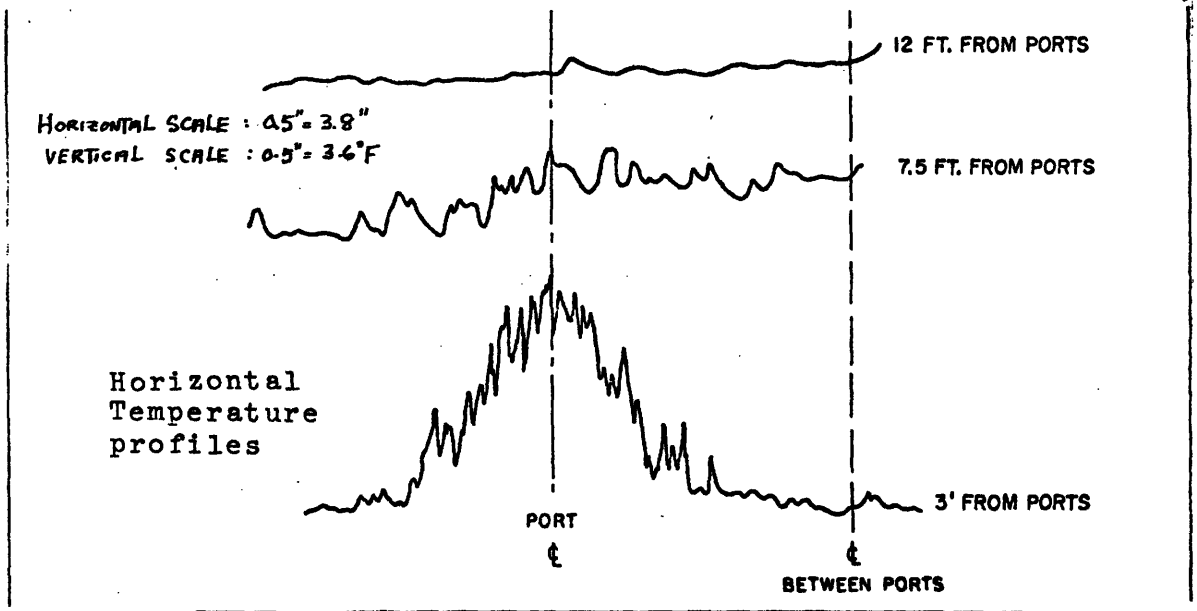

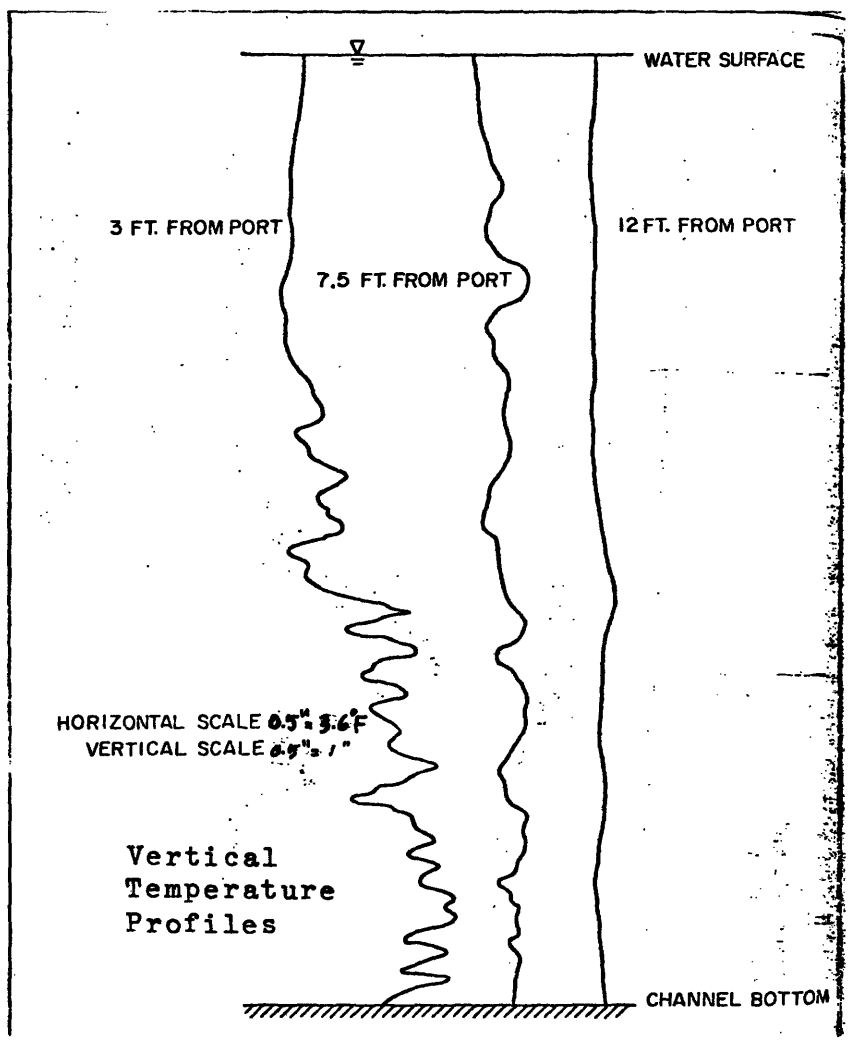

Fig. 2-5 Temperature profiles downstream of heated jets placed in a channel

Jirka and Harleman (1973) gave a theoretical treatment of the stability of a two dimensional buoyant slot jet in stagnant shallow water. It was found that for a certain combination of H/B (a measure of shallowness) and F_S (a measure of the buoyancy of the discharge) no stably stratified flow is possible near the jet. Intense vertical mixing is created and consequently the temperature profile downstream is vertically homogenous.

Whereas the instability in the case of a buoyant slot jet in a confined flowing environment is primarily induced by the ambient current, the instability of a buoyant slot jet in stagnant water is dominated by discharge conditions: the jet momentum and the shallowness of the receiving water.

It should be pointed out that the rate of initial mixing of a multiport diffuser in a river is determined by the ratio of the river flow to the condenser flow. Also, for diffusers with length comparable to the width of the river (the Quad Cities Plant or the Browns Ferry Plant, for example), the mixing downstream is strongly influenced by lateral boundaries.

2.4.2 Unidirectional multiport diffusers in a laterally unconfined shallow environment

A theory on the initial mixing performance of a unidirectional multiport diffuser in an unconfined environment was first proposed by Adams (1971). Assuming full vertical mixing a control volume analysis indicates a contraction of the mixed

flow downstream. The theory predicts the total induced flow downstream from the diffuser in a coflowing current. However, the two-dimensional nature of the flow field was not discussed. The location of the contraction, the boundary conditions along the diffuser, the extent and nature of the flow field cannot be obtained from the solution. Adams's analysis is further discussed in Chapter III.

Boericke (1975) studied the interaction of multiple jets with an ambient current by solving the vertically averaged equations of motion numerically. Predictions of flow patterns surrounding the proposed thermal outfall for the D.C. Cook Nuclear Plant on Lake Michigan were in qualitative agreement with dye studies reported by the Alden Research Laboratories (Fig. 2-6). The numerical solution reveals large scale recirculation (in which the discharge flow is re-entrained in a circulatory flow pattern) can occur when the ambient current is not strong enough to supply the entrainment demand. This would impair the dilution cooling near the diffuser as heat is being recirculated.

Although the numerical modelling approach holds much promise for a more complete description of the flow and temperature field, there are several shortcomings; In Boericke's work the velocity boundary conditions around the thermal outfall are obtained by adding the velocities due to each individual slot jet at the outfall vectorially. However, even

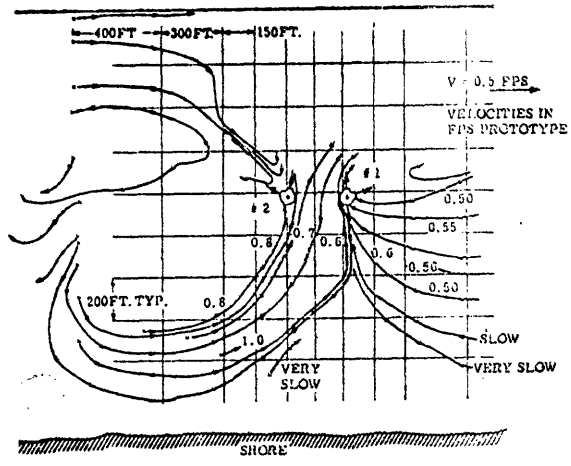

FIG. 1.—Recirculation Patterns Observed in Dye Studies of Hydraulic Model (1 ft = 0.305 m; 1 fps = 0.305 m/s)

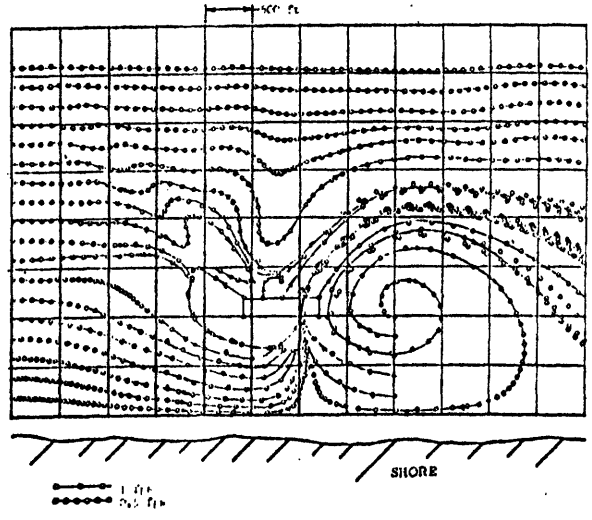

FIG. 4.—Calculated Flow Pattern for 0.5-fps Ambient Current (1 fps = 0.305 m/s; 1 ft = 0.305 m)

Fig. 2-6 Numerical predictions of diffuser-induced flow patterns (from Boericke,1975)

if the water body can be considered infinite, only the momentum fluxes can be superposed and not the velocities. Furthermore, as discussed before, in shallow water pressure can hardly be considered constant and therefore even superposition of momentum fluxes is not justified. The error introduced in the particular case cited may not be large as there are only four slots oriented in different directions in the thermal outfall. In the general case of a unidirectional multiport diffuser with many closely spaced ports, the interaction of the jets in shallow water have to be accounted for in order to arrive at the correct boundary conditions to be imposed around the diffuser. In some cases, the near field mixing of a diffuser may be strongly influenced by the presence of an ambient current, i.e., the boundary conditions for the vertically averaged equations may be coupled with an ambient condition and cannot be specified independently.

2.5 Criterion for unstable near field: basis of a two dimensional approach

Fig. 2-7 shows the stability criterion given by Jirka and Harleman for a horizontal slot buoyant jet in stagnant water. On the same diagram the (F_s, H/B) values of unidirectional diffuser experiments in a laterally unconfined water body for which direct temperature measurements have verified the vertical homogeneity of the temperature field downstream are plotted. From all the available data, we

see that the prediction of stability for a two dimensional slot jet is a good indication of the near field stability of a three dimensional unidirectional diffuser.

The foregoing discussion suggests it is useful to look at the diffuser induced temperature field two dimensionally and ignore the vertical variations as a valid approximation. Except for an initial jet mixing region of limited extent, this approach is valid up to the point where stratification becomes important in determining the flow field. In practice the region of validity will cover the surface isotherms of interest. Furthermore, under prototype conditions, wind induced mixing and turbulence created by heat flux out of the water surface will enhance the vertical homogeneity of the temperature field.

2.6 Summary of previous work

It has been recognised both experimentally and theoretically that the heat discharged by thermal multiport diffusers in shallow water will be vertically fully mixed. Buoyant jet or plume like patterns cannot be maintained and the nature of the flow field is changed considerably.

For unidirectional multiport diffusers in an open water body, simulating the Great Lakes or ocean coastal regions, existing theory can only predict the total induced flow near the diffuser. To date no comprehensive treatment of the temperature field induced by a unidirectional diffuser

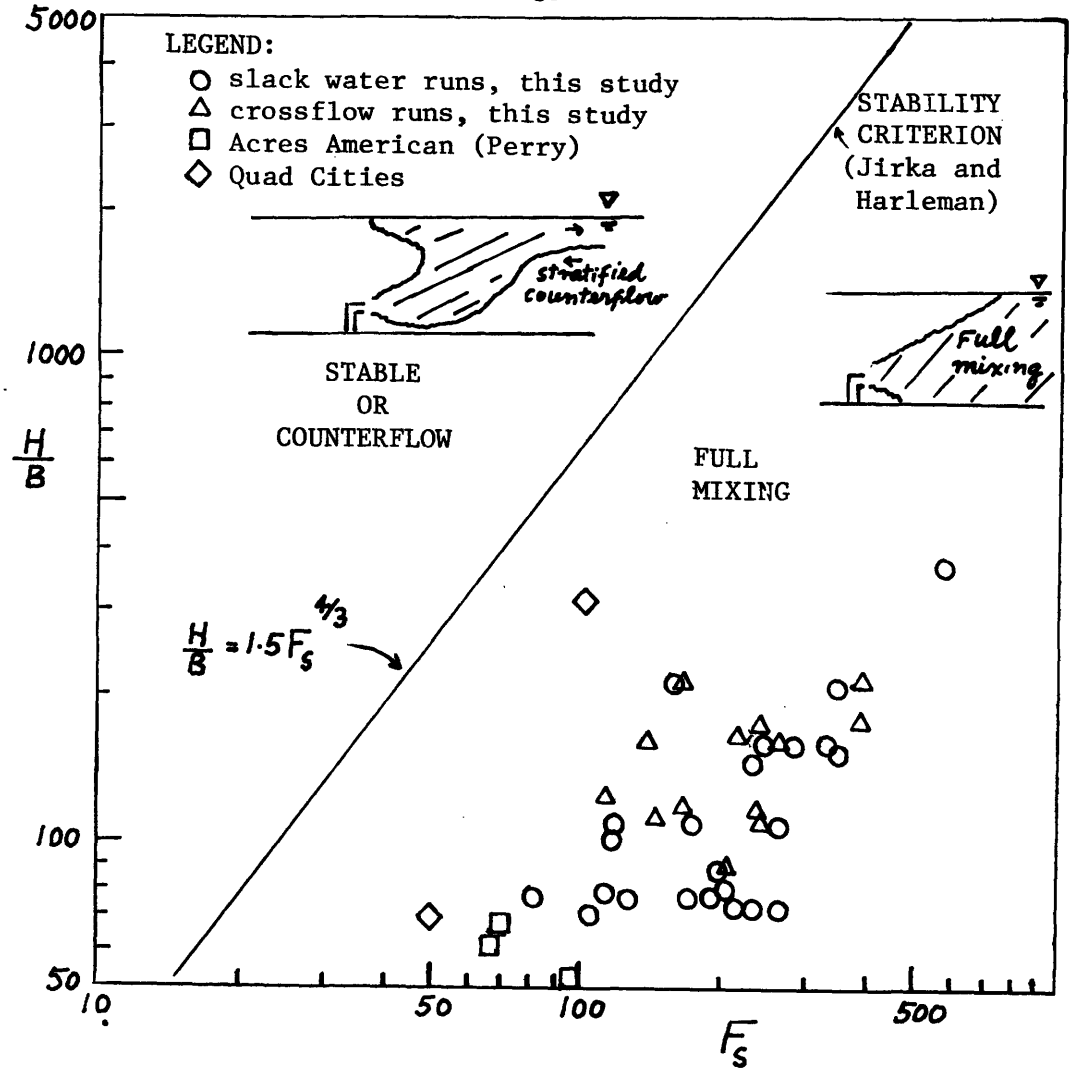

$$F_s = \frac{u_s}{\sqrt{g\frac{\Delta\rho_o}{\rho_a}B}}$$

u_s equivalent slot jet velocity
$\Delta\rho_o$ initial density difference
ρ_a ambient density
H water depth
B equivalent slot jet width

Fig. 2-7 Near Field Instability of Unidirectional thermal diffusers in shallow water

has been done. Data reported by previous workers are limited to hydraulic scale model studies of specific sites and as such little general insights can be extracted from these scattered experimental data.

Numerical modelling of thermal discharges in shallow water has been attempted. However, previous efforts suffer from the lack of knowledge of the correct boundary conditions for the flow and temperature field near the diffuser.

Areas of knowledge requiring further research include:

1. A better understanding of the diffuser induced flow field.
2. A predictive model of the temperature field as a function of diffuser design parameters.
3. A comprehensive set of experiments that can provide a data base for validation of existing or future theoretical modelling efforts, as well as providing meaningful empirical guidelines in situations that are too difficult to model analytically.
4. An understanding of the nature of heat return from the far field; this may be self-induced by the pumping action of the diffuser over prolonged periods of slack in a tidal situation, or due to the interaction of an ambient current with the diffuser flow.

All the above points are addressed in this study.

CHAPTER III

A THEORY FOR THE TEMPERATURE FIELD INDUCED BY A UNIDIRECTIONAL DIFFUSER IN A COFLOWING CURRENT: THE NEAR FIELD SOLUTION

The next two chapters are devoted to a theoretical discussion of the diffuser induced temperature field for the case when the diffuser momentum is aligned in the same direction as the ambient current. This simulates a diffuser operating in a coastal zone and in particular, the limiting case, when there is no current, often reprsents the most severe design condition for thermal diffusers. A near field theory is presented in this chapter. The coupling of the near field solution with an intermediate field theory is treated in the next chapter. The near field theory does not consider the question of heat return from the far field.

3.1 General Statement of the Problem

Consider a unidirectional multiport diffuser consisting of N identical ports of cross-sectional area a_o, equal spacing s, and discharging heated water in the form of turbulent jets at temperature T_o and velocity u_o in the same direction into an infinite receiving water body of depth H and uniform temperature T_a. The ports are located near the bottom. The diffuser length, L_D, is defined as the distance between the first and the last port. The upstream current velocity is u_a. The problem is schematized in Fig. 3-1 and the relevant parameters are defined.

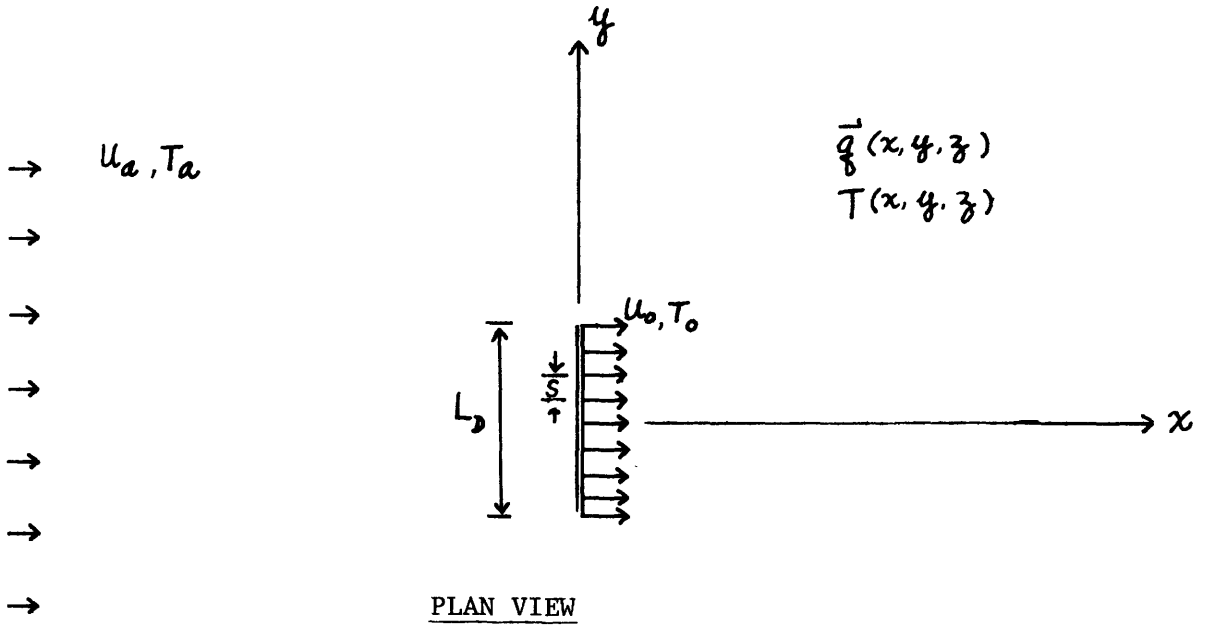

PLAN VIEW

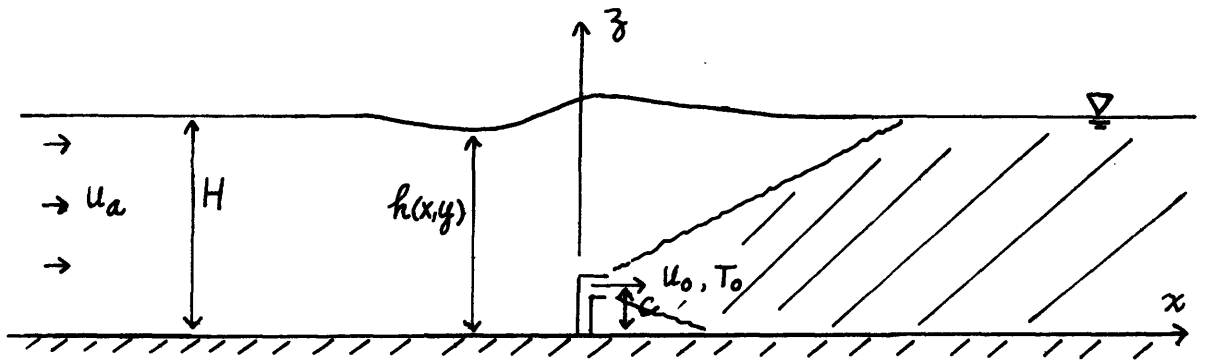

ELEVATION

u_o	discharge velocity	u_a	ambient current velocity
a_o	port area	T_a	ambient temperature
N	number of ports	H	receiving water depth
s	port spacing	h(x,y)	free surface elevation
L_D	diffuser length	$\Delta T=T-T_a$	temperature excess
T_o	discharge temperature	$\Delta h=h-H$	free surface deviation
c	port clearance from bottom		

Fig. 3-1 Unidirectional diffuser in a coflowing current: Problem Definition

3.2 The Complete Three-dimensional Formulation

Setting up a Cartesian co-ordinate system (x,y,z) with the origin at the center of the diffuser and defining

velocity: $\vec{q}\ (x,y,z) = [u,v,w]\ (x,y,z)$

temperature: $T\ (x,y,z)$

free surface: $h\ (x,y)$
level

A turbulent flow situation is considered and the quantities are time-averaged over the scale of turbulence. Assuming an incompressible fluid and neglecting molecular viscosity and transport terms, the following governing equations are obtained for steady flow:

Continuity:

$$\frac{\partial u}{\partial x} + \frac{\partial v}{\partial y} + \frac{\partial w}{\partial z} = 0 \tag{3.1}$$

Momentum:

$$\rho\left(u\frac{\partial u}{\partial x} + v\frac{\partial u}{\partial y} + w\frac{\partial u}{\partial z}\right) = -\frac{\partial p}{\partial x} - \rho\left(\frac{\partial \overline{u'^2}}{\partial x} + \frac{\partial \overline{u'v'}}{\partial y} + \frac{\partial \overline{u'w'}}{\partial z}\right) \tag{3.2}$$

$$\rho\left(u\frac{\partial v}{\partial x} + v\frac{\partial v}{\partial y} + w\frac{\partial v}{\partial z}\right) = -\frac{\partial p}{\partial y} - \rho\left(\frac{\partial \overline{u'v'}}{\partial x} + \frac{\partial \overline{v'^2}}{\partial y} + \frac{\partial \overline{v'w'}}{\partial z}\right) \tag{3.3}$$

$$\rho\left(u\frac{\partial w}{\partial x} + v\frac{\partial w}{\partial y} + w\frac{\partial w}{\partial z}\right) = \rho g - \frac{\partial p}{\partial z} - \rho\left(\frac{\partial \overline{u'w'}}{\partial x} + \frac{\partial \overline{v'w'}}{\partial y} + \frac{\partial \overline{w'^2}}{\partial z}\right) \tag{3.4}$$

Heat conservation:

$$u \frac{\partial T}{\partial x} + v \frac{\partial T}{\partial y} + w \frac{\partial T}{\partial z} = - \frac{\partial \overline{u'T'}}{\partial x} - \frac{\partial \overline{v'T'}}{\partial y} - \frac{\partial \overline{w'T'}}{\partial z} \quad (3.5)$$

For small temperature differences the equation of state can be written as:

$$\rho - \rho_a = \beta_e \rho_a (T - T_a) \quad (3.6)$$

where β_e is the coefficient of thermal expansion of water at T_a.

The Boundary conditions are:

<u>On the free surface</u>, $z = h(x,y)$

$$u \frac{\partial h}{\partial x} + v \frac{\partial h}{\partial y} = w \qquad p = o$$

<u>At large distances from the diffuser</u>, $(x,y) \to \infty$

$$(u,v,w) \to u_a$$

$$h(x,y) \to H \qquad T(x,y,z) \to T_a \quad (3.7)$$

<u>At the bottom</u>, $z=0$

$$\vec{q} = 0$$

$$\frac{\partial T}{\partial z} = 0$$

<u>At each discharge port</u>

$$(u,v,w) = (u_o, o, o)$$

$$T = T_o$$

The system of governing equations (3.1 - 3.6) with the associated boundary conditions presents a formidable task in arriving at a complete solution valid for the entire region. Instead a zone modelling approach is taken. Physical insight gained from experimental experience allows the division of the entire solution domain into several regions, each with distinct hydrodynamic properties. In the following sections, the approximate governing equations for each region are presented; the solution is sought in each region and the solutions are coupled to give a global solution for the entire field.

3.3 Dimensional Analysis

As a prelude to the ensuing theoretical discussion, a dimensional analysis is presented in this section to single out the important dimensionless parameters of the problem.

Letting $\Delta T = T - T_a$ be the temperature excess above the ambient temperature, we can write the functional relationship

$$f(\Delta T, \Delta T_o, x, y, z, a_o, N, H, L_D, u, v, w, c, u_o, g, T_a, u_a) = 0 \quad (3.8)$$

Choosing $\Delta T_o, H, u_o$ as the fundamental variables, the following parameter groupings can be obtained,

$$\left(\frac{\Delta T}{\Delta T_o}, \frac{(u,v,w)}{u_o}\right) = F\left(\frac{(x,y,z)}{H}, \frac{L_D H}{N a_o}, \frac{u_a}{u_o}, \frac{u_o}{\sqrt{g\beta_e \Delta T_o \frac{NH}{L_D}}}, \right.$$

$$\left. \frac{c}{H}, \frac{s}{H}, \frac{u_o}{\sqrt{gH}}\right) \quad (3.9)$$

Dimensionless Parameter	Nomenclature in this study	Typical range of values	physical interpretation and comments
$\frac{L_D H}{N a_o}$ or $\frac{sH}{a_o}$ For N large	β / H/B	50-500	ratio of intercepted cross-sectional area per port to port area: relative submergence of equivalent slot jet. $B = a_o/s$ is the width of the slot jet having the same discharge flow and momentum per unit length
$\frac{L_D}{H}$		10-50	relative diffuser length
$\frac{u_a}{u_o}$	γ	< 0.1	strength of ambient current
$\frac{u_o}{\sqrt{g\beta_e \Delta T_o \frac{a_o}{s}}}$	F_S	50-500	densimetric Froude number of the equivalent slot jet: measure of the buoyancy of the discharge
$\frac{s}{H}$		< 3.0	relative spacing: important only in initial jet mixing zone where temperature field is three dimensional
$\frac{c}{H}$		< 0.2	relative clearance of the ports
$\frac{u_o}{\sqrt{gH}}$		$\sim O(1)$	jet Froude number based on the water depth

Table 3-1 Summary of Governing Dimensionless Parameters

The physical interpretation of each parameter is given in Table 3-1; typical values are also indicated.

Under vertically fully mixed conditions variations in the z direction can be neglected and the two dimensional problem ceases to depend on the details of the diffuser design described by $\frac{c}{H}$, $\frac{s}{H}$.

$$\left(\frac{\Delta T}{\Delta T_o}, \frac{(u,v)}{u_o}\right) = F\left(\frac{(x,y)}{H}, \frac{L_D H}{Na_o}, \frac{L_D}{H}, \frac{u_a}{u_o}, \frac{u_o}{\sqrt{g\beta_e \Delta T_o}\ \frac{Na_o}{L_D}}, \frac{u_o}{\sqrt{gH}}\right)$$

3.4 The vertically Averaged Equations

In this section, the equations of motion and energy are integrated in the z direction to yield a set of equations for the depth averaged quantities.

Assuming u,v>>w, so that pressure is hydrostatic we integrate eq. 3.1, 3.2, 3.3, and 3.5 vertically from z = 0 to z = h(x,y). Invoking the kinematic boundary condition at the free surface and the no slip condition at the bottom, and with repeated use of Leibnitz's rule, we arrive at

Continuity

$$\frac{\partial}{\partial x}\int_o^{h(x,y)} u\, dz + \frac{\partial}{\partial y}\int_o^{h(x,y)} v\, dz = 0 \qquad (3.10)$$

Momentum

$$\rho \left(\frac{\partial}{\partial x}\int_o^h u^2 dz + \frac{\partial}{\partial y}\int_o^h uv dz\right) = -g\int_o^h \frac{\partial}{\partial x}(\rho h)\, dz$$

$$-\frac{\partial}{\partial x}\int_o^h \rho\,\overline{u'^2}\, dz - \frac{\partial}{\partial y}\int_o^h \rho\,\overline{u'v'}\, dz - \tau_{zx}\Big|_{z=0} \qquad (3.11)$$

$$\rho \left(\frac{\partial}{\partial x}\int_o^h uv dz + \frac{\partial}{\partial y}\int_o^h v^2 dz\right) = -g\int_o^h \frac{\partial}{\partial y}(\rho h) dz$$

$$-\frac{\partial}{\partial x}\int_o^h \rho\,\overline{u'v'}\, dz - \frac{\partial}{\partial y}\int_o^h \overline{v'^2}\, dz - \tau_{zy}\Big|_{z=0} \qquad (3.12)$$

Heat conservation

$$\frac{\partial}{\partial x}\int_o^h uT dz + \frac{\partial}{\partial y}\int_o^h vT dz = -\frac{\partial}{\partial x}\int_o^h \overline{u'T'}\, dz$$

$$-\frac{\partial}{\partial y}\int_o^h \overline{v'T'}\, dz - \overline{w'T'}\Big|_{z=h} \qquad (3.13)$$

Defining the vertically averaged quantities

$$\bar{u} = \frac{1}{h}\int_o^h u\, dz \tag{3.14}$$

$$\bar{v} = \frac{1}{h}\int_o^h v\, dz \tag{3.15}$$

we have

$$\int_o^h u^2 dz = \left(\frac{\int_o^h u^2 dz}{h\,\bar{u}^2}\right) h\bar{u}^2 \tag{3.16}$$

$$\int_o^h v^2 dz = \left(\frac{\int_o^h v^2 dz}{h\,\bar{v}^2}\right) h\,\bar{v}^2 \tag{3.17}$$

$$\int_o^h uv dz = \left(\frac{\int_o^h uv dz}{h\,\bar{u}\,\bar{v}}\right) h\,\bar{u}\,\bar{v} \tag{3.18}$$

The following assumptions are made:

i) The coefficients resulting from the averaging in eq. 3.16-3.18 are close to unity. For turbulent open channel flows, for example, the vertical variation of velocity can be assumed to obey a 1/7 power law; the coefficient computed for this profile is 1.015.

ii) Changes in free surface level are small, $\Delta h/H, << 1$.

iii) Density differences are small, $\frac{\Delta\rho}{\rho_a} << 1$, and can be neglected except when multiplied by the gravity term in the equations of motion (The Boussinesq approximation).

iv) A quadratic friction law is assumed for the bottom shear

$$\tau_{zx} = \frac{f_o}{8} \rho \sqrt{u^2+v^2}\, u \qquad (3.19)$$

f_o: Friction Factor

$$\tau_{zy} = \frac{f_o}{8} \rho \sqrt{u^2+v^2}\, v \qquad (3.20)$$

v) Turbulent transfers in the x direction is neglected.

vi) Surface heat transfers are neglected.

Incorporating these assumptions into eq. (3.10 - 3.13) we obtain the vertically averaged equations. For simplicity the depth averaged quantities will henceforth appear without bars.

$$\frac{\partial u}{\partial x} + \frac{\partial v}{\partial y} = 0 \qquad (3.21)$$

$$u \frac{\partial u}{\partial x} + v \frac{\partial u}{\partial y} = - g \frac{\partial h}{\partial x} - \beta_e g \int_o^h \frac{\partial \Delta T}{\partial x} dz - \frac{\partial \overline{u'v'}}{\partial y} - \frac{f_o}{8H} \sqrt{u^2+v^2}\, u \qquad (3.22)$$

$$u \frac{\partial v}{\partial x} + v \frac{\partial v}{\partial y} = - g \frac{\partial h}{\partial y} - \beta_e g \int_o^h \frac{\partial \Delta T}{\partial y} dz - \frac{\partial \overline{v'^2}}{\partial y} - \frac{f_o}{8H} \sqrt{u^2+v^2}\, v \qquad (3.23)$$

$$u \frac{\partial T}{\partial x} + v \frac{\partial T}{\partial y} = -\frac{\partial \overline{v'T'}}{\partial y} \qquad (3.24)$$

3.5 A synopsis of the flow field

A brief description of a physical picture of the diffuser induced flow field is given in this section.

Turbulent mixing is created by the high velocity shear near each discharge port. The jets merge with one another and the

spreading reaches the water surface at approximately 5 to 10 H away. The interaction of the multiple jets produces a predominantly two dimensional flow field as shown in Fig.3-2a. A negative pressure zone is created behind the diffuser, to which a fluid particle at infinity would tend to converge; the flow pattern behind the diffuser resembles that of a sink flow. The momentum input raises the pressure across the diffuser, creating a positive pressure in front of it. The induced flow from behind 'separates' from the ambient fluid at the ends of the diffuser and is confined in a contracting stream tube. Fig. 3.2b illustrates an instantaneous snapshot of the flow field in an experiment.

3.5.1 Scaling

Through a proper choice of characteristic scales for the physical variables we can estimate the relative importance of the terms in eq. (3.21-3.23) for each region.

Let

(U,V) be characteristic velocities in the x,y direction

(L,δ) be characteristic lengths in the x,y direction

$\rho_a g\Delta H$ be characteristic pressure deviation

$\Delta\rho$ be a characteristic density difference

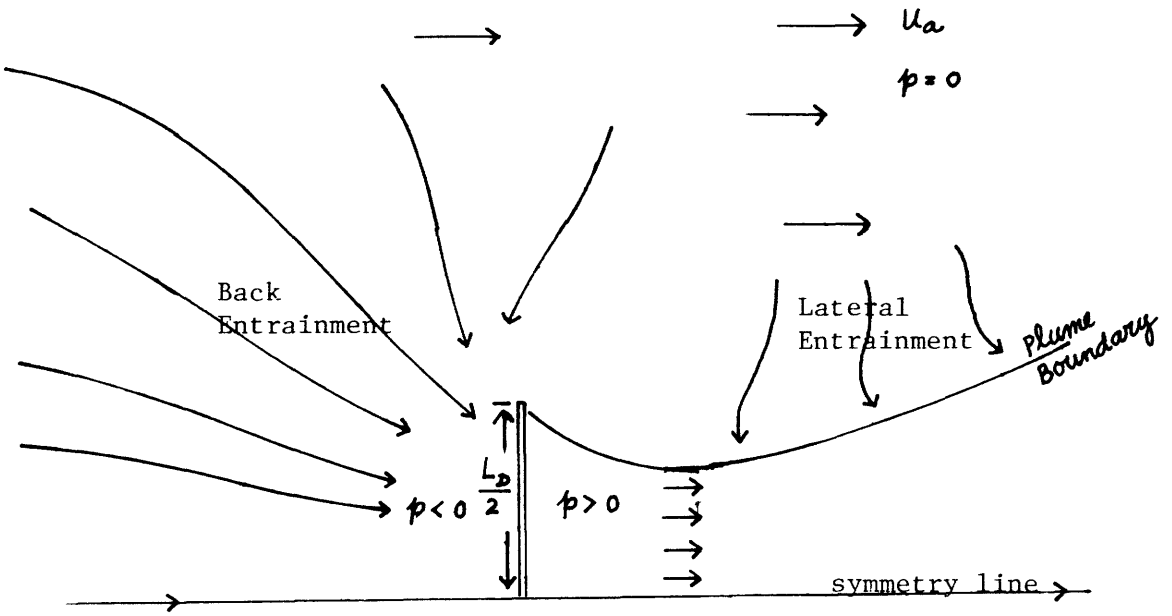

Fig. 3-2 a) Schematic of surface flow field

Fig. 3-2 b). An instantaneous snapshot of the diffuser induced flow field in slack water
(photo by C. Almquist)

Thus in eq. 3.22, 3.23

inertia $\sim U^2/L$

pressure $\sim g\Delta H/L$

buoyancy $\sim \frac{\Delta\rho}{\rho} gH/_L$

The magnitude of the lateral turbulent shear stress terms can be estimated and related to mean flow quantities by mixing length concepts commonly used in free shear flows (Abramovich)

$$\overline{-u'v'} \sim \ell^2 \left(\frac{\partial u}{\partial y}\right)^2$$

where ℓ: mixing length

The mixing length can be assumed to be proportional to the transverse length scale $\ell = c'\delta$

where c' is an empirical constant. For free jets $c' \sim 10^{-1}$

a) <u>The Near Field:</u> In a region close to the diffuser $L \sim L_D$ the following scales apply:

$L \sim L_D \quad \delta \sim L_D$

$U \sim V \quad \Delta H \sim U^2/2g$

Using typical values of

L_D = 1000 ft.

H = 20 ft.

U = 2 fps

$\Delta\rho/\rho$ = 0.0004 (corresponding to an induced temperature rise of 4^{o}F)

f_o = 0.02

The relative importance of each term can be estimated:

$$\frac{\text{pressure}}{\text{inertia}} \sim \frac{g\,H}{U^2} \sim O(1)$$

$$\frac{\text{lateral shear}}{\text{inertia}} \sim \frac{c'\,2U^2L^2/\delta^3}{U^2/L} \sim c'^2\left(\frac{L}{\delta}\right)^3 \sim O\ (10^{-2})$$

$$\frac{\text{buoyancy}}{\text{inertia}} \sim \frac{\frac{\Delta\rho}{\rho}\,gH}{U^2} \sim 0\ (10^{-2})$$

$$\frac{\text{bottom shear}}{\text{inertia}} \sim \frac{f_o L_D}{8H} \sim 0\ (10^{-1})$$

We therefore conclude that pressure must balance inertia in this region. Lateral shear, buoyancy and bottom friction are not important in the near field. The approximate equations for the near field are then

$$\frac{\partial u}{\partial x} + \frac{\partial v}{\partial y} = 0$$

$$u\frac{\partial u}{\partial x} + v\frac{\partial u}{\partial y} = -g\frac{\partial h}{\partial x}$$

$$u\frac{\partial v}{\partial x} + v\frac{\partial v}{\partial y} = -g\frac{\partial h}{\partial y} \qquad (3.25a)$$

$$u\frac{\partial T}{\partial x} + v\frac{\partial T}{\partial y} = -\frac{\partial \overline{v'T'}}{\partial y}$$

b) The Intermediate Field

In a region beyond the near field, $L \sim 10L_D$, the flow takes on a boundary layer character, so that

$$\delta << L$$

$$V << U$$

The scale of free surface deviation is then due to turbulent side entrainment

$$\Delta H \sim \frac{(\alpha U)^2}{2g}$$

where α = entrainment coefficient = 0.06

Then

$$\frac{\text{pressure}}{\text{inertia}} \sim \alpha^2 \sim 10^{-3}$$

so that the dominant balance is among the convective terms, lateral shear and bottom friction. This region of extent $10^3 H$ is called the 'intermediate field'. Beyond a certain point, when friction has reduced the velocity to a scale that

$$\frac{g \frac{\Delta\rho}{\rho} H}{U^2} \sim 0(1)$$, buoyancy effects will have to be accounted.

The governing equations for the intermediate field are then

$$\frac{\partial u}{\partial x} + \frac{\partial v}{\partial y} = 0$$

$$u \frac{\partial u}{\partial x} + v \frac{\partial u}{\partial y} = - \frac{\partial \overline{u'v'}}{\partial y} - \frac{f_o}{8H} u|u| \qquad (3.25b)$$

Cont.
(3.25b)

$$u \frac{\partial v}{\partial x} + v \frac{\partial v}{\partial y} = - \frac{\overline{\partial v'^2}}{\partial y} - \frac{f_o}{8H} v |u|$$

$$u \frac{\partial T}{\partial x} + v \frac{\partial T}{\partial y} = - \frac{\overline{\partial v' T'}}{\partial y}$$

3.6 Outline of Near Field Theory

A two dimensional model for the flow field downstream of the undirectional diffuser is presented in the following sections. A vertically fully mixed condition is hypothesized, the equations of motion are then independent of the temperature field. The total induced flow near the diffuser is first derived by a control volume analysis. This is then used as an integral boundary condition to obtain a potential flow solution of the near field. In Chapter IV the near field solution is coupled into an intermediate field theory that predicts the global temperature field.

A definition sketch of the near field problem is illustrated in Fig. 3-3. The following assumptions are made:

1) As a first approximation, turbulent side entrainment is neglected in this region and Laplace's equation is assumed to hold. As far as the depth-averaged motion is concerned, in the region beyond the initial jet mixing zone, vorticity can be generated only by turbulent lateral shear. It then follows that if turbulent entrainment has a negligible effect on the fluid motion in this region (as shown by the scaling arguments),

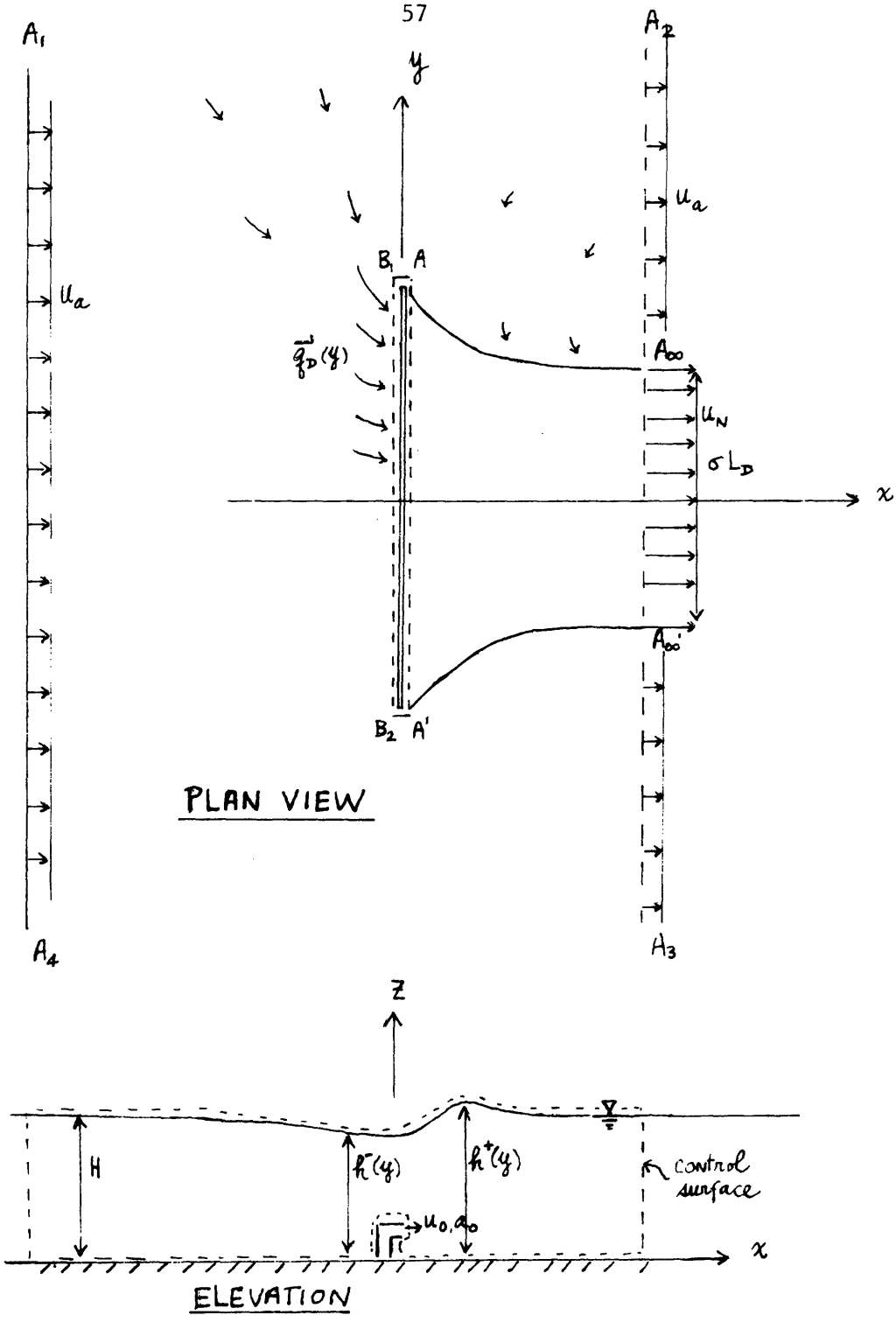

Fig. 3-3 Control volume analysis of a unidirectional diffuser in a coflowing current

the two dimensional fluid motion can be considered irrotational. Furthermore, a solution of Laplace's equation also satifies eq. (3.25a).

2) The induced flow from behind the diffuser 'separates' from the ambient fluid at the ends of the diffuser, and is confined in a streamtube A $A_\infty A'_\infty A'$. The slip streamline can then be regarded as a locus of velocity discontinuity separating the flow within the streamtube from the ambient fluid. Pressure is continuous across the slip streamline.

In a real fluid the discontinuity in velocity is of course unstable and generates eddies that will draw the ambient fluid into the streamtube. This correction is small and can be included as a perturbation in the development of the intermediate field theory in Chapter IV.

3) A high rate of mixing is assumed; i.e. the induced flow is large compared with the discharge flow.

4) The momentum input of the diffuser creates a pressure discontinuity across the diffuser; but velocities are continuous across it. Alternatively, depth changes are small $\Delta H/H << 1$. In principle, this amounts to a "rigid lid" assumption.

5) Bottom friction is neglected.

3.6.1 Control Volume Analysis

In this section an integral quantity of interest, the total induced flow Q_N, is derived using a control volume analysis of the two dimensional flow field. The approach is the same as given by Adams (1972). The analysis is included here for completeness; unnecessary assumptions are removed and issues relating to the formulation of a complete two dimentional problem are discussed in greater detail.

The following quantities are defined:

$Q_N = SQ_o$ total induced flow from behind

S near field dilution

$\vec{q}_D(y)$ velocity distribution along the diffuser

$(x=0, -L_D/2 \leq y \leq L_D/2)$

$q_D(y) = |\vec{q}_D(y)|$

As shown in Fig. 3-3, two control volumes are chosen: Bounded by the free surface and the bottom in the vertical direction, the outer control volume $A_1A_2A_3A_4$ is chosen such that A_1A_4 is sufficiently far upstream from x=0, A_2A_3 at a downstream position where h=H. The four corners are at $y = \pm \infty$. The inner control volume, $B_1AA'B_2$, is chosen to just enclose the diffuser.

The boundary conditions along the control surfaces are then:

Along

$$A_1A_2 \qquad \vec{q} = (u_a, 0)$$

$$A_4A_3 \qquad h = H \tag{3.26}$$

$$A_1A_4$$

$$A_2A_\infty$$

$$A_3A'_\infty$$

Along

$$A_\infty A'_\infty \qquad \vec{q} = (u_N, 0)$$

$$h = H$$

Along

$$B_1B_2 \qquad \vec{q} = \vec{q}_D(y)$$

$$h = h^-(y)$$

$$AA' \qquad \vec{q} = \vec{q}_D(y)$$

$$h = h^+(y)$$

Applying Bernoulli's theorem along any streamline that extends from A_1A_4 to B_1B_2, we have

$$\frac{u_a^2}{2g} + H = \frac{q_D^2(y)}{2g} + h^-(y) \tag{3.27}$$

Similarly for the same streamline leading from AA' to $A_\infty A'_\infty$

$$\frac{u_N^2}{2g} + H = \frac{q_D^2(y)}{2g} + h^+(y) \tag{3.28}$$

Subtracting eq. 3.27 from eq. 3.28, we have an expression for the head rise Δh along the diffuser:

$$\Delta h(y) = h^{+}(y) - h^{-}(y) = \frac{u_N^2 - u_a^2}{2g} \tag{3.29}$$

we see that regardless of the velocity distribution $\vec{q}_D(y)$, the head rise is constant along the diffuser,

$$\Delta h = \text{constant} \tag{3.30}$$

Applying the momentum theorem in the x-direction to the outer control volume described by $A_1A_2A_3A_4$ we obtain

$$\rho S Q_o u_a + \rho Q_o u_o = \rho S Q_o u_N \tag{3.31}$$

As there is no net contribution of pressure forces, the difference in the x-momentum fluxes out of A_2A_3 and into A_1A_4 must be equal to $(\rho S Q_o u_N - \rho S Q_o u_a)$, assuming $S \simeq S-1$; this is equal to the momentum input $\rho S Q_o u_o$.

Similarly for the inner control volume $B_1AA'B_2$,

$$Q_o u_o = g \int_{-\frac{L_D}{2}}^{\frac{L_D}{2}} 1/2 \left[h^{+}(y)^2 - h^{-}(y)^2 \right] dy \tag{3.32}$$

The momentum input is balanced by an increase in pressure force across the diffuser. For a small deviation in the

free surface level $\frac{1}{2}(h^+ + h^-) \approx H$, and by virture of eq. 3.30 eq. 3.32 then becomes

$$Q_o u_o = gL_D H\Delta h \tag{3.33}$$

Recapitulating the complete set of equations for the control volume analysis:

$$\Delta h = \frac{u_N^2 - u_a^2}{2g} \tag{3.34}$$

$$Q_o u_o = gL_D H\Delta h \tag{3.35}$$

$$SQ_o u_a + Q_o u_o = SQ_o u_N \tag{3.36}$$

Noting $Q_o = Na_o u_o$, and rearranging, an equation for S, the near field dilution can be obtained

$$S^2 - \left(\frac{L_D H}{Na_o}\right)\left(\frac{u_a}{u_o}\right) S - \frac{1}{2}\left(\frac{L_D H}{Na_o}\right) = 0 \tag{3.37}$$

The solution is

$$S = \frac{\beta\gamma + \sqrt{\beta^2\gamma^2 + 2\beta}}{2} \tag{3.38}$$

where

$$\beta = \frac{L_D H}{Na_o} \qquad \gamma = \frac{u_a}{u_o}$$

The width of $A_\infty A_\infty'$ can be obtained by equating

$$SQ_o = u_N \sigma L_D H \tag{3.39}$$

from which we get the contraction coefficient

$$\sigma = \frac{S\gamma + 0.5}{S\gamma + 1} \tag{3.40}$$

3.6.2 Limiting Cases

Considerable insight can be gained by examining the limiting case of no ambient current, $u_a = 0$. Setting $\gamma = 0$ in eqs. 3.36, 3.38, 3.40 gives

$$S = \sqrt{\frac{L_D H}{2Na_o}}$$

$$\sigma = 1/2$$

$$u_N = u_o/S \tag{3.41}$$

Thus, the contraction of the mixed flow away is always 1/2 regardless of the diffuser length. The pressure deviation can be evaluated as $\frac{\Delta h}{H} = \frac{u_N^2}{2gH}$. Using typical values of

$$S = 10 \qquad u_o = 20 \text{ fps} \qquad H = 20 \text{ ft}$$

$$u_N = u_o/S = 2 \text{ fps}$$

gives $\frac{\Delta h}{H} = 0.003$, confirming that the pressure deviation is indeed small; Δh is less than an inch in 20 feet of water.

In the limit of high crossflows $L_D H u_a >> N a_o u_o$, or $\beta\gamma >> 1$ eqs. 3.38, 3.40 gives

$$S = \beta\gamma$$

and

$$\sigma = 1 \tag{3.42}$$

The dilution is then equal to the ratio of the intercepted crossflow and the discharge flow.

It should be pointed out the assumption of high dilutions, $S>>1$, is not a restrictive one. A similar analysis that is valid for all dilutions is included in Appendix A. However, even for S=3, the deviation in the prediction for the near field dilution is only a few per cent.

3.7 A Potential Flow Model for the Near Field

From the control volume analysis we have derived the total induced flow confined in a streamtube $AA_\infty A'_\infty A'$. However, the location of the contraction, the shape of the streamtube, and the extent of the flowfield are unknown.

In this section, the boundary conditions along the diffuser are derived. The position of the slip streamline is solved by free streamline theory and a potential flow solution is obtained in the near field by the method of finite differences.

By symmetry we need consider only one half of the streamtube (Fig. 3-4). Assuming potential flow we can define a complex potential $W(z)$ of the flow field as a function of a complex variable $z = x + iy$ corresponding to a point in the physical plane.

$$\nabla^2 \phi = 0$$

$$\frac{\partial \phi}{\partial x} = u \qquad \frac{\partial \phi}{\partial y} = v$$

$$W(z) = \phi(x,y) + i\psi(x,y)$$

$$\vec{q}(x,y) = \overline{\frac{dW}{dz}} = qe^{i\theta} \tag{3.43}$$

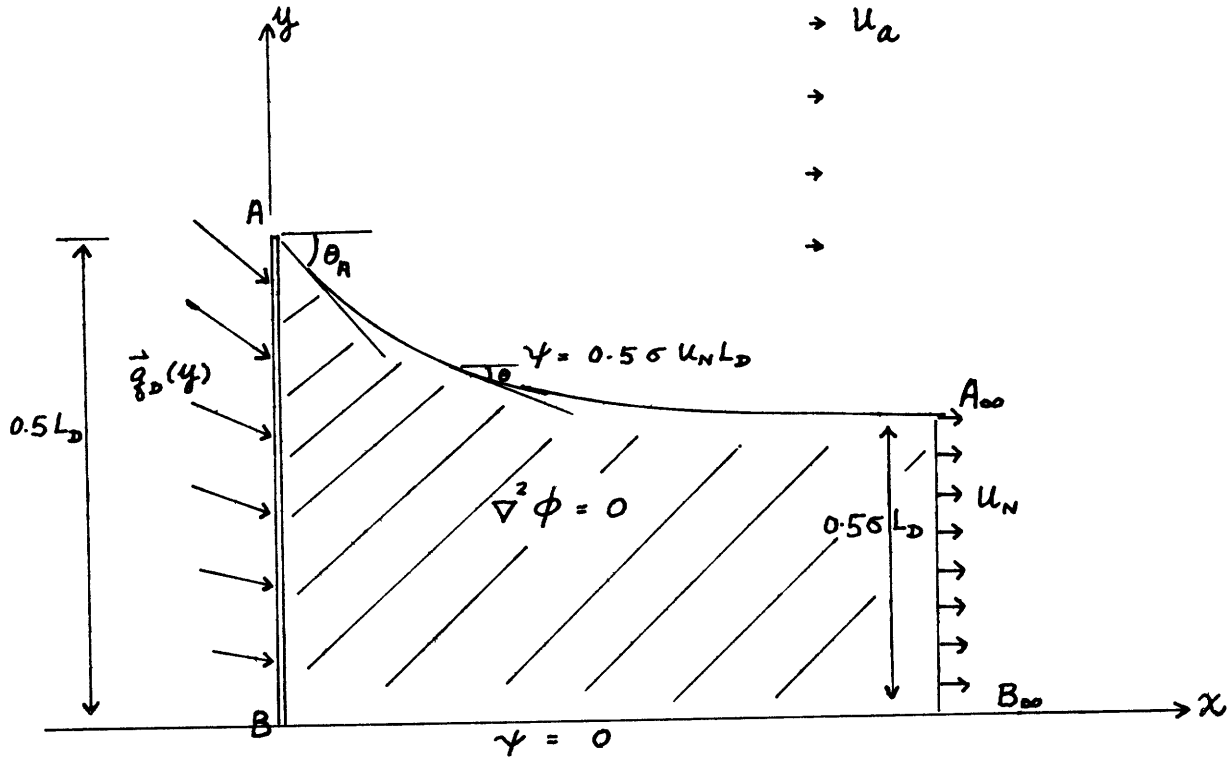

Fig. 3-4 A potential flow model for the near field

where

ϕ = velocity potential

ψ = stream function

$\vec{q}$ = complex velocity u(x,y) + iv(x,y)

$q = \left|\frac{dW}{dz}\right|$

θ = inclination of velocity vector from x-axis

$\vec{q}_D$ = velocity along diffuser line

$\vec{q}_A$ = velocity at point of separation A

W_A = complex potential at A

W_B = complex potential at diffuser center B

3.7.1 Basic Assumption

Consider a general case where the induced flow from behind the diffuser is given by $0.5\sigma L_D u_N$ where

u_N : velocity at A_∞

σ : contraction coefficient of streamtube

u_N, σ are given by eqs. 3.38-3.40. This may be conceived as an integral boundary condition.

We suppose that locally near x=0, each section of the diffuser induces the same amount of flow: i.e., each individual jet entrains the same amount of ambient flow.

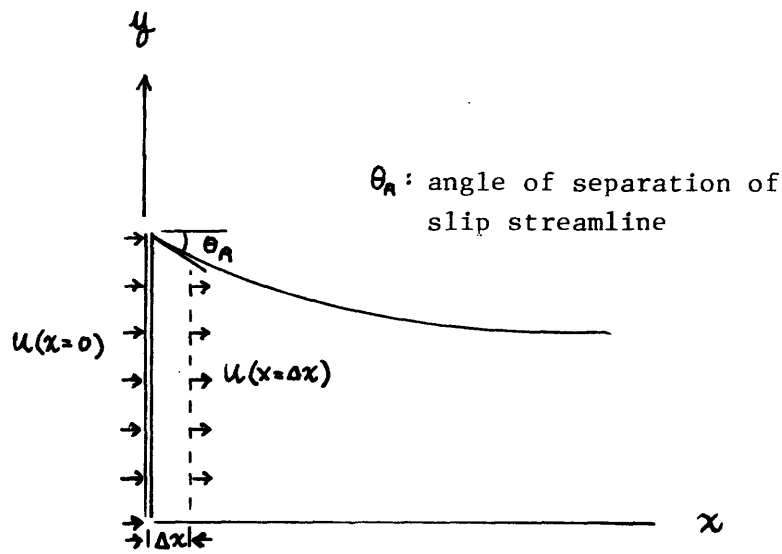

Fig. 3-5 Boundary conditions along the diffuser line

This assumption implies that locally near x=0, the horizontal velocity gradient, $\frac{\partial u}{\partial x}$, is also not a function of y. Applying conservation of mass to an infinitesimal portion of the streamtube near x=0, as shown in Fig. 3-5, we have

$$\begin{aligned} u(x=0) &= (1 - \Delta x \tan \theta_A)\, u(x = \Delta x) \\ &= (1 - \Delta x \tan \theta_A)(u(x=0) + \left.\frac{\partial u}{\partial x}\right|_{x=0} \Delta x) \end{aligned} \tag{3.44}$$

Equating terms of order Δx

$$\left.\frac{\partial u}{\partial x}\right|_{x=0} = u(0) \tan \theta_A = \text{constant} \tag{3.45}$$

Thus

$$u|_{x=0} = \text{constant}$$

$$\left.\frac{\partial u}{\partial x}\right|_{x=0} = \text{constant} \tag{3.46}$$

3.7.2 Derivation of the Boundary Conditions

By symmetry BB_∞ is a streamline.

If we define $\psi = 0$ on BB_∞

it follows $\psi = 0.5\sigma L_D u_N$ on AA_∞ (3.48)

Along the slip streamline AA_∞

$$p = p_\infty$$

Applying Bernoulli's theorem to any point on the slip streamline

$$p_\infty + \frac{1}{2}\rho q^2 = p_\infty + \frac{1}{2}\rho u_N^2$$

therefore $q = u_N$ (3.48)

The magnitude of the velocity on the slip streamline is constant and equal to the speed at the contraction, u_N.

Along the diffuser axis AB

i) Since u=constant by continuity we have

$$u = \sigma u_N \tag{3.49}$$

and $$q_D = \frac{\sigma u_N}{\cos\theta}\text{ , by definition} \tag{3.50}$$

ii) Since $\frac{\partial u}{\partial x}$ = constant

invoking continuity again we have

$$\frac{\partial v}{\partial y} = \text{constant}$$

By symmetry

$v = 0$ at the diffuser center B

therefore $v(y) = v_A \frac{2y}{L_D}$ (3.51)

where v_A = y component of velocity at A

Whilst the x-component of $\vec{q}_D(y)$ is constant along the diffuser axis, the y-component varies linearly.

At the point of separation A

$$q_A = u_N$$

and $$u_A = \sigma u_N \tag{3.52}$$

since $q_A \text{Cos}\theta_A = u_A$

we have $\cos\theta_A = \sigma$

or $\theta_A = \cos^{-1}\sigma$ (3.53)

where θ_A is the angle of separation

As $v_A = q_A \sin\theta_A$, by virtue of eq. 3.49-3.51

$$v_A = u_N \text{Sin}\theta_A \frac{2y}{L_D} \tag{3.54}$$

Recapitulating the boundary conditions, and defining the velocity potential at the diffuser center $\phi_B = 0$, we have

Along AA_∞

$\psi = 0.5\sigma L_D u_N$

ϕ = varies from ϕ_A at A to ∞ at A_∞

$q = u_N$

θ varies from θ_A at A to 0 at A_∞

Along BB_∞

$\psi = 0$

ϕ varies from 0 at B to ∞ at B_∞ (3.55)

$v = 0$

$\theta = 0$

Along AB

$$\frac{d\psi}{dy} = \sigma u_N = u$$

$$\frac{d\phi}{dy} = u_N \text{Sin}\theta_A \frac{2y}{L_D} = v$$

$\phi(0) = 0 \qquad \psi(0) = 0$

$$q = \frac{\sigma u_N}{\cos\theta}$$

θ varies from 0 at B to θ_A at A

3.7.3 Solution of the slip streamline

The position of the slip streamline is solved by Kirchoff's method (alternatively called the Hodograph plane method) which has been commonly used in classical free streamline theory (Milne-Thomson, 1968; Gurevich, 1965). The idea is to map the complex potential W and the complex velocity $\frac{dW}{dz}$ onto an intermediate common variable ζ. If each mapping is kept one-to-one, we will have obtained a one-to-one correspondence between W and $\frac{dz}{dW}$, thus solving the problem.

The complex potential W diagram for the case when $u_a=0$ is illustrated in Fig. 3-6. The shaded portion within $A_\infty ABB_\infty$ corresponds to the flow within the streamtube. The positions of the points A,A_∞,B,B_∞ on the W plane, represent the (ϕ,ψ) values at the locations A,A_∞,B,B_∞ in the physical plane (x,y). The boundaries of the shaded portion is derived using eq. 3.55.

Let the hodograph plane Q be defined as

$$Q = \log(u_N \frac{dz}{dW})$$

$$= \ln (\frac{u_N}{q}) - i\theta \qquad (3.56)$$

The hodograph plane Q is illustrated in Fig. 3-7. Again the shaded portion describes the flow field within the streamtube. The points A,A_∞,B,B_∞ on the Q plane represent the $(\ln \frac{u_N}{q} ,\theta)$ values at the locations A,A_∞,B,B_∞ in the physical plane (x,y). The boundaries of the shaded portion is derived using eq.3.55

If we can find intermediate transformations

$$\frac{W}{0.5\sigma L_D u_N} = f_1(\zeta)$$

$$Q = f_2(\zeta) \qquad (3.57)$$

then

$$\frac{dz}{dW} = \frac{1}{u_N} \exp\ (Q)$$

$$d\left(\frac{z}{0.5L_D}\right) = \sigma \exp\ [Q(\zeta)]\ \frac{d\left[\frac{W}{0.5\sigma L_D u_N}\right]}{d\zeta}\, d\zeta \qquad (3.58)$$

Replacing z,W by its non-dimensionalized counterparts:

$$z = z_o + \int \sigma \exp(f_2(\zeta))\ \frac{df_1}{d\zeta}\, d\zeta \qquad (3.59)$$

Given the path in the ζ plane corresponding to the slip streamline, eq. 3.59 will give the position of z by intergrating along the ζ plane.

Both the W-diagram and the Q diagram are approximated by polygons and the interior of these polygons are mapped onto the upper half plane ζ by the Schwartz-Christoffel Transformation, with the following correspondences specified, as shown in Fig. 3-6, 3-7.

W,Q plane		ζ plane
A_∞	<———>	$(-\infty,0)$
A	<———>	$(-1,0)$
B	<———>	$(+1,0)$

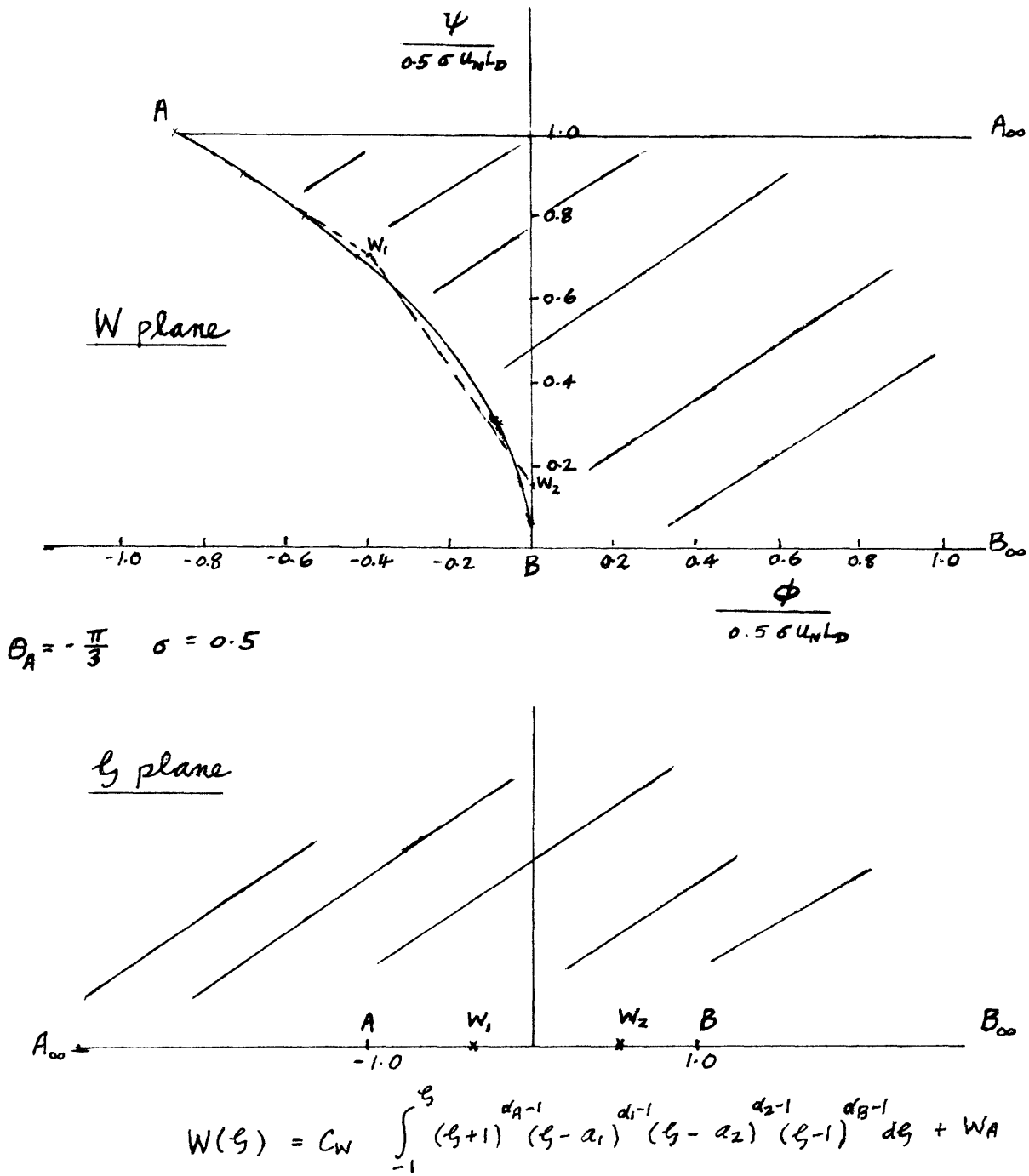

Fig. 3-6 Conformal mapping of the complex potential plane W onto the upper half plane

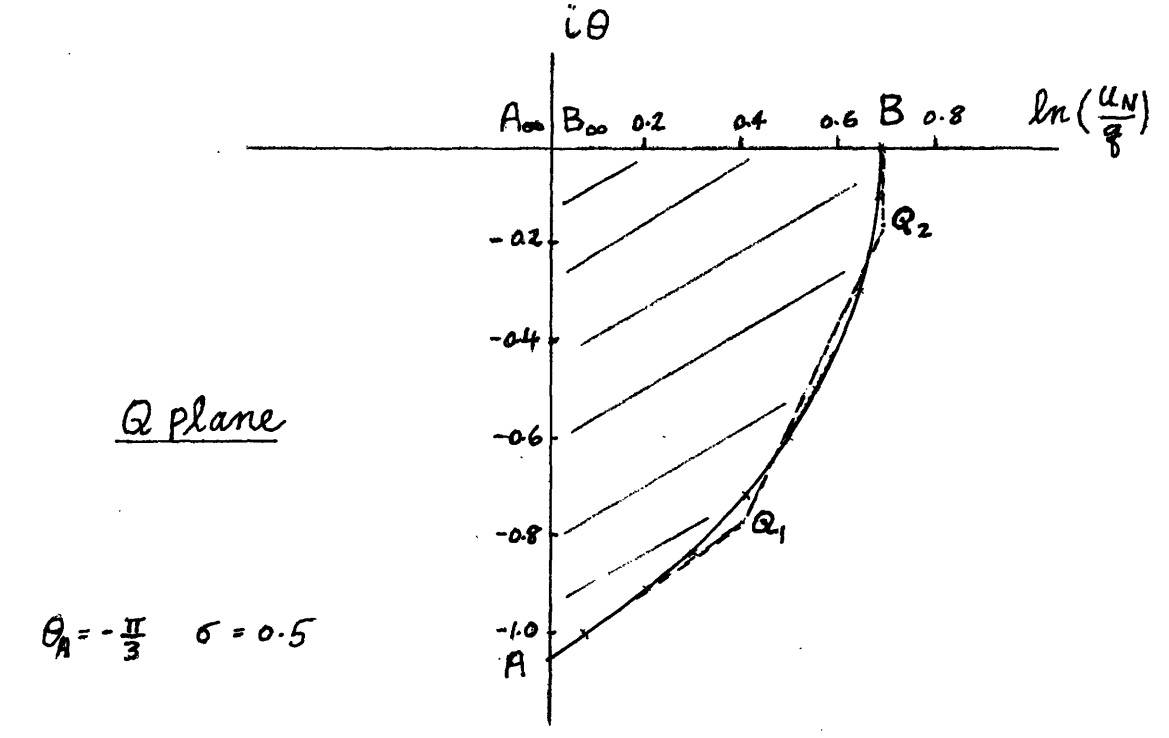

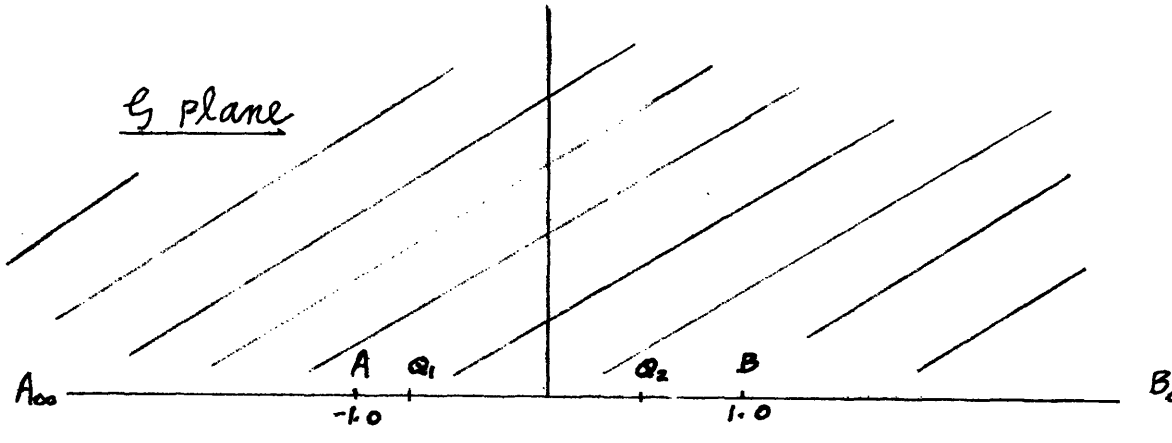

$$Q(\zeta) = C_Q \int_{-1}^{\zeta} (\zeta+1)^{\beta_A-1} (\zeta-b_1)^{\beta_1-1} (\zeta-b_2)^{\beta_2-1} (\zeta-1)^{\beta_B-1} d\zeta + Q_A$$

Fig. 3-7 Conformal mapping of the hodograph plane onto the upper half plane

The points A_∞, A, B for the W and Q diagrams are mapped onto three arbitrary choices on the real axis. It can be shown B_∞ is then mapped onto $(+\infty, 0)$

The curvilinear boundary $A_\infty ABB_\infty$, in the W plane is approximated by a six sided polygon $A_\infty AW_1W_2BB_\infty$.

By the Schwartz-Christoffel Transformation, we have

$$W(\zeta) = C_W \int_{-1}^{\zeta} (\zeta+1)^{\alpha_A - 1} (\zeta - a_1)^{\alpha_1 - 1} (\zeta - a_2)^{\alpha_2 - 1} (\zeta - 1)^{\alpha_B - 1} d\zeta + W_A \quad (3.60)$$

where α_i : interior angles of the W polygon in units of π

W_A : co-ordinate of point A in the W plane

C_W : constant

It can be shown that W_1, W_2 will be mapped onto points $(a_1, 0)$, $(a_2, 0)$ where $-1 < a_1 < a_2 < 1$

The computational details required to calculate C_W, a_1, a_2 are included in Appendix B.

In an entirely analogous manner the Q diagram is approximated by a six-sided polygon $A_\infty AQ_1Q_2BB_\infty$. The Q-$\zeta$ transformation is given by

$$Q(\zeta) = C_Q \int_{-1}^{\zeta} (\zeta+1)^{\beta_A - 1} (\zeta - b_1)^{\beta_1 - 1} (\zeta - b_2)^{\beta_2 - 1} (\zeta - 1)^{\beta_B - 1} d\zeta + Q_A \quad (3.61)$$

where

β_i : interior angles of the Q-polygon in units of π

$(b_1,0),(b_2,0)$: corresponding points of Q_1,Q_2 on the real axis

Q_A : co-ordinate of the point A in the Q plane

Substituting the expression for $W(\zeta)$ and $Q(\zeta)$ in eq. 3.59 we obtain

$$z = z_o + \sigma \int_{-1}^{\zeta} \exp\left[C_Q \int_{-1}^{\zeta} (\zeta+1)^{\beta_A-1} (\zeta-b_1)^{\beta_1-1} (\zeta-b_2)^{\beta_2-1} (\zeta-1)^{\beta_B-1} d\zeta + Q_A\right]$$

$$C_W(\zeta+1)^{\alpha_A-1} (\zeta-a_1)^{\alpha_1-1} (\zeta-a_2)^{\alpha_2-1} (\zeta-1)^{\alpha_B-1} d\zeta$$

$$z_o = (0,1) \qquad (3.62)$$

Since the slip streamline AA_∞ corresponds to the strip $(-1,0)$ to $(-\infty,0)$ in the ζ plane, the (x,y) position of the slip streamline can then be evaluated using eq.(3.62) by integrating from $\zeta = -1$ to $\zeta = -\infty$.

3.7.4 Results

For a given diffuser design and ambient current, the contraction coefficient can be calculated by eq. 3.38, 3.40. The angle of separation θ_A is then obtained by eq. 3.53. The W and Q diagrams are generated accordingly by eq. 3.55. After finding the W-ζ, Q-ζ transformations, the positions of the slip streamlines can be evaluated by eq. 3.62.

In table 3-2 computed values of the near field dilution and the contraction coefficient are presented for typical

$\frac{L_D H}{N a_o}$	$\frac{u_a}{u_o}$	S	σ
50.0	0.0	5.0	0.5
150.0	0.0	8.7	0.5
300.0	0.0	12.3	0.5
50.0	0.025	5.7	0.56
150.0	0.025	10.7	0.60
300.0	0.025	16.6	0.65
50.0	0.04	6.1	0.60
150.0	0.04	12.2	0.67
300.0	0.04	19.6	0.72
50.0	0.067	6.9	0.65
150.0	0.067	15.0	0.75
300.0	0.067	25.9	0.82

Table 3-2 Near Field Dilution and Contraction coefficient for typical values of

$$\beta = \frac{L_D H}{N a_o} \quad \text{and} \quad \gamma = \frac{u_a}{u_o}$$

values of β and γ. It should be pointed out that different diffuser designs (different combinations of β and γ) can lead to the same near field dilution and contraction coefficient.

The predicted slip streamline is computed for different values of θ_A, the angle of separation, that encompass the range of practical interest. The results are illustrated in Fig. 3-8. The results show that

i) The slip streamline reaches an asymptotic value at $x \simeq 0.5L_D$. This means the extent of the near field is $0.5L_D$; this result coincides with visual observation of experiments performed over a wide range of diffuser lengths, and is illustrated in Fig. 3-2b.

ii) The slip streamline matches asymptotically the contraction coefficient given by eq. 3.40 for all θ_A. This is considered sufficient proof that the basic assumption stated in section 3.7.1 (from which the boundary conditions along the diffuser are derived) is correct. It is emphasized that an incorrect specification of the velocity distribution along the diffuser will lead to an erroneous asymptotic value that does not agree with the contraction coefficient given by eq. 3.40.

Details of the computations are given in Appendix D.

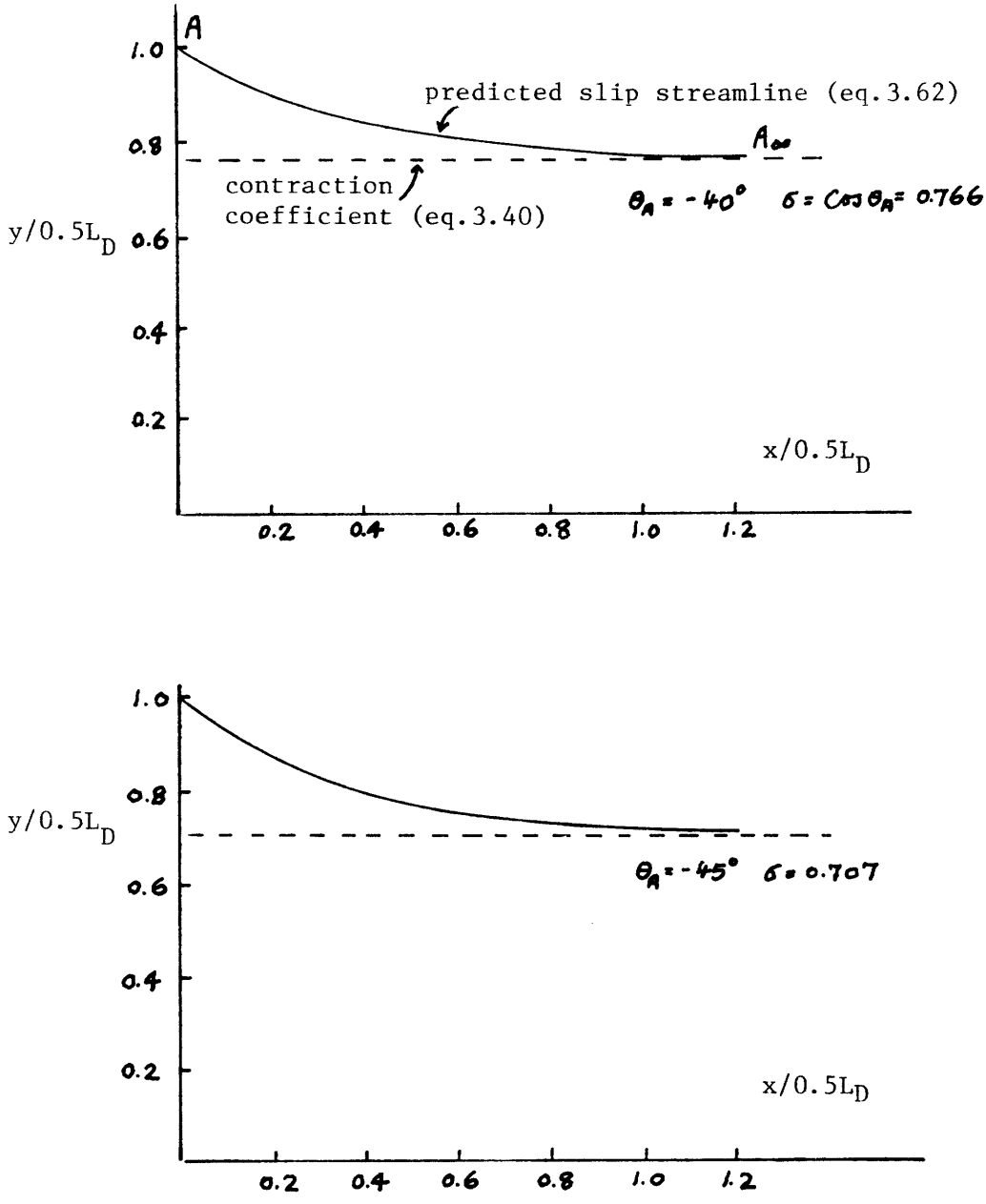

Fig. 3-8 Theoretical solution of slip streamline for different angles of separation θ_A

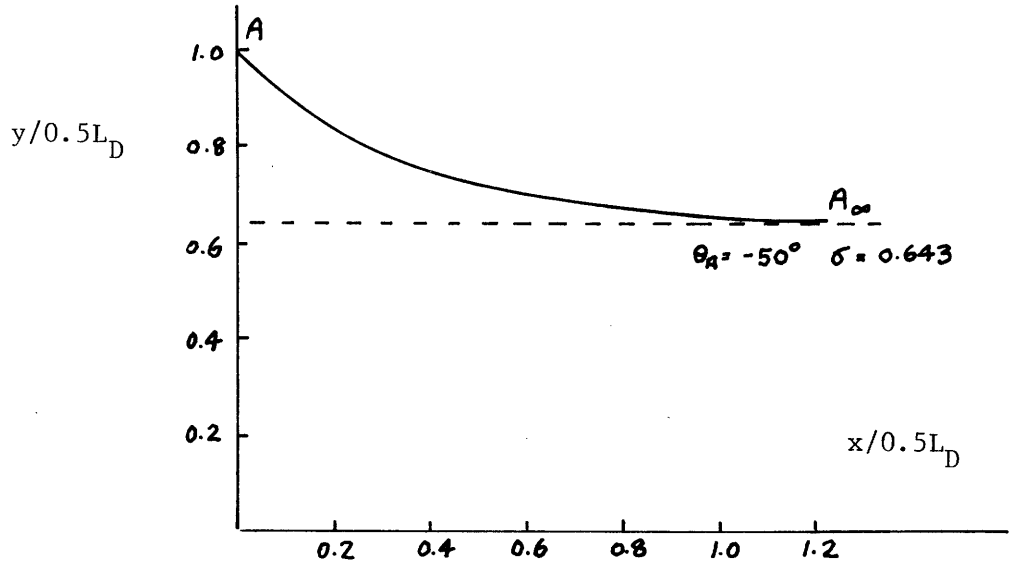
A
1.0
0.8
0.6
0.4
0.2
y/0.5L_D
A∞
θ_A = -50° σ = 0.643
x/0.5L_D
0.2
0.4
0.6
0.8
1.0
1.2

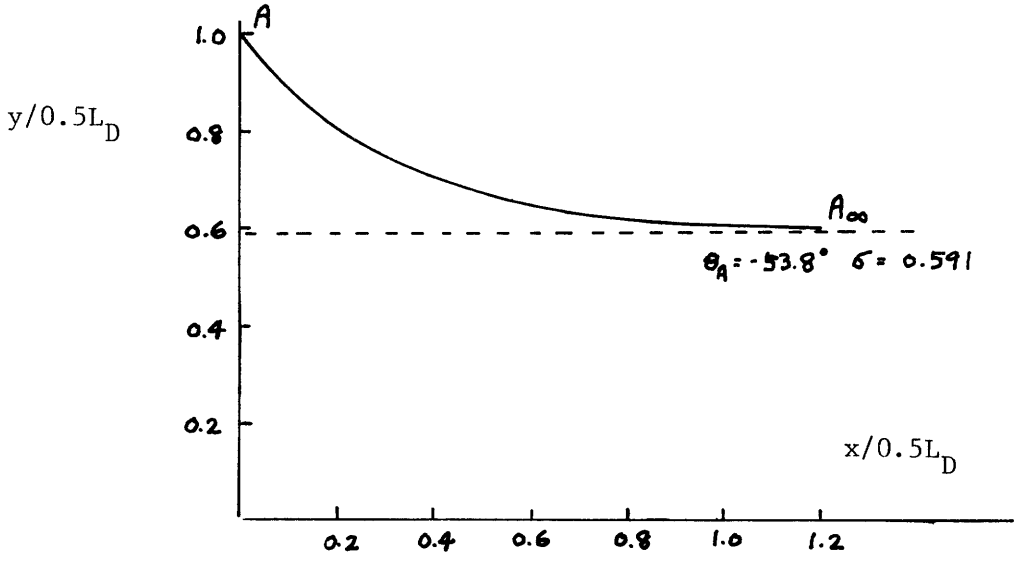
A
1.0
0.8
0.6
0.4
0.2
y/0.5L_D
A∞
θ_A = -53.8° σ = 0.591
x/0.5L_D
0.2
0.4
0.6
0.8
1.0
1.2

Fig. 3-8 cont'd

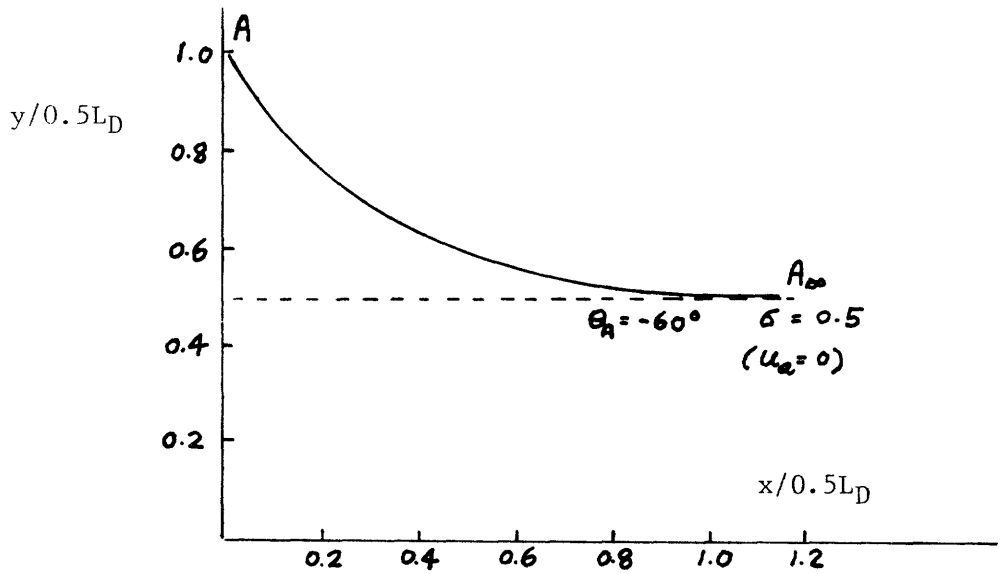

Fig. 3-8 cont'd

3.7.5 Sensitivity of results to the polygonal approximation

It was shown in Fig. 3-7 that the curvilinear boundaries along AB in both the W plane and the Q plane are approximated by polygonal boundaries AW_1W_2B and AQ_1Q_2B respectively. The straight boundaries AW_1,W_2B and AQ_1,Q_2B are chosen to closely approximate the slopes of the curvilinear boundary near A and B. The exact positions of W_1,W_2 or Q_1,Q_2 are chosen such that the polygon closely resembles the W, Q diagrams. Fig. 3-9 illustrates two quite different approximations of the W,Q diagrams for $\theta_A = -60^o$, $\sigma = 0.5$. Approximation A is indicated by the solid lines AW_1,W_2B,AQ_1Q_2B.

Approximation B is indicated by the dotted lines $AW'_1W'_2B$,$AQ'_1Q'_2B$. Fig. 3-10 illustrates the computed slip streamlines based on the two approximations. The difference in the predictions for the two cases is very small, demonstrating the limited sensitivity of the results to the polygonal approximations.

3.7.6 Solution for the flow field

It is found that for $0 \leq \frac{x}{0.5L_D} \leq 1.0$ the slip streamline can be well approximated by a 4th order polynomial

$$g(x^*) = x^{*4} - (\tan|\theta_A| + 2\sigma)x^{*3} + (2\tan|\theta_A| + 3\sigma - 2)x^{*2} - \tan|\theta_A|x^* + 1 \qquad (3.63)$$

$$x^* = \frac{x}{0.5L_D}$$

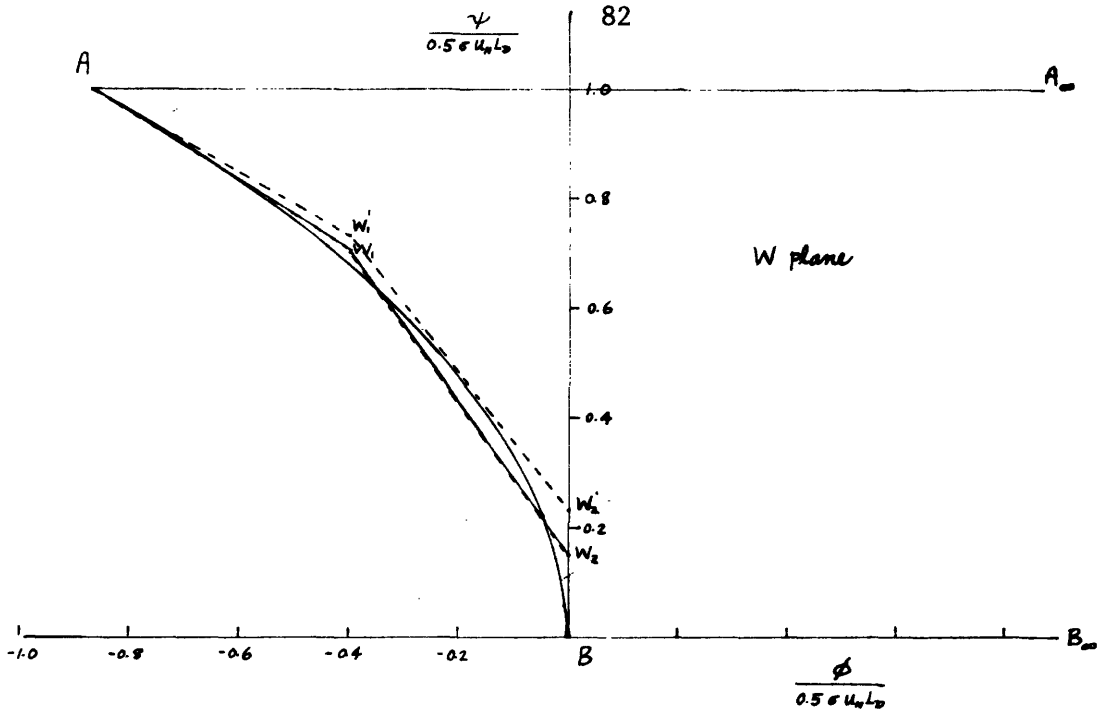

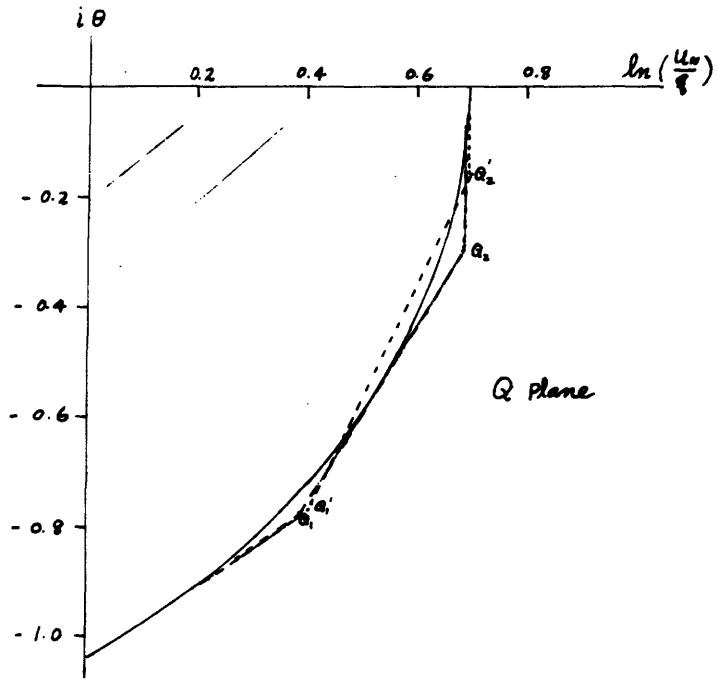

Fig. 3-9 Two different approximations of the W and Q diagram
Approximation A _____
Approximation B -----

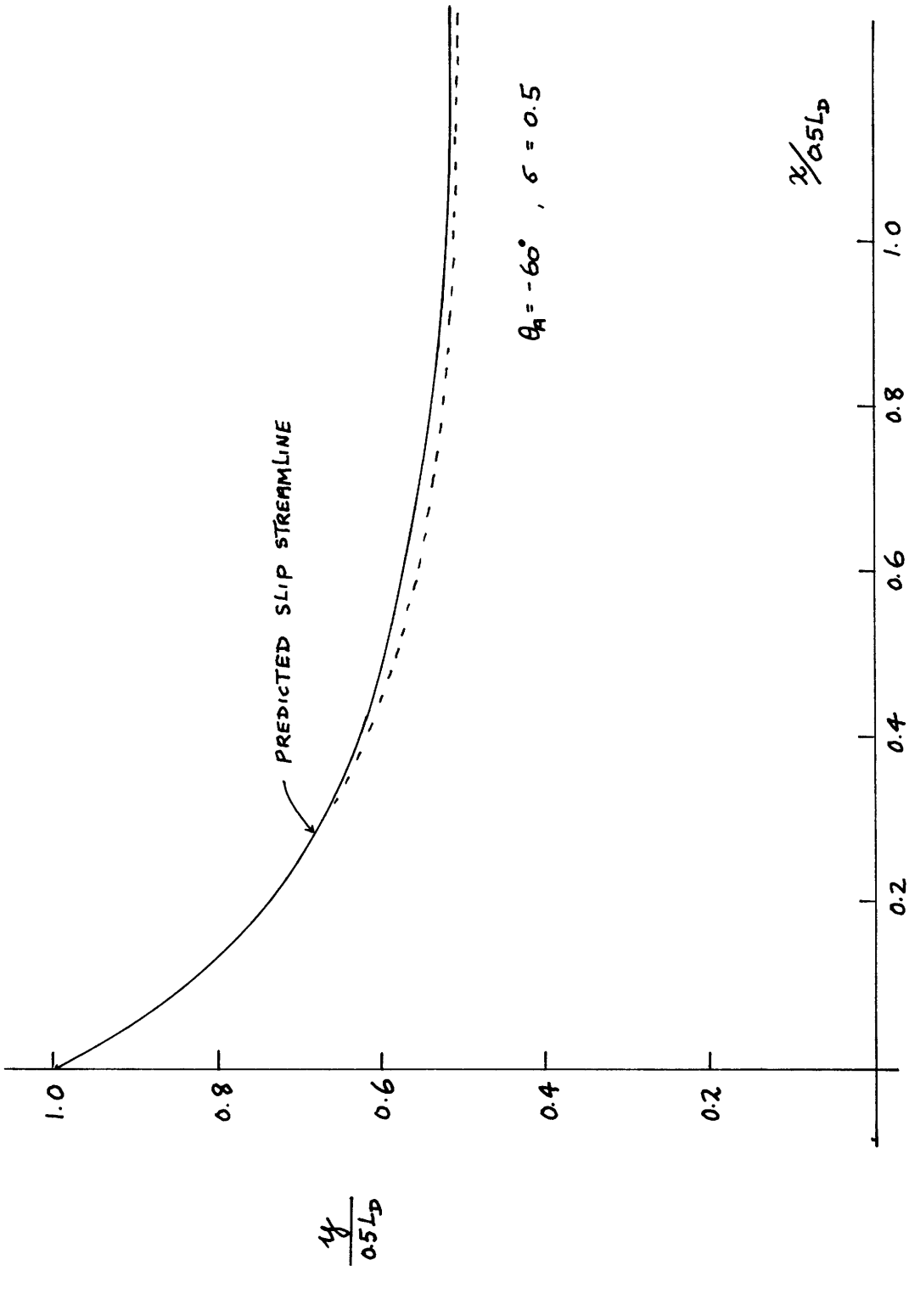

Fig. 3-10 Comparison of predicted slip streamlines of approximation A ——— and that of approximation B -----

Given g(x*), a numerical solution of the flow field can be solved in terms of the stream function ψ by the method of finite differences in the region $A_\infty ABB_\infty$. The boundary conditions are indicated in Fig. 3-11

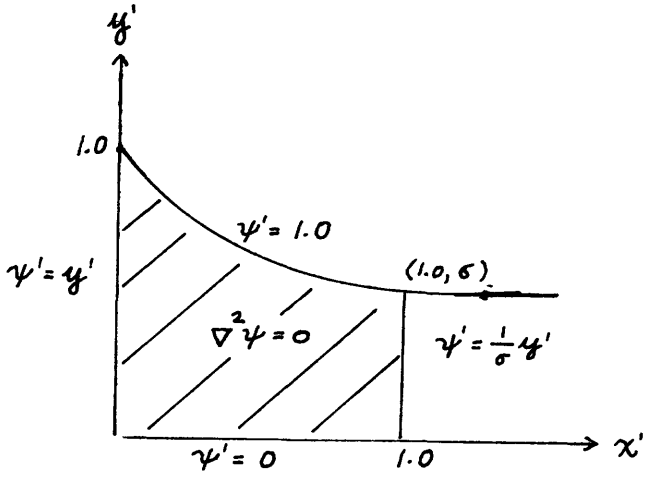

$$\psi' = \frac{\psi}{0.5\sigma L_D u_N} \qquad x', y' = \frac{(x,y)}{0.5 L_D}$$

Fig. 3-11 Boundary conditions for the stream function in the near field

A uniform grid system is used. Fig. 3-12 shows the grid system for $\theta_A = -60^\circ$, σ=0.5. A second order finite difference approximation is employed.

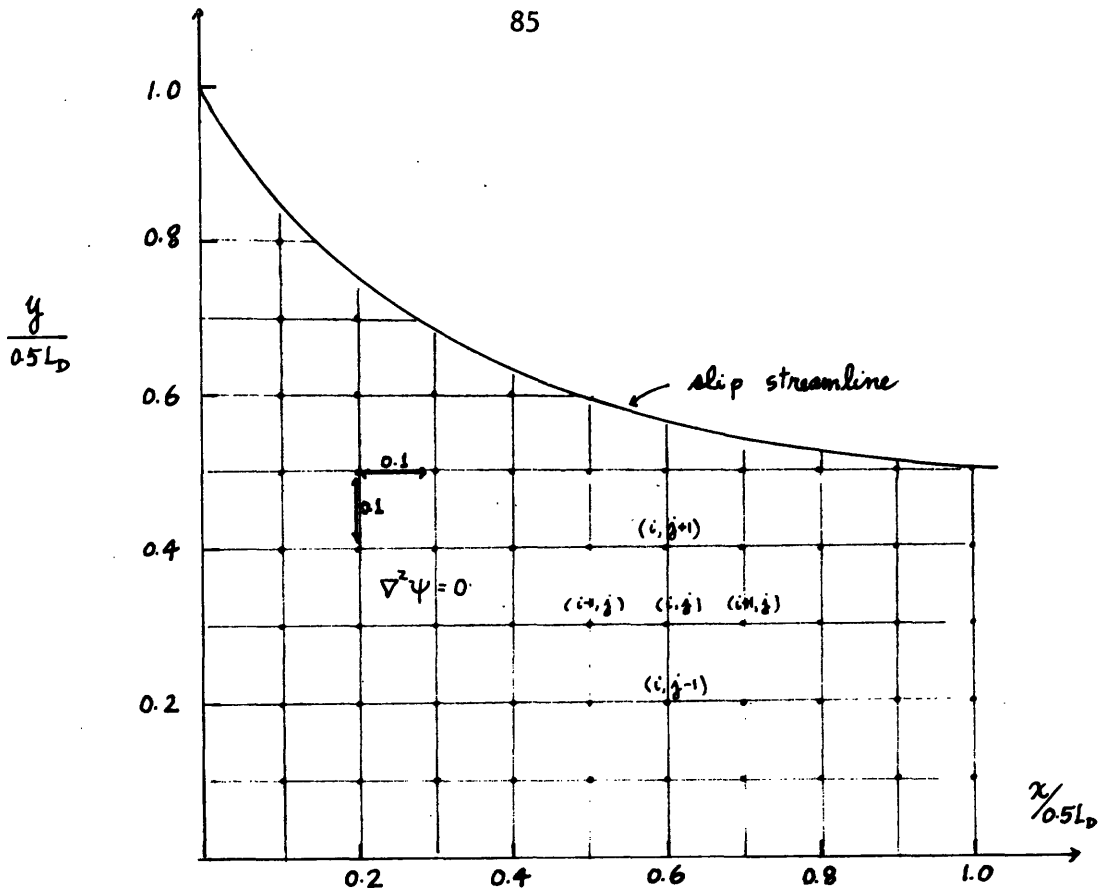

Fig. 3-12 Grid system used for finite difference solution; step size=0.1

At an interior node,

$$\psi(i,j)=\psi(i\Delta,j\Delta)=\frac{1}{4}[\psi(i-1,j)+\psi(i+1,j)+\psi(i,j-1)+\psi(i,j+1)] \quad (3.64)$$

where Δ= step size

Details for treating grid points near the boundaries can be found in Ref. (9) and will be omitted here.

Fig. 3.-13 shows the computed streamlines for the slack tide case ($\theta_A = -60^\circ$ $\sigma = 0.5$), and the transverse variations of pressure at different longitudinal positions x. The near

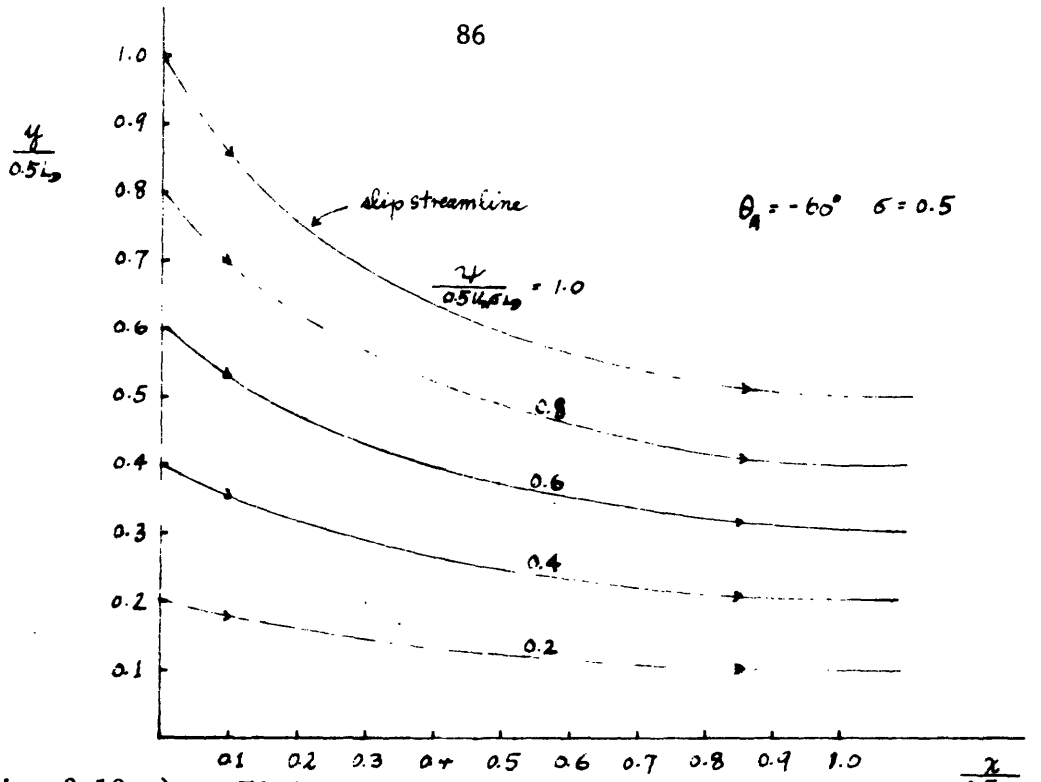

Fig. 3-13 a) Finite difference solution for the potential flow model. Illustrated streamlines ($\Upsilon = 0$)

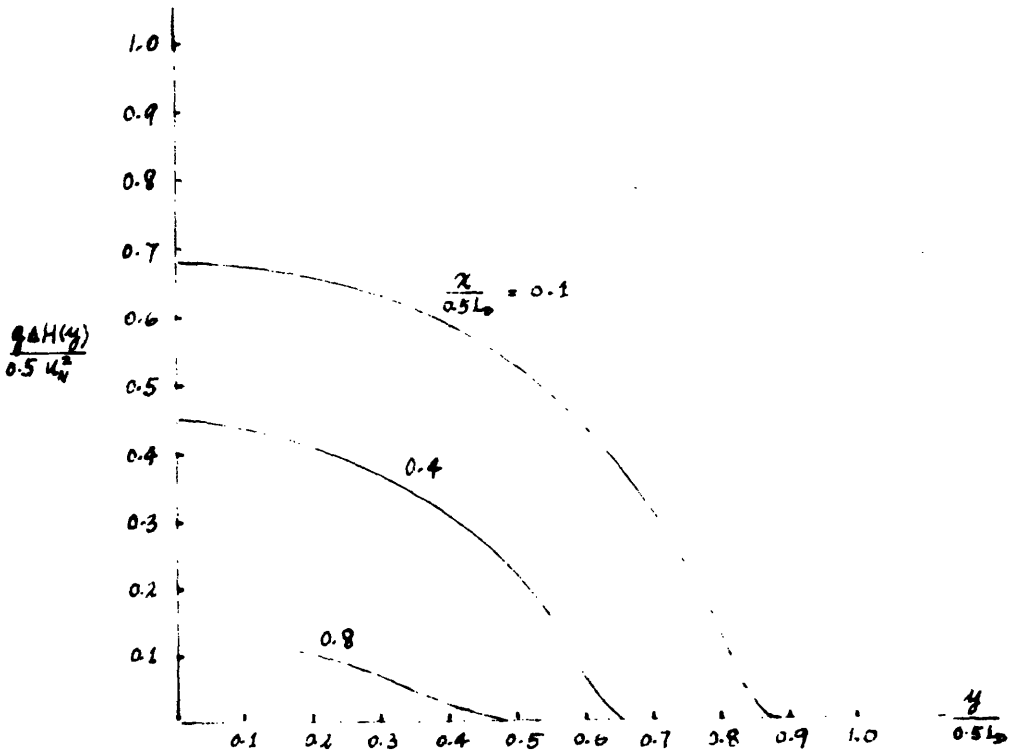

Fig. 3-13 b) Transverse pressure distribution at different longitudinal positions in the near field ($\Upsilon = 0$)

field in front of the diffuser is marked by a region of high pressure, $h(x,y)>H$. The excess potential energy gained from the diffuser momentum input is redirected into longitudinal momentum as the flow contracts and accelerates downstream.

The finite difference approximations are checked using two step sizes $\Delta=0.1$ and $\Delta=0.05$. The solutions at the common nodal points agree to within three decimal places; thus convergence of the numerical scheme is assured, and a step size $\Delta=0.1$ is judged sufficiently small for the calculations.

3.8 SUMMARY

A two-dimensional model for the flow field near a unidirectional diffuser in a coflowing current has been presented in this chapter.

The vertically averaged equations are derived; it is shown that in the 'near field', pressure and inertial effects dominate. In the 'intermediate field' beyond the region, turbulent entrainment and bottom friction become important determinants of the flow. A control volume analysis yields two important integral quantities (the total induced flow and the contraction coefficient of the mixed flow away) as a function of two physical parameters

$$\beta = \frac{L_D H}{N a_o} \quad , \gamma = \frac{u_a}{u_o} \quad .$$

A potential flow model for the near field is formulated and solved. The position of the slip streamline bounding the induced flow from behind is computed by classical free streamline theory. The theory indicates the extent of the near field is $0.5L_D$. The velocity distribution along the diffuser can also be inferred as:

$$u = SQ_o/L_D$$

$$v(y) = \frac{u\sin\theta_A 2y}{\sigma L_D}$$

CHAPTER IV

THE INTERMEDIATE FIELD SOLUTION

In chapter III a two dimensional potential flow model is formulated and solved for the diffuser flow in the near field In this chapter an integral model for the temperature and velocity field downstream of a unidirectional diffuser in stagnant water or a coflowing current is derived from the vertically averaged equations of motion. The near field solution is coupled into the model to give a global solution of the induced temperature rises. The characteristic features of the solution are discussed and physical interpretations are given.

4.1 Formulation of the Intermediate Field Theory

4.1.1 Model Structure

The postulated structure of the model is illustrated in Fig. 4-1. The flow is assumed to be vertically fully mixed at x=0. The diffuser extends from $(0,-L_D/2)$ to $(0, L_D/2)$. By symmetry only one half of the flow and temperature field have to be considered. The flow field is divided into two regions:

i) Region I $(0 \leq x \leq x_I)$, the region of flow establishment, refers to the zone where turbulent side entrainment has not penetrated to the axis of the diffuser plume. At any x, the flow characteristics can be described as consisting of a

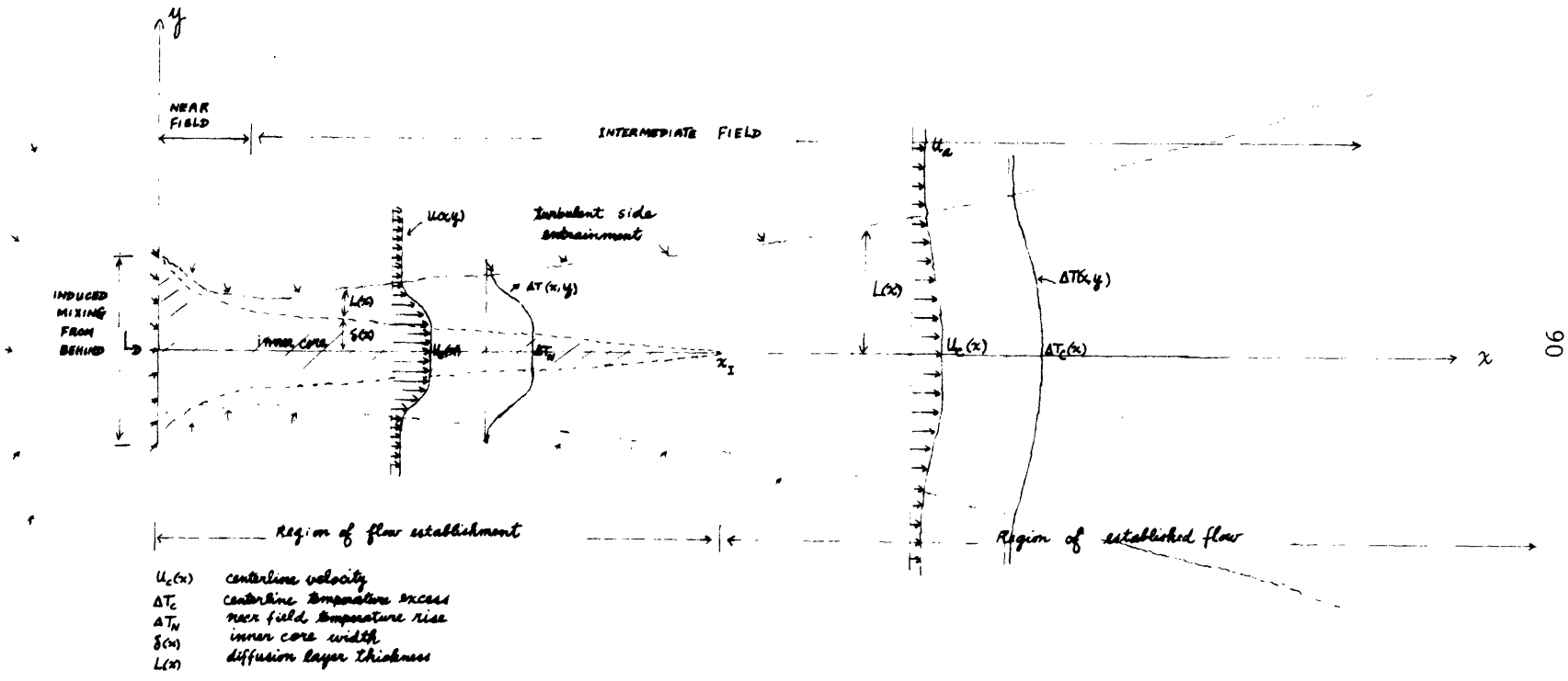

Fig. 4-1 A unidirectional diffuser in a coflowing current

'potential' layer of width $\delta(x)$, and a diffusion layer of width $L(x)$. The temperature in this potential layer is assumed to be equal to the near field temperature rise $\Delta T_N = \frac{\Delta T_o}{S}$, S being predicted by eq. 3.38. The velocity and temperature profiles take on the form:

$$u(x,y) = u_c(x)$$

$$\Delta T(x,y) = \Delta T_N = \frac{\Delta T_o}{S} \qquad 0 \leq y \leq \delta(x)$$

$$u(x,y) - u_a = \{u_c(x) - u_a\}\, e^{-(\frac{y-\delta}{L})^2}$$

$$\Delta T(x,y) = \Delta T_N\, e^{-(\frac{y-\delta}{L})^2}$$

$$\delta(x) \leq y \leq \delta(x) + L(x)$$

The unknowns in this region are $u_c(x), \delta(x), L(x)$. The extent of region I, x_I, is defined by $\delta(x_I)=0$, and is obtained as a solution of the problem.

ii) Region II($x \geq x_I$), the region of established flow, refers to the zone where turbulent side entrainment has reached the center of the plume. The velocity and temperature profiles are assumed to be:

$$u(x,y) - u_a = \{u_c(x) - u_a\}\, e^{-(\frac{y}{L})^2}$$

$$\Delta T(x,y) = \Delta T_c(x)\, e^{-(\frac{y}{L})^2}$$

In this region, the unknowns are $u_c(x), L(x), \Delta T_c(x)$.

The implicit assumption involved in the foregoing is that the width of the plume is small compared with the longitudinal extent, and that the velocity and temperature profiles are similar at all x. Differences in transverse heat and momentum transfer are neglected.

4.1.2 Governing Equations

Letting $b(x) = \delta(x) + L(x)$, the vertically averaged equations in the previous chapter, eq. 3.25b, can be integrated across the diffuser plume (in the y direction) from y=0 to y=b, i.e. to the edge of the plume. The resulting equations for conservation of mass, momentum and heat are:

Continuity
$$\frac{d}{dx}\int_o^b u\,dy = u_a\frac{db}{dx} - v_e \qquad (4.1)$$

Momentum
$$\frac{d}{dx}\int_o^b u^2 dy = u_a\left(u_a\frac{db}{dx} - v_e\right) - \frac{d}{dx}\int_o^b g\Delta h\,dy - \frac{f_o}{8H}\int_o^b u^2\,dy \qquad (4.2)$$

Heat
$$\frac{d}{dx}\int_o^b u\Delta T\,dy = 0 \qquad (4.3)$$

where
u_a : ambient current velocity

v_e : entrainment velocity at plume edge

4.1.3 Basic Assumptions

Two basic assumptions are employed in the subsequent analysis:

a) The entrainment assumption, first proposed by Morton, Taylor and Turner (1956) relates the rate of turbulent entrainment to a characteristic velocity in a plume. It is recognised that in turbulent mixing the eddies causing transfer of heat between two parallel streams are characterised by the relative velocity of the two streams. The rate of increase of the volume flux of the plume, $u_a \frac{db}{dx} - v_e$, is assumed to be proportional to the centerline velocity excess:

$$u_a \frac{db}{dx} - v_e = \alpha(u_c - u_a) \qquad (4.4)$$

$u_a \frac{db}{dx}$ is the incremental flow addition by the coflowing current; v_e is the incremental inflow perpendicular to the plume axis. α is the entrainment coefficient that takes on different values in the two regions. Its value is determined from well established data on classical free jets.

b) As shown in Chapter III, in the near field, $0 \leq x \leq 0.5L_D$ pressure and inertia effects dominate and the longitudinal gradient of the pressure force acting over the plume cross-section $- - \frac{d}{dx} \int_o^b g\Delta h \, dy$, therefore does not vanish. As the diffusion layer in this region is expectedly small, the pressure force is approximated by the solution of the potential flow model that neglects turbulent side entrainment.

$$\frac{dP}{dx} = -\frac{d}{dx}\int_o^b g\Delta h\ dy = \frac{d}{dx}\int^{g(x^*)0.5L_D} u^2_p(x,y)\ dy \qquad (4.5)$$

where P = pressure force over plume cross-section

$g(x^*)$ = dimensionless slip streamline given by eq. 3.63

$u_p(x,y)$ = induced velocity as given by the potential flow solution, equals the total induced flow per unit depth divided by the width of the bounding slip streamline, or

$$u_p(x,y) = \frac{SQ_o}{g(x^*)L_D H} \qquad x^* = \frac{x}{0.5L_D} \qquad (4.6)$$

Beyond the near field, the pressure deviation is due to the turbulent side entrainment and can be neglected as was shown in section 3.5.1.

Thus the pressure gradient is evaluated as

$$\frac{dP}{dx} = \frac{d}{dx}\left[\left(\frac{SQ_o}{L_D H}\right)^2 \frac{0.5L_D}{g(x^*)}\right] \quad 0 \le x \le 0.5\ L_D$$

$$= 0 \qquad x \ge 0.5L_D \qquad (4.7)$$

4.1.4 System of Integrated Equations

Invoking the previous assumptions, the postulated forms of the velocity and temperature profiles are substituted into Eq. 4.1-4.3. Carrying out the integrations, we obtain the following system of equations:

Region I

$$\frac{dQ}{dx} = \alpha_I(u_c - u_a) \qquad (4.8)$$

$$\frac{dM}{dx} = u_a \frac{dQ}{dx} + \frac{dP}{dx} - \frac{f_o M}{8H} \tag{4.9}$$

$$\frac{0.5 Q_o \Delta T_o}{H} = \Delta T_N \left[u_c \delta + L\{c_2(u_c - u_a) + c_1 u_a\} \right] \tag{4.10}$$

where

$$Q = \int_o^b u\,dy = \text{volume flux across plume}$$

$$= u_c \delta + L \left[c_1(u_c - u_a) + u_a \right] \tag{4.11}$$

$$M = \int_o^b u^2\,dy = \text{momentum flux across plume}$$

$$= u_c^2 \delta + L \left[c_2 u_c^2 + 2u_a u_c (c_1 - c_2) + u_a^2 (1 - 2c_1 + c_2) \right] \tag{4.12}$$

c_1, c_2 are integration constants

$$c_1 = \int_o^\infty e^{-k^2}\,dk = \sqrt{\pi}/2 \tag{4.13}$$

$$c_2 = \int_o^\infty e^{-2k^2}\,dk = \frac{1}{2}\sqrt{\pi/2}$$

Region II

$$\frac{dQ}{dx} = \alpha_\Pi (u_c - u_a) \tag{4.14}$$

$$\frac{dM}{dx} = u_a \frac{dQ}{dx} - \frac{f_o M}{8H} \tag{4.15}$$

$$\frac{0.5 Q_o \Delta T_o}{H} = \Delta T_c L \left[c_2(u_c - u_a) + c_1 u_a \right] \tag{4.16}$$

where $$Q = L \left[c_1(u_c - u_a) + u_a \right] \tag{4.17}$$

$$M = L \left[c_2 u_c^2 + 2u_c u_a (c_1 - c_2) + u_a^2 (1 - 2c_1 + c_2) \right] \tag{4.18}$$

α_I, α_{II} : entrainment coefficient in region I, II respectively.

4.2 Solution of the Intermediate Field Equations

4.2.1 Non-dimensionalization

The system of equations (4.8-4.18) can be cast in dimensionless form by defining the following dimensionless varibles

$$(x^*, \delta^*, L^*) = (x, \delta, L)/0.5L_D$$

$$\Delta T_c^* = \Delta T_c/\Delta T_o$$

$$u_c^* = u_c/u_o$$

$$Q^* = Q/(u_o 0.5L_D)$$

$$M^* = M/(u_o^2 0.5L_D)$$

$$P^* = P/(u_o^2 0.5L_D)$$

The length scale is chosen to be the half-diffuser length $0.5L_D$, the velocity is scaled by the nozzle velocity u_o, the temperature rise by ΔT_o, the condenser temperature rise.

Recalling that $\gamma = \frac{u_a}{u_o}$, $Q_o = Na_o u_o$, $\beta = \frac{L_D H}{Na_o}$ the following set of dimensionless equations in stantard form can be obtained:

Region I

$$\frac{dQ^*}{dx^*} = \alpha_I (u_c^* - \gamma) \qquad (4.19)$$

$$\frac{dM^*}{dx^*} = \gamma \frac{dQ^*}{dx^*} + \frac{dP^*}{dx^*} - \frac{f_o L_D}{16H} M^* \qquad (4.20)$$

where

$$\frac{dP^*}{dx^*} = \left(\frac{S}{\beta}\right)^2 \frac{d\left(\frac{1}{g(x^*)}\right)}{dx^*} \qquad 0 \leq x^* \leq 1.0 \qquad (4.21)$$

$$= 0 \qquad x^* \geq 1.0$$

and

from heat conservation:

$$\frac{S}{\beta} = u_c^*\delta^* + L^* [c_2(u_c^*-\gamma) + c_1\gamma] \quad (4.22)$$

from integration of the profiles:

$$Q^* = u_c^*\delta^* + L^* [c_1(u_c^*-\gamma) + \gamma] \quad (4.23)$$

$$M^* = u_c^{*2}\delta^* + L^* [c_2 u_c^{*2} + 2u_c^*\gamma(c_1-c_2) + \gamma^2(1-2c_1+c_2)] \quad (4.24)$$

By rearranging eq. 4.22-4.24 u_c^*, L^*, δ^* can be expressed in terms of M^*, Q^*:

$$u_c^* = \gamma + \frac{\beta}{S}(M^* - \gamma Q^*) \quad (4.25)$$

$$L^* = \frac{Q^* u_c^* - M^*}{(u_c^*-\gamma)[(c_1-c_2)u_c^* + \gamma(1-2c_1+c_2)]} \quad (4.26)$$

$$\delta^* = \frac{Q^* - L^*[c_1(u_c^*-\gamma) + \gamma]}{u_c^*} \quad (4.27)$$

$\delta^*(x_I^*) = 0$ defines the length of the region of flow establishment.

Region II

$$\frac{dQ^*}{dx^*} = \alpha_{II}(u_c^* - \gamma) \quad (4.28)$$

$$\frac{dM^*}{dx^*} = \gamma \frac{dQ^*}{dx^*} - \frac{f_o L_D}{16H} M^* \quad (4.29)$$

where

$$\frac{1}{\beta} = \Delta T_c^* L^* [c_2(u_c^* - \gamma) + c_1\gamma] \quad (4.30)$$

$$Q^* = L^* [c_1(u_c^* - \gamma) + \gamma] \quad (4.31)$$

$$M^* = L^* [c_2 u_c^{*2} + 2u_c^*\gamma(c_1-c_2) + \gamma^2(1-2c_1+c_2)] \quad (4.32)$$

By rearranging eq. 4.30-4.32, $u_c^*, L^*, \Delta T_c^*$ can be related to M^*, Q^*:

$$u_c^* - \gamma = \frac{-(\frac{c_1}{c_2})(2\gamma - \frac{M^*}{Q^*}) + \sqrt{(\frac{c_1}{c_2})^2(2\gamma - \frac{M^*}{Q^*})^2 + \frac{4}{c_2}(\frac{M^*}{Q^*}\gamma - \gamma^2)}}{2} \tag{4.33}$$

$$L^* = \frac{Q^*}{c_1(u_c^* - \gamma) + \gamma} \tag{4.34}$$

$$\Delta T_c^* = \frac{1}{\beta L^*[c_2(u_c^* - \gamma) + c_1\gamma]} \tag{4.35}$$

4.2.2 Numerical Solution Procedure

The set of first order ordinary differential equations (4.19-4.20, 4.28-4.29) in M^* and Q^* can in general be solved numerically using a fourth-order Runge-Kutta scheme by marching out the solution in x^* with initial values specified at $x^*=0$. The plume characteristics $u_c^*(x^*), L^*(x^*), \delta^*(x^*), \Delta T_c(x^*)$ can be related to (Q^*, M^*) at any x^* by virtue of eq. 4.25-4.27, 4.33-4.35, thus enabling the derivatives $\frac{dQ^*}{dx^*}$, $\frac{dM^*}{dx^*}$ to be computed.

4.2.3 Initial Conditions

From section 3.7, we have obtained

$$u(x=0,y) = \frac{SQ_o}{L_D H}$$

Hence, the initial conditions for the volume flux and the momentum flux are:

a) $$Q^*(0) = \frac{Q(0)}{u_o 0.5L_D}$$

$$= \frac{\int_o^{0.5L_D} (\frac{SQ_o}{L_D H})\,dy}{u_o 0.5L_D} = \frac{S}{\beta} \qquad (4.36)$$

b) $$M^*(0) = \frac{M(0)}{u_o^2 0.5L_D}$$

$$= \frac{\int_o^{0.5L_D} (\frac{SQ_o}{L_D H})^2\,dy}{0.5L_D\, u_o^2} = (\frac{S}{\beta})^2 \qquad (4.37)$$

4.2.4 Entrainment Coefficients

The values for the entrainment coefficients α_I, α_{II} are obtained from the experimental data for a two-dimensional free jet published by Albertson et al (1950). The rate of flow across the jet can be related to the centerline velocity $u_c(x)$.

i) In the region of flow establishment of a free jet,

$$\frac{Q(x)}{Q_o} = 1 + \sqrt{\pi}(\sqrt{2}-1)\ 0.109\ \frac{x}{B_o},\ u_c = u_o$$

where Q_o : initial jet flow

B_o : initial jet width

The two equations can be combined to give, for the half-diffuser plume,

$$\frac{dQ}{dx} = \frac{\sqrt{\pi}(\sqrt{2}-1)0.109}{2}\ u_c(x)$$

$$\alpha_I = 0.040 \qquad (4.38)$$

ii) In the region of established flow,

$$\frac{Q(x)}{Q_o} = \sqrt{2\sqrt{\pi}\, C_1 \frac{x}{B_o}} \quad ; \quad \frac{u_c(x)}{u_o} = \sqrt{\frac{1}{\sqrt{\pi C_1}} \frac{B_o}{x}}$$

The two equations can be combined to give

$$\frac{dQ}{dx} = \frac{0.109}{4} \sqrt{2\pi} u_c(x)$$

therefore

$$\alpha_{II} = 0.068 \qquad (4.39)$$

4.3 Solution

The entire problem can be seen to be dependent on $\gamma = \frac{u_a}{u_o}$ the relative strength of ambient to nozzle velocity; $\beta = \frac{L_D H}{N a_o}$, a near field design parameter which together with γ determines the near field dilution A (eq. 3.38); and $\beta_2 = \frac{f_o L_D}{16H}$ an intermediate field parameter measuring the momentum dissipation of the diffuser plume.

In the limiting case of no ambient current, $\gamma = 0$, the system of equations (4.19-4.20, 4.28-4.29) can be solved analytically. Considerable insight can be gained by examining the characteristics of the analytical solution which elucidates the essential feature of the diffuser plume.

Hencforth all starred subscripts will be dropped and all variables encountered later on are dimensionless variables.

4.3.1 Analytical Solution in the absence of a current

Setting $\gamma=0$ in eq. 4.19, 4.20, 4.22 gives

Region I

$$\frac{d}{dx}\left[u_c(\delta+c_1L)\right] = \alpha_I u_c \tag{4.40}$$

$$\frac{d}{dx}\left[u_c^2(\delta+c_2L)\right] = \beta_1^2 \frac{d}{dx}\left(\frac{1}{g(x)}\right) - \beta_2\left[u_c^2(\delta+c_2L)\right] \tag{4.41}$$

$$u_c(\delta+c_2L) = \beta_1 \tag{4.42}$$

where

$$\beta_1 = \frac{s}{\beta} \qquad \beta_2 = \frac{f_o L_D}{16H}$$

Eliminating $\delta+c_2L$ from eq. 4.41 and eq. 4.42 gives

$$\frac{du_c}{dx} + \beta_2 u_c = \beta_1 \frac{d}{dx}\left(\frac{1}{g(x)}\right) \tag{4.43}$$

Using an integrating factor $e^{\beta_2 x}$

and invoking $u_c(0) = \beta_1$, eq. 4.43 can be solved to give

$$u_c(x) = e^{-\beta_2 x}\beta_1\left[1.0 + \int_o^x e^{\beta_2 x}\frac{d}{dx}\left(\frac{1}{g(x)}\right)dx\right] \tag{4.44}$$

The entrainment relationship eq. 4.40 gives

$$u_c(\delta+c_1L) = \alpha_I \int_o^x u_c(x)\,dx + \beta_1 \tag{4.45}$$

Substracting eq. 4.45 from eq. 4.42, the solution of the diffusion layer L(x) can be obtained as

$$L(x) = \frac{\alpha_I \int_o^x u_c(x)dx}{(c_1-c_2)\,u_c(x)} \tag{4.46}$$

and the core thickness $\delta(x)$ as

$$\delta(x) = \frac{\beta_1}{u_c(x)} - c_2L(x) \tag{4.47}$$

Region II:

Setting $\gamma = 0$ in Eq. 4.28, 4.29, we have

$$C_1 \frac{d}{dx} (u_c L) = \alpha_I u_c \tag{4.48}$$

$$\frac{d}{dx} (u_c^2 L) = - \beta_2 (u_c^2 L) \tag{4.49}$$

Eq. 4.49 can be solved to give

$$m(x) = u_c^2 L(x) = u_c^2 L\Big|_{x_I} \exp [-\beta_2 (x-x_I)] \tag{4.50}$$

i.e. the momentum flux is dissipated exponentially by bottom friction; in a classical free jet the momentum flux is constant.

Substituting the expression for $u_c^2 L(x)$ in eq. 4.50 into eq. 4.48 and expanding, the following Bernoulli type differential equation in u_c can be derived:

$$\frac{d}{dx} (u_c^2) + 2\beta_2 u_c^2 + 2\alpha_{II} m(x) (u_c^2)^2 = 0 \tag{4.51}$$

Since m(x) is known by virtue of eq. 4.50, the Region II solution can be obtained:

$$u_c(x) = u_I \left\{ \frac{e^{-\frac{f_o L_D}{8H}(x-x_I)}}{(1-\beta_3) + \beta_3 e^{\frac{-f_o L_D}{16H}(x-x_I)}} \right\}^{1/2}$$

$$L(x) = L_I \left\{ \beta_3 + (1-\beta_3) e^{\frac{f_o L_D}{16H}(x-x_I)} \right\} \qquad (4.52)$$

$$\Delta T_c(x) = \frac{1}{S} \left\{ (1-\beta_3) + \beta_3 \, e^{\frac{f_o L_D}{16H}(x-x_I)} \right\}^{-1/2}$$

where

$$\beta_3 = \frac{-32\alpha_{II} H}{c_1 L_I f_o L_D}$$

$$u_I = u_c(x_I) \qquad (4.53)$$

$$L_I = L(x_I)$$

4.3.2 Physical Interpretation of the Intermediate Field Solution

The features of this intermediate field solution is best demonstrated by plotting the variables relative to their respective values at the beginning of region II, $\frac{u_c(x)}{u_I}$, $\frac{L(x)}{L_I}$, $\Delta T_c S$, against the distance from the beginning of region II, $\frac{(x-x_I)}{L_D}$. Using typical values of

$$\frac{L_D}{H} = 100, 50, 25, 5$$

$$f_o = 0.02$$

the solution is plotted in Fig. 4-2. It should be pointed out that as the variables are plotted against $\frac{(x-x_I)}{L_D}$ the figure does not illustrate the tradeoff among different diffuser designs (e.g. a long diffuser vs a short diffuser). The implication of the theory on diffuser design will be treated in a later chapter.

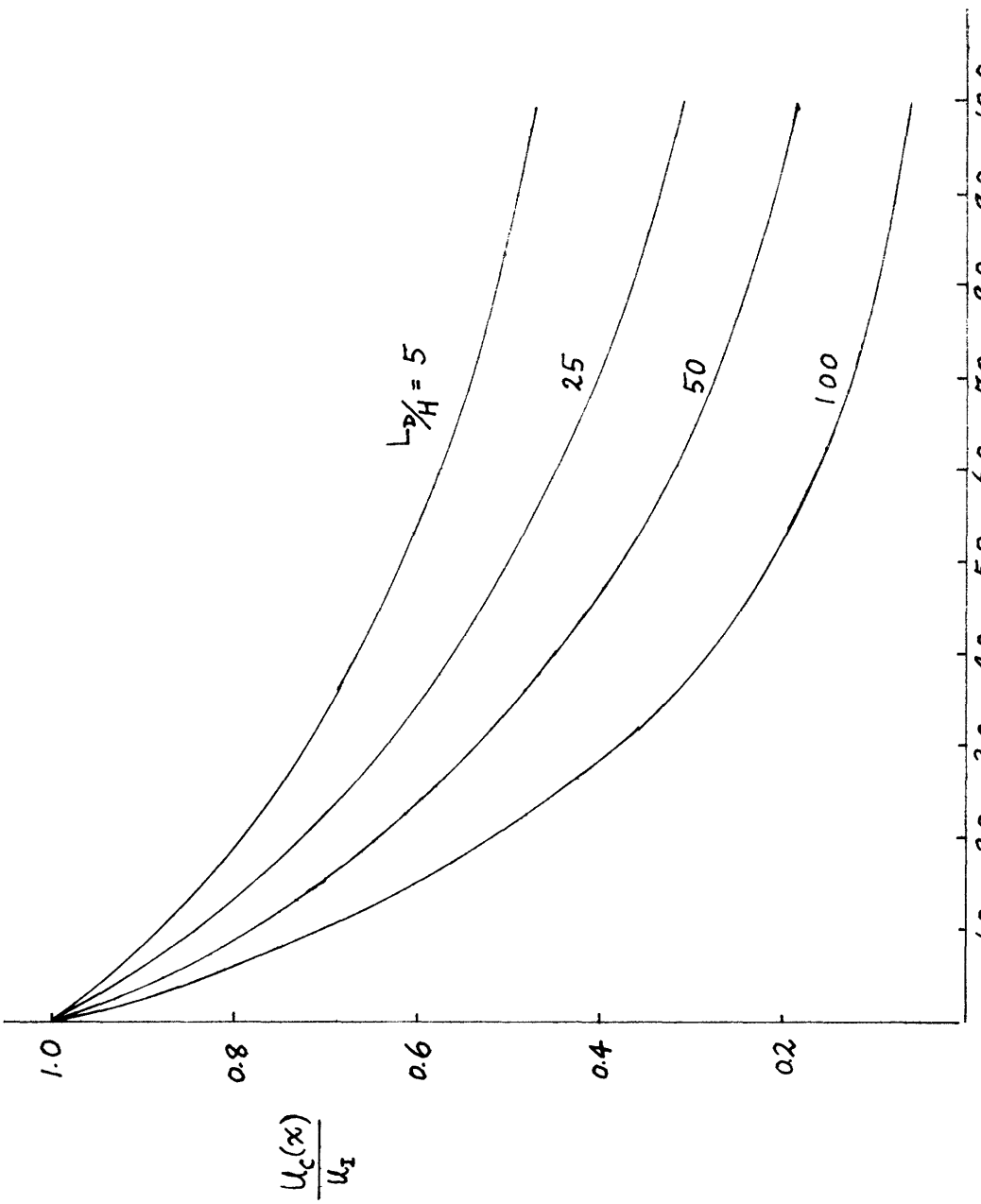

Fig. 4-2 a) Centerline velocity decay in a two dimensional friction jet

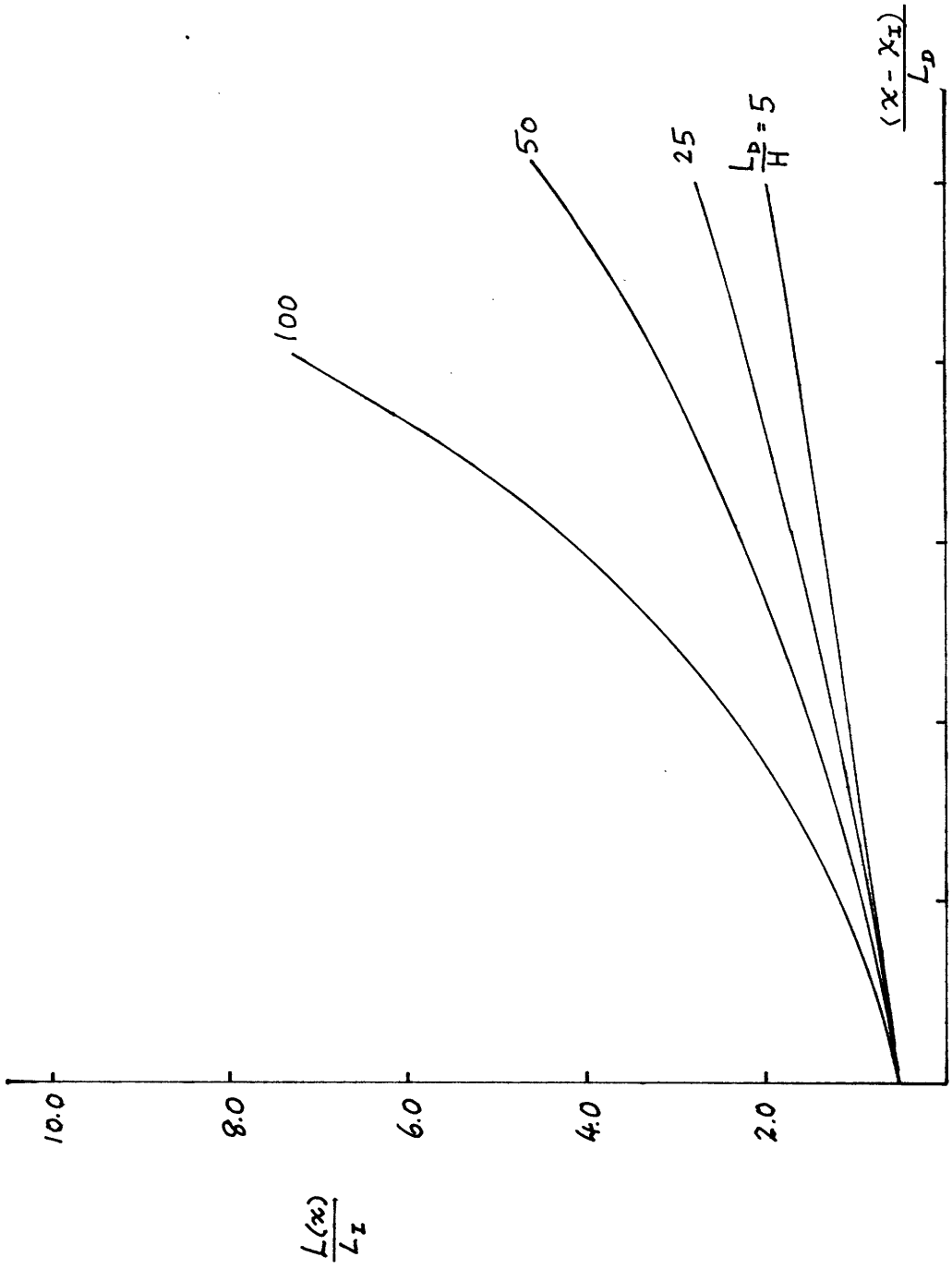

Fig. 4-2 b) Plume width of a two dimensional friction jet

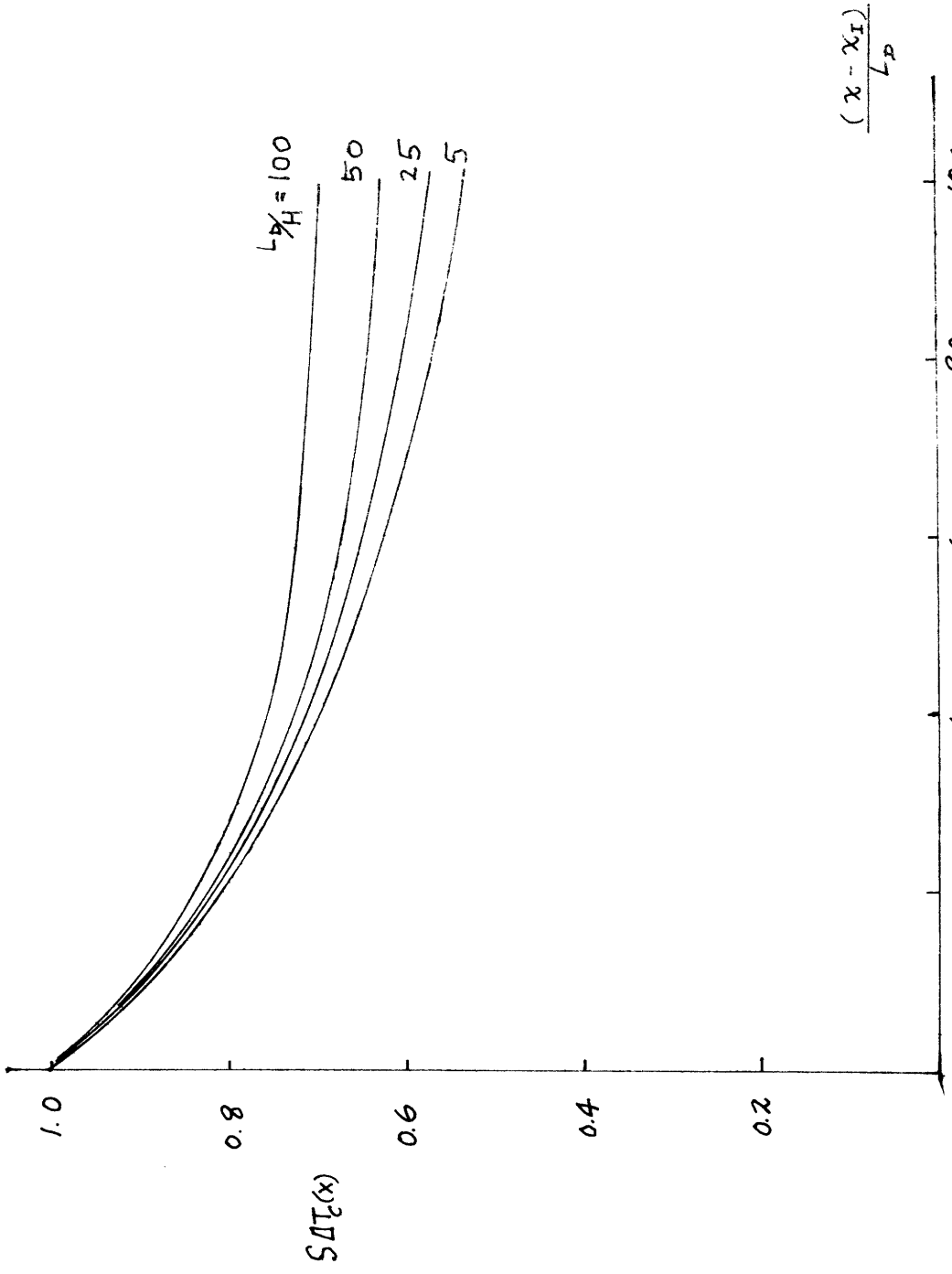

Fig. 4-2 c) Centerline temperature decay in a two dimensional friction jet

It is interesting to note that in contrast to a classical two dimensional jet in which the centerline velocity decays as $x^{-1/2}$, the velocity in a two dimensional friction jet decays exponentially with x, due to turbulent side entrainment and momentum dissipation. Also, the width of the plume L(x) increases exponentially. This diverging behavior is distinctly different from the two dimensional free jet ($u_c \sim x^{-1/2}$, $L \sim x$).

It can be seen from eq. 4.52, that as $x \to \infty$ ΔT_c approaches an asymptotic value.

$$\Delta T_\infty = \lim_{x \to \infty} \Delta T_c(x) = \frac{1}{S} (1-\beta_3)^{-1/2} \qquad (4.54)$$

This is again in sharp contrast to the behavior of the free jet, which predicts that $\Delta T_c \sim x^{-1/2}$, and hence $\Delta T_c \to 0$ as $x \to \infty$. This behavior stems from the strong exponential decay in velocity and the exponential spread of the diffuser plume, so that at large x there is virtually no turbulent entrainment due to the relative velocity of the plume and the ambient fluid. This feature also places a limit on the mixing capacity of any unidirectional diffuser.

The above features together imply that

a) At some distance from the diffuser, due to the divergent nature of the plume spreading, the lateral scale of the plume is no longer small compared with the longitudinal scale, and the boundary layer asumption ceases to be valid.

b) At any x, a measure of the degree of stratification in the flow is given by a characteristic densimetric Froude number based on the water depth defined as:

$$F_H = \frac{u_c(x)}{\sqrt{g\beta_e \Delta T_c H}} \tag{4.55}$$

The densimetric Froude number decreases with x, so that buoyancy effects will become important at large distances from the diffuser, as $F_H \to 0$.

Both a) and b) suggest that the diffuser mixed flow is prone to heat recirculation into the near field. This phenomenon is experimentally confirmed and discussed in detail in Chapter VIII As will be seen later, the intermediate field solution is valid for a region of extent $10^3 H$, a sufficiently large area over which the importance of the thermal impact of diffuser discharges can be assessed.

In the limiting case of $f_o \to 0$, the solution given by eq. 4.52 can be shown to possess the same behavior as a two dimensional free jet. At each x, as $f_o \to 0$,

$$e^{-\frac{f_o L_D}{16H}(x-x_I)} \simeq 1 - \frac{f_o L_D}{16H}(x-x_I)$$

Thus $u_c(x)$ can be written as

$$\frac{u_c(x)}{v_I} = \left\{\frac{1 - \frac{f_o L_D}{8H}(x-x_I)}{\left(1+\frac{32\alpha_{II}H}{c_1 L_I f_o L_D}\right) - \frac{32\alpha_{II}H}{c_1 L_I f_o L_D}\left(1-\frac{f_o L_D}{16H}(x-x_I)\right)}\right\}^{1/2} \tag{4.56}$$

therefore

$$\lim_{f_o \to 0} \frac{u_c(x)}{u_I} = \frac{1}{\left(1+ \frac{2\alpha_{II}}{c_1 L_I} (x-x_I)\right)^{1/2}} \tag{4.57}$$

In an entirely analogous manner,

$$\lim_{f_o \to 0} \frac{L(x)}{L_I} = 1 + \frac{2\alpha_{II}}{c_1 L_I} (x-x_I) \tag{4.58}$$

revealing the linear spread of the free jet.

4.4 Numerical Solution for $u_a \neq 0$

In the presence of a coflowing current, $\gamma \neq 0$, the theoretical solution to the system of equations (4.19-4.20, 4.28-4.29) has to be obtained numerically as discussed in section 4.2. In Fig. 4-3 the numerical results are illustrated for two sets of parameters ($\frac{L_D}{H} = 10, \beta = 50$; $\frac{L_D}{H} = 30, \beta = 150$) for $\gamma = 0.04$ and contrasted with the slack tide solution for $\gamma = 0$ Two interesting observations can be made:

a) The $\frac{\Delta T_c}{\Delta T_o}$ diagram shows the near field temperature rise is less than the slack tide case. This is evident from Eq. 3.38, as the near field dilution is greater in a coflowing current. This leads to a more pronounced velocity field; however, the velocity excess ($\frac{u_c}{u_o} - \gamma$) is smaller implying a lesser mixing capacity in the intermediate field. The results show the extent of Region I is larger, and that difference in $\Delta T_c(x)$ is small after several diffuser lengths.

b) The plume width is much narrower in extent than the slack tide case. This is consistent with the behavior of a constant pressure free jet in a coflowing stream and suggest a lesser tendency for the heat in the diffuser plume to recirculate.

It should be noted that the calculations are discontinued when $u_c(x) \simeq u_a$, as further mixing may not be governed by the relative velocity $(u_c - u_a)$, but by the turbulence initially present in the ambient stream.

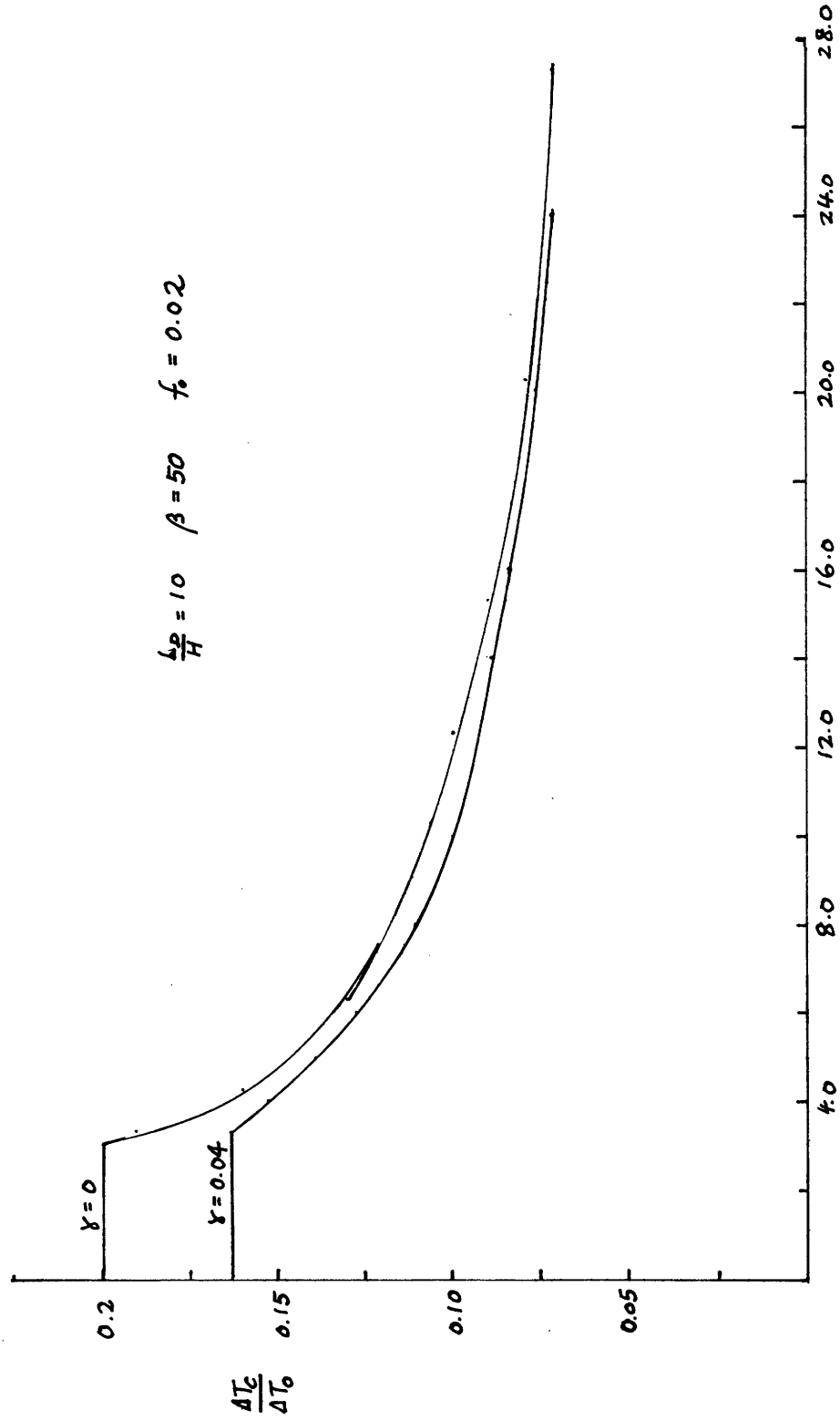

Fig. 4-3 a) Numerical solution in a coflowing current: Centerline temperature rise

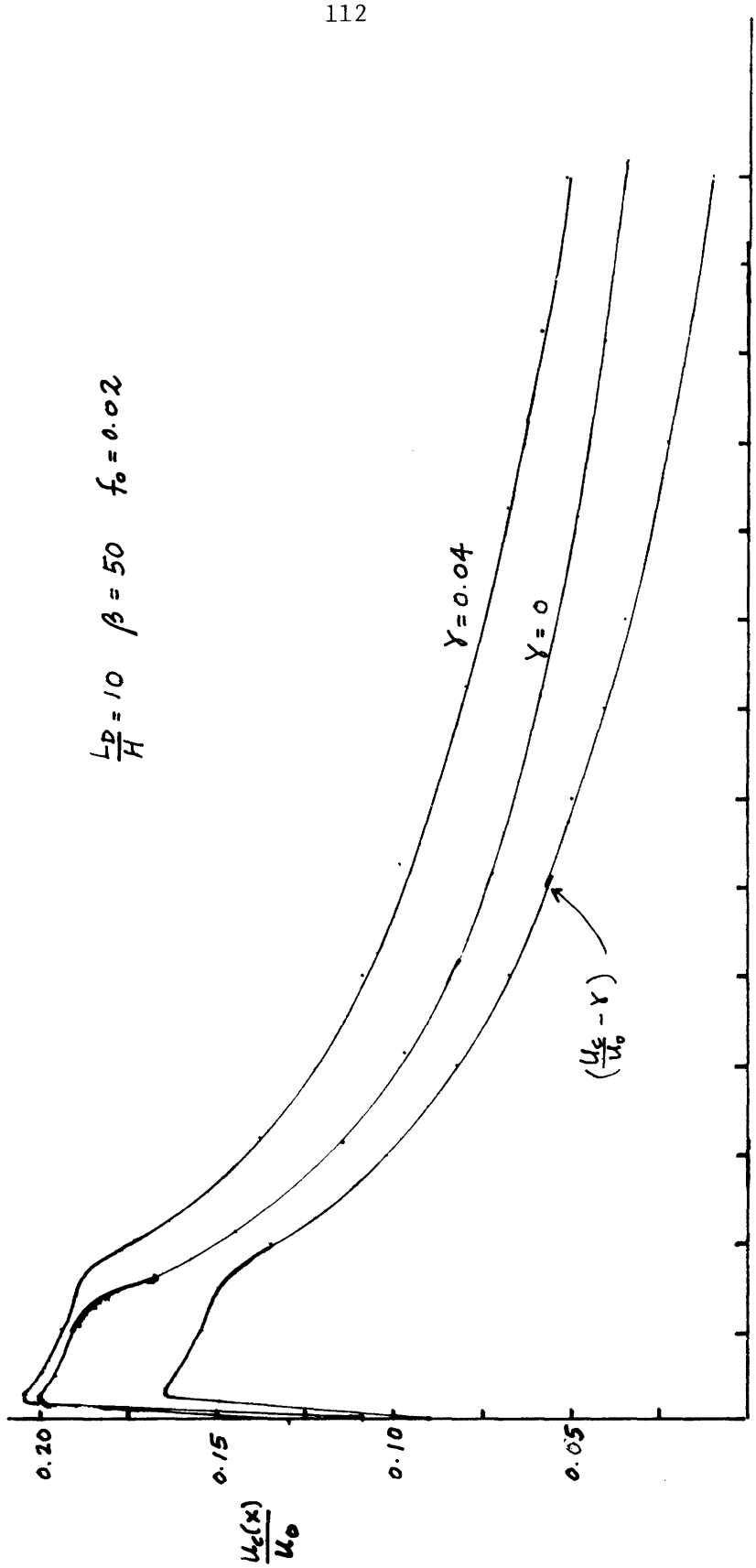

Fig. 4-3 a) cont'd Centerline velocity in diffuser plume

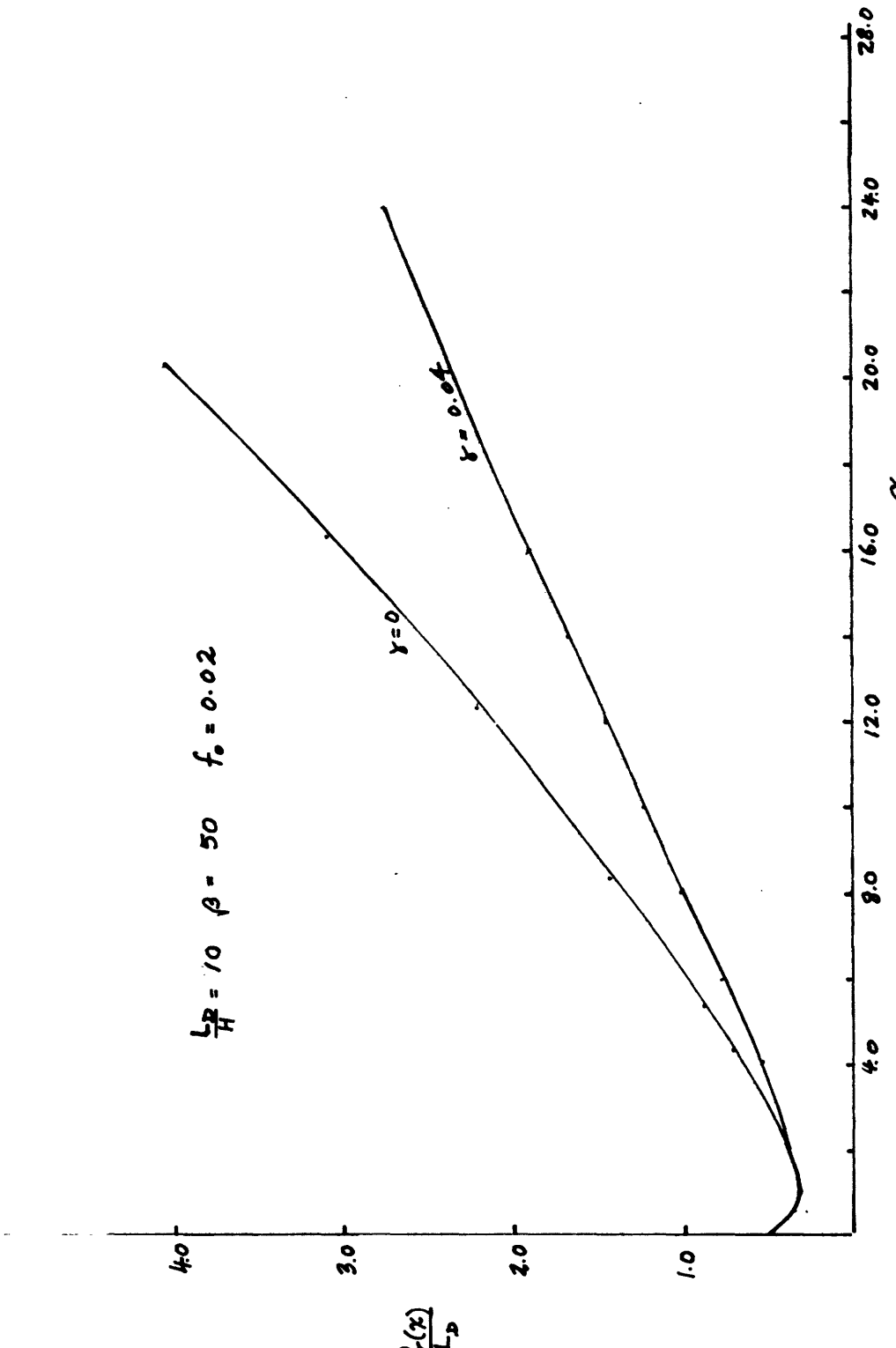

Fig. 4-3 a) cont'd Diffuser plume width

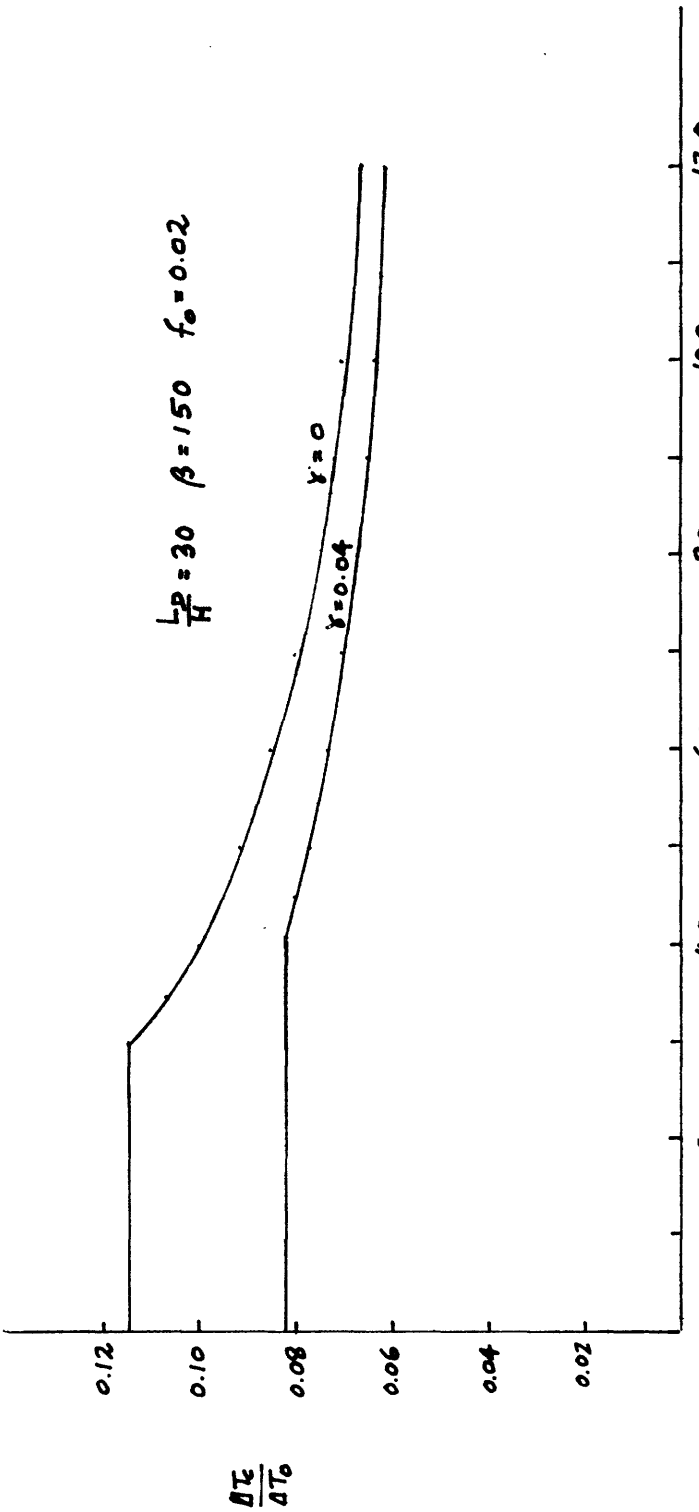

Fig. 4-3 b) Numerical solution in a coflowing current: centerline temperature rise

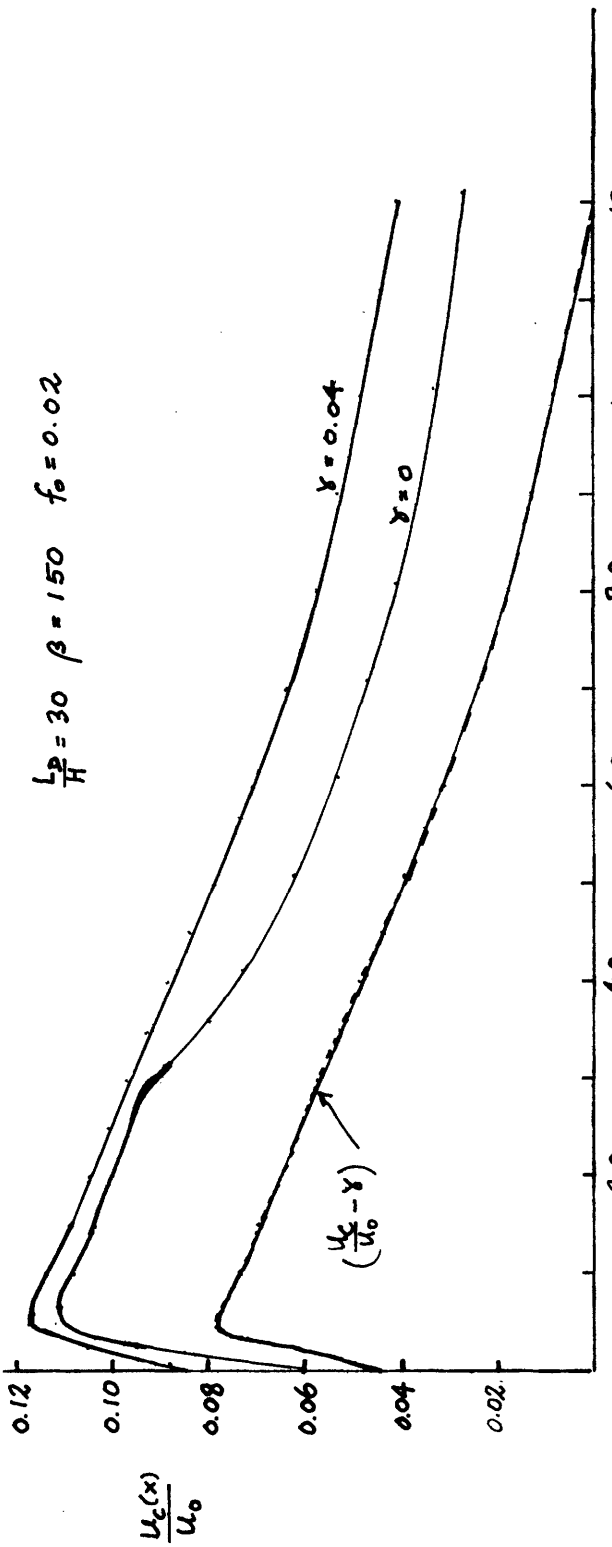

Fig. 4-3 b) cont'd Centerline velocity in diffuser plume

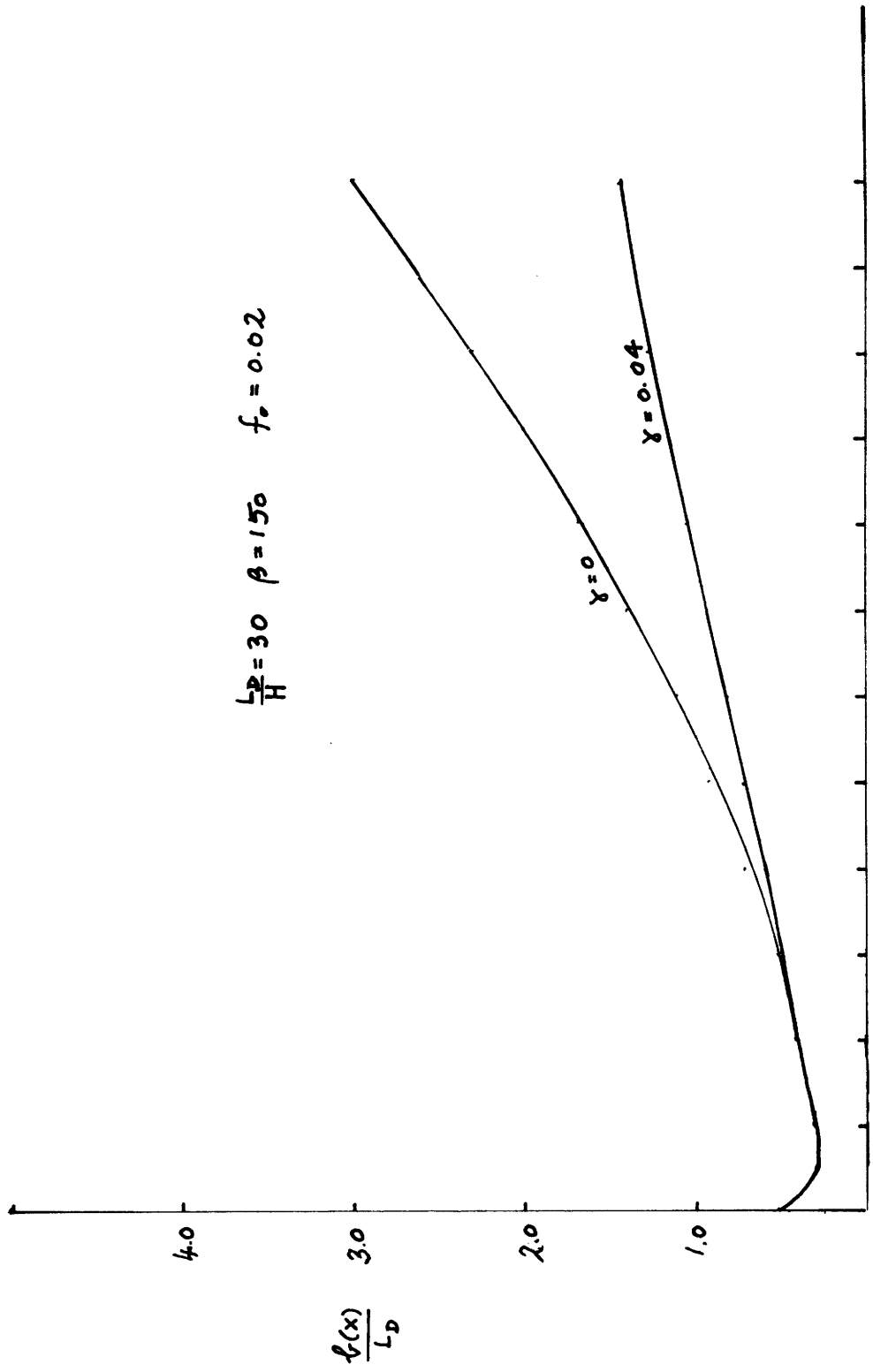

Fig. 4-3 b) cont'd Diffuser plume width

CHAPTER V

EXPERIMENTAL INVESTIGATION

The objectives of the experimental program are:

1) To provide experimental insights into the global circulation patterns and temperature configurations associated with a wide range of diffuser designs and ambient conditions.

2) To establish a comprehensive set of laboratory data of sufficient spatial resolution for comparison with theoretical model predictions.

Details of the experimental setup and procedure are described in the following sections.

5.1 General experimental setup

Three sets of experiments (Series MJ, Series FF, Series 200) were carried out in a 40'x60'x1.5' model basin. An artificial floor was constructed in the basin using 16"x8"x2" concrete blocks so as to insure a completely horizontal bottom. Discharge water at a desired temperature is obtained from a heat exchanger and constant head tank. To ensure a constant water level, water is withdrawn at the same rate at one end of the model.

Currents can be generated by a crossflow system installed at the two basin ends. Water can be pumped from either end of the basin through PVC manifolds into a large reservoir and vice versa. The lateral uniformity of the crossflow is improved

by horsehair matting and vertical slotted weirs at the basin ends. The crossflow system can be used to mix the water in the basin to ensure a uniform ambient temperature before the start of each experiment. All flows are monitored by calibrated Brooks rotameter flowmeters.

A schematic of the plan view of the experimental setup is shown in Fig. 5-1. For full diffuser tests the diffuser is placed in position B or C roughly midway between the sides of the basin. For half-diffuser tests the diffuser is placed at the edge of one side of the basin (position A) which then simulates a plane of symmetry for the induced temperature field.

5.2 Multiport diffuer design

A special multiport diffuser injection device was designed and constructed to allow maximum flexibility in the operation of the experimental program.

The entire diffuser discharge system is mounted on an 6' x 2.5' aluminum frame that is supported on four galvanized steel threaded rods (Fig.5-2). To ensure uniformity of the nozzle discharge, discharge water is fed from a 15" long 3" PVC pipe manifold into one side of a large 6' long 3" diffuser manifold through four 3/4" hoses, valves and couplings uniformly spaced apart. Discharge water is fed on the other side of the manifold to a system of copper nozzles via flexible tygon tubings and brass fittings. For priming purposes, two air bleed valves are installed at either end of the diffuser manifold.

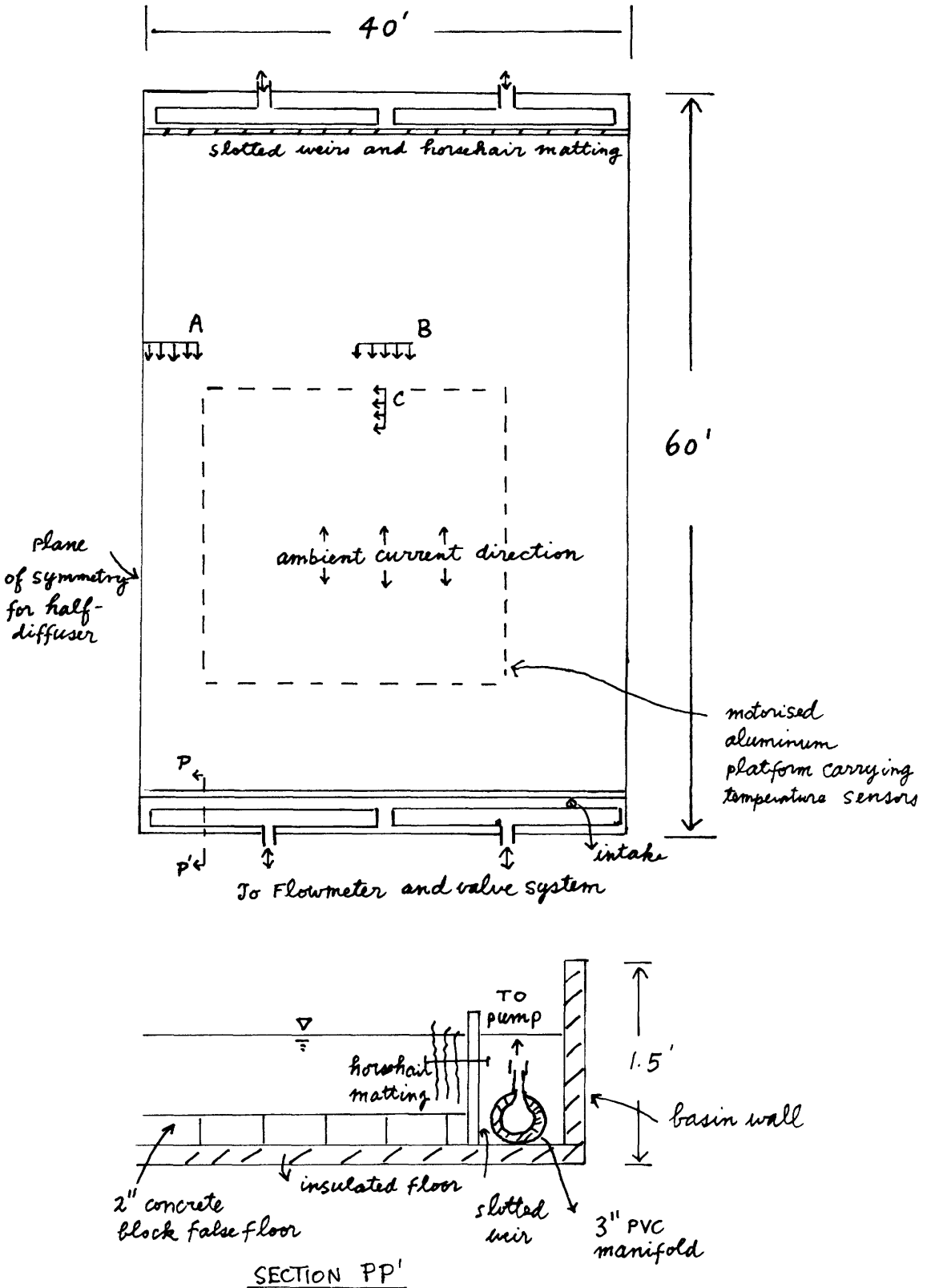

Fig. 5-1 Schematic of Experimental Setup

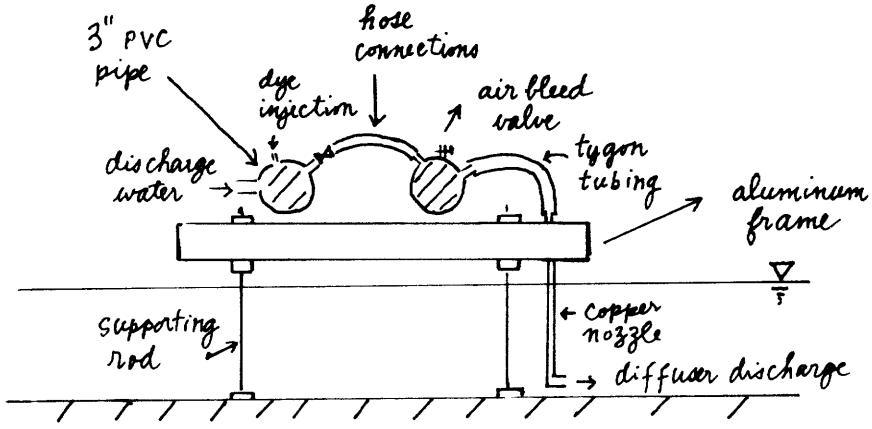

Side View

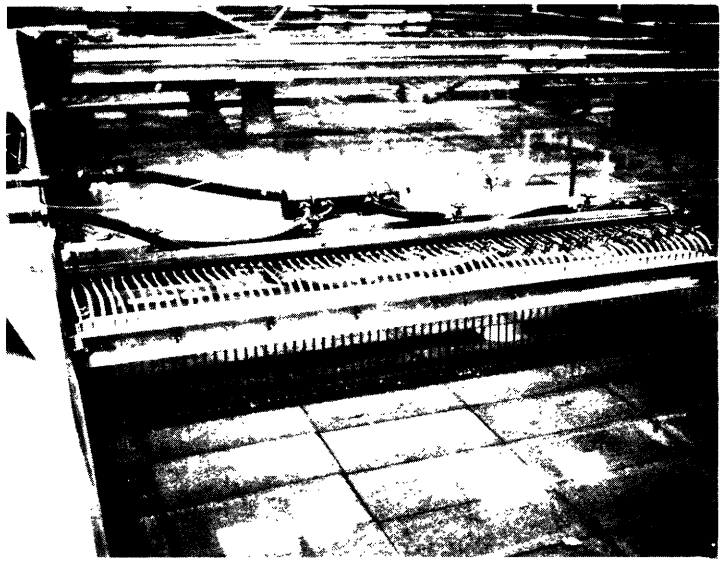

Top View

Fig. 5-2 Multiport diffuser injection device

The copper tubes can be fitted between two aluminum plates with indentations made to accomodate the tubes. Tightening the plates together fixes the position of the copper tubes.

5.3 Temperature measurement system

A temperature measurement system consisting of 90 Yellow Springs thermistor probes (Series 701, time constant = 9 sec) is mounted at the same level on a motorized aluminum platform (vertical speed 1.5"/min.), thus enabling vertical temperature profiles to be taken. Nearly instantaneous temperature readings are recorded by an electronic scanner manufactured by Data Entry Systems (Scanning rate 100 records/min.) and printed on paper as well as punched on tape. The data on paper tape was converted to computer cards by passing the tape through a tape-to-card reader. The thermistor probes are individually calibrated against a mercury-in-glass thermometer in a steam bath at several temperatures within an expected range of temperatures. The measurement accuracy of the calibrated probes is $\pm$ 0.1^{o} F.

5.4 Flow visualisation and velocity measurement

Rhodamine blue dye is injected into the discharge line to visualize the flow. Velocity measurements were made using a time of travel method: light styrofoam particles are dropped onto the water surface and their pathlines are recorded either photographically or visually. The concrete blocks that constitute the floor form a clear grid system that greatly facilitates

locating the particle at any given time. Crosses are also marked at about 6 foot intervals on the floor with orange fluorescent dye.

Surface velocity measurements are made by taking time-lapse pictures of the trajectory of a light floating particle with a Topcon Super Dm autowinder camera mounted on a tripod placed on a walkway above the model. The pictures are taken using high speed Ektachrome film with shutter speeds in excess of 1/30 sec.

When steady conditions are assumed to prevail (usually about 30 minutes from the start of the experiment) a styrofoam particle is carefully dropped onto the water surface at the center of the diffuser. When the flow starts to drag the particle along the first shot is taken. Subsequent photographs were taken at timed intervals, the length of which are chosen to reflect the magnitude of the observed velocities (smaller Δt for larger velocities and vice versa). The distance of the particle from the diffuser are then measured off from the projections of the photos or slides. Thus a set of data in the form of $(x_o,t_o),(x_1,t_1),x_2,t_2),(x_m,t_m)$ is obtained. Usually two sets of measurements are made for each run to assure repeatability of the results. For half-diffuer tests great care is taken to make sure the particle stays out of the boundary layer near the basin wall that simulates a plane of symmetry.

Typical raw data recorded are illustrated below:

Run MJ 06

Set 1

Time (sec.) t_i	0	5	10	20	30	40
x_i (# of blocks)	0.9	3.2	5.5	10.6	15.1	19.1
x_i (ft.)	0.57	2.04	3.49	6.72	9.6	12.1

Set 2

Time (sec.) t_i	0	5	10	20	40	60	90
x_i (# of blocks)	1.0	3.0	5.3	10.5	18.8	25.7	33.2
x_i (ft.)	0.67	1.87	3.39	6.66	11.97	16.32	21.08

5.5 Experimental Runs

In this section the motivation and experimental procedure for each series of runs will be described.

Before the start of each experiment the water in the basin is thoroughly mixed to attain a uniform ambient temperature by operating the crossflow system. The discharge system is primed under high pressure to drive away any air that might be present in the diffuser system. Discharge water at a desired temperature is allowed to run through the bypass system until the temperature of the discharge water is steady. The discharge temperature is monitored throughout the experiment by a mercury-in-glass thermometer inserted into the PVC manifold feeding into the copper nozzles.

5.5.1 Series MJ

Due to the limited size of usual experimental setups previous studies have been unable to study the behaviour of the diffuser plume beyond the near field. It is desirable to investigate under what conditions a diffuser will induce recirculation patterns that carry heat back into the near field.

Series MJ was performed to study the circulation patterns induced by a thermal diffuser discharging under shallow water conditions. As discussed in section 3.5, it was judged that for diffusers of practical interest, the velocity field would be independent of the temperature field. As such, experiments

in the MJ series were done by discharging at about the same temperature as the ambient water.

A typical run usually lasts for about 45 minutes. A one-minute dye injection is made at 15 minutes from the start of the experiment to visualize the flow pattern. Subsequent dye patterns at different times are recorded. Two sets of velocity measurements are made at t=30 minutes, when steady state of the near field is usually attained.

Only slack water conditions were tested in this series. The diffuser length as well as the nozzle spacing were kept constant. Only the water depth and the jet velocity were varied to produce different flow patterns. 18 runs were performed for a half-diffuser with the basin wall approximating a plane of symmetry. Effectively doubling the basin size helps to minimize model boundary effects. Six additional runs were done with a full diffuser to corroborate the results of the half-diffuser tests. The run parameters for the MJ series are listed in Table. 5-1.

5.5.2 Series FF

In this series of tests, heated multiple jets are discharged at about 25 to 30^{o}F above ambient temperature. Tests were made to investigate how the recirculation changes the temperature configuration in the near field of the diffuser. The effect of the diffuser length and its orientation with respect to a cross current on the overall performance of the

MOMENTUM JET EXPERIMENT

Series MJ

RUN NO.	Q_o (GPM)	N	H (in)	T_a (^oF)	u_o (FPS)	ν_o x10^5 ft^2/sec	R_D	$0.5L_D/H$
MJ04	2.32	30	0.91	59.5	2.66	1.22	1980	32.9
MJ05	2.88	30	0.66	59.0	3.29	1.22	2450	45.5
MJ06	2.3	30	1.21	56.0	2.63	1.28	1866	24.8
MJ07	2.88	30	1.21	61.0	3.29	1.18	2533	24.8
MJ08	1.73	30	1.21	61.0	1.98	1.18	1524	24.8
MJ09	2.88	30	0.98	61.0	3.29	1.18	2533	30.5
MJ10	1.73	30	0.97	60.0	1.98	1.20	1499	30.9
MJ11	2.88	30	0.77	57.0	3.29	1.26	2372	39.1
MJ12	1.73	30	0.73	59.0	1.98	1.22	1474	41.0
MJ13	1.73	30	0.68	58.0	1.98	1.24	1450	43.9
MJ14	1.0	30	1.57	64.0	1.14	1.14	908	19.1
MJ15	1.0	30	1.33	67.0	1.14	1.10	941	22.5
MJ16	1.0	30	1.07	66.0	1.14	1.1	941	28.1
MJ17	2.0	30	1.08	58.0	2.28	1.24	1670	27.8
MJ18	2.0	30	0.66	61.0	2.28	1.18	1755	45.5
MJ19	2.0	30	0.98	65.0	2.28	1.12	1849	30.5
MJ20	1.0	30	0.98	62.0	1.14	1.16	893	30.5
MJ21	2.0	30	0.6	60.0	2.28	1.20	1726	50.0
*MJ22	0.8	30	1.43	62.0	0.91	1.16	713	10.5
*MJ23	1.0	30	0.66	62.0	1.14	1.16	893	22.7
*MJ24	1.0	30	0.84	69.0	1.14	1.06	977	17.9
*MJ25	2.0	30	0.72	66.2	2.28	1.10	2060	20.8
*MJ26	4.0	40	1.13	67.1	3.42	1.10	3091	17.7
*MJ27	1.5	40	1.13	67.1	1.28	1.10	1157	17.7

Table 5-1 Run parameters for Series MJ experiments

s, nozzle spacing = 1.0"

D, nozzle Diameter = 0.109"

N, No. of nozzles

* RUNS WITH FULL DIFFUSER IN MIDDLE OF BASIN

ν_o = kinematic viscosity of water at discharge temperature

R_D = Reynolds number based on jet diameter

$= \frac{u_o D}{\nu_o}$

heat dissipation scheme was also studied.

Runs FF02-29 were half-diffuser tests. The arrangement of the temperature sensors for these runs is shown in Fig.5-3a; the probe spacing is of the order of the diffuser length. Runs FF 30-36 were done with a full diffuser placed in the middle of the model and discharging perpendicularly with respect to a current (Fig. 5-3b)

As these tests are designed to study the recirculation of heat into the near field, the experiments usually took a little over two hours, when it was judged that the model boundaries had significantly distorted the test results. Temperature scans were made every ten minutes from the start of the experiment. Dye patterns and path lines are recorded and velocity measurements are made. For crossflow runs, steady state is usually achieved after about forty minutes, when temperature rises change by only fractions of a degree. The run parameters are listed in Table 5-2.

5.5.3 Series 200

The objective of the Series 200 experiments is to provide a data base for comparison with the theory presented in Chapter III and IV. All previous experiments on the three-dimensional temperature field of a unidirectional diffuser in an open, shallow receiving waterbody employ a temperature measurement grid much larger than the nozzle spacing. Because these tests are mostly either aimed at testing plume behavior on a large scale (e.g. far field recirculation) or providing global

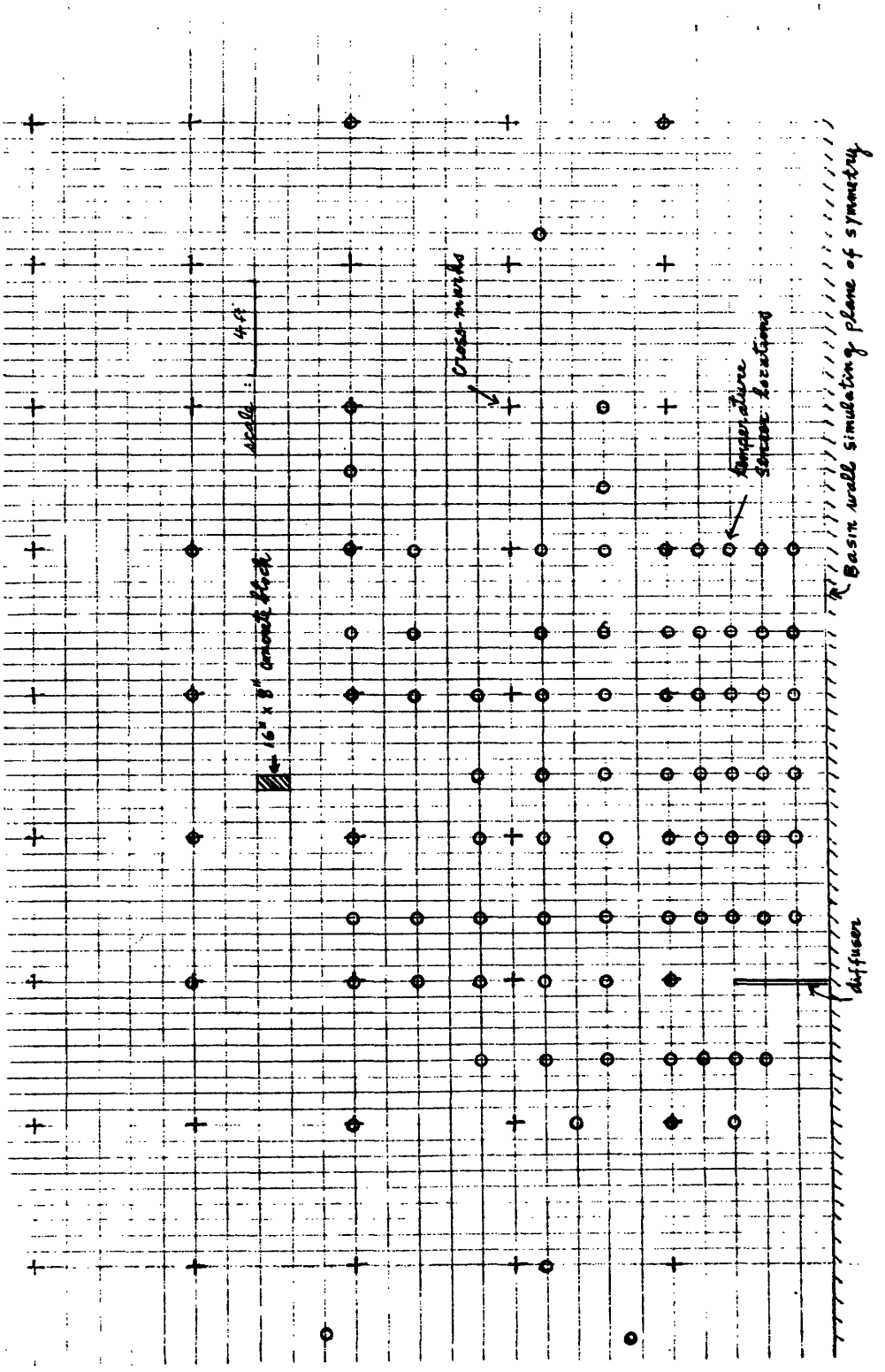

Fig. 5-3 a) Temperature probe arrangement for half-diffuser tests: Series FF

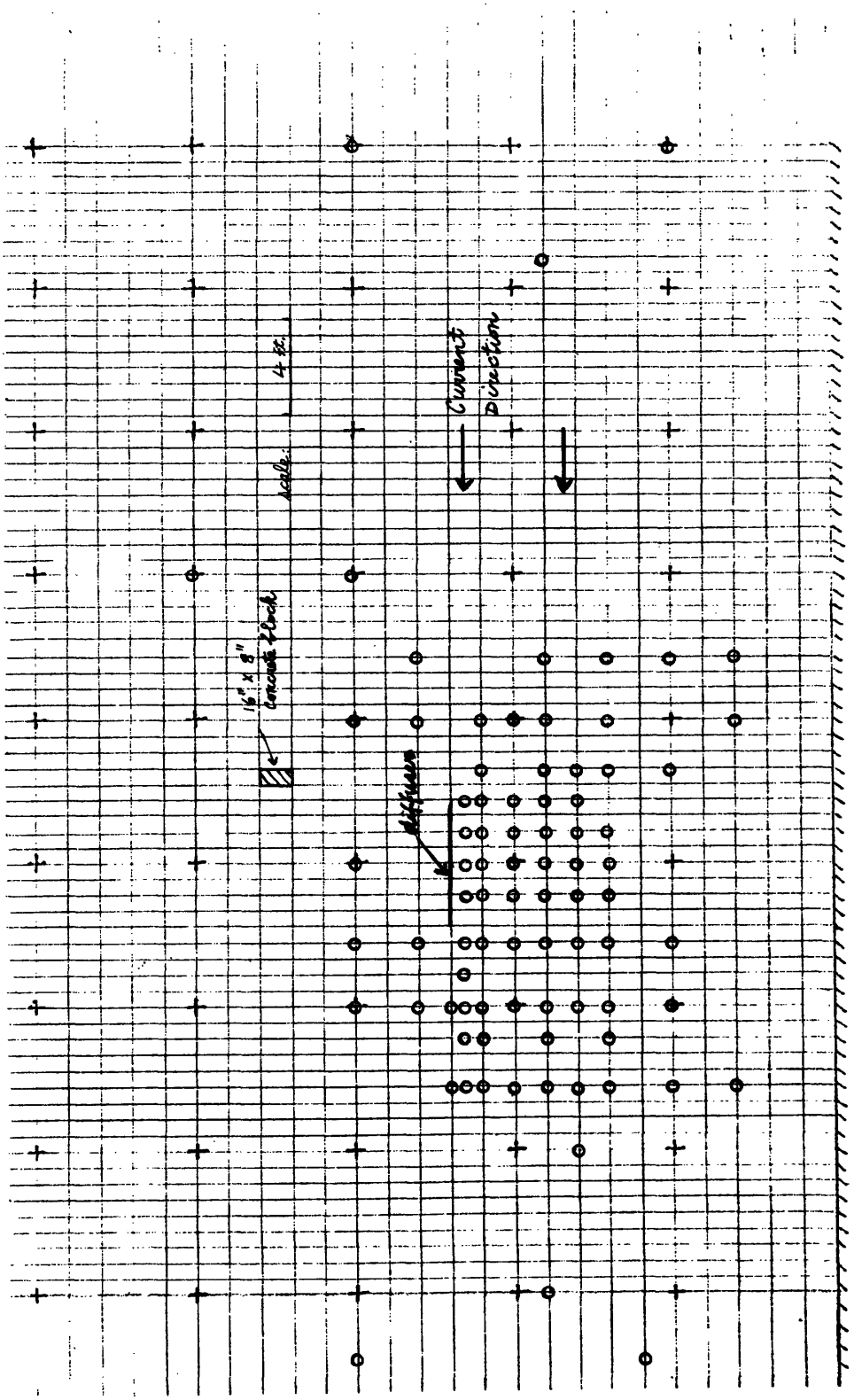

Fig. 5-3 b) Temperature probe arrangement for full diffuser tests:
Series FF

Table 5-2 Run Parameters for Series FF experiments

SERIES FF

	BASIC VARIABLES								SECONDARY VARIABLES						
RUN No.	Q_o (GPM)	$L_D/2$ (ft)	s (in)	N	H (in)	u_a (FPS)	T_a (^oF)	ΔT_o (^oF)	u_o (FPS)	R_D	R_a	F_D	F_S	H/B	$0.5L_D/H$
FF02	1.0	2.5	1.0	30	1.18	0.02	73.0	24.5	1.18	1458	195	34.3	117.3	126.5	25.4
FF03	1.73	2.5	1.0	30	0.82	0.0	66.9	27.2	2.05	2399	-	58.1	198.6	87.5	36.8
FF04	2.0	2.5	1.0	30	0.69	0.0	71.6	29.9	2.37	3098	-	62.4	213.3	73.9	43.5
FF05	2.0	2.5	1.0	30	0.72	0.018	74.5	26.8	2.37	3089	109	64.0	218.6	77.2	41.7
FF06	1.5	2.5	1.0	30	1.0	0.017	74.8	24.3	1.78	2240	143.6	50.9	174.0	107.2	30.0
FF07	1.5	2.5	1.0	30	1.03	0.0	75.2	23.8	1.78	2234	-	51.0	174.3	110.6	29.1
FF08	1.0	2.5	1.0	30	1.03	0.022	75.2	22.3	1.18	1458	192.5	35.4	121.1	110.6	29.1
FF09	1.0	2.5	1.0	30	1.03	0.0	75.4	22.7	1.18	1469	-	35.1	120.6	110.6	29.1
FF10	1.5	1.67	1.0	20	1.03	0.023	75.2	24.8	2.66	3408	201.3	75.3	257.4	110.6	19.4
FF11	1.5	1.67	1.0	20	1.01	0.0	75.4	23.3	2.66	3338	-	77.2	263.7	108.0	19.8
FF12	1.5	1.67	1.0	20	1.04	0.009	75.8	23.5	2.66	3370	80.2	77.9	266.1	111.9	19.2
FF13	1.5	1.67	1.0	20	1.5	0.0	77.3	23.8	2.66	3466	-	75.7	258.6	160.8	13.3
FF14	1.5	1.67	1.0	20	1.5	0.02	78.8	22.3	2.66	3466	265.1	78.5	268.4	160.8	13.3
FF15	1.0	2.5	1.0	30	0.96	0.0	77.4	22.3	1.18	1506	-	35.0	119.5	102.9	31.3
FF16	2.0	2.5	1.0	30	1.02	-0.038	79.0	20.9	2.37	3021	343.2	72.1	246.3	109.3	29.4
FF17	1.4	2.5	1.0	30	1.02	-0.048	78.8	18.9	1.66	2046	432.6	53.1	181.6	109.3	29.4
FF18	1.73	2.5	1.0	30	0.8	-0.034	78.4	21.6	2.05	2620	240.3	60.7	207.5	86.2	37.3
FF19	1.73	2.5	1.0	30	0.83	0.014	78.6	22.1	2.05	2650	102.2	60.3	206.2	88.7	36.2
FF20	1.0	1.67	1.0	20	1.5	-0.035	79.2	21.7	1.78	2304	465.8	52.6	179.9	160.8	13.3
FF21	1.5	3.33	2.0	20	1.01	0.022	79.5	20.4	2.66	3398	197.6	82.3	397.7	216.1	39.7
FF22	1.5	3.33	2.0	20	1.01	0.022	80.0	1.6	2.66	2653	199.0	333.2	446.1	216.1	39.7
FF23	1.5	3.33	2.0	20	0.98	0.0	80.6	23.9	2.66	3663	-	73.7	356.3	210.9	40.7
FF24	1.0	5.0	2.0	30	1.02	0.027	78.9	22.0	1.18	1536	243.8	34.8	168.2	218.6	58.8
FF25	1.0	5.0	2.0	30	1.00	0.0	79.3	22.7	1.18	1563	-	33.5	161.9	214.3	60.0
FF26	0.6	1.67	2.0	10	0.74	0.0	79.5	20.0	2.13	2704	-	65.3	315.5	159.5	26.9
FF27	0.6	0.83	1.0	10	0.76	0.0	79.2	22.0	2.13	2773	-	60.4	206.4	81.0	13.2
FF28	0.8	1.25	1.0	15	0.73	0.0	79.2	20.1	1.89	2397	-	56.5	193.1	78.5	20.5
FF29	0.8	2.5	2.0	15	0.74	0.0	79.7	19.0	1.89	2370	-	59.0	295.1	159.5	40.3
FF30	1.5	1.25	1.0	30	1.10	0.034	75.2	25.0	1.78	2278	318	49.7	169.7	118.3	13.6
FF31	1.25	1.25	1.0	30	1.06	0.047	75.4	23.0	1.48	1847	422	43.5	148.6	113.2	14.2
FF32	2.0	1.25	1.0	30	1.07	0.047	75.7	22.4	2.37	2939	428	70.5	241.0	114.5	14.1
FF33	1.25	1.25	1.0	30	1.51	0.03	76.6	24.5	1.48	1925	391	41.6	142.1	162.0	9.9
FF34	2.0	1.25	1.0	30	1.51	0.03	77.0	26.1	2.37	3180	393	64.0	218.6	162.0	9.9
FF35	0.75	1.25	2.0	15	0.8	0.049	77.5	23.4	1.78	2304	343	50.8	245.8	172.3	18.6
FF36	1.25	1.25	2.0	15	0.83	0.049	77.9	25.2	2.96	3975	355	81.0	391.5	177.5	18.1

Table 5-2 Run parameters for Series FF experiments

F_D: densimetric Froude number based on jet diameter

$$= \frac{u_o}{\sqrt{g\frac{\Delta\rho_o}{\rho_a} D}}$$

R_a: Reynolds number of crossflow based on the water depth

$$= \frac{u_a H}{\nu}$$

information (e.g. maximum temperature rise)they do not reveal the basic structure of the temperature field to a degree that can be used for quantitative comparison with theoretical predictions. In this series of experiments, the spatial resolution of the temperature sensors is equal to the nozzle spacing close to the diffuser. Beyond the near field mixing region, the spread of the plume is taken into account, and the sensor spacing is adjusted accordingly. The temperature measurement grid is shown in Fig. 5-4. Vertical temperature profiles are recorded along the centerline and across six transverse sections of the diffuser plume. Altogether 10 full diffuser tests were performed under stagnant ambient conditions. The diffuser is placed in position B as is shown in Fig. 5-1. No velocity measurement is made. The run parameters are presented in Table. 5-3.

As the limiting case of long diffusers with strong potential for heat recirculation has been treated previously, this program concentrates on relatively short diffuser ($L_D/H \leq 10$). This enables the study of the temperature field for many diffuser lengths in the experimental setup. Furthermore, as will be seen later, these short diffusers are characterized by large scales of recirculation (weak recirculation effects). Hence, the detailed temperature field can be observed in the absence of heat recirculation

A typical run usually takes about 30 minutes when the result begins to be distorted by heat recirculated due to the

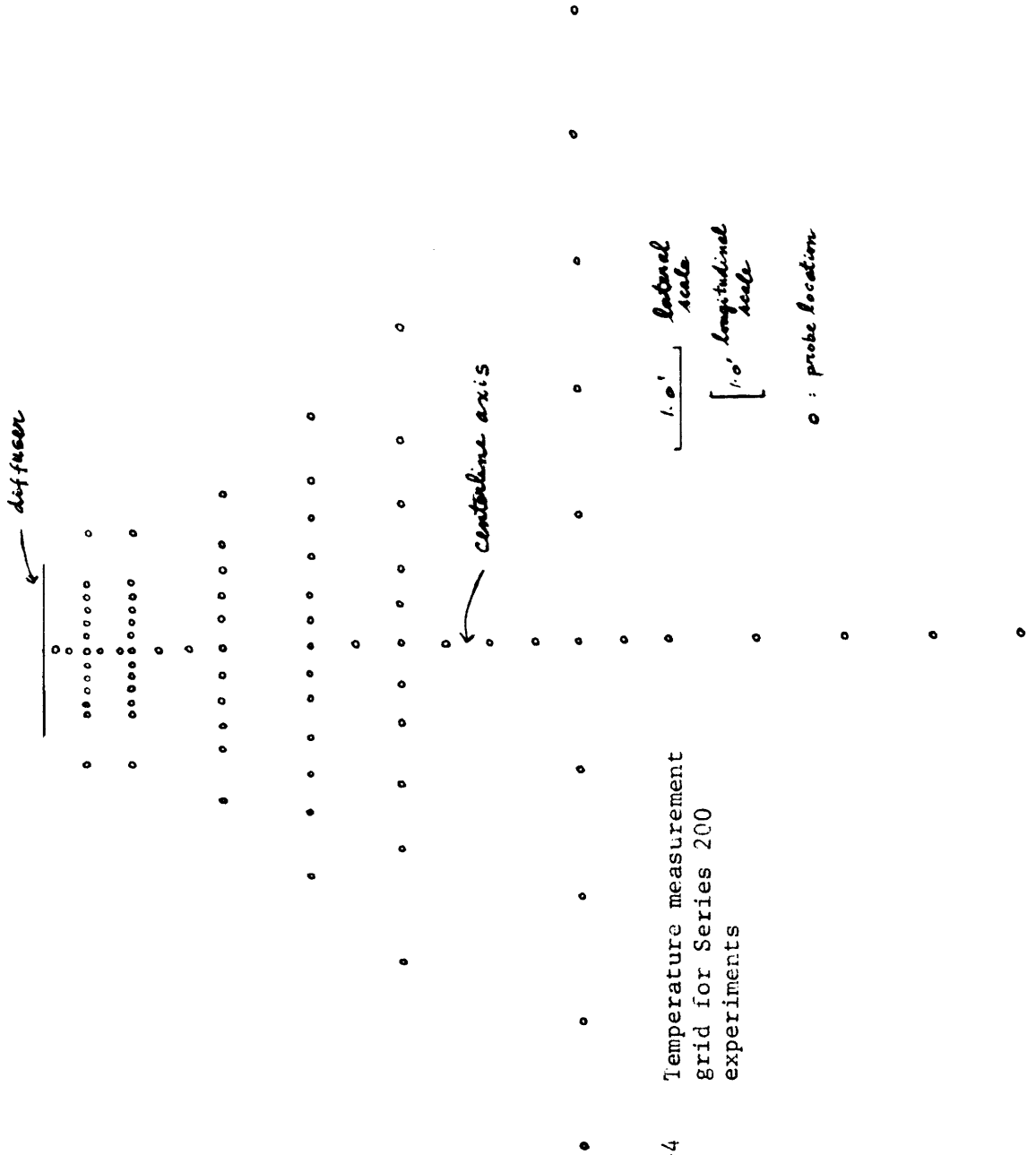

Fig. 5-4 Temperature measurement grid for Series 200 experiments

	BASIC VARIABLES								SECONDARY VARIABLES					
RUN No.	Q_o (GPM)	L_D (ft)	s (in)	N	H (in)	T_a (^oF)	ΔT_o (^oF)	u_o (FPS)	R_D	F_D	F_s	H/B	H/D	L_D/H
201	4.0	1.63	1.5	14	2.15	65.5	30.3	2.09	5543	38.3	108.0	71.3	8.96	9.1
202	3.0	1.63	1.5	14	2.32	68.8	28.0	1.57	4206	29.3	82.7	76.9	9.67	8.4
203	30	0.75	1.5	7	2.30	70.1	26.0	3.14	8315	60.9	171.7	76.3	9.58	3.9
204	3.0	1.13	1.5	10	2.34	70.6	26.8	2.2	5950	41.5	117.0	77.6	9.75	5.8
205	2.0	0.63	1.5	6	2.29	71.7	26.2	2.4	6661	46.3	130.5	75.9	9.54	3.3
206	2.0	0.38	1.5	4	2.29	71.5	24.9	3.66	9771	11.30	265.6	73.0	9.54	2.0
207	3.0	1.5	3.0	7	2.24	69.7	28.2	3.14	8564	57.8	230.7	148.5	9.33	8.0
208	3.0	1.0	3.0	5	2.29	70.5	27.4	4.39	11990	81.9	326.8	151.9	9.54	5.2
209	2.0	1.25	7.5	3	2.22	70.3	26.6	4.9	13125	92.8	585.6	368.0	9.25	6.8
210	2.4	0.38	1.5	4	2.22	69.4	27.0	4.4	11726	83.4	235.7	73.6	9.25	2.0

D_o = 0.24"

Table 5-3 Run Parameters for Series 200 Experiments

the model boundaries. Steady state is usually attained in less than 10 minutes.

5.6 Data reduction

Temperature Data

For each run the ambient temperature T_a is defined as the average of the recordings of all the temperature sensors before the start of the experiment. At each time instant the temperature excess of each probe is defined as

$$\Delta T(x_i,y_i,t) = T(x_i,y_i,t) - T(x_i,y_i,0)$$

where (x_i,y_i) is the co-ordinate of the i th probe.

The near field dilution S is inferred from the temperature data as

$$S = \frac{\Delta T_o}{\Delta T_{max}} = \frac{T_o - T_a}{T_{max} - T_a}$$

where T_{max} is the maximum surface temperature recorded in the absence of any heat recirculation.

Velocity Data

The reduced velocity data are obtained from the photographic measurements in the form of

$$(x_o,t_o),\ (x_1,t_1)\ldots(x_n,t_n)$$

where x_i is the distance of the particle from the diffuser at time t_i.

We assume that the centerline velocity variation $u_c(x)$ can be inferred from the trajectory of a straight pathline in the following manner.

An average velocity is computed for the interval (x_i, x_{i+1})

$$u_c\left(\frac{x_i+x_{i+1}}{2}\right) \simeq \frac{x_{i+1}-x_i}{t_{i+1}-t_i}$$

The error in locating a particle can be estimated to be $\delta x \simeq 0.4x$ width of a concrete block $\simeq 0.25'$.

The error in recording t_i can be regarded as negligible for the range of velocities being measured. Thus, the relative error in measuring the velocity can be estimated as

$$\frac{\delta u}{u} = \frac{\dfrac{x_{i+1}-x_i+\delta x}{\Delta t} - \dfrac{x_{i+1}-x_i}{\Delta t}}{\dfrac{x_{i+1}-x_i}{\Delta t}} = \frac{\delta x}{x_{i+1}-x_i}$$

For the record illustrated in section 5.4, the error of measurement can be estimated to be 18% for the average velocity in the first interval and 5% for the last interval.

CHAPTER VI

COMPARISON OF THEORY WITH EXPERIMENTAL RESULTS

In this chapter the theoretical predictions presented in Chapter III and IV are compared with experimental results of this study and results reported by other investigators. Experimental observations are also described. The comparisons are made for runs that do not exhibit heat recirculations into the near field. This topic will be separately discussed in a later chapter.

6.1 Near Field Mixing

As indicated in section 3.5 , vertical temperature measurements near the diffuser show that the temperature is vertically homogenous, demonstrating the flow is vertically fully mixed. Surface pathlines for a wide range of diffuser lengths ($\frac{L_D}{H} \simeq 3$ - $\frac{L_D}{H} \simeq 100$) show that the induced flow from behind is concentrated in a contracting stramtube that 'separates' the toal induced flow from the ambient fluid. (Fig. 6-1a). The diffuser acts as a sink as far as the external flow is concerned. The contraction occurs at about 0.5 L_D from the diffuser and the contraction coefficient is observed visually to be about 0.5 for the slack tide case (cf. Fig. 3-2b.) Dye injection patterns usually indicate a contraction coefficient greater than predicted by eq. 3.40 as shown in Fig. 6-1b. The experimentally observed value of the near field dilution

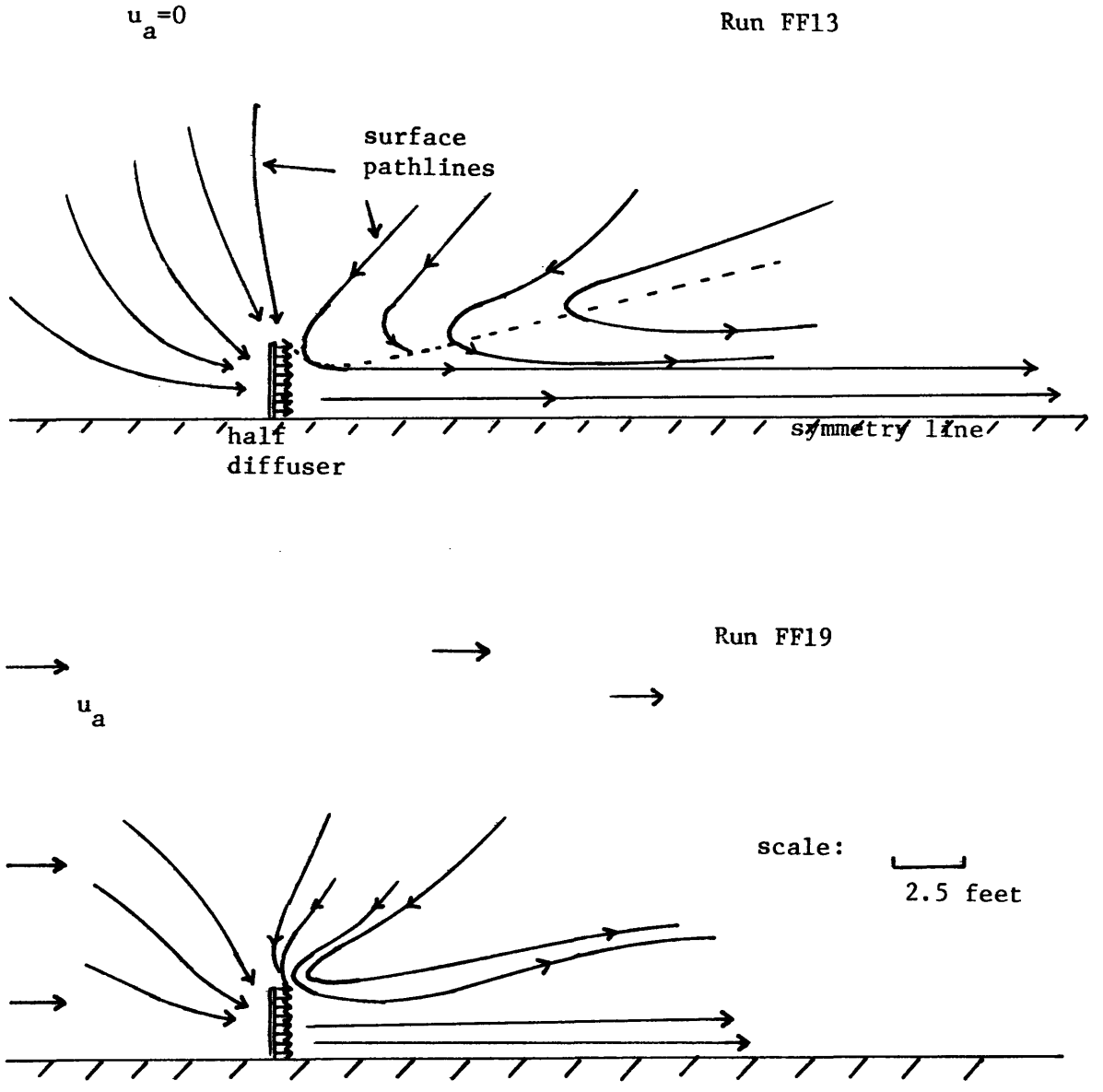

Fig. 6-1 a) Recorded surface flow patterns for a unidirectional diffuser in shallow water; with and without current

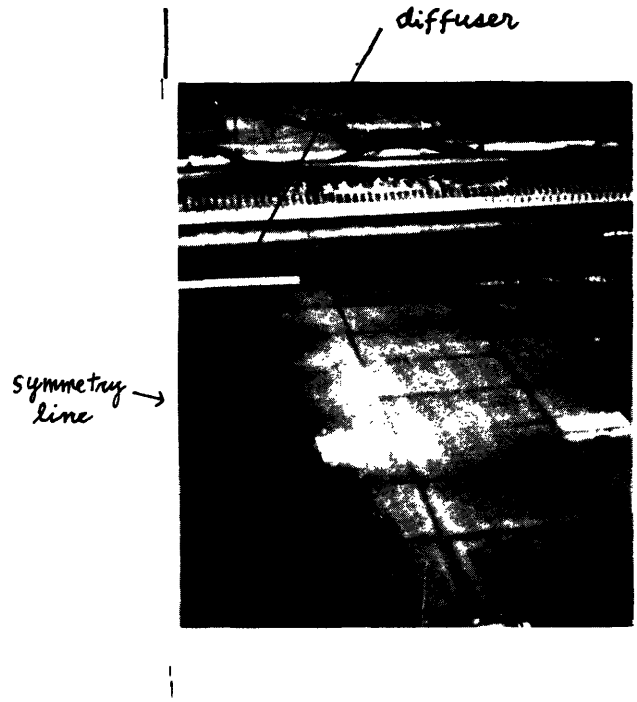

Fig. 6-1 b) Dye injection pattern in the near field of a unidirectional diffuser

is taken to be

$$S \text{ (observed)} = \frac{\Delta T_o}{\Delta T_{Max}}$$

where ΔT_{MAX} is the maximum surface temperature rise recorded in the near field in the absence of any heat recirculation.

i.e., $\Delta T_{max} = \max \Delta T_i$

ΔT_i being the temperature excess recorded by the ith probe .

In Fig. 6-2, we compare the theoretical predictions of S given by eq. 3.38 with the experimental results. Good agreement is obtained for a wide range of S. It should be noted the relative error in S (observed) introduced by temperature measurement errors is greater for larger dilutions.

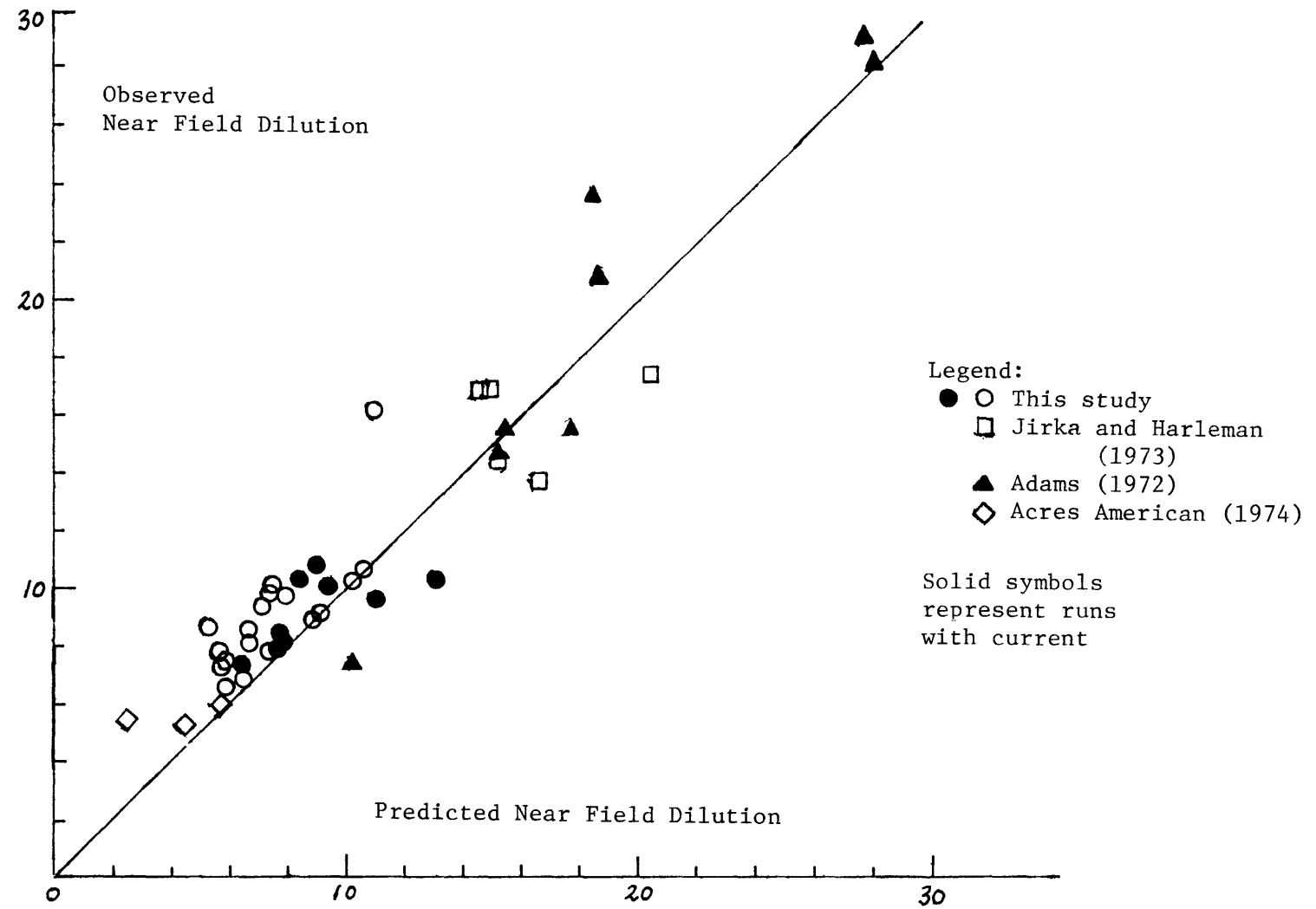

Fig. 6-2 Comparison of predicted near field dilution S(eq.3.38) with experimental results

6.2 Comparison of theory with data: Series FF, MJ

In Fig. 6-3, the predicted isotherms are compared with the observed surface temperature field for the FF Runs of a unidirectional diffuser in a coflowing current with no heat recirculation into the near field. The recorded temperatures are shown to within 0.1 F on the diagram; the decimal point locates the temperature probe relative to the diffuser and the figure is drawn to scale. For each run, the system of equations 4.19-4.20, 4.28, 4.29 are solved numerically for the set of governing parameters $\beta=\frac{L_D H}{N a_o}$, $\gamma=\frac{u_a}{u_o}$, and $\frac{f_o L_D}{H}$. The friction coefficient is assumed to be $f_o = 0.035$ for all the laboratory experiments. The solution yields the centerline velocity $u_c(x)$, the centerline temperature excess $\Delta T_c(x)$, and the plume width $L(x)$. At each x, knowing ΔT_c and $L(x)$, the position of a particular isotherm can be calculated using the assumed temperature profiles given in section 4.1.1. Both the quantitative and qualitative features of the model are well supported by the data. In general the spread of the plume is larger than predicted; this can be attributed to the slight stratification observed at the edge of the plume in these experiments.

In Fig. 6-4, the prediction of centerline velocities are compared with measured surface velocities for runs in the FF and MJ series. The method of determining the velocity was described in section. 5.6. The agreement between theory and data is

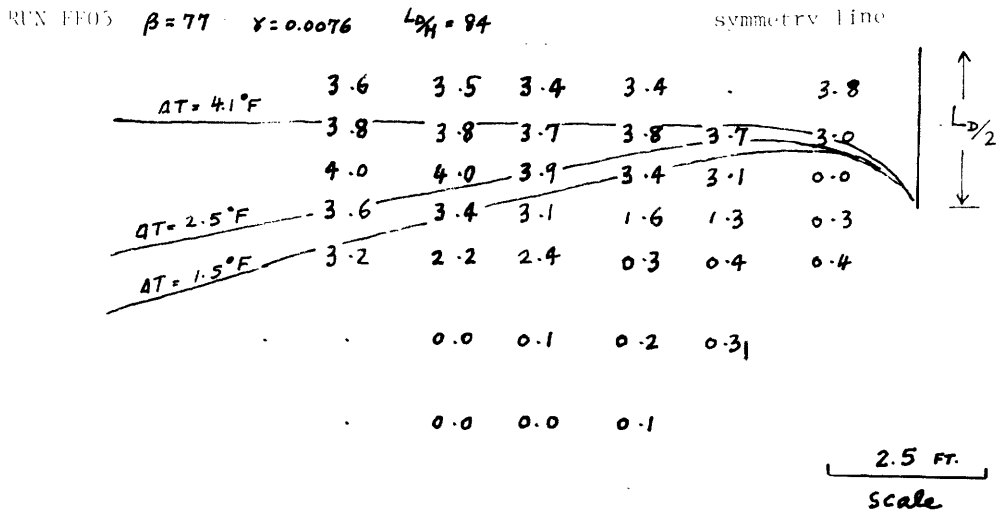

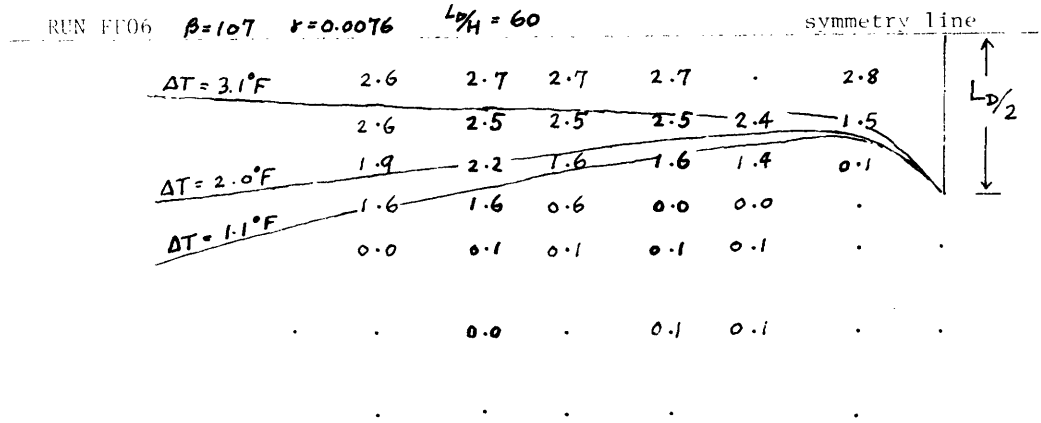

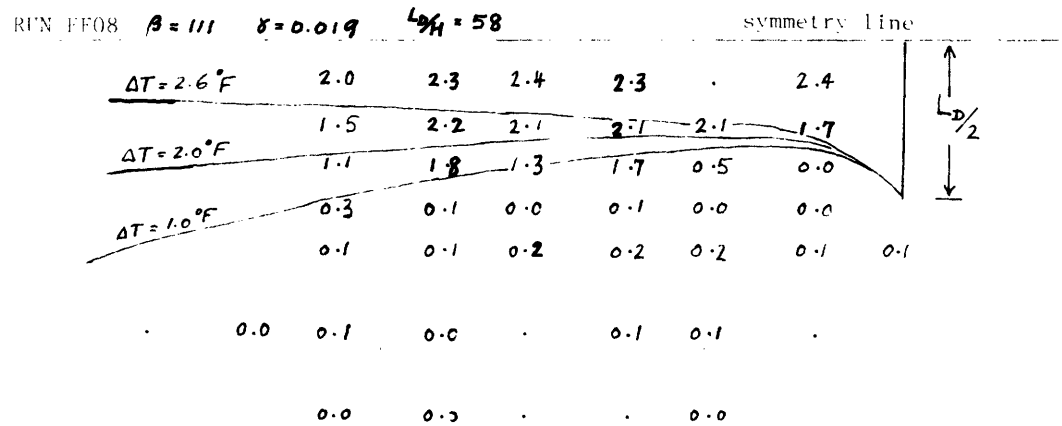

Fig.6-3: Comparison of predicted isotherms——— with temperature measurements in Series FF (eq. 4.19-4.20, 4.28-4.29)

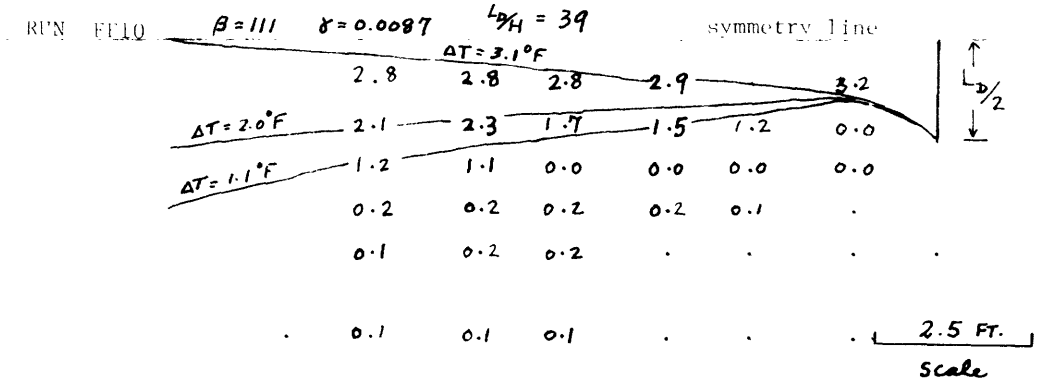
RUN FF10
β = 111
γ = 0.0087
L_D/H = 39
symmetry line
ΔT = 3.1°F
ΔT = 2.0°F
ΔT = 1.1°F
2.8 2.8 2.8 2.9 3.2
2.1 2.3 1.7 1.5 1.2 0.0
1.2 1.1 0.0 0.0 0.0 0.0
0.2 0.2 0.2 0.2 0.1
0.1 0.2 0.2
0.1 0.1 0.1
L_D/2
2.5 FT.
Scale

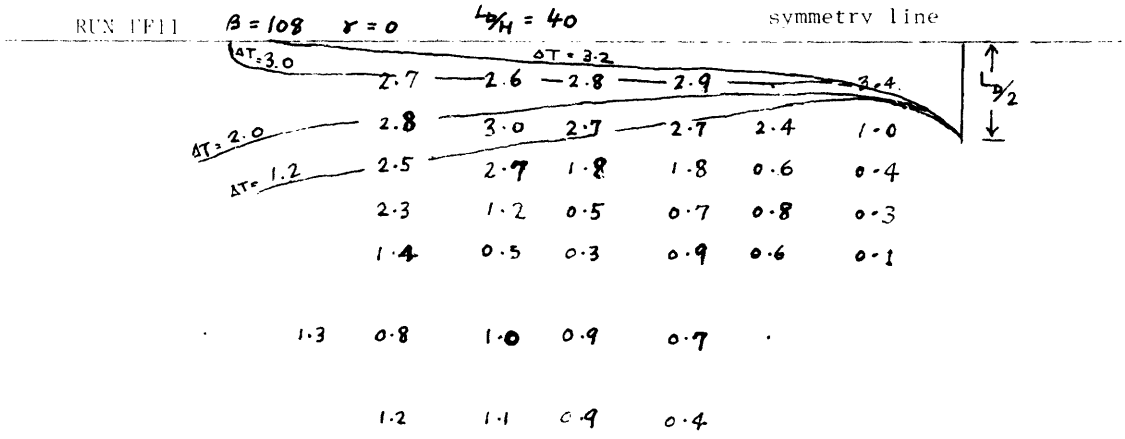
RUN FF11
β = 108
γ = 0
L_D/H = 40
symmetry line
ΔT = 3.0
ΔT = 3.2
ΔT = 2.0
ΔT = 1.2
2.7 2.6 2.8 2.9 3.4
2.8 3.0 2.7 2.7 2.4 1.0
2.5 2.7 1.8 1.8 0.6 0.4
2.3 1.2 0.5 0.7 0.8 0.3
1.4 0.5 0.3 0.9 0.6 0.1
1.3 0.8 1.0 0.9 0.7
1.2 1.1 0.9 0.4
L_D/2

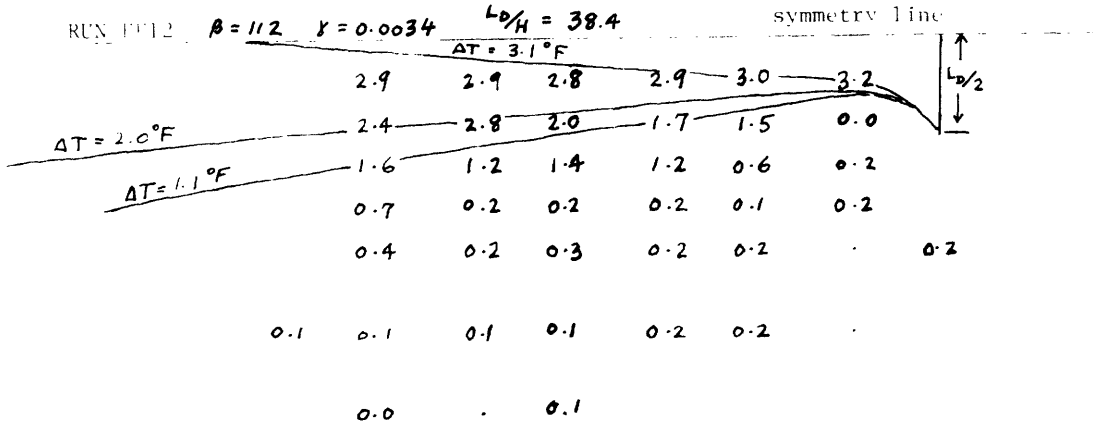
RUN FF12
β = 112
γ = 0.0034
L_D/H = 38.4
symmetry line
ΔT = 3.1°F
ΔT = 2.0°F
ΔT = 1.1°F
2.9 2.9 2.8 2.9 3.0 3.2
2.4 2.8 2.0 1.7 1.5 0.0
1.6 1.2 1.4 1.2 0.6 0.2
0.7 0.2 0.2 0.2 0.1 0.2
0.4 0.2 0.3 0.2 0.2 0.2
0.1 0.1 0.1 0.1 0.2 0.2
0.0 0.1
L_D/2

Fig.6-3 cont'd:

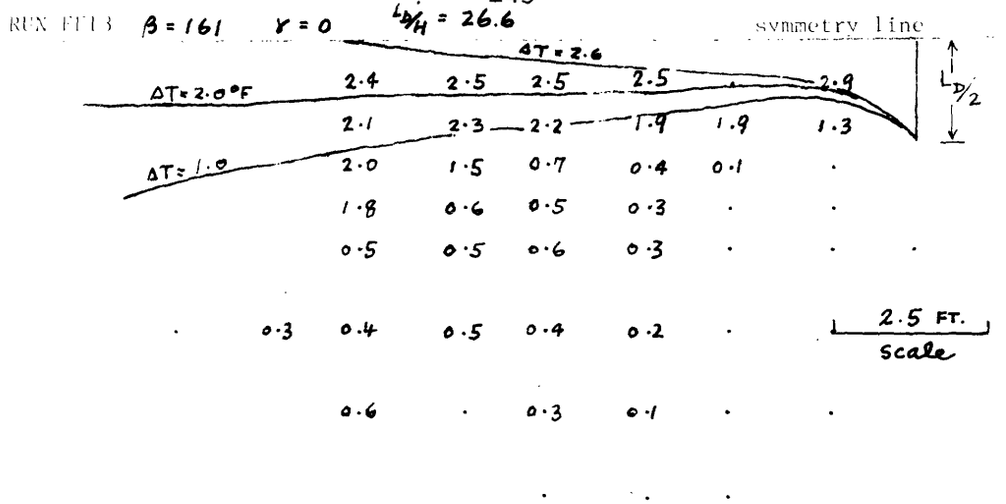
RUN FF13 β = 161 γ = 0 L_D/H = 26.6
symmetry line
ΔT = 2.6
ΔT = 2.0°F
ΔT = 1.0
2.4 2.5 2.5 2.5 2.9
2.1 2.3 2.2 1.9 1.9 1.3
2.0 1.5 0.7 0.4 0.1
1.8 0.6 0.5 0.3
0.5 0.5 0.6 0.3
0.3 0.4 0.5 0.4 0.2
0.6 0.3 0.1
$L_D/2$
2.5 FT.
scale

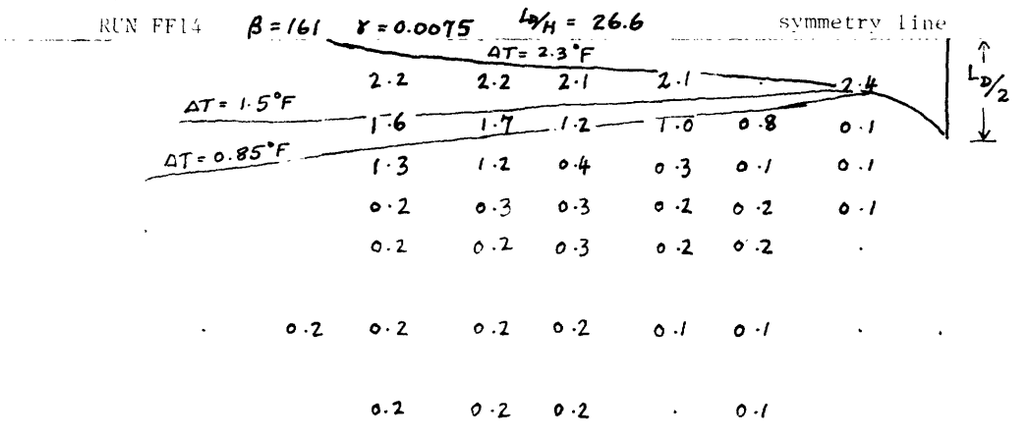
RUN FF14 β = 161 γ = 0.0075 L_D/H = 26.6
symmetry line
ΔT = 2.3°F
ΔT = 1.5°F
ΔT = 0.85°F
2.2 2.2 2.1 2.1 2.4
1.6 1.7 1.2 1.0 0.8 0.1
1.3 1.2 0.4 0.3 0.1 0.1
0.2 0.3 0.3 0.2 0.2 0.1
0.2 0.2 0.3 0.2 0.2
0.2 0.2 0.2 0.2 0.1 0.1
0.2 0.2 0.2 0.1
$L_D/2$

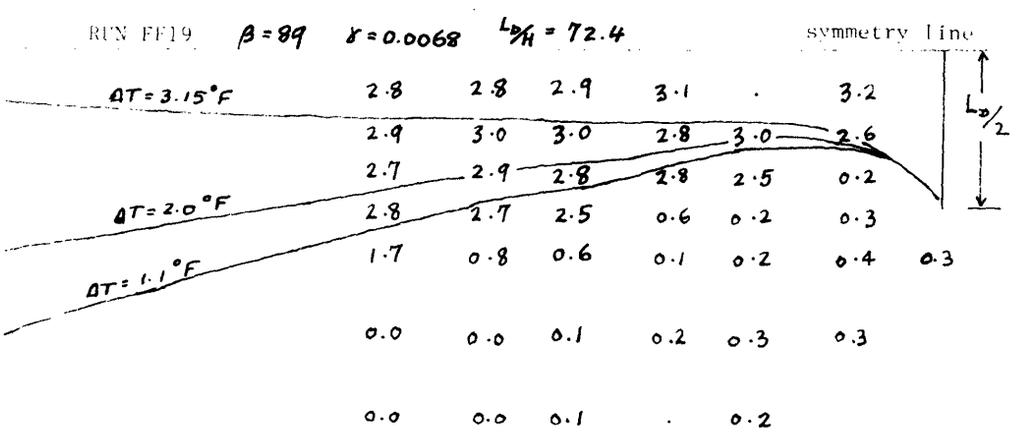
RUN FF19 β = 89 γ = 0.0068 L_D/H = 72.4
symmetry line
ΔT = 3.15°F
ΔT = 2.0°F
ΔT = 1.1°F
2.8 2.8 2.9 3.1 3.2
2.9 3.0 3.0 2.8 3.0 2.6
2.7 2.9 2.8 2.8 2.5 0.2
2.8 2.7 2.5 0.6 0.2 0.3
1.7 0.8 0.6 0.1 0.2 0.4 0.3
0.0 0.0 0.1 0.2 0.3 0.3
0.0 0.0 0.1 0.2
$L_D/2$

Fig. 6-3 cont'd:

fairly good. For some runs there is scatter in the data and the recorded velocities are lower than predicted values; this may be due to surface tension effects, an intrinsic limitation in the time-of-travel velocity measurement technique at low velocities.

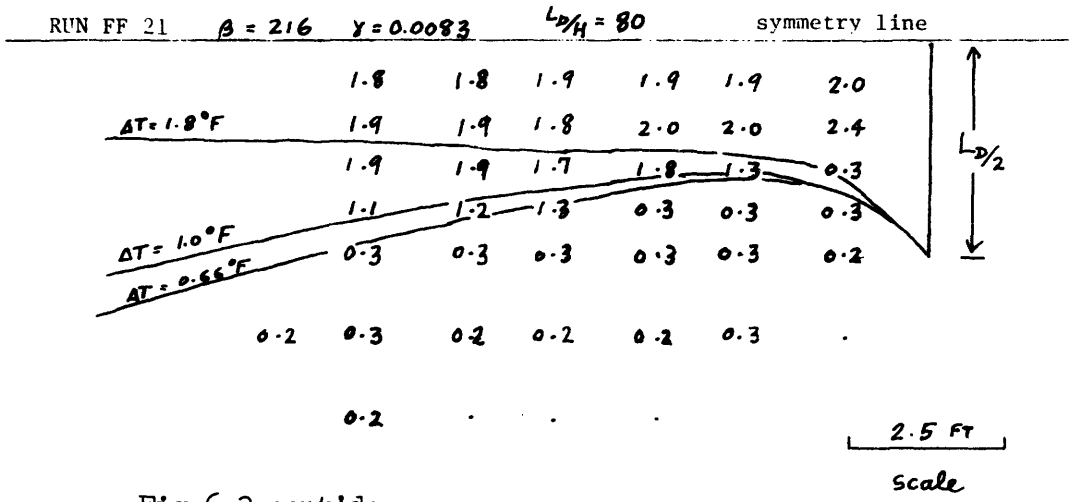

Fig.6-3 cont'd:

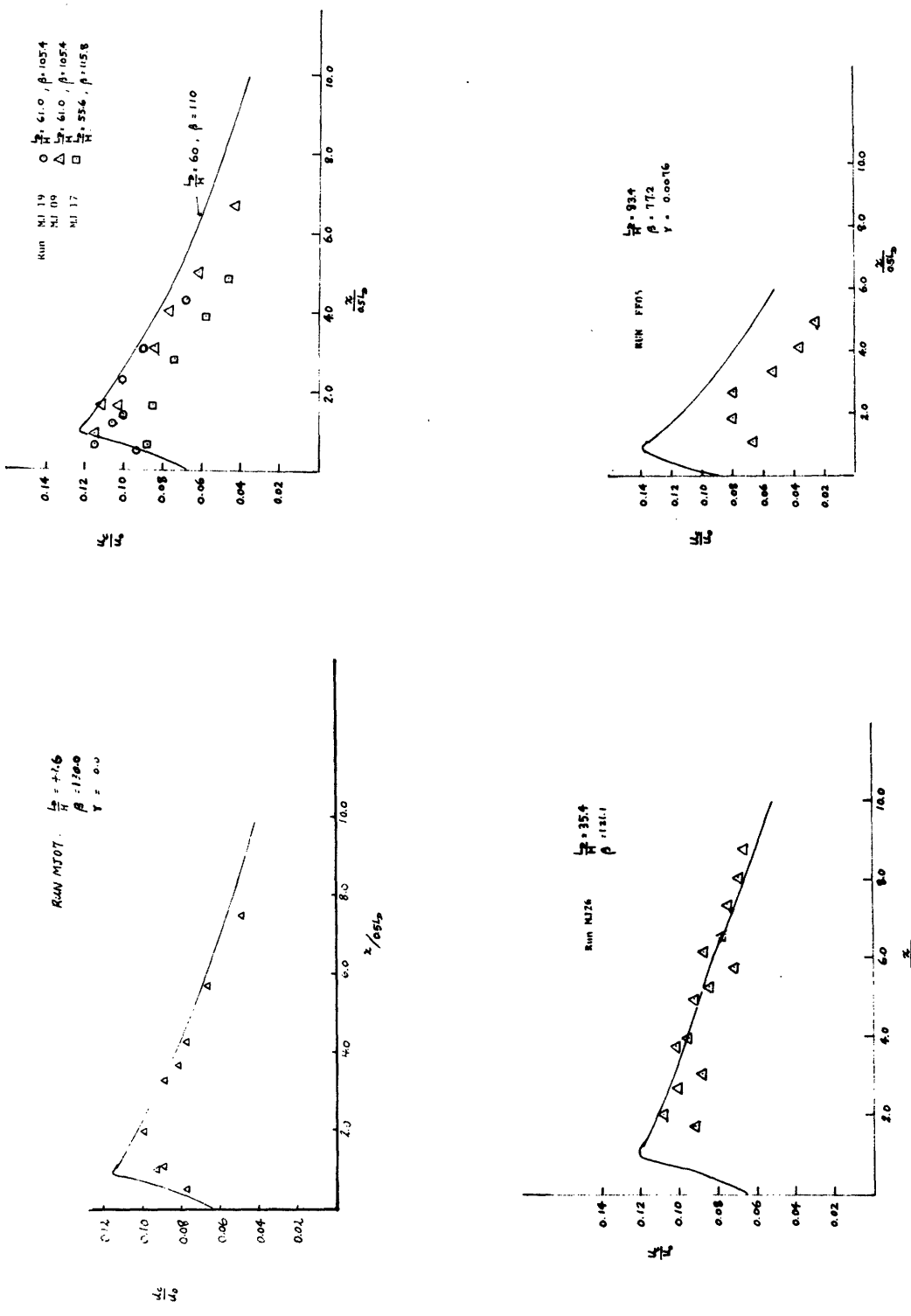

Fig.6-4: Comparison of predicted centerline velocities ——— with experimental data
(eq. 4.19-4.20, 4.28-4.29)

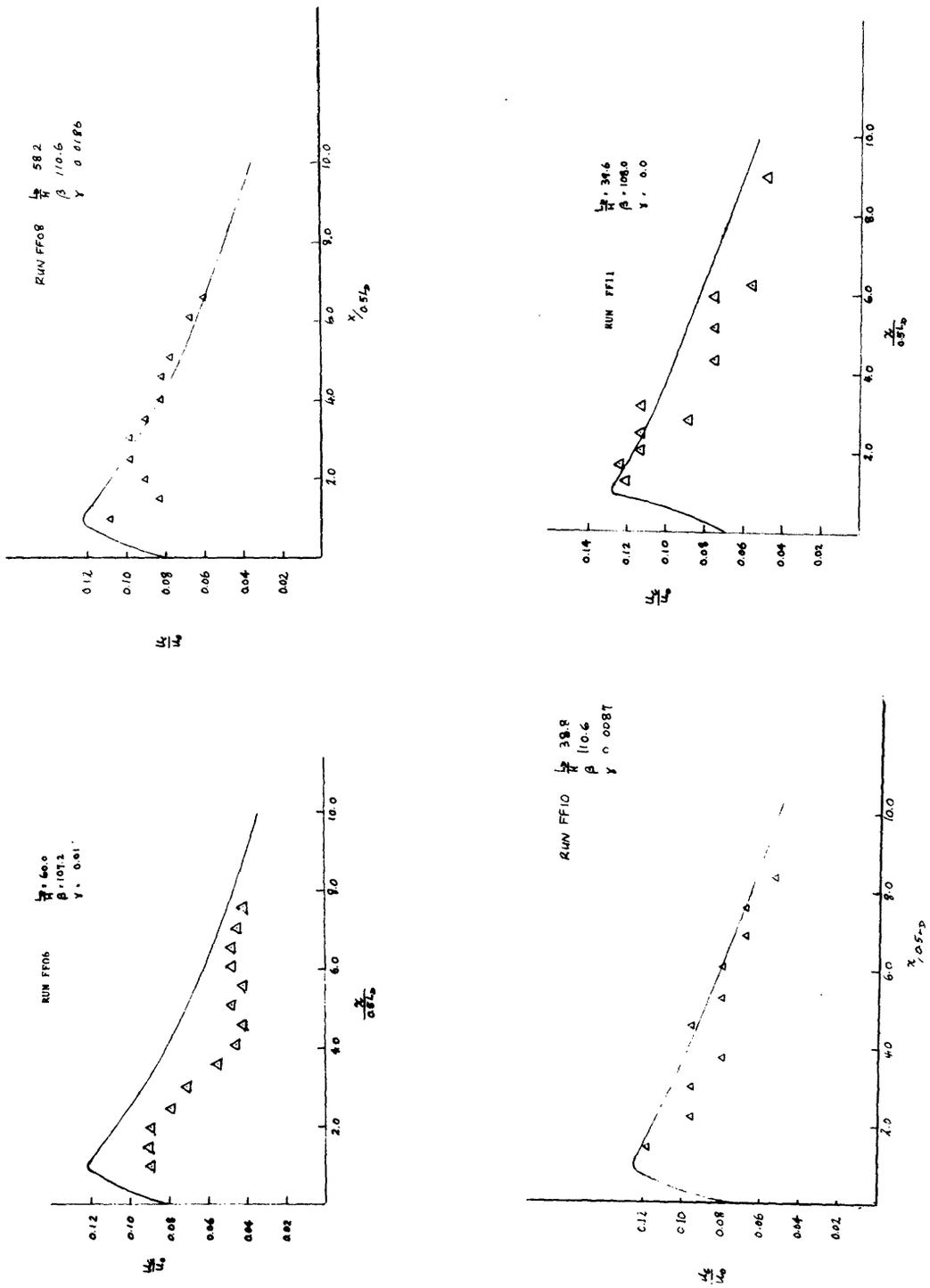

Fig. 6-4 cont'd

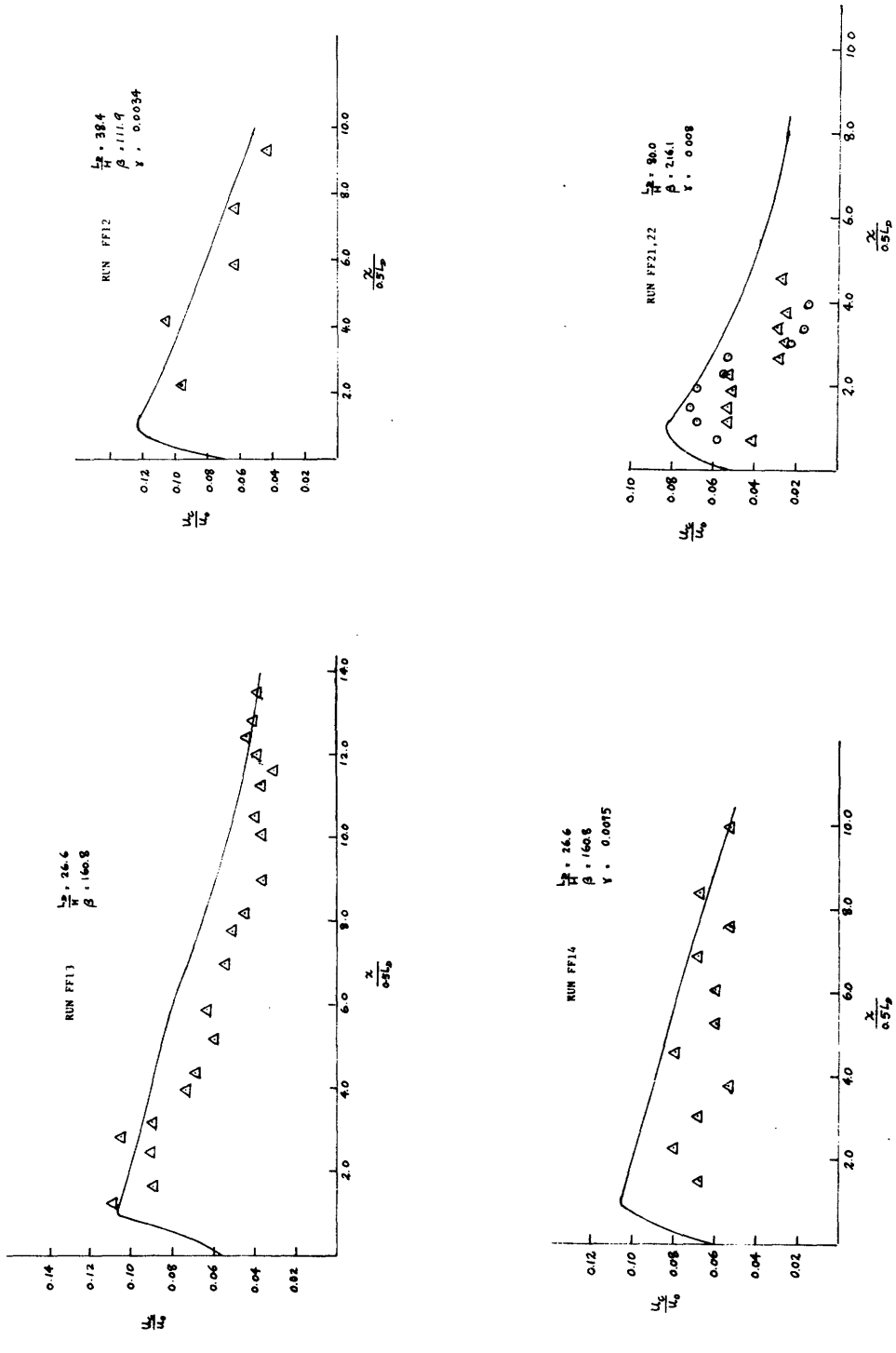
RUN FF12
$\frac{L_B}{W}$ = 38.4
β = 111.9
γ = 0.0034
RUN FF21, 22
$\frac{L_B}{W}$ = 90.0
β = 216.1
γ = 0.008
RUN FF13
$\frac{L_B}{W}$ = 26.6
β = 160.8
RUN FF14
$\frac{L_B}{W}$ = 26.6
β = 160.8
γ = 0.0015
$\frac{u'_c}{U_0}$
$\frac{x}{0.5L_B}$

Fig. 6-4 cont'd

6.3 Comparison of theory and laboratory results: Series 200

For this set of experiments dye injection patterns show the plume is symmetrical for a distance of approximately 40 H (Fig. 6-5). Beyond this point the plume meanders and somewhat loses its shear structure.

In Fig. 6-6 the theoretical predictions of eqs. 4.44,4.47, 4.52 and 4.53 are compared with the series 200 experimental data. Both centerline temperatures and areas within surface isotherms are illustrated. (Details of the computation of isotherm areas are included in Appendix C). The centerline temperature rise normalised with the predicted near field temperature rise, $\Delta T/\Delta T_N$, is plotted against distance from the diffuser x/L_D. At every x, the different symbols represent temperatures recorded at six vertical positions from just beneath the free surface to near the bottom. Thus the vertical spread of these points is a measure of the vertical homogeneity of the thermal structure. For a region close to the diffuser, where the temperature field is strongly three dimensional (the individual submerged jets have not completely merged with each other and the flow not yet vertically fully mixed), the prediction of the two dimensional model is not valid. Beyond the initial jet mixing zone, however, good agreement is obtained. The data clearly shows a shorter diffuser mixes more efficiently in the intermediate field. In general the vertical scatter of temperature data at any point is less than 10% of the mean, suggesting a 2D

approximation is sufficient for practical purposes.

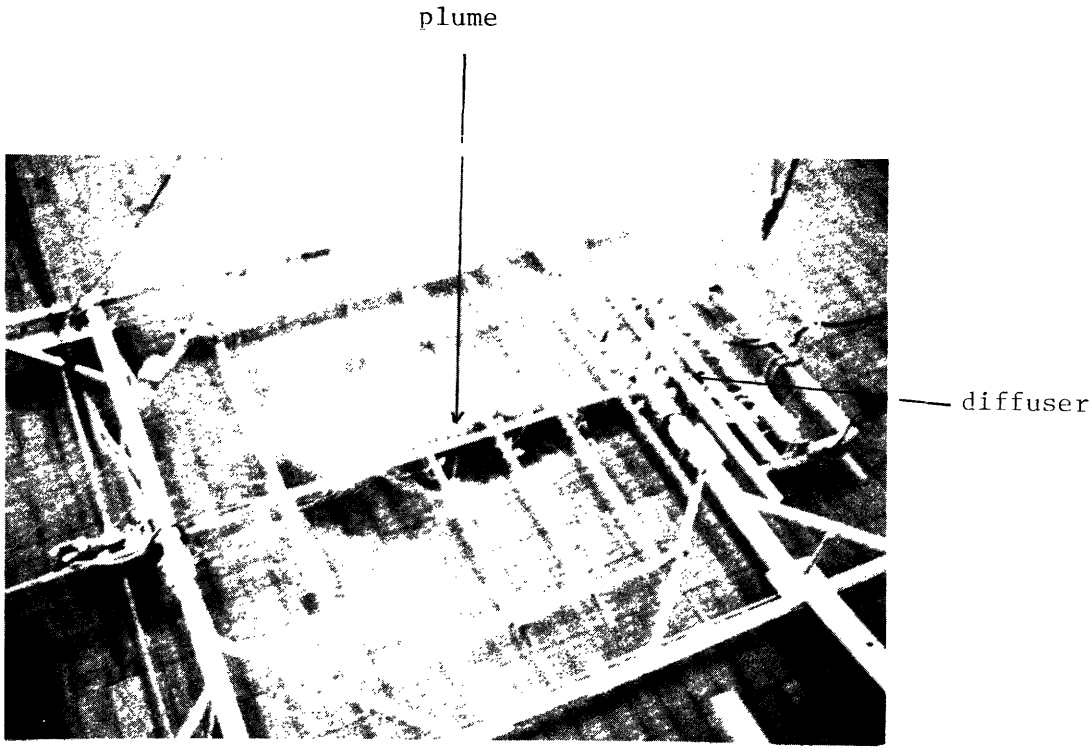

Fig. 6-5: Dye Injection Pattern of Diffuser Plume: Series 200

Fig. 6-7 shows the comparison of predicted surface isotherm areas with the series 200 results. Good agreement is obtained. In general the model overpredicts for the higher induced temperature rises. This can be attributed to the 2D nature of the model. The area of the initial jet mixing zone (in which $\Delta T < \Delta T_N$) is of the order of $L_D H$, and can account for a substantial portion of the predicted isotherm areas for ΔT close to ΔT_N in the short diffuser tests.

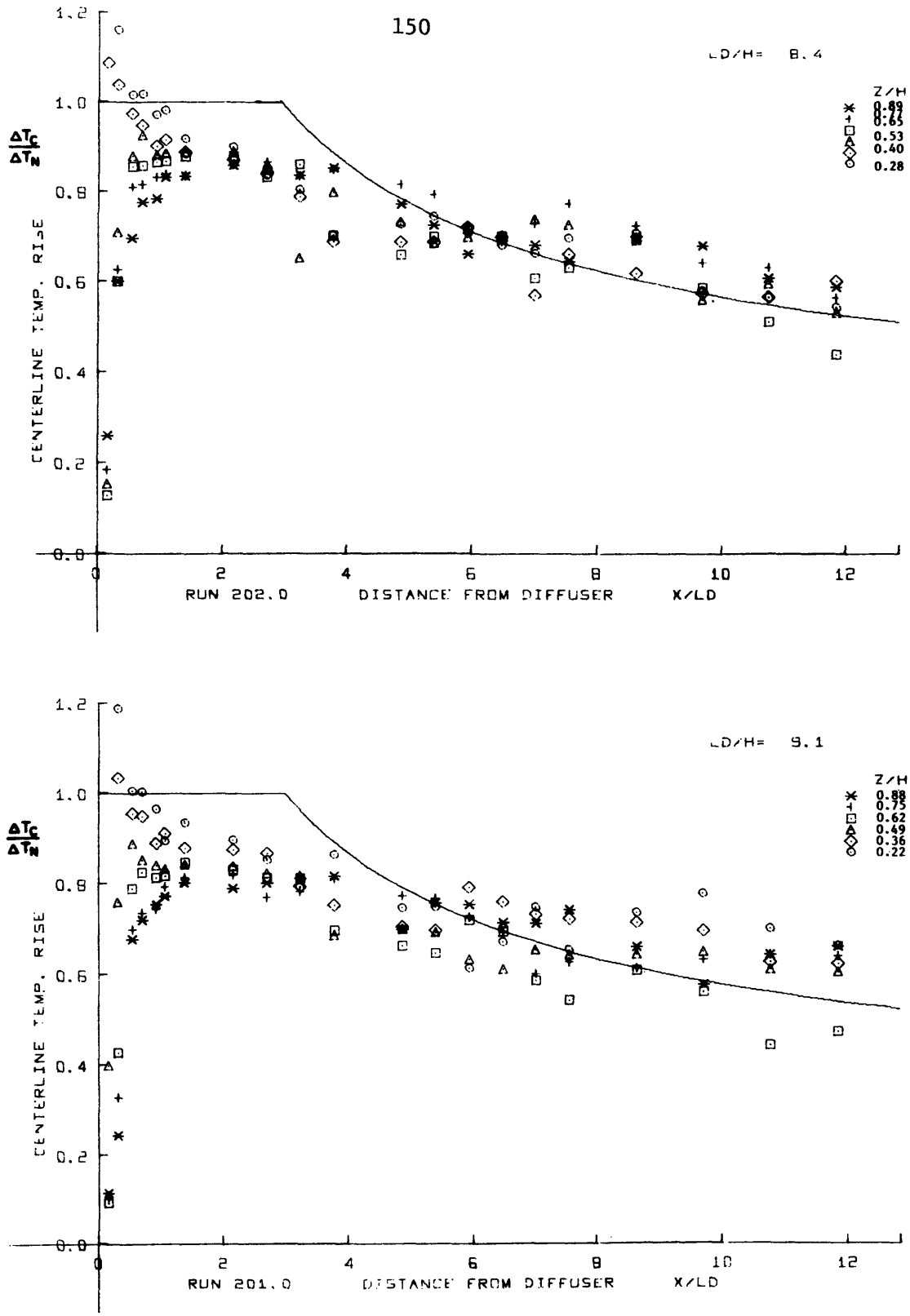

Fig.6-6: Comparison of predicted centerline temperature rises ——— with Series 200 experiments (eq. 4.44-4.47, 4.52-4.53)

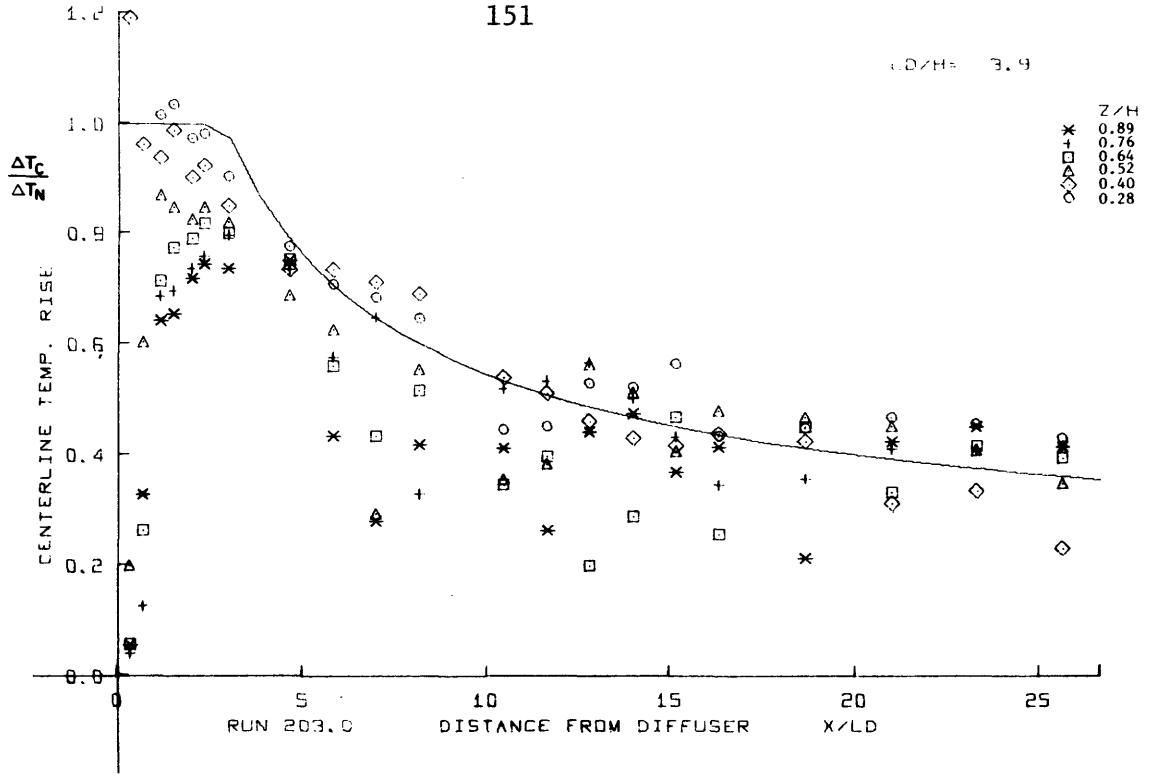
LD/H= 3.9
Z/H
0.89
0.76
0.64
0.52
0.40
0.28
ΔTc/ΔTN
CENTERLINE TEMP. RISE
1.0
0.8
0.6
0.4
0.2
0.0
0
5
10
15
20
25
RUN 203.0
DISTANCE FROM DIFFUSER
X/LD

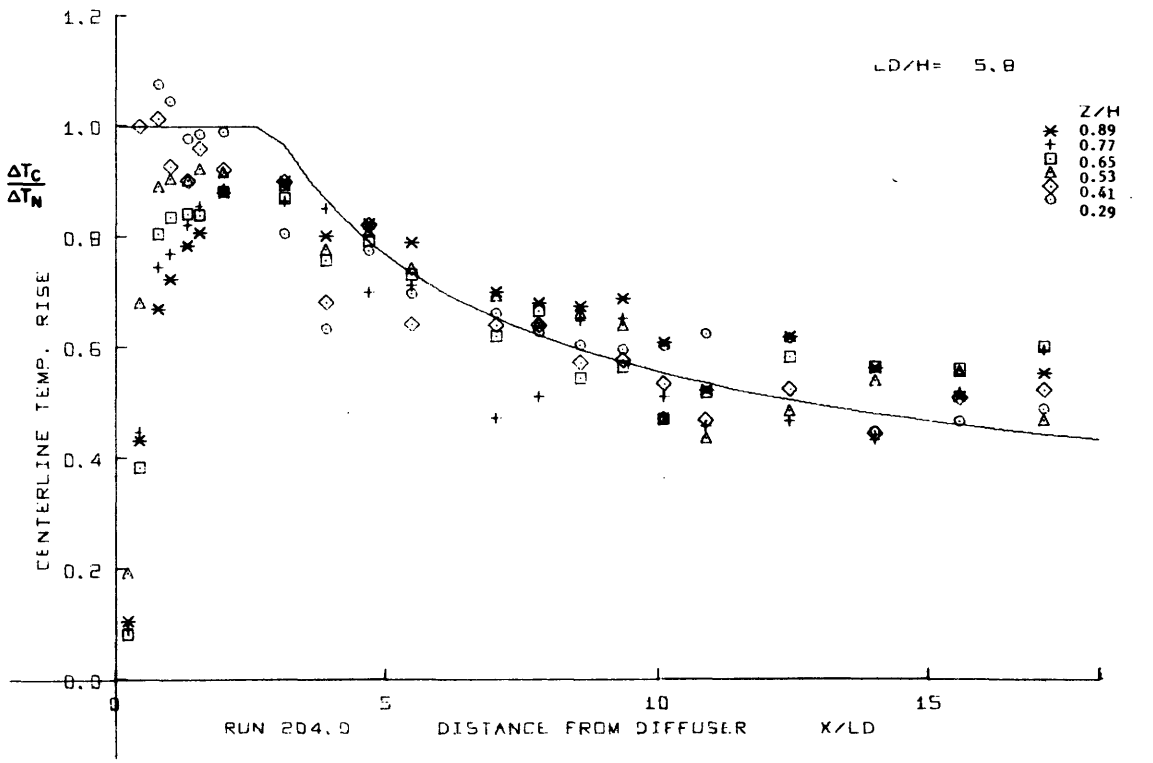
LD/H= 5.8
Z/H
0.89
0.77
0.65
0.53
0.41
0.29
ΔTc/ΔTN
CENTERLINE TEMP. RISE
1.2
1.0
0.8
0.6
0.4
0.2
0.0
0
5
10
15
RUN 204.0
DISTANCE FROM DIFFUSER
X/LD

Fig.6-6 cont'd

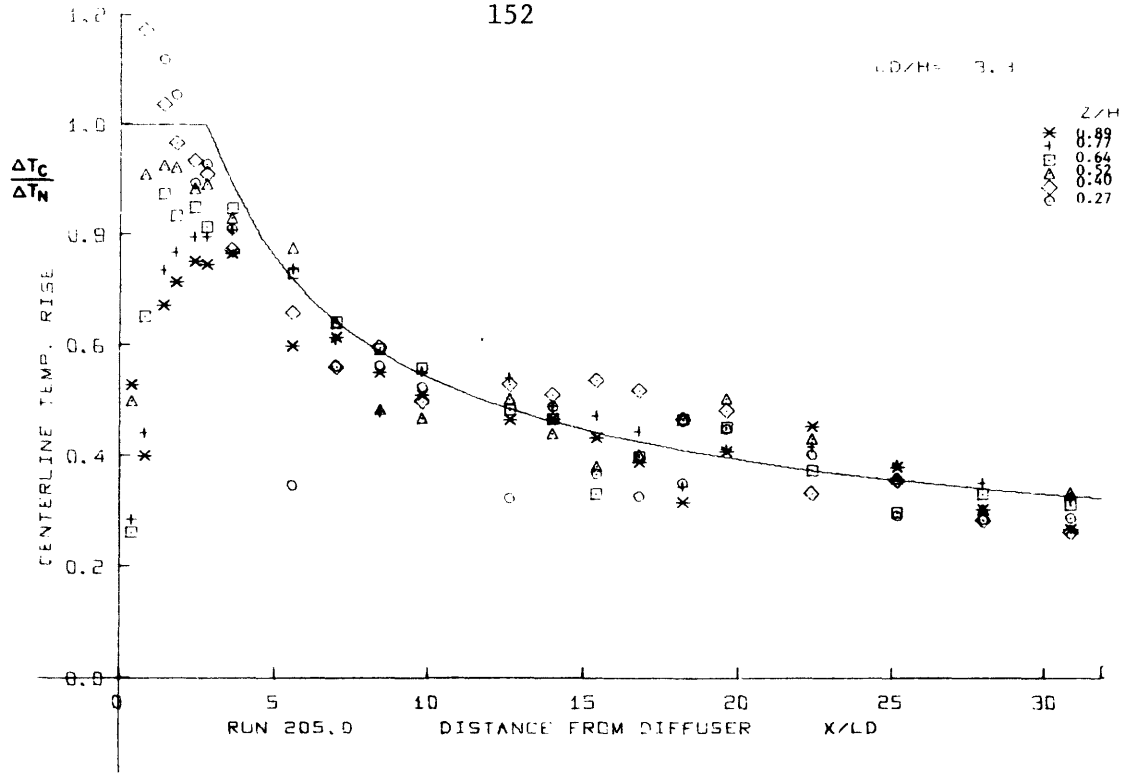
LD/H= 3.1
Z/H
0.89
0.77
0.64
0.52
0.40
0.27
ΔTc/ΔTN
CENTERLINE TEMP. RISE
1.2
1.0
0.8
0.6
0.4
0.2
0.0
0
5
10
15
20
25
30
RUN 205.0
DISTANCE FROM DIFFUSER
X/LD

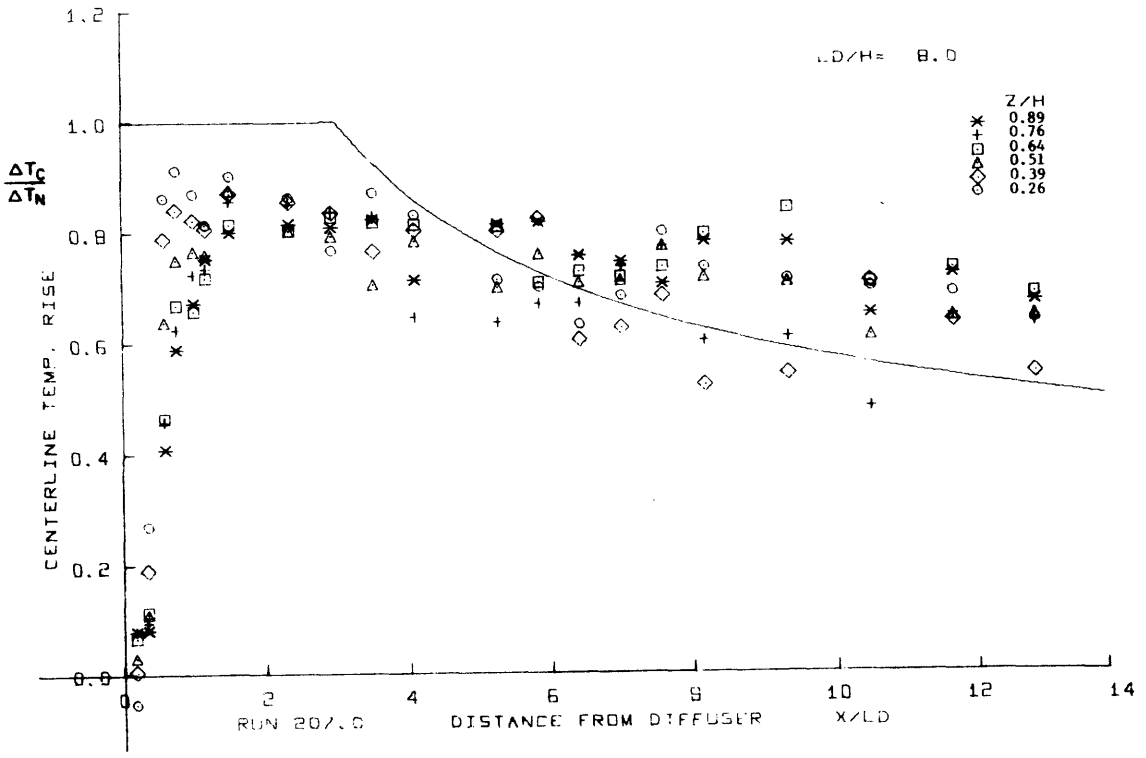
LD/H= 8.0
Z/H
0.89
0.76
0.64
0.51
0.39
0.26
ΔTc/ΔTN
CENTERLINE TEMP. RISE
1.2
1.0
0.8
0.6
0.4
0.2
0.0
0
2
4
6
8
10
12
14
RUN 207.0
DISTANCE FROM DIFFUSER
X/LD

Fig.6-6 cont'd

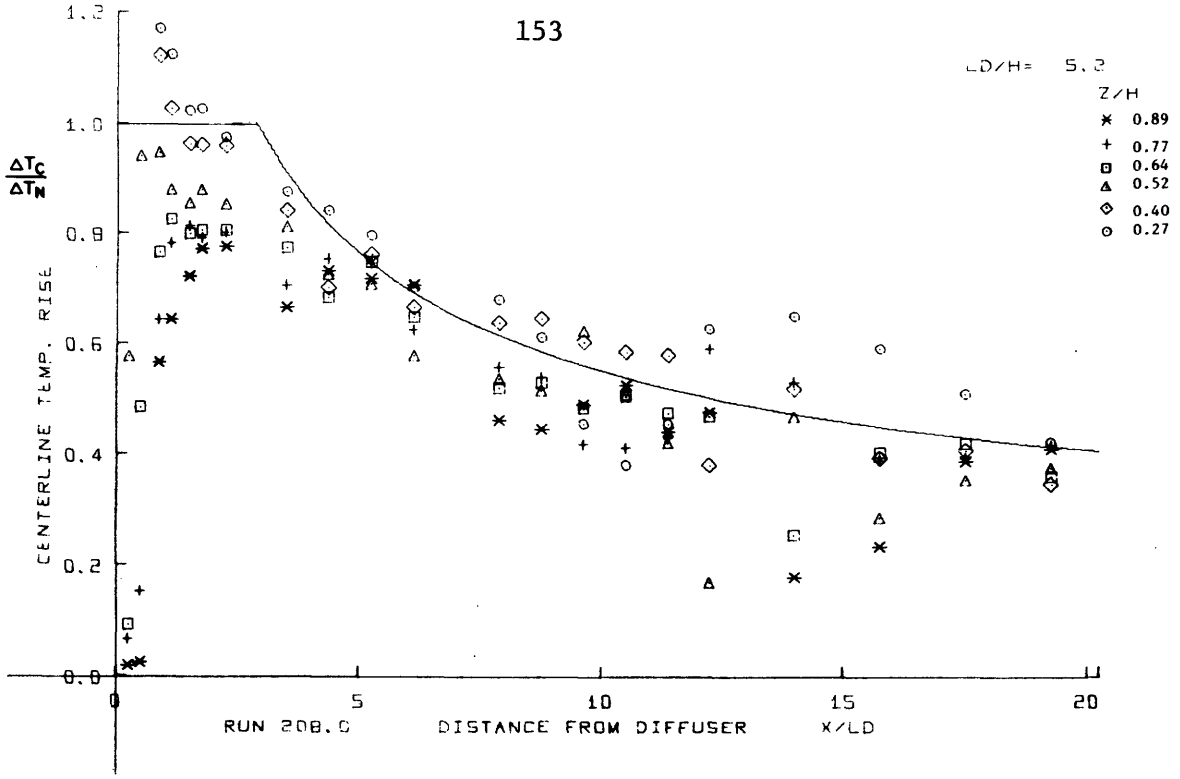
LD/H= 5.2
Z/H
0.89
0.77
0.64
0.52
0.40
0.27
ΔTc/ΔTN
CENTERLINE TEMP. RISE
1.2
1.0
0.8
0.6
0.4
0.2
0.0
0
5
10
15
20
RUN 208.0
DISTANCE FROM DIFFUSER
X/LD

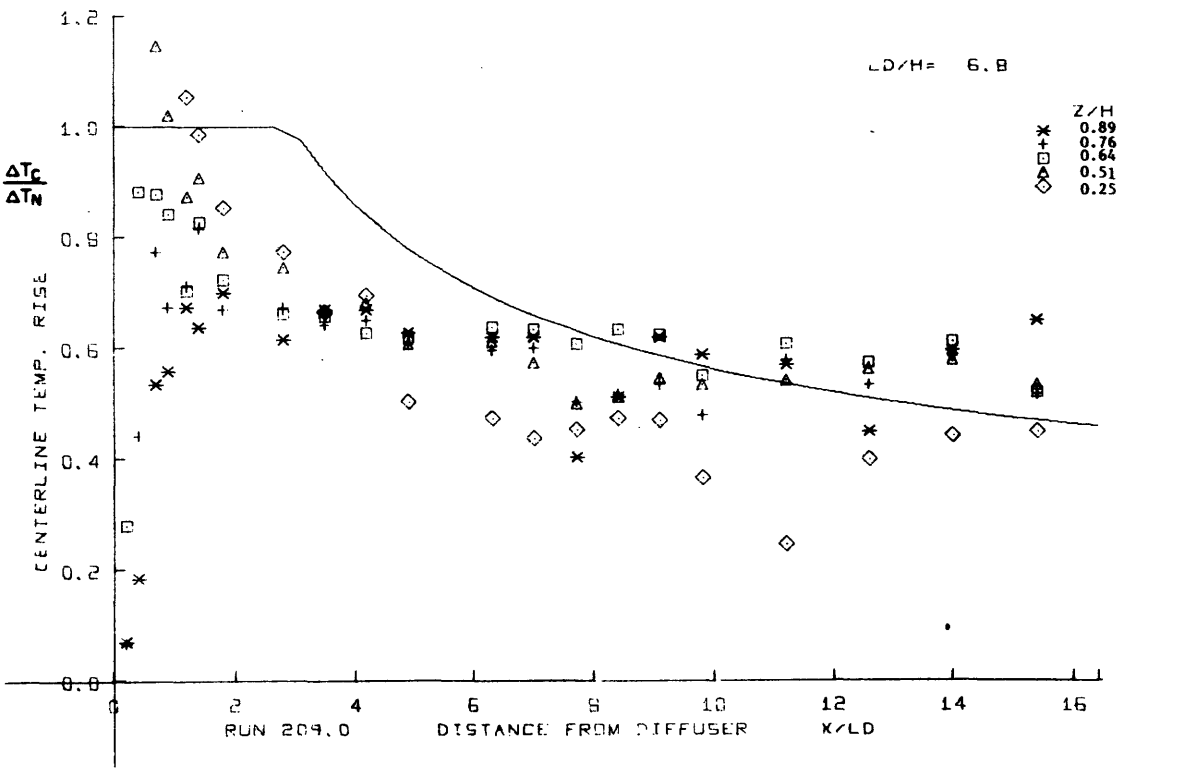
LD/H= 6.8
Z/H
0.89
0.76
0.64
0.51
0.25
ΔTc/ΔTN
CENTERLINE TEMP. RISE
1.2
1.0
0.8
0.6
0.4
0.2
0.0
0
2
4
6
8
10
12
14
16
RUN 209.0
DISTANCE FROM DIFFUSER
X/LD

Fig.6-6 cont'd

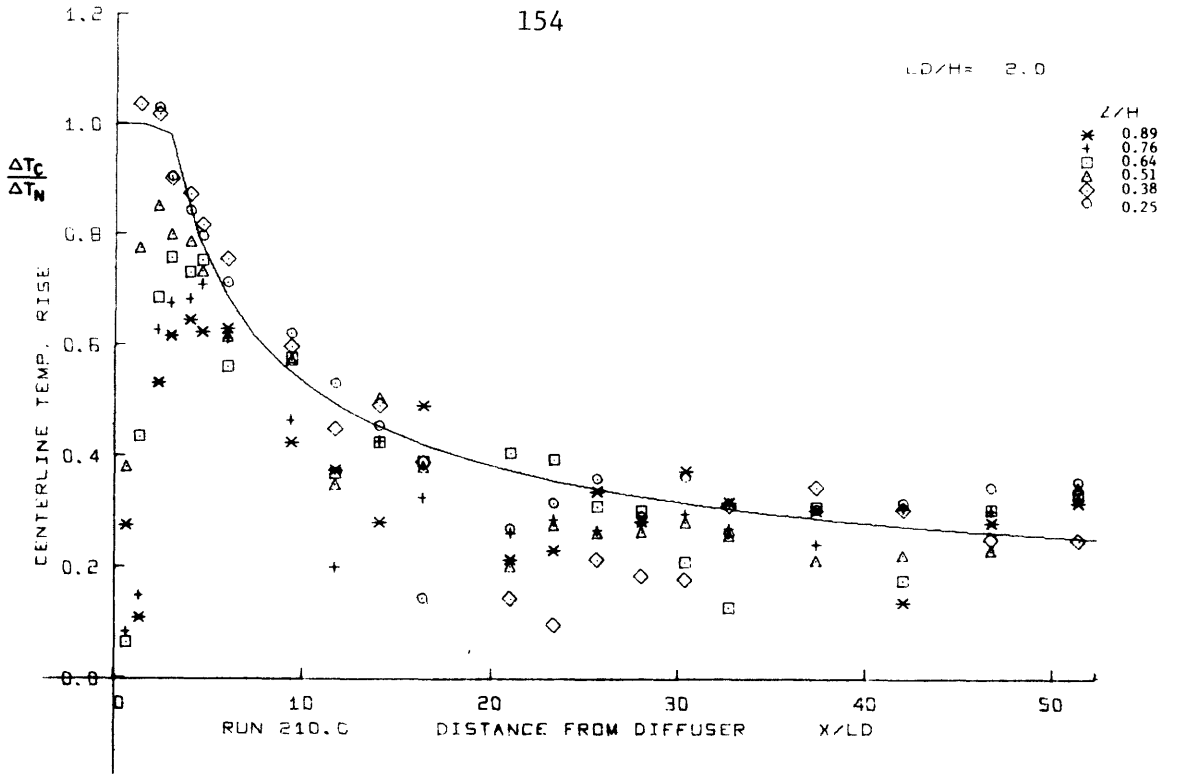

Fig.6-6 cont'd

6.4 Detailed thermal structure

In Fig. 6-8 typical transverse surface temperature profiles at different longitudinal positions are illustrated along with the theoretical predictions. The surface centerline temperatures indicate a constant temperature rise plateau region of $\sim 3L_D$, confirming the assumption of a zone of flow establishment. In Fig. 6-9 the cross-sectional transverse temperature profiles are also illustrated. The temperature measurements show that beyond the region of near field mixing the details of the diffuser design are not important and the diffuser length L_D is the correct length scale. The exact 3D temperature distribution, as influenced by the merging and

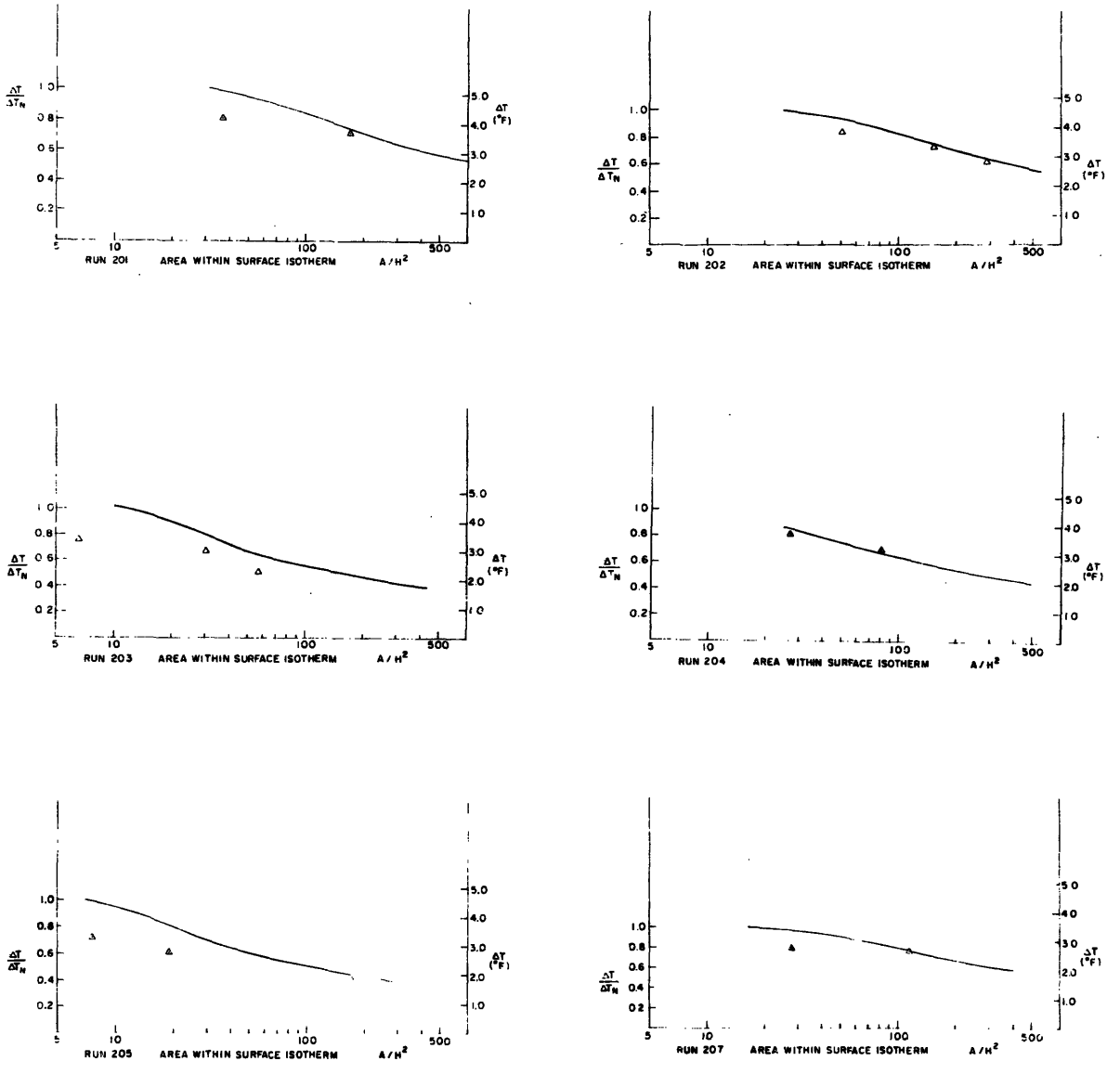

Fig. 6-7: Comparison of predicted isotherm areas ——— with Series 200 experiments (eq. 4.44-4.47, 4.52-4.53)

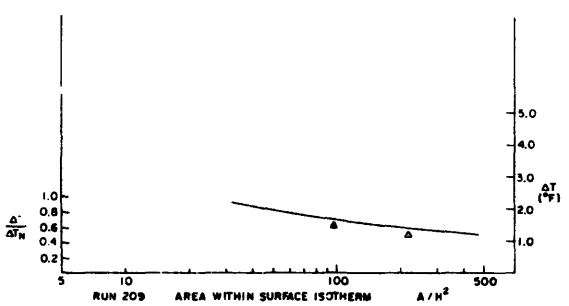
RUN 209
AREA WITHIN SURFACE ISOTHERM
A/H²
ΔT (°F)

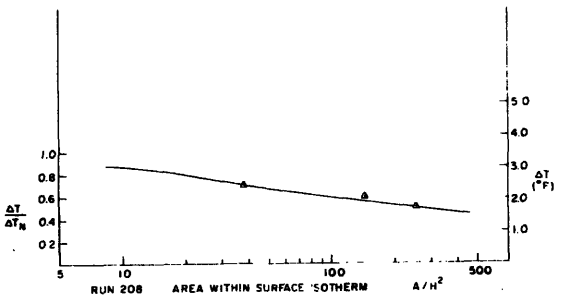
RUN 208
AREA WITHIN SURFACE ISOTHERM
A/H²
ΔT (°F)

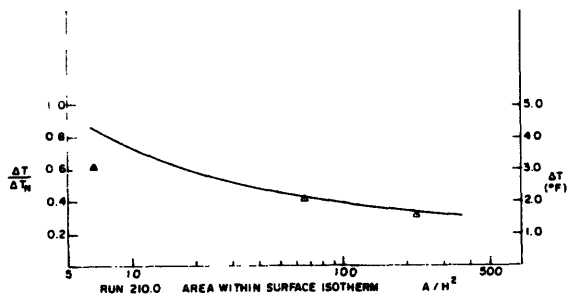
RUN 210.0
AREA WITHIN SURFACE ISOTHERM
A/H²
ΔT (°F)

Fig.6-7 cont'd

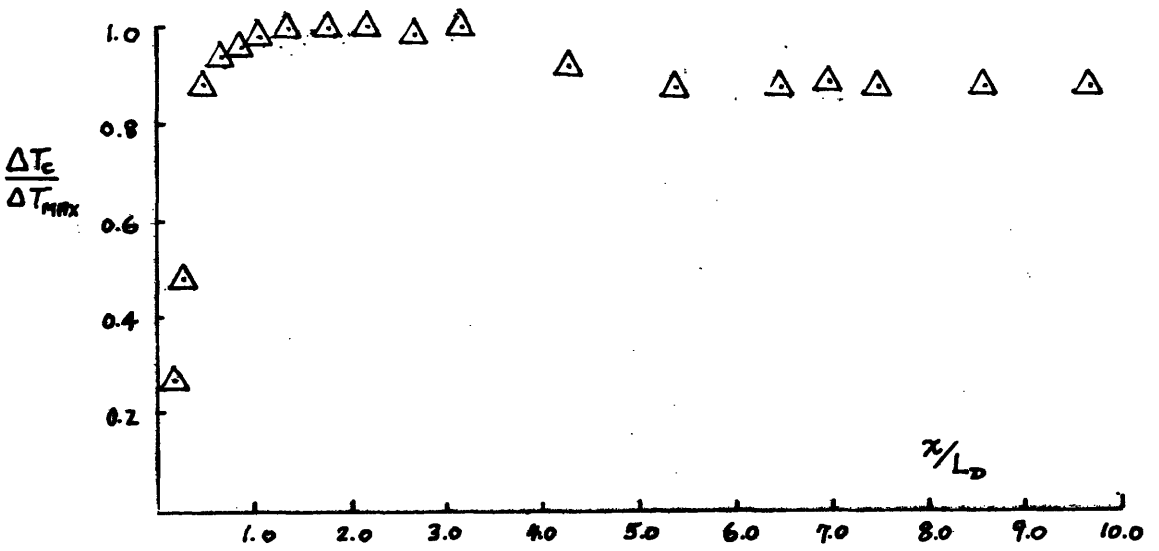

Fig. 6-8a) Typical centerline surface temperature profile along diffuser axis (RUN 201)

and bending of the individual jets, surface and bottom interaction, is very complicated. The temperature is more homogenous vertically at the center than at the edge of the plume. The flow becomes more stratified with increasing x. It is expected that the low Reynolds number in the experimental setup enhances the degree of stratification and that in the prototype the flow will have a stronger tendency to stay fully mixed.

It cannot be inferred from the temperature data alone that the temperature profile is well predicted by the standard profiles (top hat or gaussian). However, for

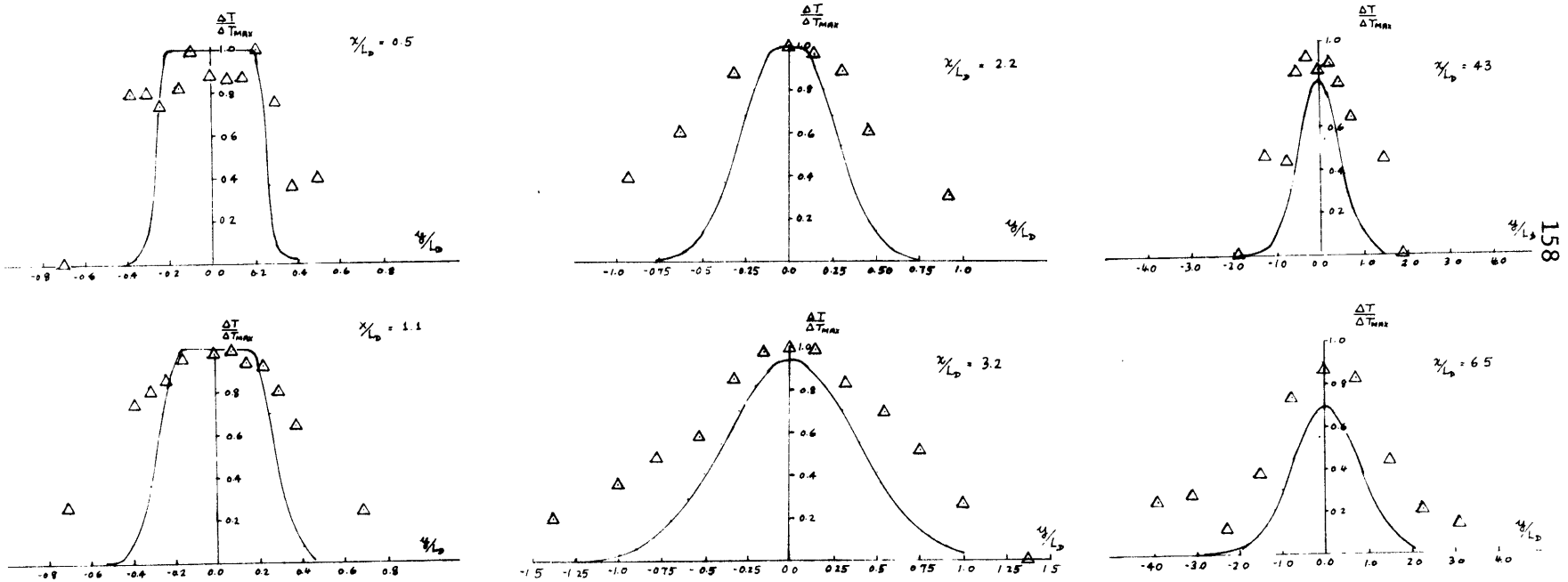

Fig. 6-8 b) Transverse surface temperature profiles at different x (Run 201)
_____ predicted profiles

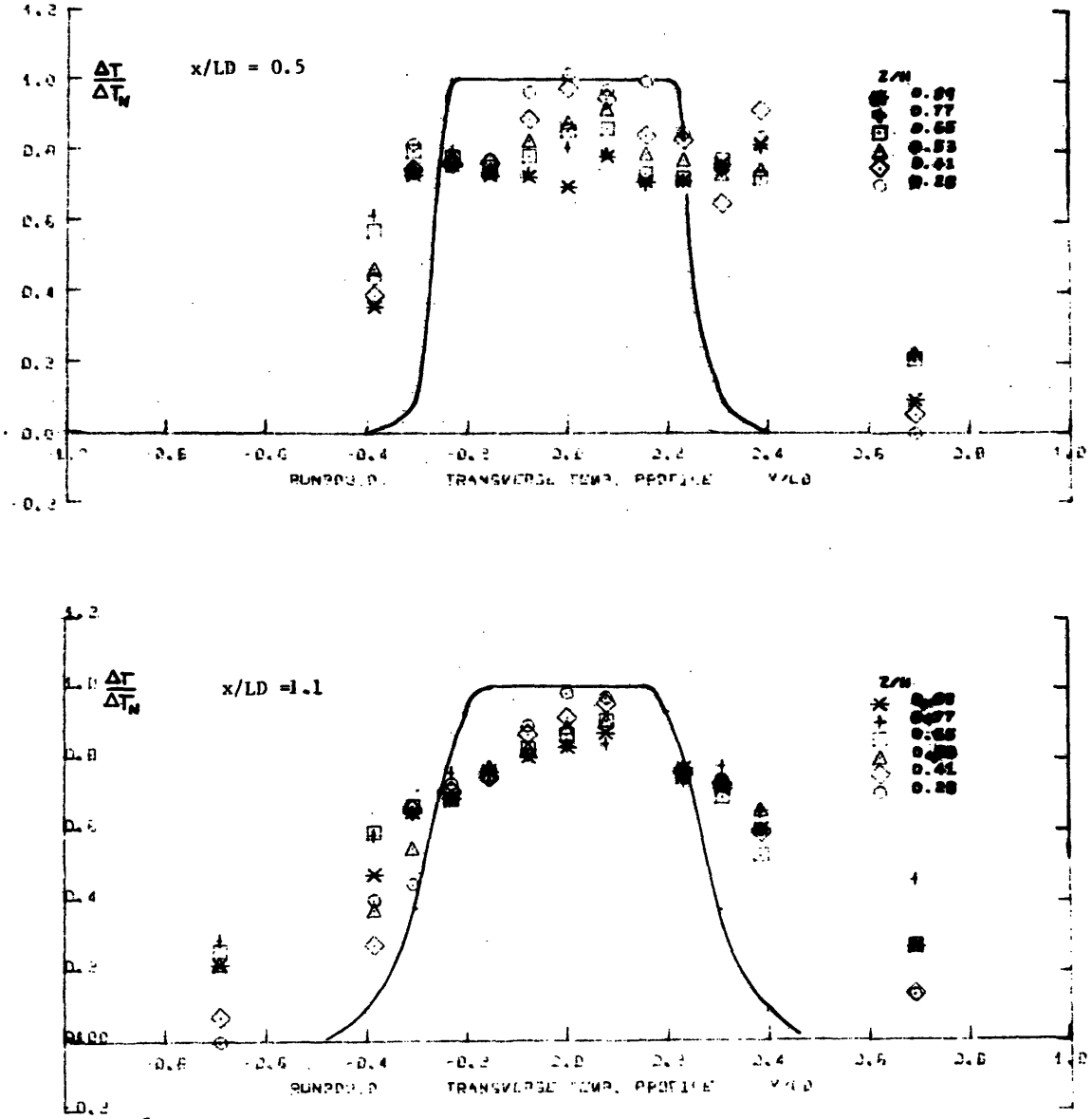

Fig. 6-9: Cross-sectional temperature transects at various longitudinal positions (____ predicted profiles)

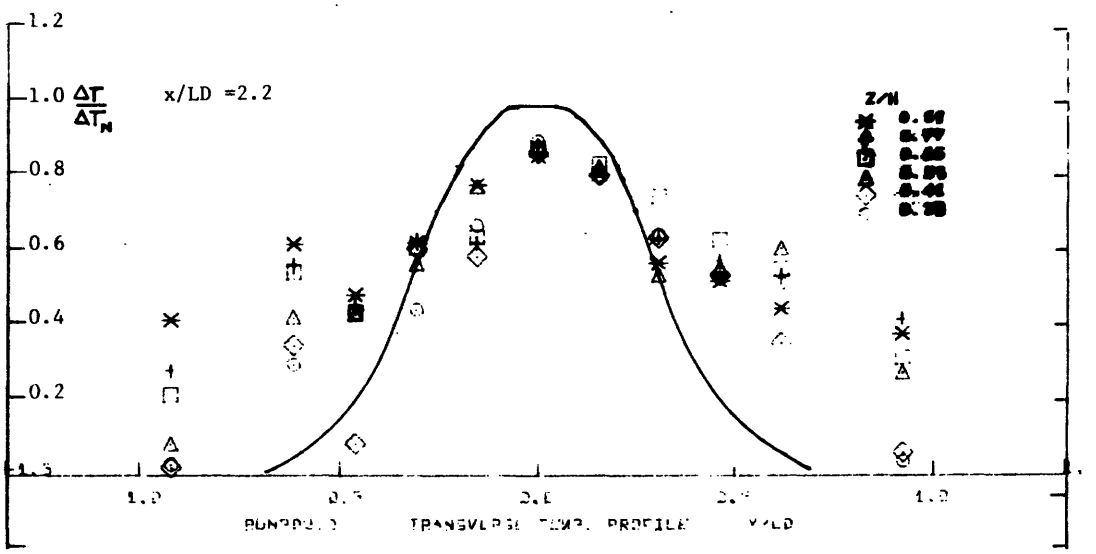

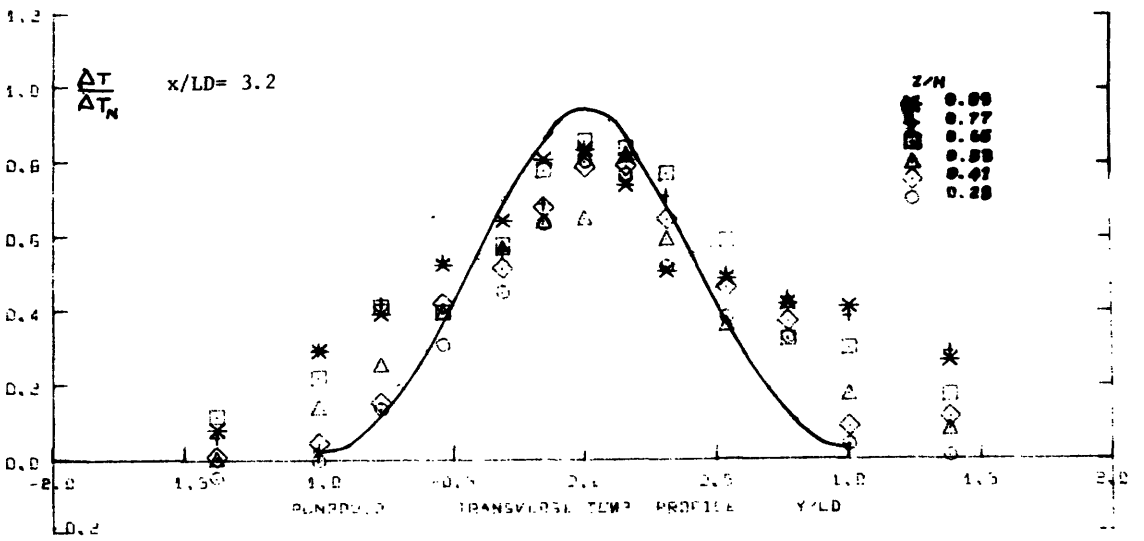

Fig. 6-9 cont'd

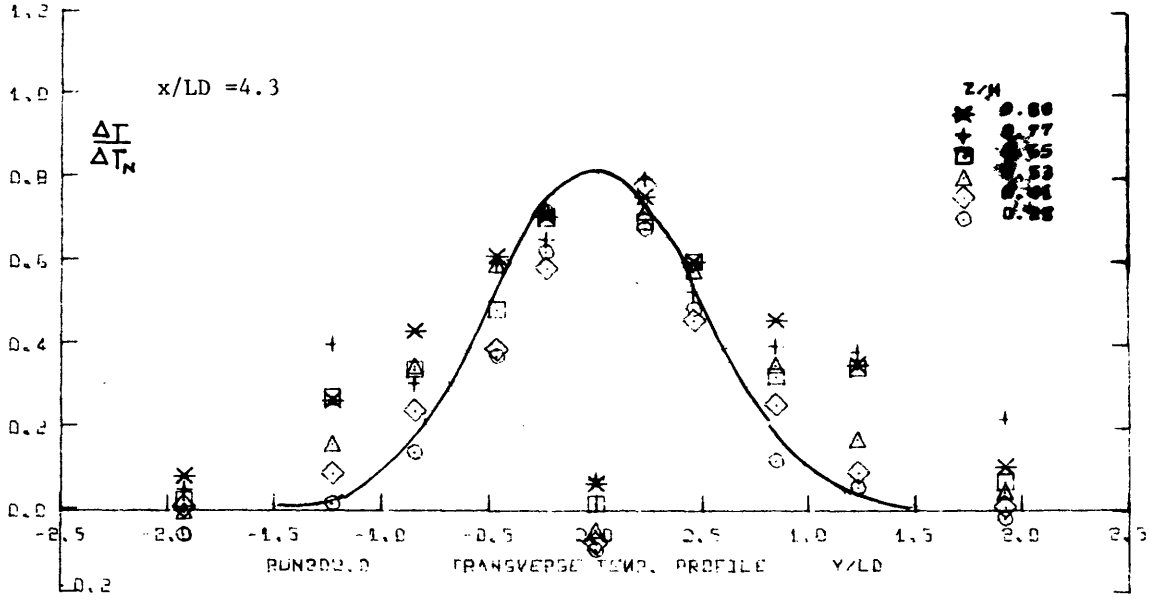
x/LD =4.3
ΔT/ΔT_N
Z/H
1.2
1.0
0.8
0.6
0.4
0.2
0.0
-2.5
-2.0
-1.5
-1.0
-0.5
0.0
0.5
1.0
1.5
2.0
2.5
RUN202.0
TRANSVERSE TEMP. PROFILE
Y/LD

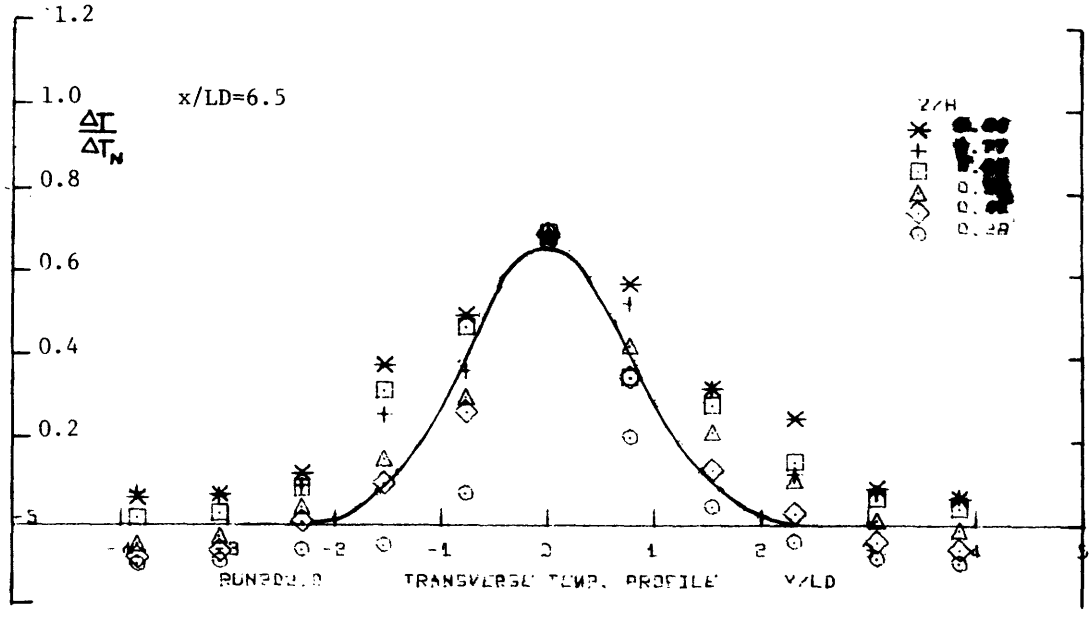
x/LD=6.5
ΔT/ΔT_N
Z/H
1.2
1.0
0.8
0.6
0.4
0.2
-2
-1
0
1
2
RUN202.0
TRANSVERSE TEMP. PROFILE
Y/LD

Fig. 6-9 cont'd

purposes of thermal prediction, the assumption of standard profiles appears to be a valid way of describing the essential features of the field variables.

The temperature recordings in the series 200 experiments are taken with a Digitec (United Systems) scanning and printing unit; each scan of 90 probes takes about three minutes. Thus the cross-sectional temperature profiles at six vertical positions are measured over an interval of about 20 minutes and as such these measurements do not represent a truly instantaneous snapshot or time-averaged values (over a long time interval) of the thermal field. However, the cross-sectional measurements are taken after the surface temperature rises indicate steady state conditions, and duplication of several runs demonstrate the experimental results can be reproduced.

6.5 Comparison of Theory with Perry model study

In this section the theory is compared with the results of hydraulic scale model studies for a proposed diffuser discharge for the Perry Nuclear Power Plant on Lake Erie. An extensive set of tests on the performance of unidirectional diffusers for this specific site has been carried out and reported by Acres American Corp. (1974). The experimental results in this report are presented in the form of surface isotherms as illustrated in Fig. 6-10. All information on the temperature field used for comparison are reduced from these diagrams. The relevant data are the unidirectional diffuser tests covered in plates 10-63 in Ref. 3.

The centerline temperature rise along the plume and isotherm areas are compared with the slack tide theoretical predictions in Fig. 6-11, 6-12. The diffuser design and ambient conditions are indicated on each diagram. For each design, the near field parameter $\beta = \frac{L_D H}{N a_o}$, and the intermediate field parameter $\frac{f_o L_D}{H}$ are computed; ΔT_N is then given by Eq. 3.41; the intermediate field solution is given by eqs. 4.44-4.47, 4.52-4.53. It can be seen that the data shows the same type of trend as observed in this study, and the comparison shows satisfactory agreement. An estimated initial jet mixing region of $\simeq$10 H is indicated on each plot. It should be pointed out that many of the Perry tests were done for rather short diffusers and as such the initial jet

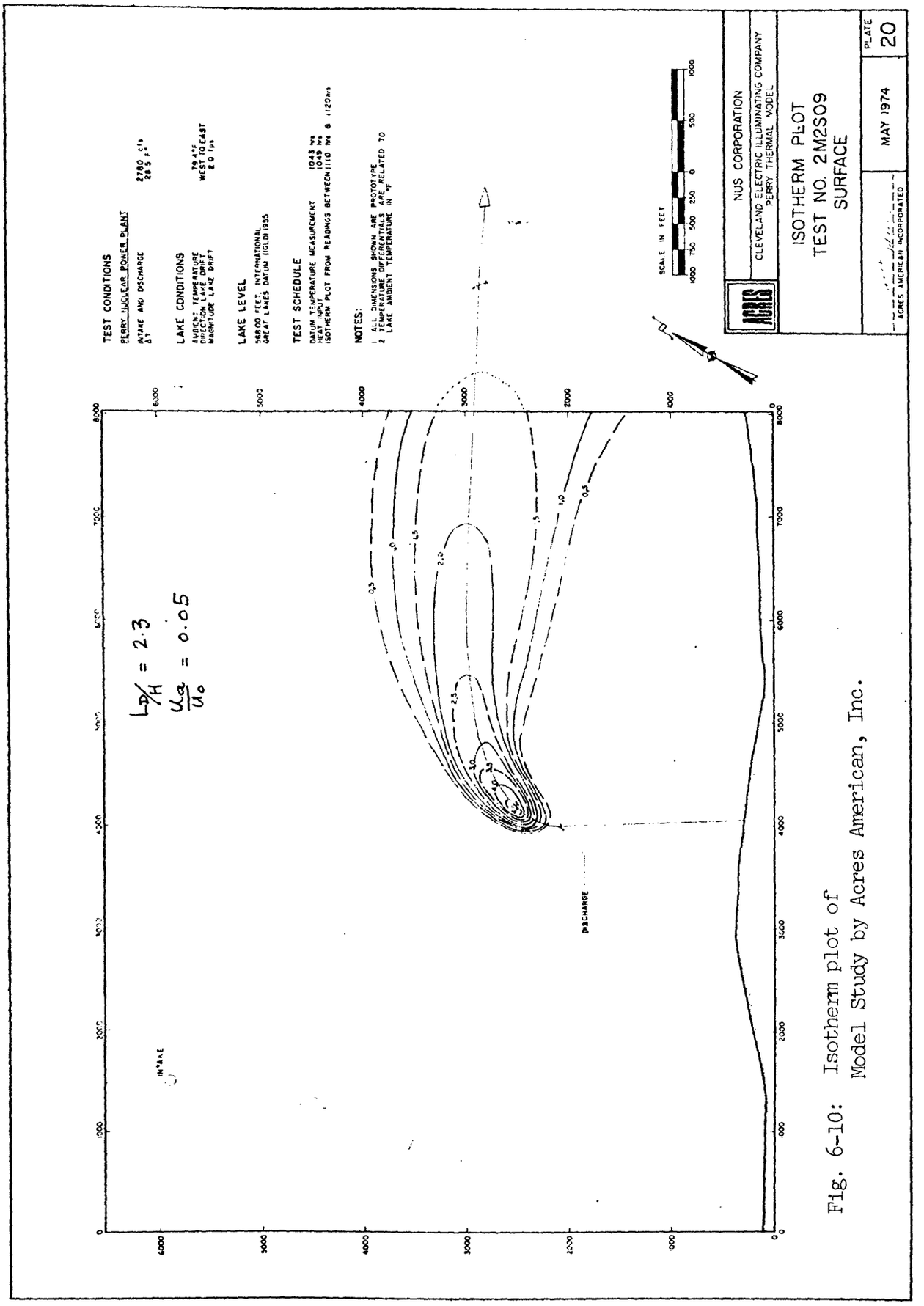

Fig. 6-10: Isotherm plot of
Model Study by Acres American, Inc.

mixing region can extend for several diffuser lengths. Furthermore, the nature of the data at hand do not permit the assessment of the spatial resolution of the temperature measurements and hence any maximum temperature rises that may be missed by the sensors.

Only tests in which the near field mixing is not severely affected by the cross-current are included. In some test with strong crossflows the near field temperature rise is considerably higher than predicted; the effect of an ambient crossflow on diffuser performance is separately discussed in the next chapter.

From eq. 4.52 it can be seen the functional relationship for isotherm areas A/L_D^2 vs $\Delta T/\Delta T_N$ is dependent only on the intermediate field parameter $f_o L_D/H$. In Fig. 6-13 all the Series 200 experimental data and Perry test data are condensed on the same diagram and compared with the theoretical predictions.

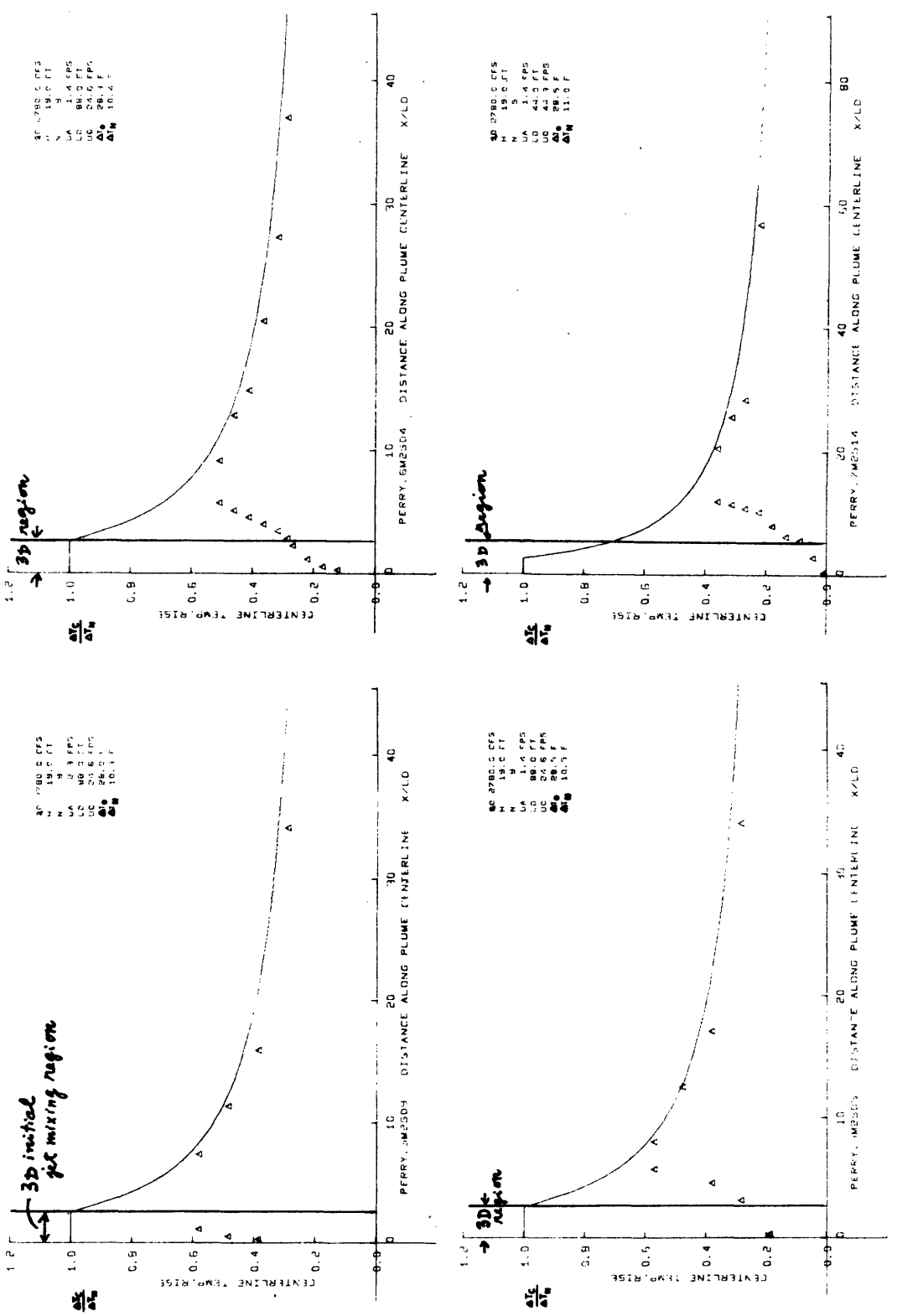

Fig.6-11: Comparison of theory ——— with Perry model tests: plume centerline temperature rises (eq. 4.44-4.47, 4.52-4.53)

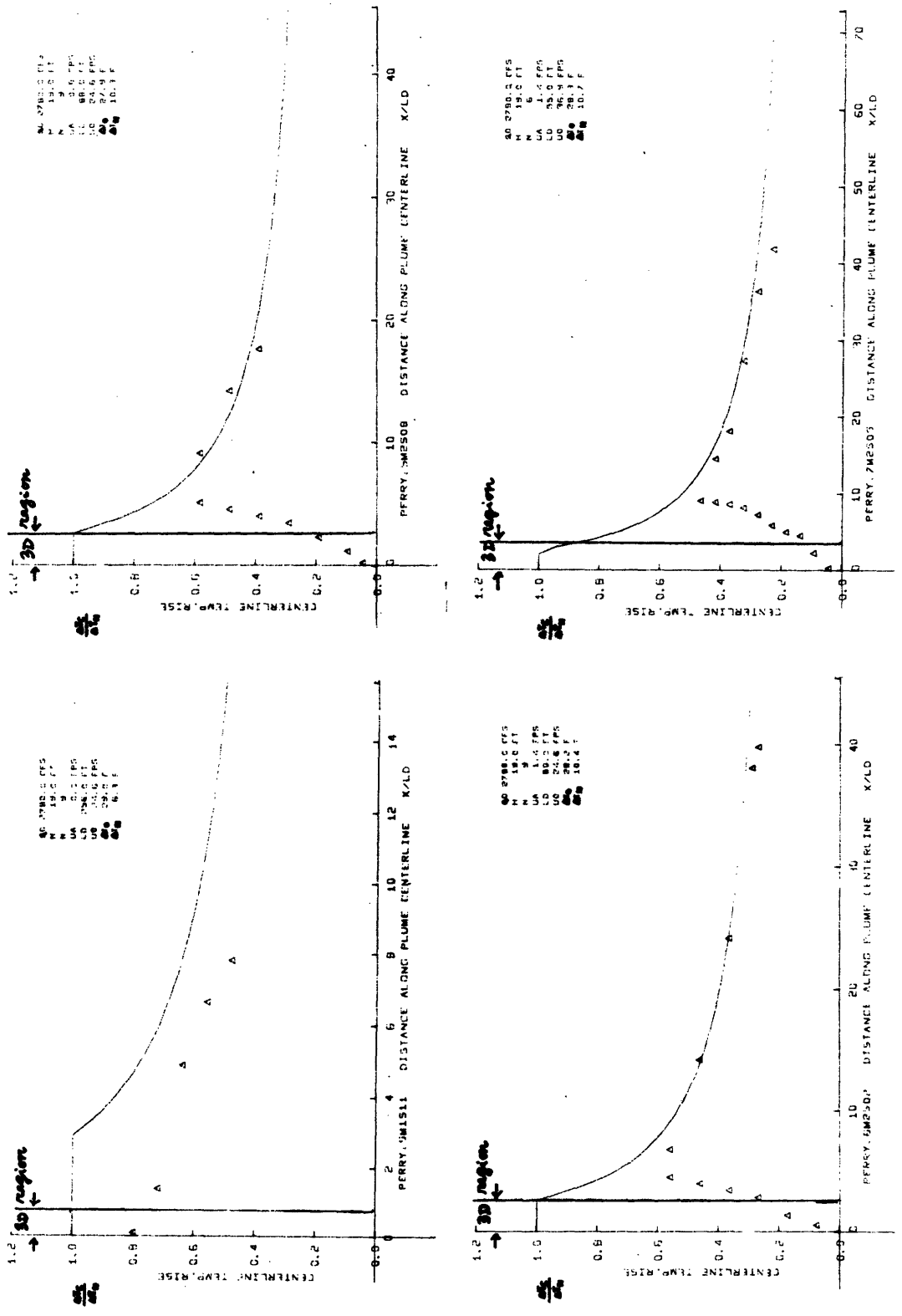

Fig. 6-11 cont'd

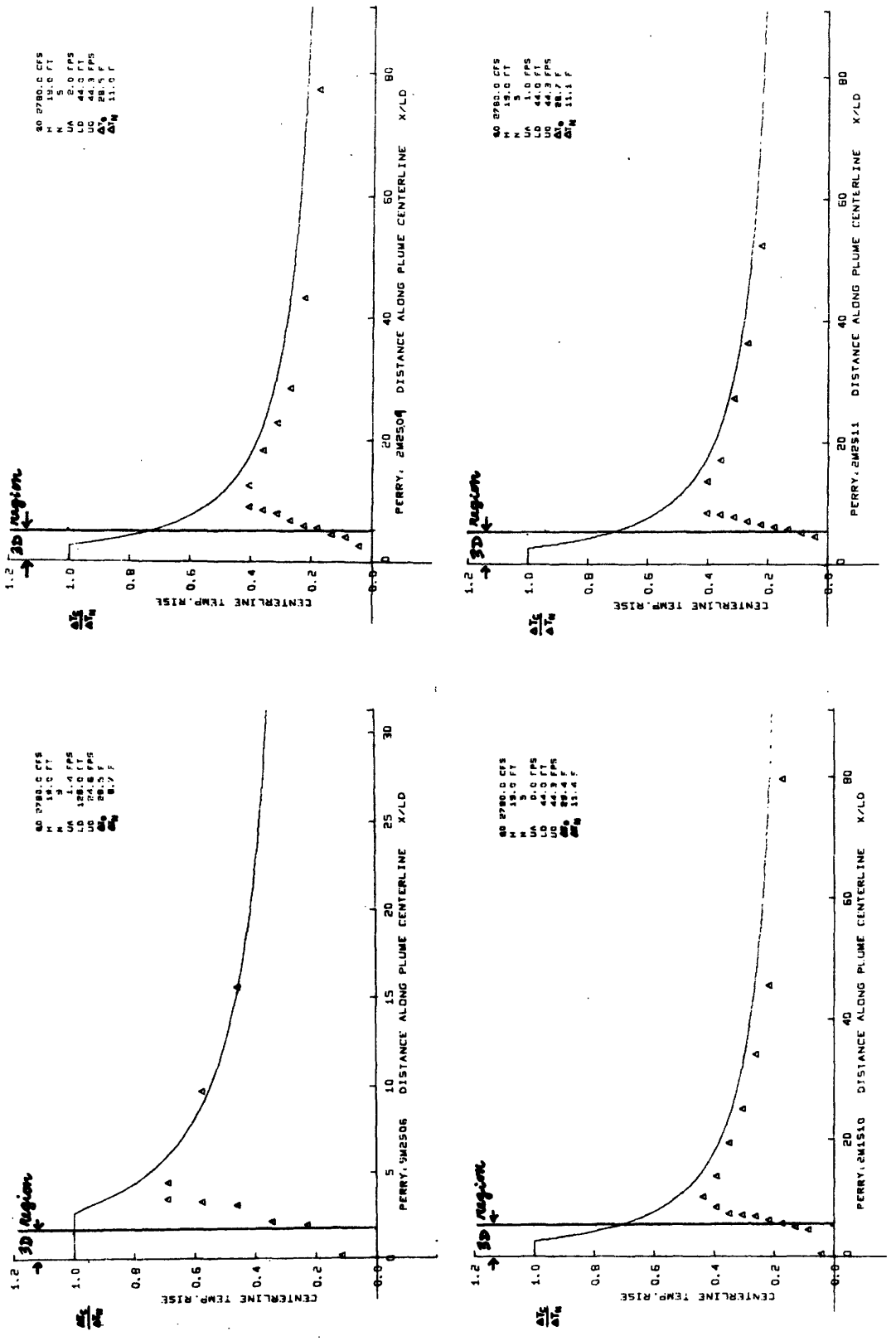

Fig. 6-11 cont'd

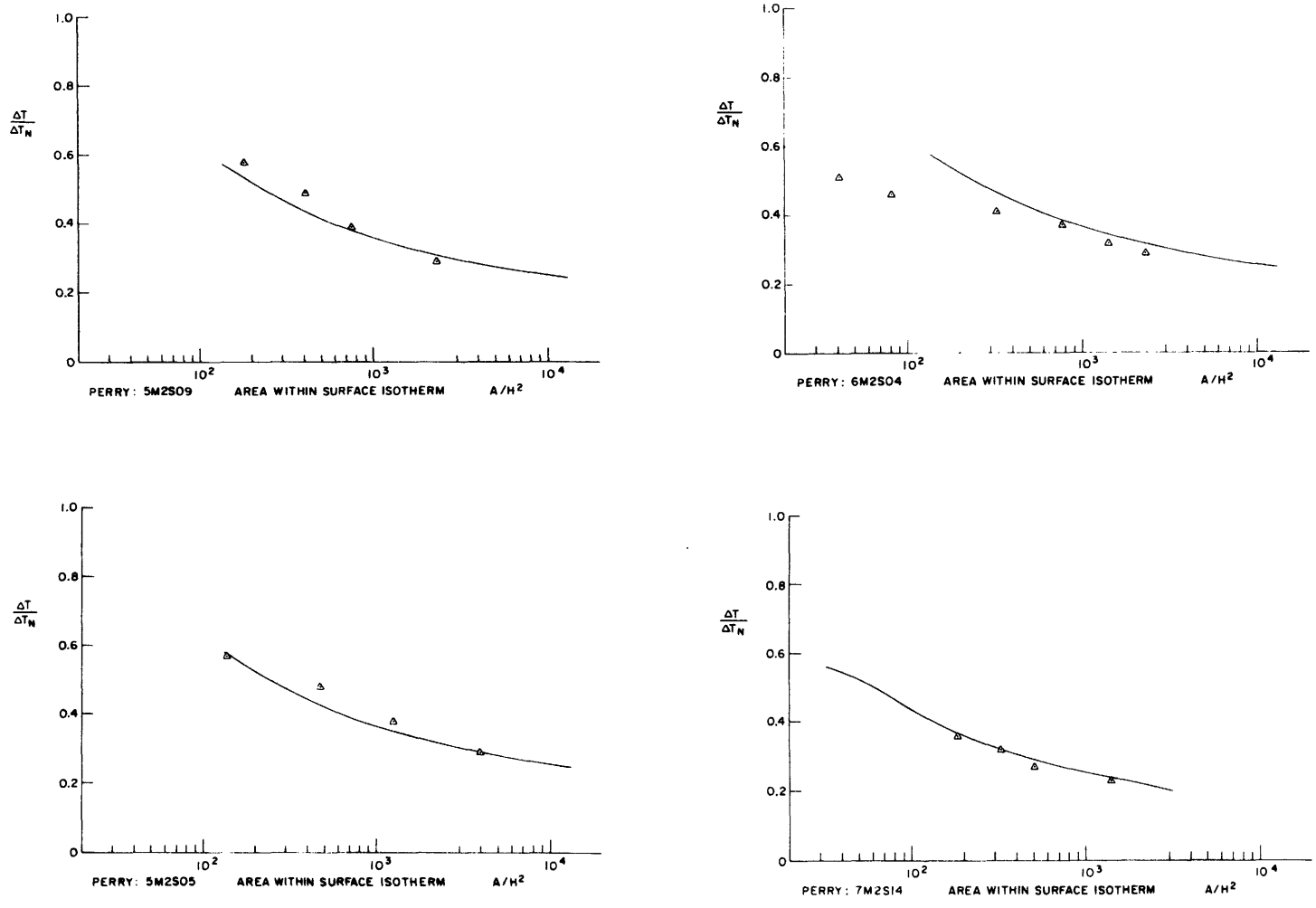

Fig. 6-12: Comparison of theory —— with Perry model tests: isotherm area
(eq. 4.44-4.47, 4.52-4.53)

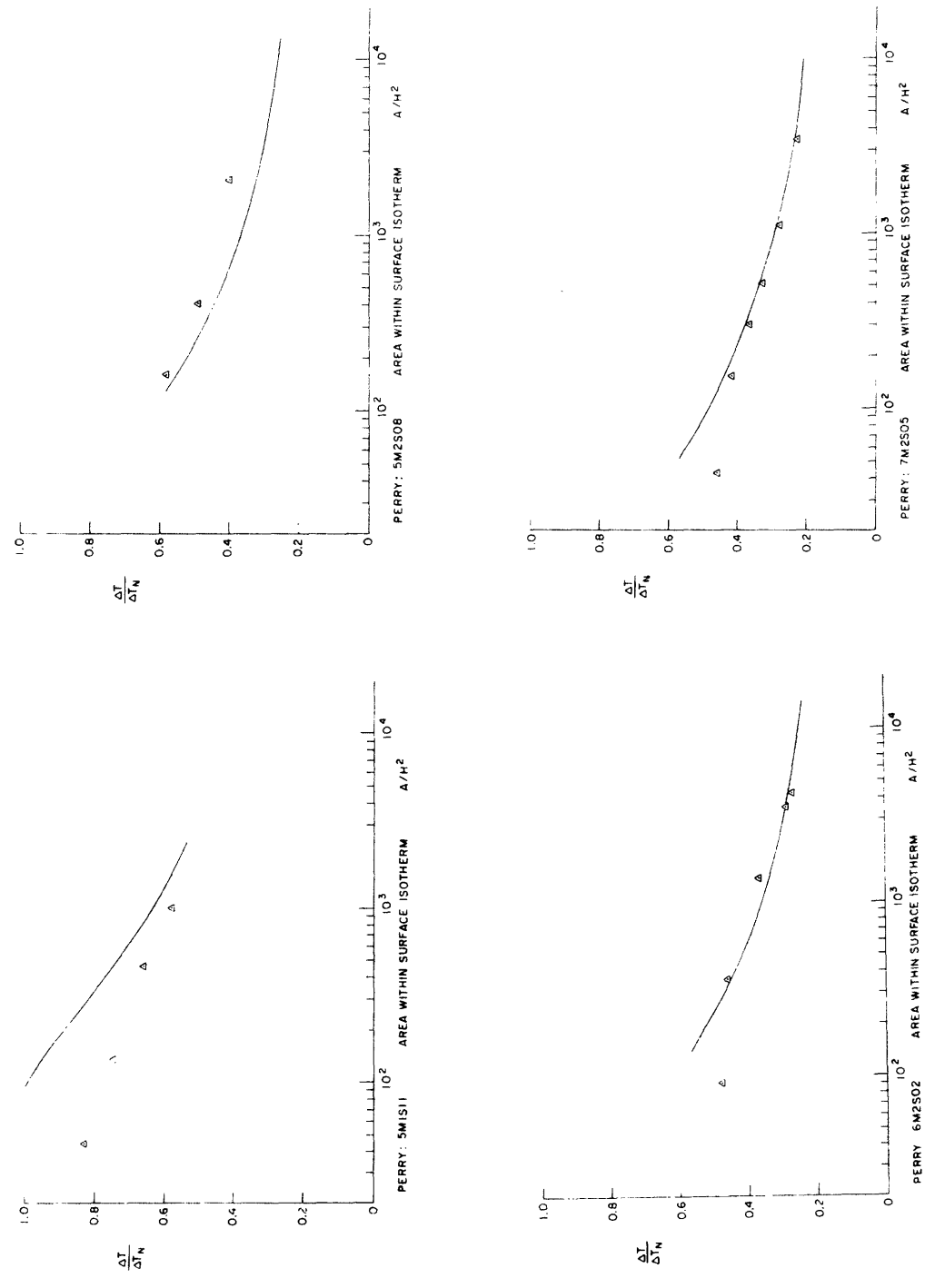

Fig. 6-12 cont'd

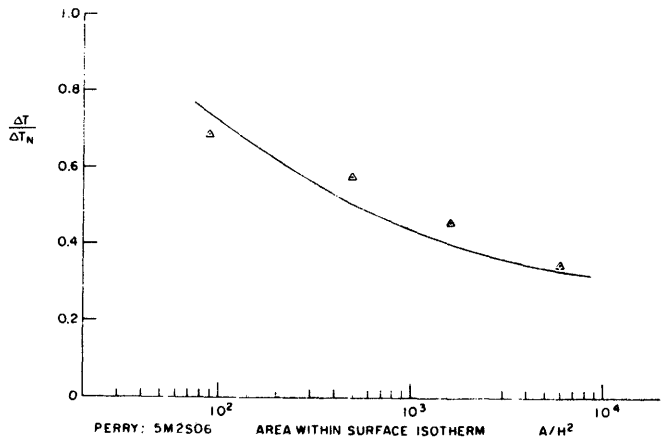

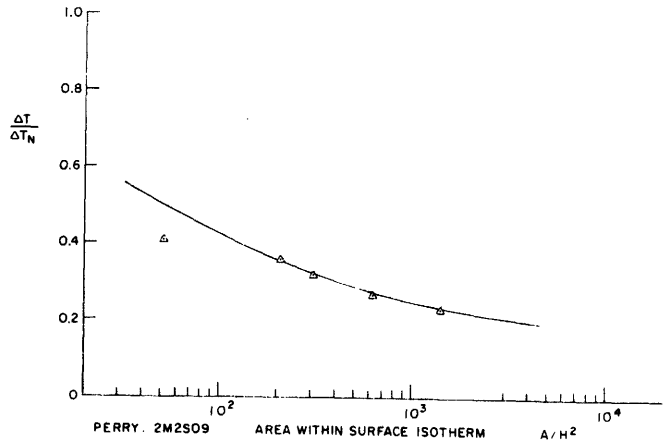

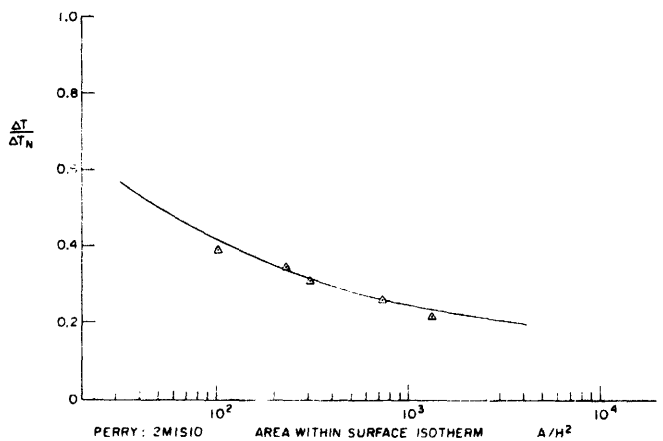

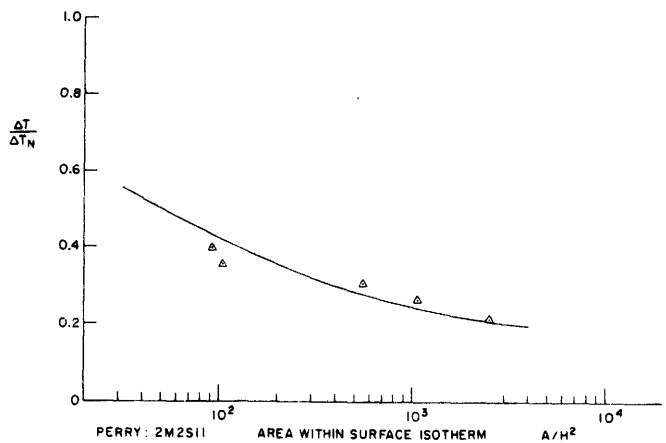

Fig. 6-12 cont'd

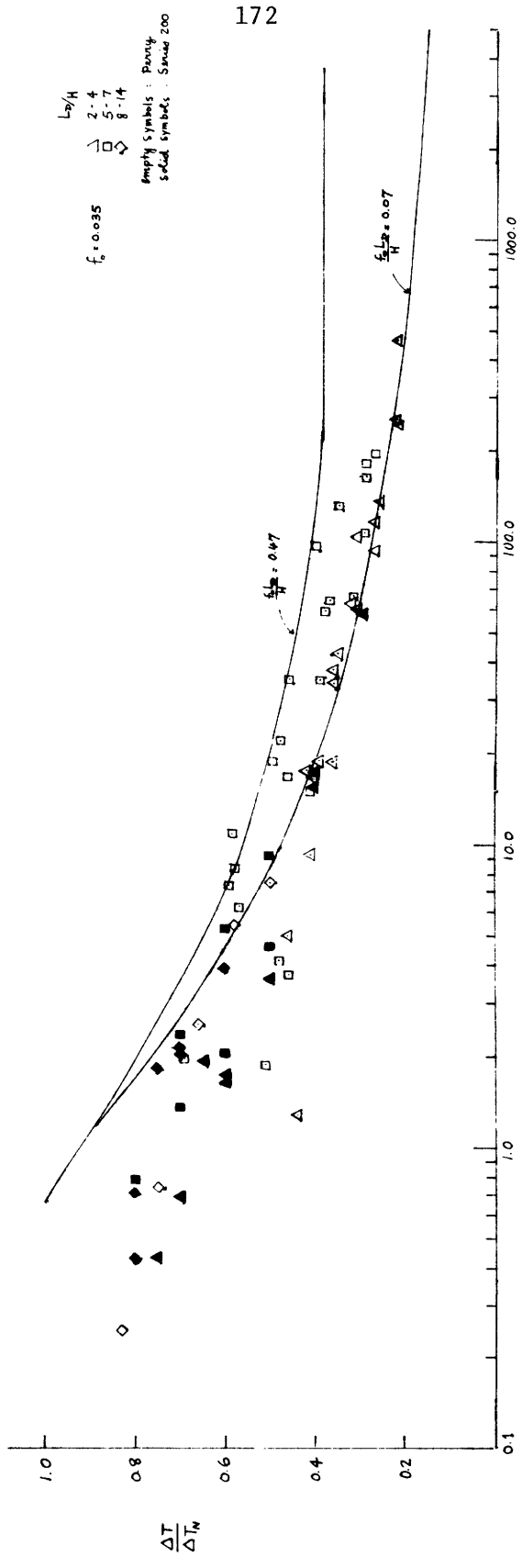

Fig. 6-13: Comparison of theoretical predictions of isotherm areas with Perry tests and Series 200 experiments (eq. 4.44-4.47, 4.52-4.53)

6.6 Comparison of theory with field data: James A. Fitzpatrick Plant

In this section the theory is compared with field data on the induced temperature field by the thermal diffuser discharge of the James A. Fitzpatrick Nuclear Power Plant on Lake Ontario. The hydrothermal survey was carried out and reported by Stone and Webster Engineering Corporation (Ref. 29). Dye at a monitored rate is injected into the discharge flow as a tracer. Meterological and hydrographic conditions are recorded; both temperature and dye concentrations are measured at various levels below the free surface.

The plant is located 3500 feet eastward of Nine Mile Point Nuclear Station, another station employing once through cooling. The diffuser discharge is located 1200 feet offshore in about 30 feet of water and discharging in the offshore direction. (Fig. 6-15) The diffuser consists of 6 double ports (included angle 42^{o}) each spaced 150 feet apart; the design values are

L_D = 750 feet

u_o = 14 fps

H = 30 feet

Q_o = 825 cfs

D = 2.5 feet

The site is characterised by a relatively strong offshore slope of 1/50.

As an ambient stratification of 3-5°F was always present during the temperature survey, it is difficult to extract information about diffuser performance from the temperature pattern, which is also affected by the discharge from the Nine Mile Point Station. The induced excess temperature ΔT is, therefore, inferred from measurements of dye concentration.

For this diffuser, the densimetric Froude number and submergence of the equivalent slot jet can be calculated by conserving momentum and volume flux per unit length along the diffuser. Accounting for the angle of inclination of the double ports to the offshore direction, we have

$$u_s = u_o \cos\left(\frac{\beta_i}{2}\right) = 13.1 \text{ fps}$$

$$B = 0.0903 \text{ ft.}$$

giving $F_S = 128$, $H/B = 332$

where β_i is the included angle between the double ports.

The stability criterion shown in Fig. 2-7 indicates the design falls marginallyin the vertically fully mixed region. In fact vertical transects of dye concentration show that beyond a small region near the diffuser the flow is always stratified.

The predicted near field dilution as given by eq. 3.41 is $S = \sqrt{\frac{L_D H}{2Na_o}} \cos\left(\frac{\beta_i}{2}\right) = 13.3$. This value compares reasonably well with the observed value of 10, as inferred from dye concentrations.

In Fig. 6-14, the stagnant prediction for isotherm area (eq. 4.44-4.47, 4.52-4.53) is compared with the field data for June 13, 1976, a day marked by very weak currents ($\sim$0.05 fps). The data is recorded over a period of 8 hours (8 a.m. to 4 p.m.). The different symbols refer to measurements at different levels below the free surface. The discrepancy between theory and data, especially for the lower temperatures, is about the same as the scatter in the data.

In Fig. 6-15 a,b the predicted isotherms are compared with the observed excess temperature contours for two different times; the lateral plume spread is larger than the predicted cigar shaped isotherms. Unfortunately, no plume measurements were carried out at a distance beyond 2000 ft. from the diffuser line.

It should be pointed out that this design is characterised by a low momentum input into a strong sloping bottom, and as such it does not strictly meet the assumptions of the model outlined in Chapter III and IV; the comparison above, however, still shows fair agreement regarding the approximate position of the diffuser plume and the isotherm areas.

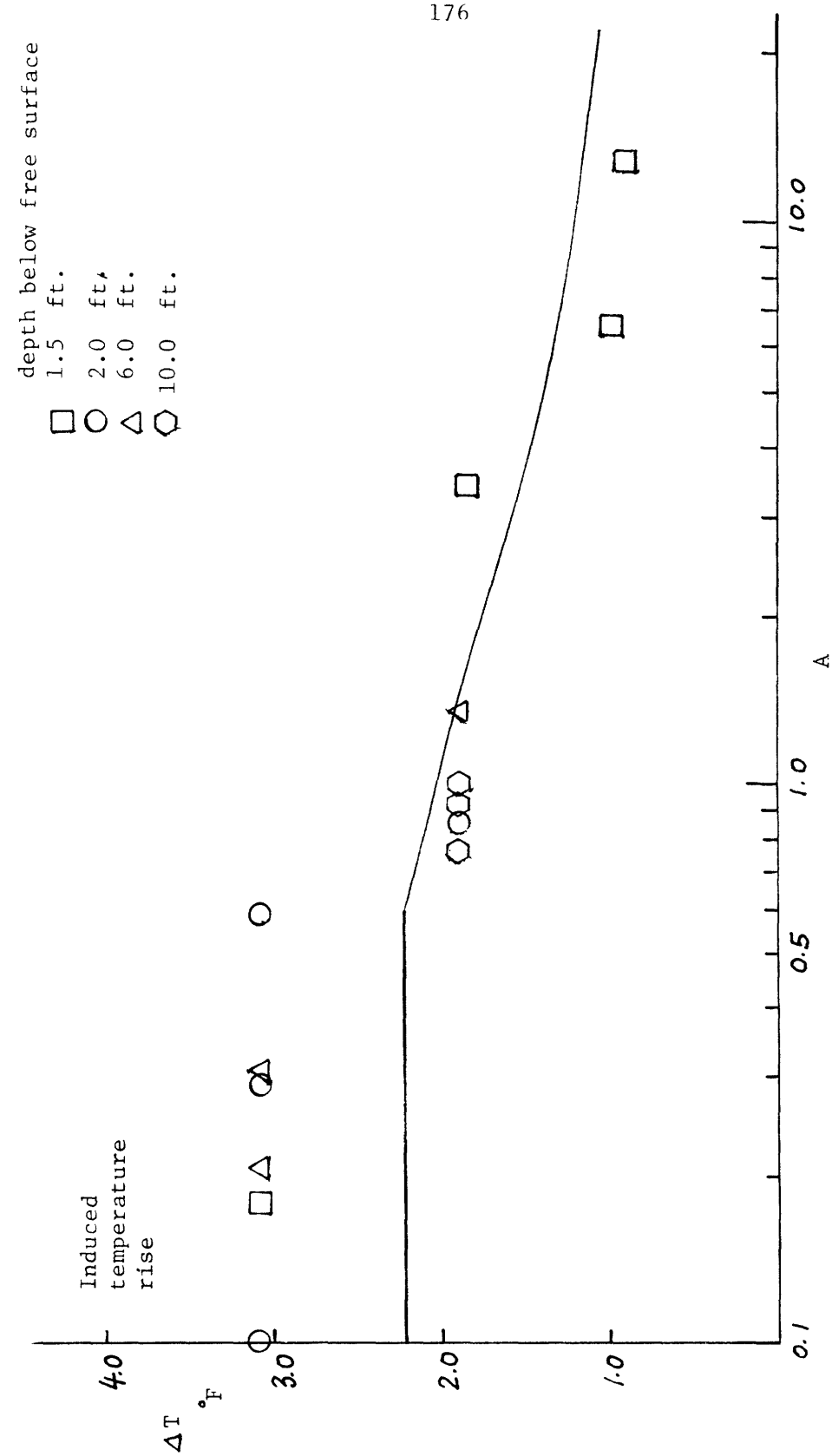

Fig. 6-14 Comparison of predicted isotherm area _____ with field data: James A. Fitzpatrick Nuclear Power Plant, New York. June 13,1976.

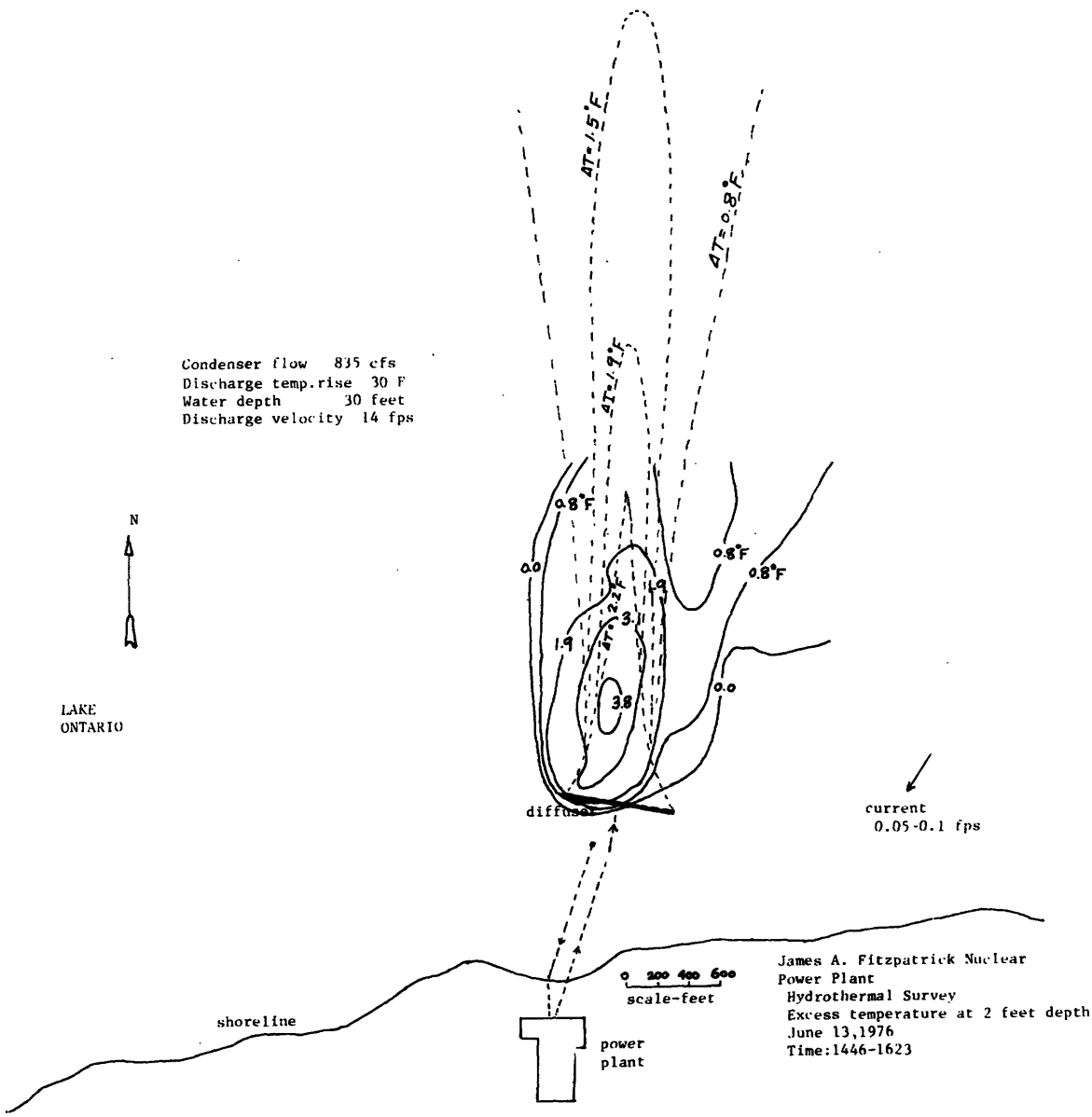

Fig. 6-15 a) Comparison of predicted isotherms -------- with field measurements _____: James A. Fitzpatrick Power Plant

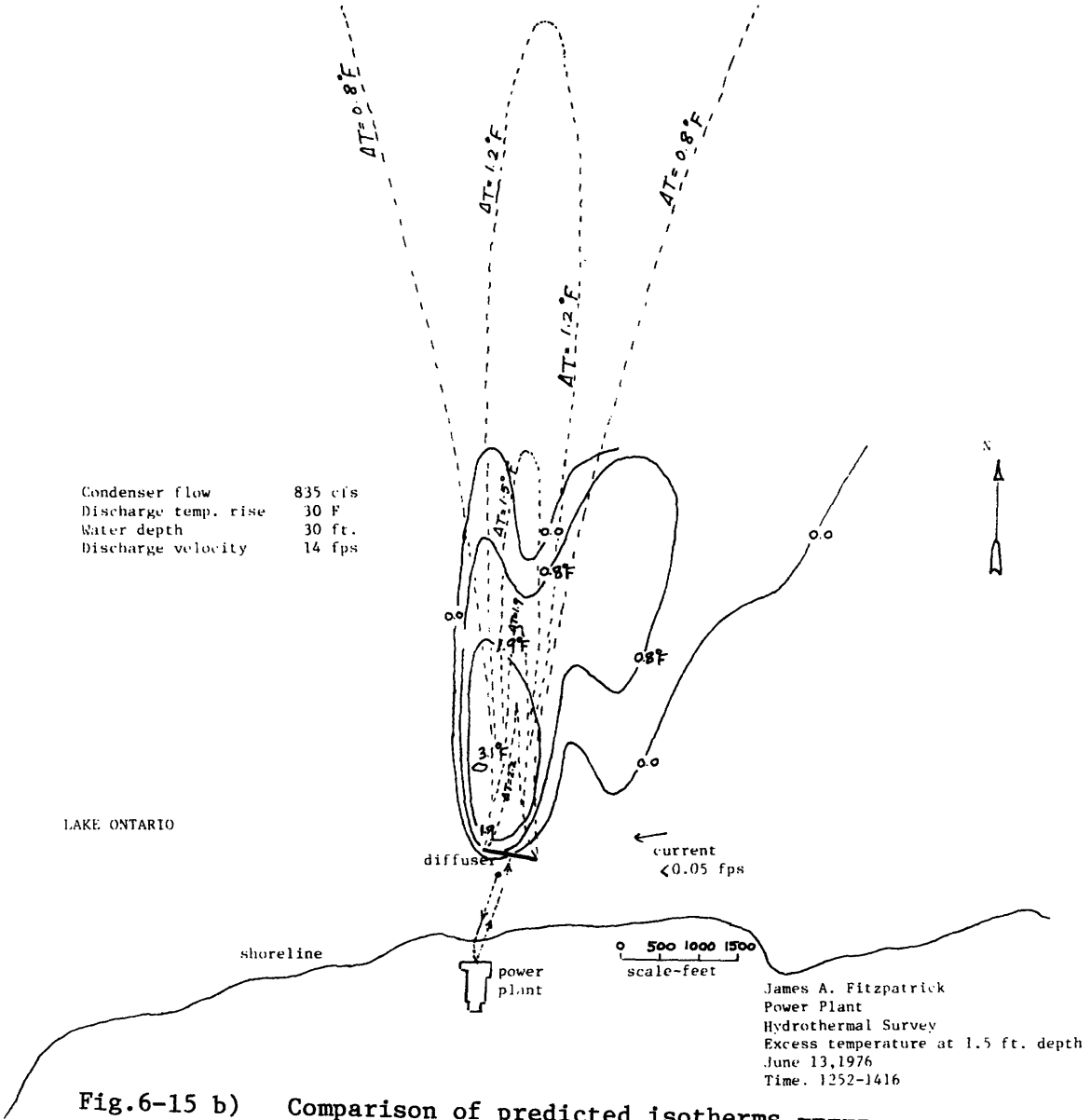

Fig.6-15 b) Comparison of predicted isotherms --------- with field measurements _____: James A. Fitzpatrick Power Plant

CHAPTER VII

UNIDIRECTIONAL DIFFUSER DISCHARGING INTO A PERPENDICULAR CROSSFLOW

The temperature field induced by a unidirectional diffuser discharging into a perpendicular crossflow is treated in this chapter. This situation is often found in coastal regions with predominantly alongshore currents. A theory is developed for calculating the total induced flow from behind the diffuser and the plume trajectory. The experimental results of this study and the Perry model tests are analysed and interpreted in light of the theoretical prediction.

7.1 T-diffuser in a crossflow

Fig. 7-1 shows the diffuser plume in the presence of a perpendicular crossflow in an open waterbody; a unidirectional diffuser discharging into the ambient current at right angles is often called a Tee-diffuser. The plume is deflected by the dynamic pressure of the intercepting stream; eventually the plume will be swept in the direction of the ambient current. In contrast to a round jet which allows the ambient flow to get around it, the vertically fully mixed plume forms an obstruction to the crossflow; the blockage deprives the lee of the plume of entrainment water from the ambient crossflow - this can, in some instances, cause recirculation of heated water(Boericke, 1975).

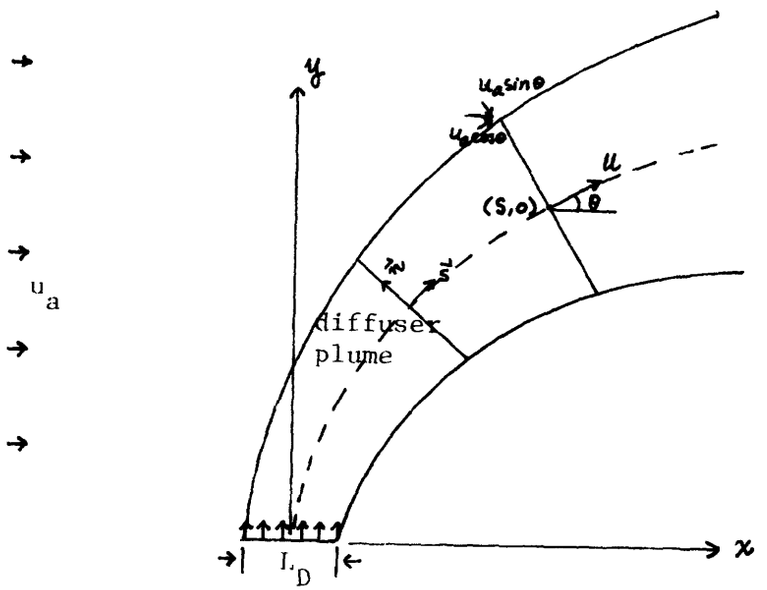

(x,y) : Cartesian co-ordinates
(s,n) : natural co-ordinates
θ : inclination of plume trajectory to x-axis
u : mean velocity inside plume

Fig. 7-1 Unidirectional diffuser in a perpendicular crossflow

In the following sections a prediction for the near field dilution and plume trajectory of a trajectory of a T-diffuser is presented. Both analyses assume vertically fully mixed conditions.

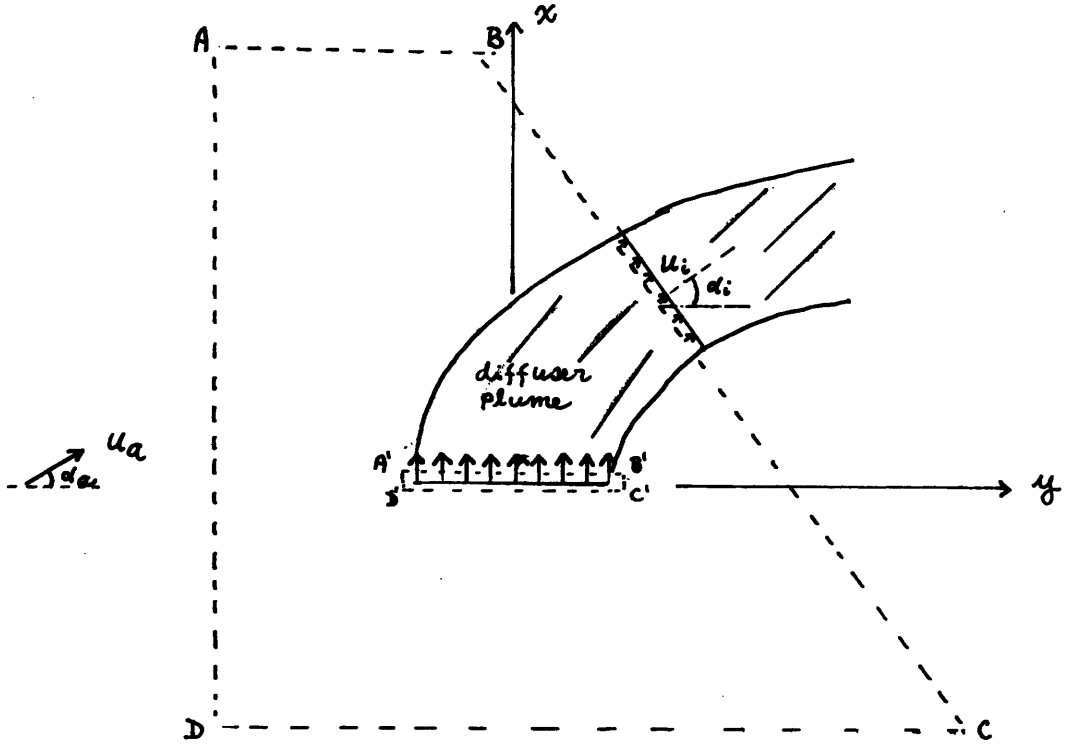

Fig. 7-2 Near field dilution induced by a unidirectional diffuser in an inclined crossflow

7.1.1 Near field dilution of a unidirectional diffuser in an inclined crossflow

Fig. 7-2 schematizes a unidirectional diffuser aligned at an angle α_a to the ambient current u_a. The special case of $\alpha_a=0$ corresponds to the case of a perpendicular crossflow. By carrying over the same assumptions stated in section 3.6, a control volume analysis is used to derive S, the near field dilution.

As in the case of a coflowing current, we assume there is negligible turbulent mixing in the near field, and let section i be the section where the free surface returns to the

undisturbed level; u_i is the velocity in the direction of the flow at section i; α_i is the inclination of the flow direction to the horizontal. ABCD is an outer control volume just enclosing the diffuser. Using the same nomenclature as presented in Cahpter III, we have for energy conservation along a streamline,

$$\frac{u_a^2}{2g} + H = h^- + \frac{q_D^2}{2g} \tag{7.1}$$

$$\frac{u_i^2}{2g} + H = h^+ + \frac{q_D^2}{2g} \tag{7.2}$$

where q_D is the magnitude of the velocity along the diffuser A momentum balance for the inner control volume A'B'C'C' gives

$$gL_D H(h^+ - h^-) = Q_o u_o \tag{7.3}$$

Equating momentum fluxes in the x and y direction for the outer control volume ABCD, we have

$$SQ_o u_i \sin\alpha_i = Q_o u_o + SQ_o u_a \sin\alpha_a \tag{7.4}$$

$$SQ_o u_i \cos\alpha_i = SQ_o u_a \cos\alpha_a \tag{7.5}$$

Combining eq. 7.1 through 7.5, α_i can be eliminated from the equations and an equation in the near field dilution can be obtained as:

$$S^2 - \beta\gamma \sin\alpha_a S - \frac{\beta}{2} = 0 \tag{7.6}$$

where

$$\beta = \frac{L_D H}{Na_o}, \gamma = u_a/u_o$$

the solution is

$$S = \frac{\beta\gamma \sin\alpha_a + \sqrt{\beta^2\gamma^2 \sin^2\alpha_a + 2\beta}}{2} \qquad (7.7)$$

Using a different argument, Adams (1972) obtained the same result by directly replacing γ by $\gamma\sin\alpha_a$ in eq. 3.38.

For the special case of a perpendicular crossflow, $\alpha_a = 0$, eq. 7.7 then gives

$$S = \sqrt{\frac{\beta}{2}} \qquad (7.8)$$

The induced near field dilution in a perpendicular crossflow is then the same as the case of no ambient current.

In the foregoing analysis, a crucial implicit assumption is that $\frac{u_a^2}{2g} << \frac{u_i^2}{2g}$, so that any correction due to the ambient current in the energy equation or the momentum balance equation can be neglected as a first approximation. The head difference $\Delta H \simeq \frac{u_a^2}{2g}$ due to the blocking of the ambient stream by the diffuser plume, provides the necessary centrifugal force for the bending of the plume, and hence it cannot be neglected in the calculation of theplume trajectory. However, its contribution in the equations necessary for calculating S can be shown to be small. For example, the more exact version of eq. 7.2 can be written as:

$$\frac{u_i^2}{2g} + H + \varepsilon = \frac{q_D^2}{2g} + h^+$$

where

$$\varepsilon \simeq \frac{u_a^2}{2g}$$

The relative importance of ε in equation 7.2 can be estimated as

$$\frac{\frac{\varepsilon}{2}}{\frac{u_i^2}{2g}} \sim \left(\frac{u_a}{u_i}\right)^2$$

As $u_i \sim u_o/S$

$$\frac{\frac{\varepsilon}{2}}{\left(\frac{u_i}{2g}\right)} \sim \left(\frac{u_a}{u_o} S\right)^2$$

Using typical values of

$u_a = 0.5$ fps

$u_o = 25$ fps

$S = 5$

The error introduced by neglecting ε is

$$\frac{\frac{\varepsilon}{2}}{\left(\frac{u_i}{2g}\right)} \sim 0.01$$

7.1.2 Calculation of T-diffuser plume trajectory

The situation is schematised in Fig. 7-1 along with the definition of symbols. s is the distance along plume centerline; u is the mean plume velocity in the stream direction; L is the plume width. For simplicity top hat profiles are assumed in the analysis, and the plume cross-section is assumed to be rectangular (i.e. extending over the entire depth.)

Integrating the continuity and momentum equations in natural co-ordinates across the plume in the normal direction yields the following conservation eqations:

Continuity

$$\frac{dQ}{ds} = \frac{d(uL)}{ds} = 2\alpha\ (u-u_a\ \cos\theta) \qquad (7.9)$$

As in the coflowing current case, the entrainment assumption relates the rate of increase of volume flux, $\frac{dQ}{ds}$, to a characteristic velocity difference in the plume direction.

Axial Momentum

$$\frac{dM}{ds} = \frac{d(u^2L)}{ds} = \frac{-f_o M}{8H} + u_a\ \cos\theta\ \frac{dQ}{ds} \qquad (7.10)$$

The momentum variation, $\frac{dM}{ds}$, is governed by the exchange of momentum with the crossflow and bottom dissipation. Pressure variations in the s direction are neglected; it is recognised that this approximation is only valid beyond the near field, (cf. coflowing current case in Chapter IV) and is judged to be a realistic simplification as far as calculating the plume trajectory is concerned.

Normal Momentum

The momentum equation in the normal direction is given by

$$u^2LH\ \frac{d\theta}{ds} = -\frac{1}{2}\ C_D\rho(u_a\ \sin\theta)^2 \qquad (7.11)$$

The main factor in determining the plume trajectory is assumed to be the centrifugal force provided by the dynamic pressure of the crossflow component perpendicular to the plume trajectory.

The bending force per unit length along the plume is

$$F_b = \frac{1}{2} C_D \rho (u_a \sin\theta)^2 \qquad (7.12)$$

where C_D: blocking coefficient.

Non-dimensionalising eq. 7.9-11 with u_o, $0.5L_D$, the following system of governing equations can be obtained.

$$\frac{dQ^*}{ds^*} = 2\alpha (u^* - \gamma\cos\theta)$$

$$\frac{dM^*}{dS^*} = -\left(\frac{f_o L_D}{16H}\right) M^* + \gamma\cos\theta \frac{dQ^*}{dS^*}$$

$$\frac{d\theta}{dS^*} = -\frac{C_D}{2}\gamma^2 \frac{\sin^2\theta}{M^*}$$

$$x^*(s^*) = \int_o^{s^*} \cos\theta \, ds^*$$

$$y^*(s^*) = \int_o^{s^*} \sin\theta \, ds^* \qquad (7.13)$$

where

$$Q^* = \frac{uL}{u_o(0.5L_D)} \quad , \quad M^* = \frac{u^2 L}{u_o^2(0.5L_D)}$$

$$u^* = \frac{u}{u_o} \quad , \quad (x^*, y^*, s^*) = (x, y, s)/0.5L_D$$

$$\gamma = \frac{u_a}{u_o}$$

such that at $s = 0$

$$\theta = 90^o$$

$$Q^*(0) = 2\left(\frac{S}{\beta}\right)$$

$$M^*(0) = 2\left(\frac{S}{\beta}\right)^2$$ where S is the near field dilution.

Given the initial conditions and the values of the coefficients α, f_o, C_D, the system of equations 7.12 can be solved numerically using a fourth order Runge-Kutta scheme.

7.1.3 Theoretical Results

It can be seen from the system of equations 7.13 that the governing parameters of the T-diffuser problem are β, γ and $\frac{f_o L_D}{H}$, as in the coflowing current case (cf. section 4.2). The theoretical solution for the plume trajectory is plotted in Fig. 7.2.1 for two diffuser lengths (L_D/H = 5,20) and different combinations of β and γ; the origin is chosen to coincide with the diffuser center. The comparison for the different input dimensionless parameters demonstrates the plume trajectory is more sensitive to γ than to β. A parameter measuring the ratio of ambient momentum to diffuser momentum can be defined as

$$F_M = \frac{u_a^2 L_D H}{Q_o u_o} = \beta\gamma^2$$

For a given relative diffuser length, there is an ordering of the plume trajectories in terms of F_M; the significance of this parameter is further discussed in later sections.

7.2 Experimental Results

In this section the experimental results of T-diffuser tests in this study are reported and analysed in conjunction with the results of the Perry model study. It is found experimentally that for low momentum input in a strong crossflow, the near field temperature rise can be considerably higher than $\Delta T_o/S$, S being given by eq. 7.8. An empirical

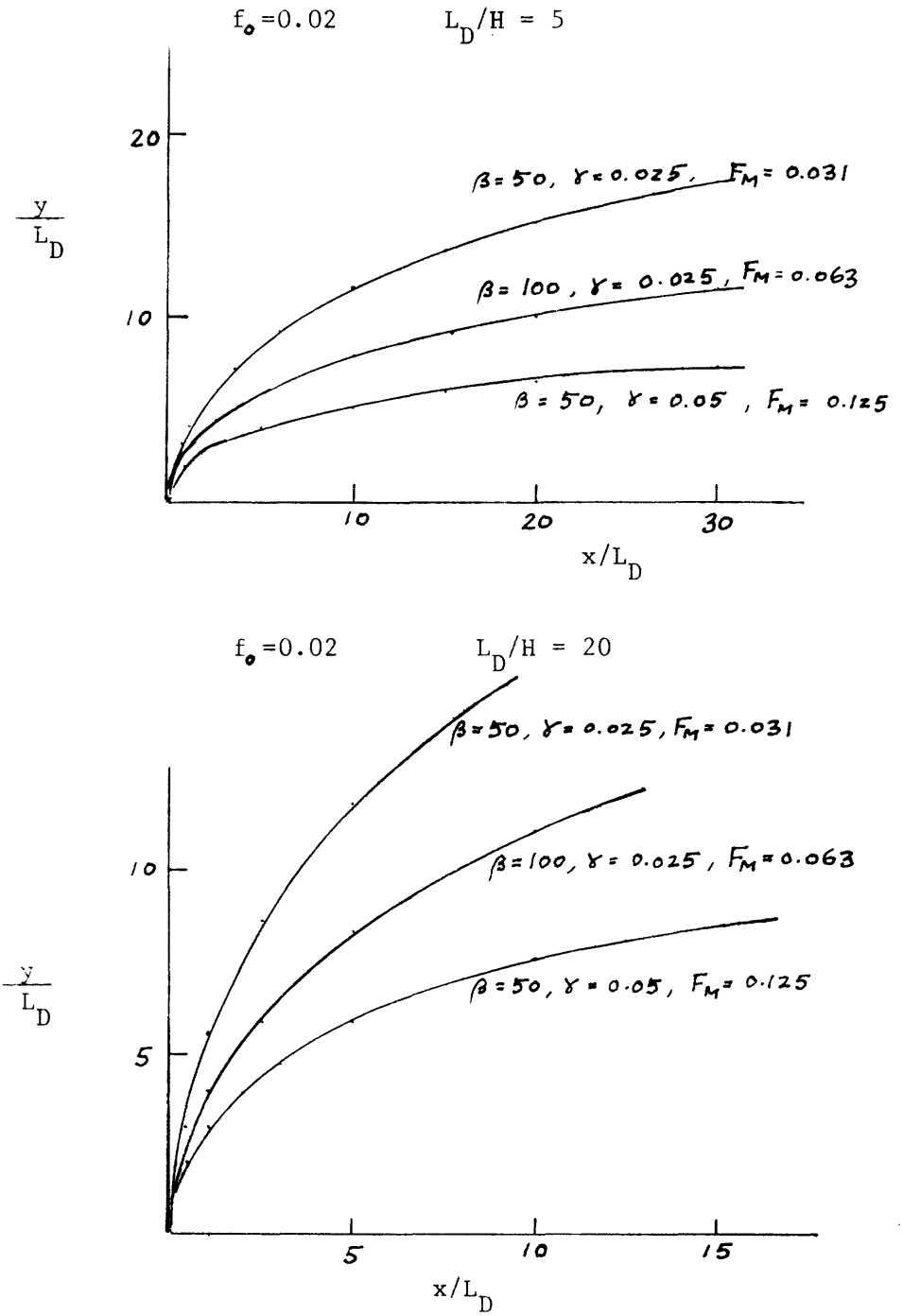

Fig. 7-2.1 Predicted plume trajectory as a function of governing parameters

correlation is developed to delimit this condition, and to give estimates of the near field dilution when this occurs.

7.2.1 Experimental observation: this study

The T-diffuser tests in this study are runs FF30-36. The gross features of these experiments can be summarised in Fig. 7-3. A high pressure region is created in front of the diffuser; the diffuser plume, as depicted by 1, is deflected by the ambient current. Some of the heat is observed to penetrate upstream and is swept downstream further away. A stagnant region is found slightly upstream of the diffuser where the maximum surface temperature rise is usually observed. Some of the heat in this region is recirculated into the entrainment flow at the back of the diffuser and is also advected downstream, as depicted by 2. Whereas the flow in 2 is well-stratified, the flow near the diffuser in 1 is well-mixed, indicating that unstable conditions are present. Away from the diffuser, the flow in 1 is also stratified. Fig. 7-4 illustrates a typical surface and bottom scan of the temperature field. It can be seen the temperature field is highly non-uniform near the diffuser. The highest temperature is found near the stagnation point. As the heat load is uniform along the diffuser, this non-uniformity of temperature suggests the induced flow is not uniform along the diffuser axis. In spite of high local temperature rises, the temperature rise beyond a diffuser length away is much closer to $\frac{\Delta T_o}{S}$ than the maximum surface temperature observed.

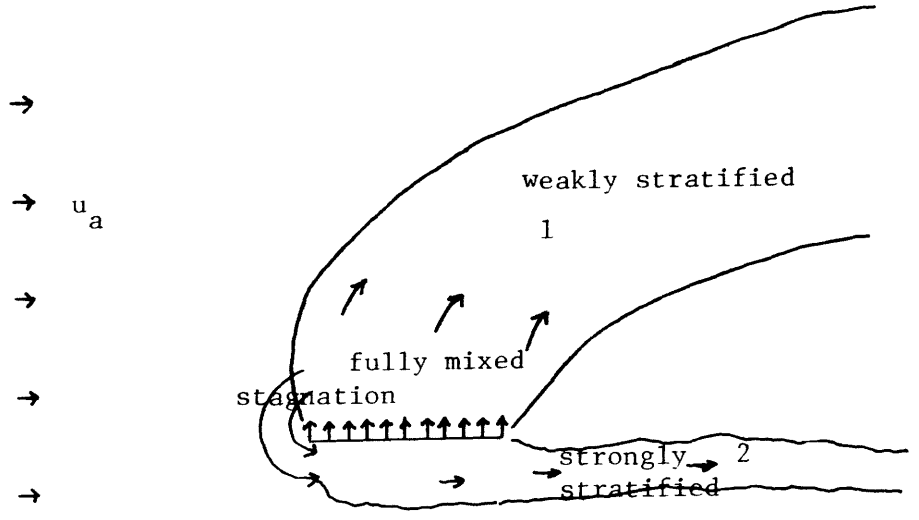

Fig. 7-3 Experimental observation of a T-diffuser test: Series FF

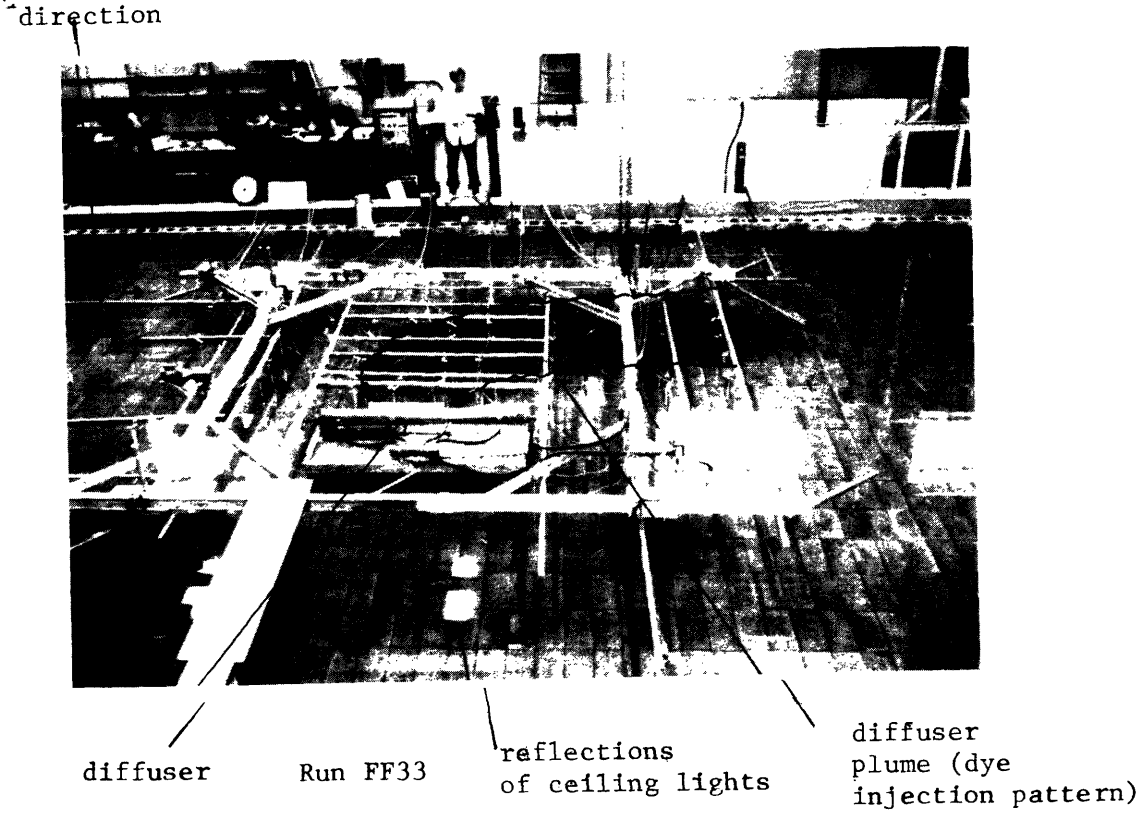

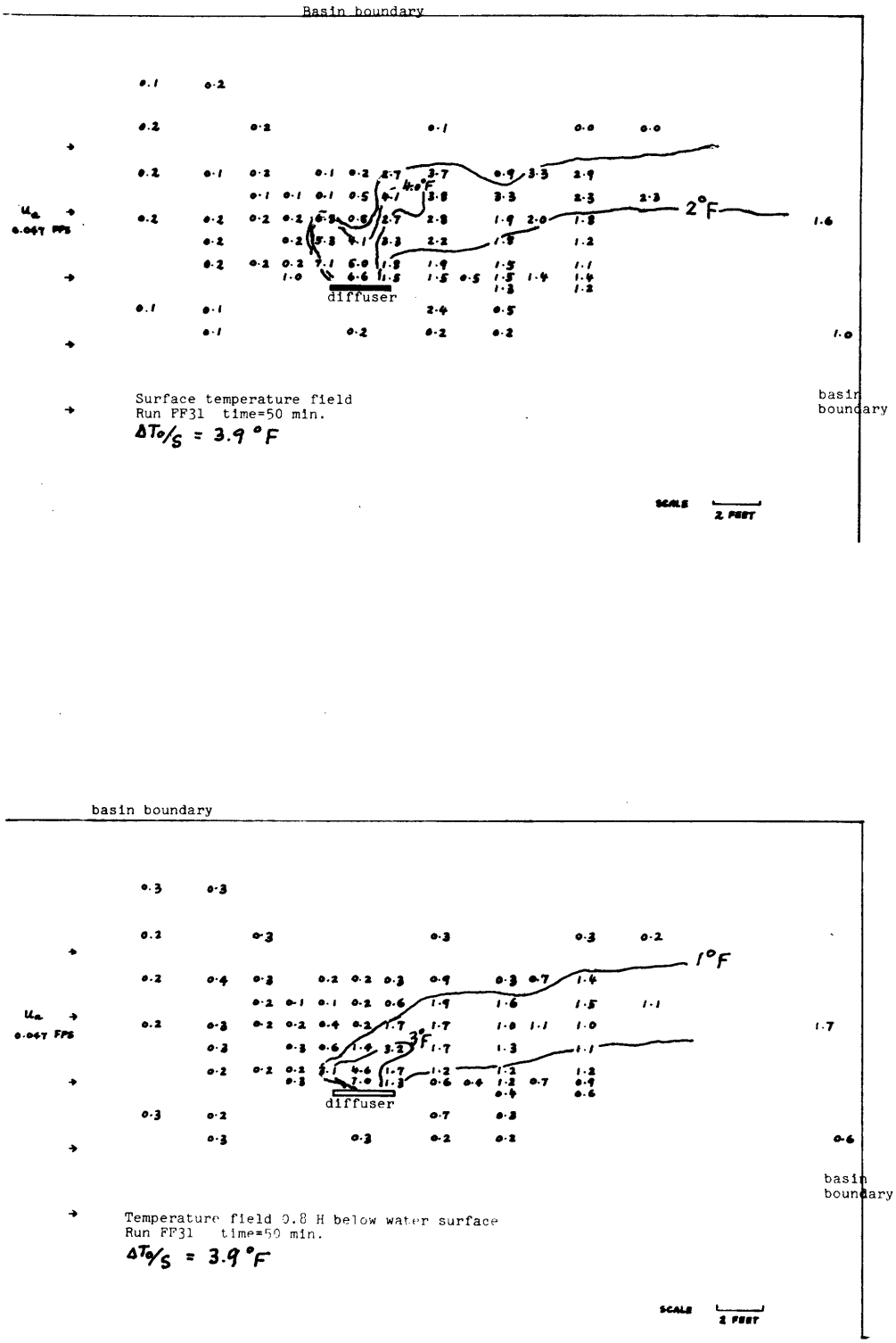

Fig.7-4 Typical recorded surface and bottom temperature field in a T-diffuser test; ∪Series FF

7.2.2 Data analysis of the Perry tests

A comprehensive analysis of the surface isotherms of the unidirectional tests in the Perry study indicates the effect of a perpendicular crossflow can be discerned in two distinct types of temperature fields: 1) Fig. 7-5 a) illustrates a temperature field little affected by the ambient current. The near field mixing is dominated by the diffuser design. The normal temperature gradient is symmetrical with respect to the centerline. 2) Fig. 7-5 b) illustrates a temperature field heavily influenced by the crossflow, resulting in temperature rises higher than $\Delta T_o/S$ extending for large distances downstream. $(\frac{\partial T}{\partial n})_{\text{current side}} >> (\frac{\partial T}{\partial n})_{\text{lee}}$ and the normal temperature gradient is not symmetrical with respect to the centerline.

In Fig. 7-6 the experimentally observed values of the near field temperature rise in this study and Perry tests are plotted versus a momentum flux ratio $F_M = \frac{u_a^2 L_D H}{Q_o u_o}$. F_M is a measure of the bending force on the plume relative to the momentum input of the diffuser. ΔT_{MAX} is defined to be the maximum surface temperature rise recorded beyond a distance $\simeq L_D$ from the diffuser; defining ΔT_{MAX} in this manner eliminates isolated heated spots due to local stagnation and stratification that are not indicative of the diffuser induced flow. $\Delta T_o/S$ is the near field temperature rise that would be obtained if the fully mixed assumption is met. In general ΔT_{MAX} deviates from $\Delta T_o/S$ for larger values of F_M. For a given $\frac{u_o}{u_o}$, a longer

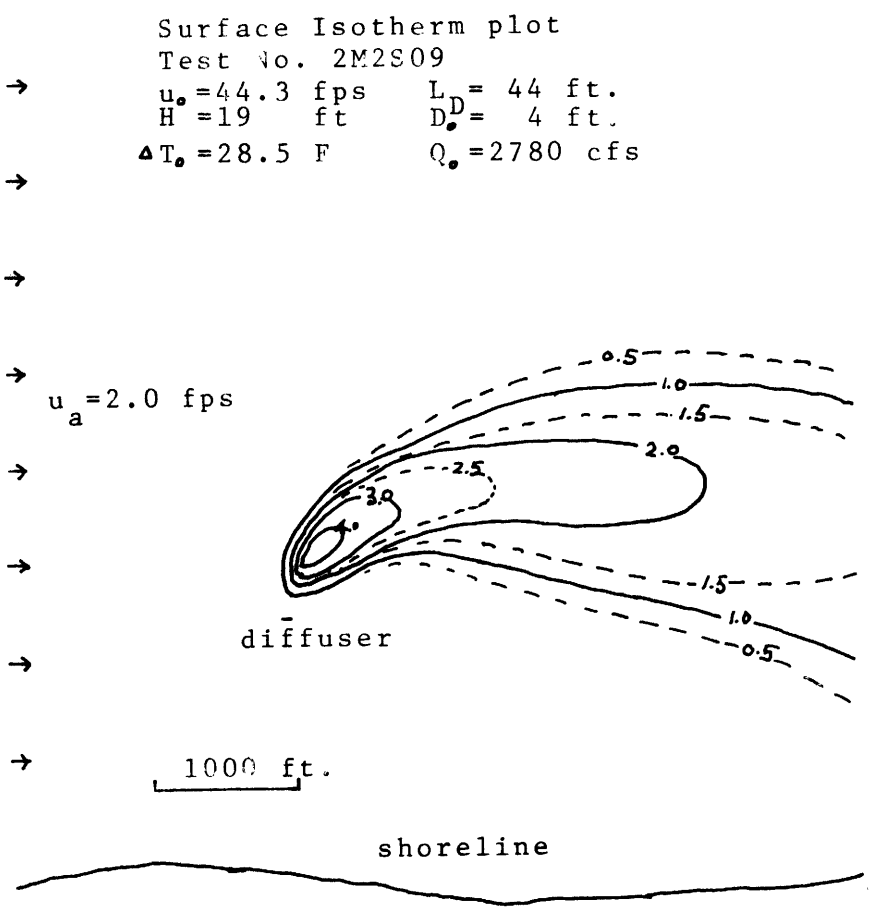

Fig. 7-5 a)

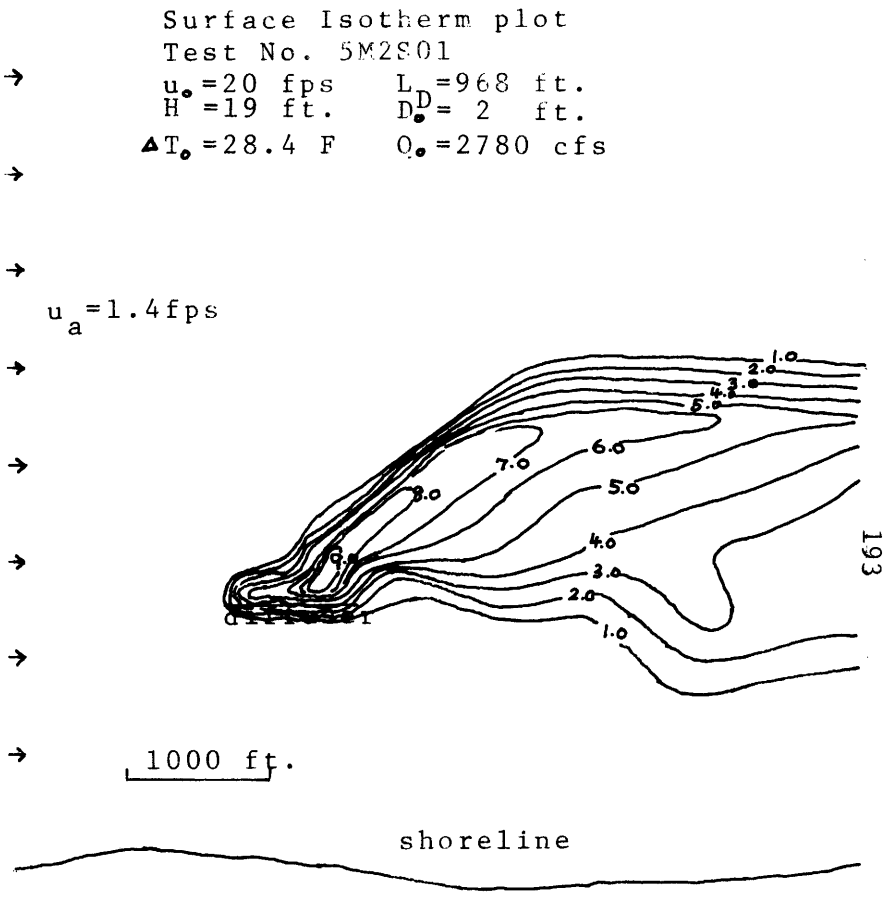

Fig. 7-5 b)

Fig. 7-5 Effect of ambient crossflow on near field mixing: surface isotherms for two diffuser designs

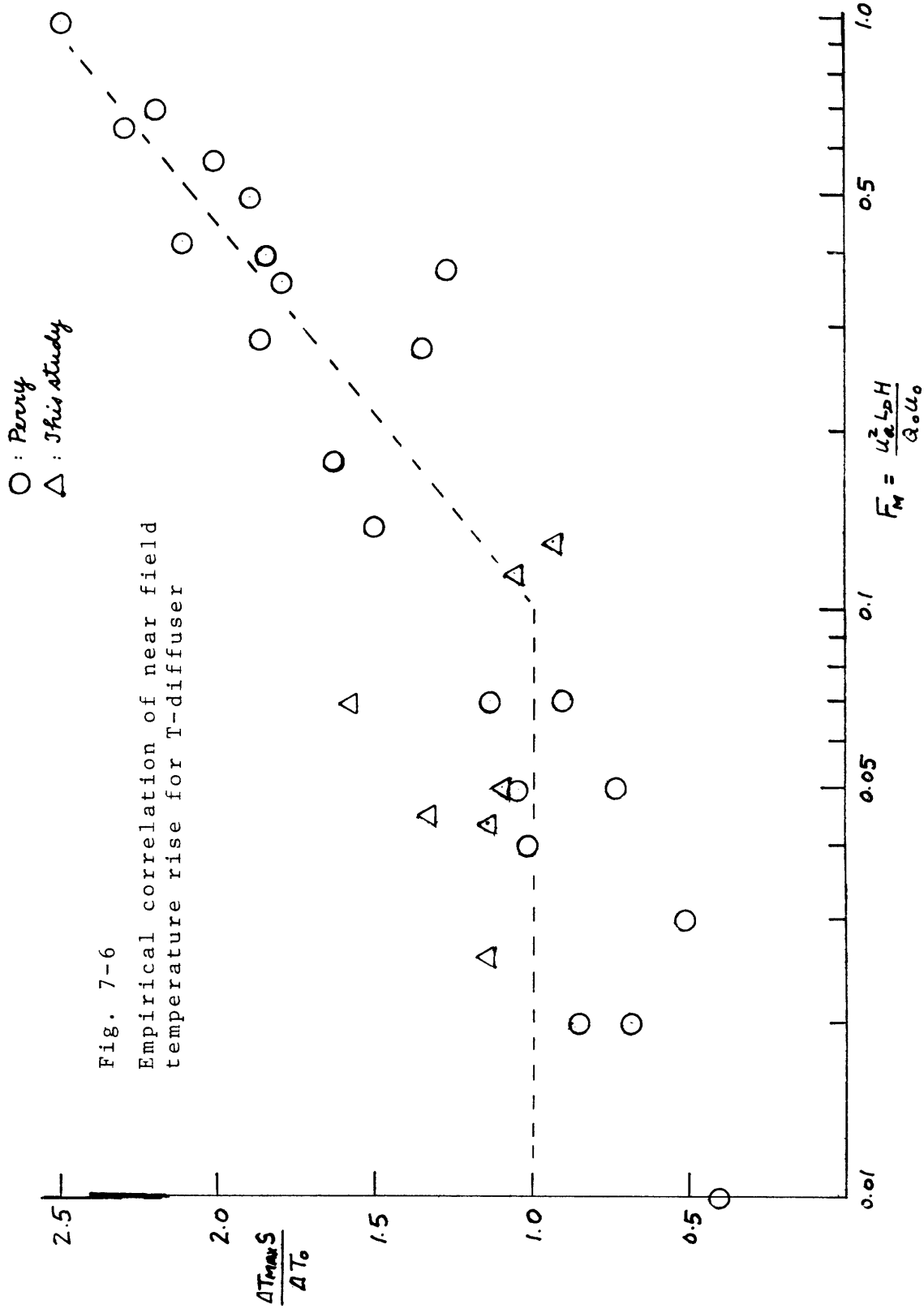

Fig. 7-6
Empirical correlation of near field temperature rise for T-diffuser

diffuser is more prone to adverse effects of an ambient current. For a given diffuser design, an increase of the ambient current velocity would likewise worsen the diffuser performance.

The correlation shows that for $F_M<0.1$ the near field mixing is not affected by the ambient current. Whereas for $F_M> 0.1$ the near field temperature rise can be considerably higher than $\Delta T_o/S$. The implication is that if a diffuser is designed with more concentrated momentum input (low values of F_M), the adverse effect of an ambient current on near field mixing can be eliminated. With the limited amount of available data, it is our speculation that for low momentum input (high F_M) the ambient current induces strong stratification near the diffuser; the fully mixed assumption breaks down, and the prediction of S ceases to be valid.

7.3 Comparison of predicted and observed plume trajectory

In this section the computed plume trajectories are compared with experimental results of this study and the Perry model studies. In all the calculations, the following values are used for the physical coefficients.

$\alpha = 0.068$

$f_o = 0.035$

$C_D = 4.0$

For each experiment, β , γ are determined from the diffuser design and ambient conditions. For $F_M<0.1$ S is given by eq. 7.8. For $F_M>0.1$, S is experimentally determined;

$S_{oBs} = \frac{\Delta T_o}{\Delta T_{MAX}}$, ΔT_{MAX} being defined in section 7.2.

7.3.1 Plume trajectory: Series FF

Fig. 7.7 shows the comparison between the predicted plume trajectory and the observed plume boundaries. The observed plume boundaries are visually recorded from dye injection patterns during the experiment. In general, the agreement is reasonable. The larger the value of F_M, the more the plume is deflected. In some runs the predicted plume trajectory (e.g. FF30, 34) extends beyond the model limit: distortion of results is expected in regions close to the boundary.

7.3.2 Plume trajectory: Perry tests

Fig. 7-8 shows the predicted plume trajectory along with the observed surface isotherms for the Perry tests. The same trend is seen in these comparisons; a larger F_M leads to stronger plume deflection. The agreement between the predicted and observed plume trajectory is satisfactory. The predicted plume width, however, is considerably smaller than the lateral extent of the surface isotherms. As the theory is based on a vertically fully mixed assumption, this suggests the plume is stratified beyond the near field.

Only tests with distinct input parameters to eq. 7.3 are included; some Perry tests differ only in design parameters that do not affect the global temperature field (e.g. clearance of the discharge ports from the bottom).

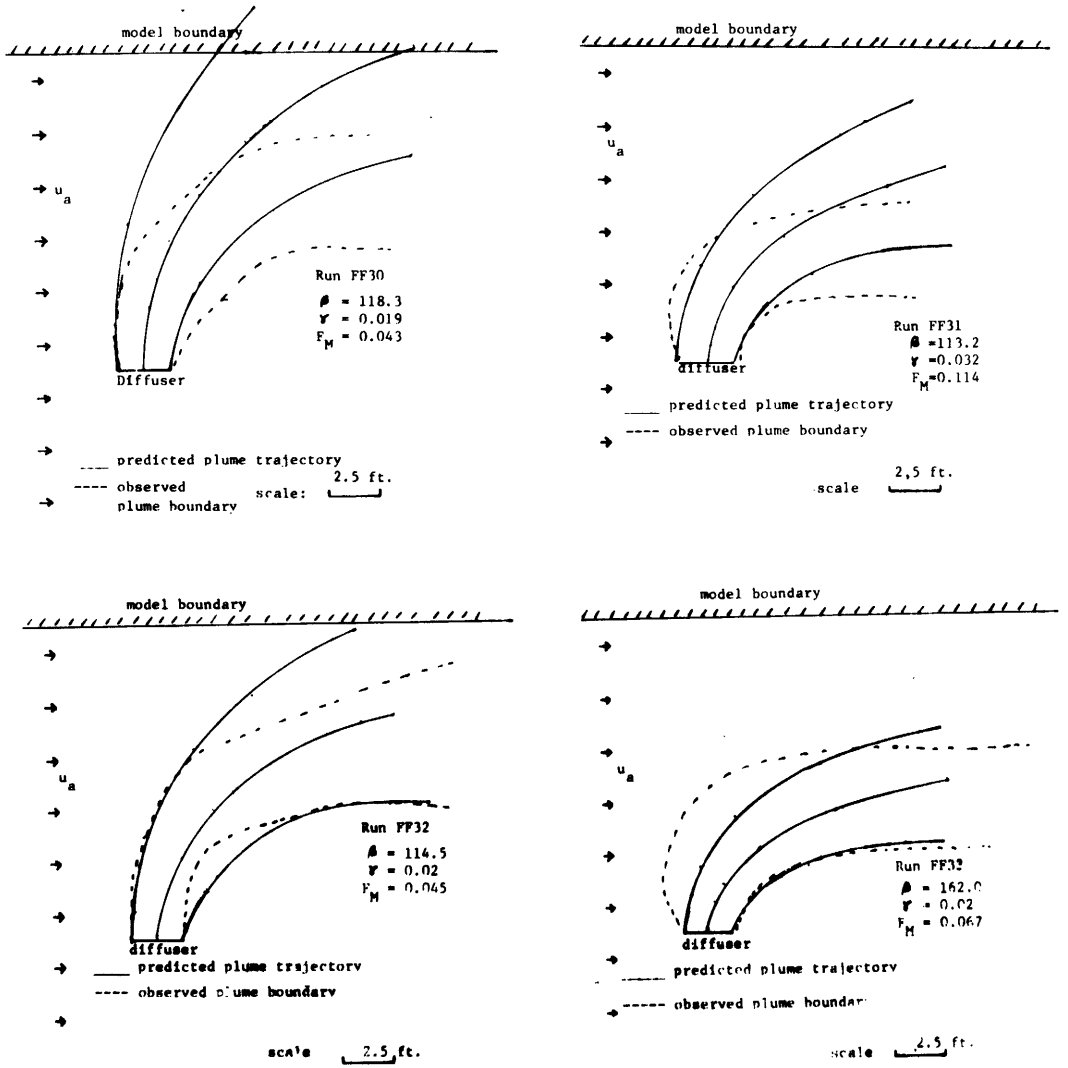

Fig. 7-7 Comparison of predicted plume trajectory _____ and observed plume boundary ------- Series FF

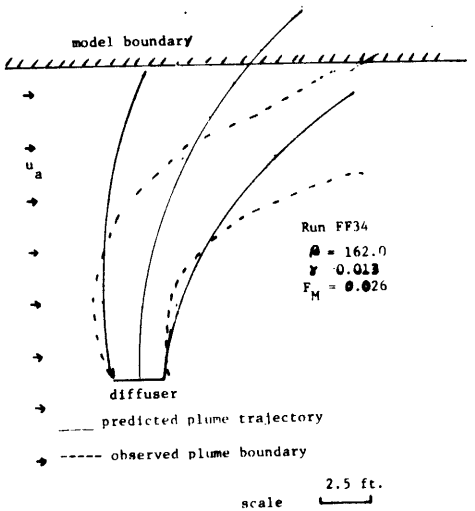
model boundary
u_a
Run FF34
β = 162.0
γ = 0.013
F_M = 0.026
diffuser
predicted plume trajectory
observed plume boundary
scale
2.5 ft.

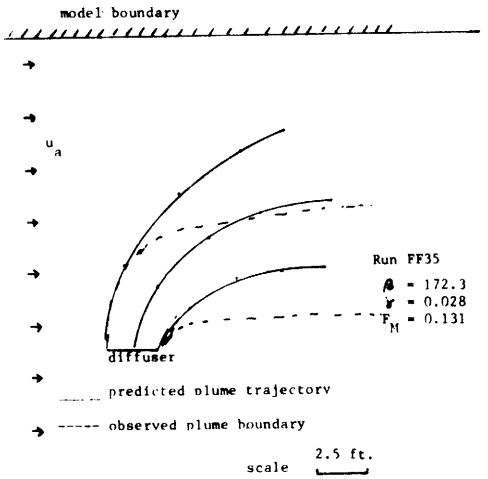
model boundary
u_a
Run FF35
β = 172.3
γ = 0.028
F_M = 0.131
diffuser
predicted plume trajectory
observed plume boundary
scale
2.5 ft.

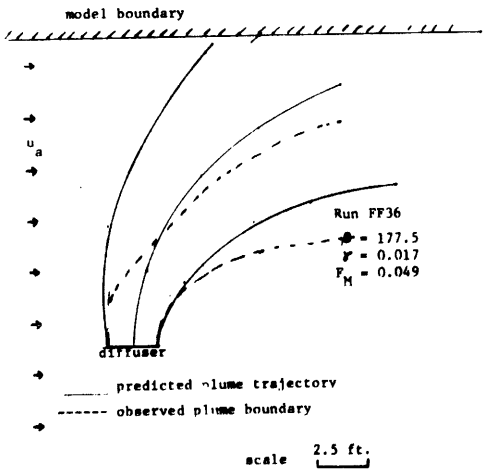
model boundary
u_a
Run FF36
β = 177.5
γ = 0.017
F_M = 0.049
diffuser
predicted plume trajectory
observed plume boundary
scale
2.5 ft.

Fig. 7-7 cont'd

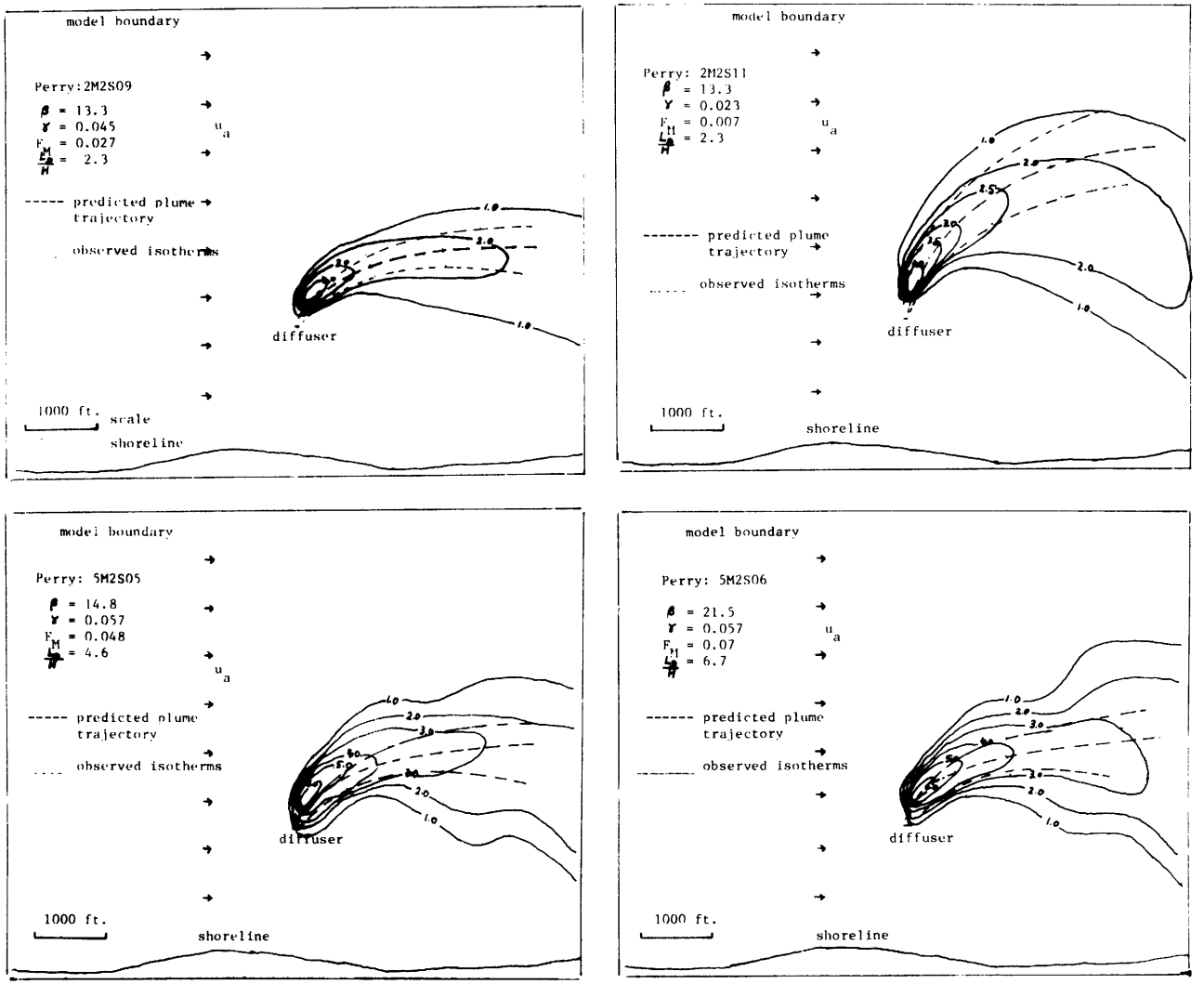

Fig. 7-8 a) Comparison of predicted plume trajectory ---------- and observed surface isotherms in Perry model study

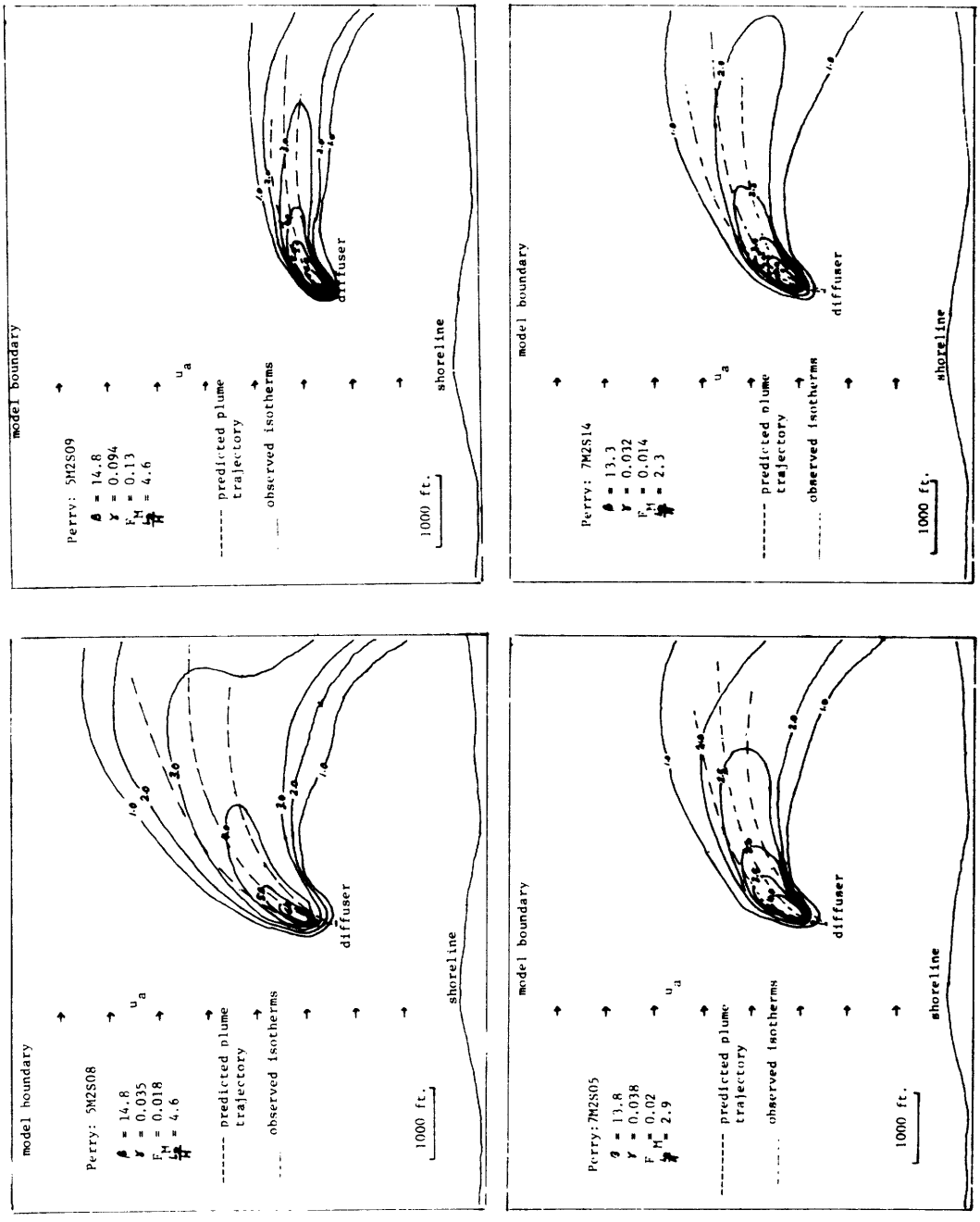

Fig. 7-8 a) cont'd

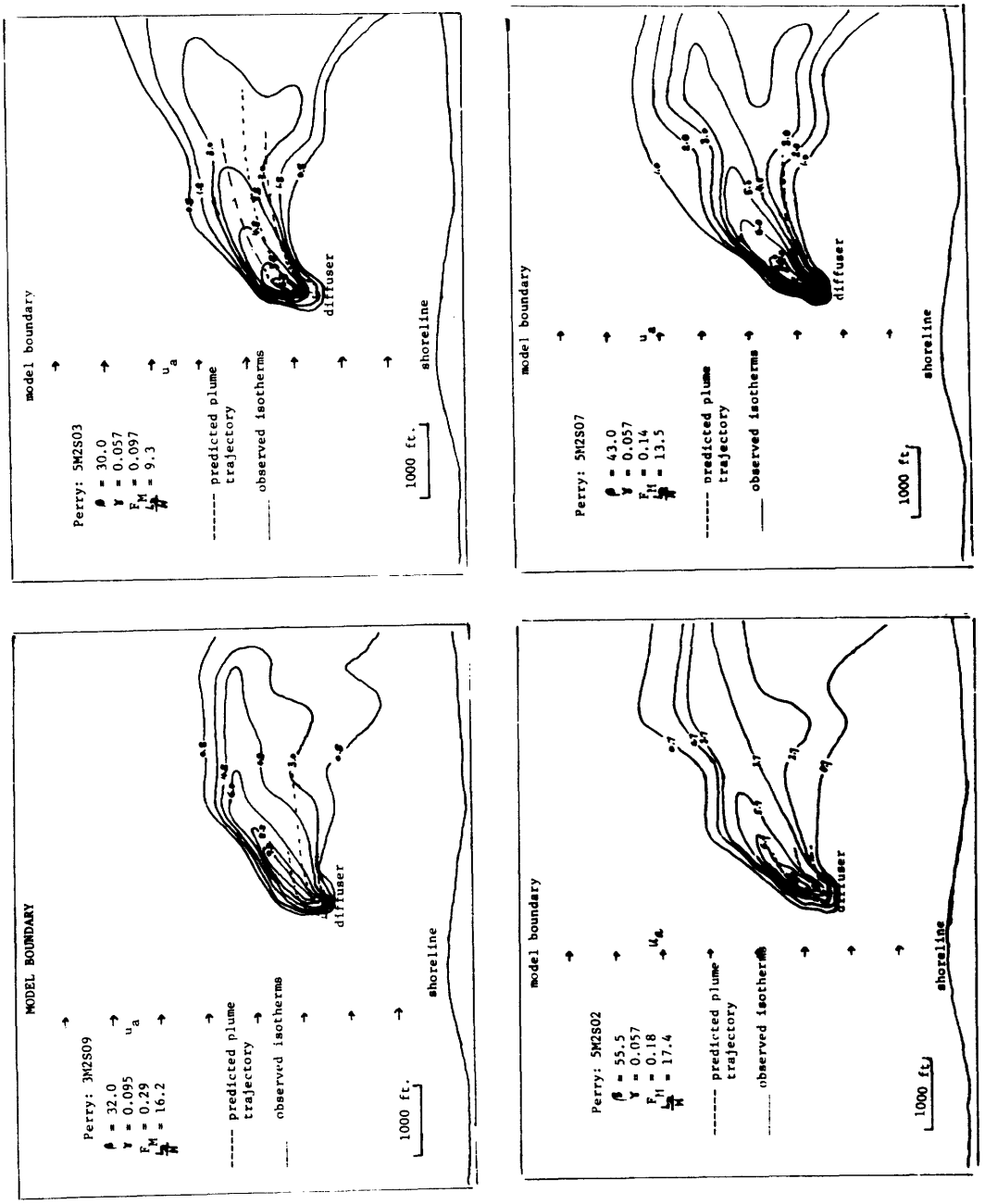
MODEL BOUNDARY
Perry: 3M2S09
β = 32.0
γ = 0.095
F_M = 0.29
$\frac{L_M}{H}$ = 16.2
u_a
predicted plume trajectory
observed isotherms
diffuser
1000 ft.
shoreline
model boundary
Perry: 5M2S03
β = 30.0
γ = 0.057
F_M = 0.097
$\frac{L_M}{H}$ = 9.3
u_a
predicted plume trajectory
observed isotherms
diffuser
1000 ft.
shoreline
model boundary
Perry: 5M2S02
β = 55.5
γ = 0.057
F_M = 0.18
$\frac{L_M}{H}$ = 17.4
u_a
predicted plume trajectory
observed isotherms
diffuser
1000 ft.
shoreline
model boundary
Perry: 5M2S07
β = 43.0
γ = 0.057
F_M = 0.14
$\frac{L_M}{H}$ = 13.5
u_a
predicted plume trajectory
observed isotherms
diffuser
1000 ft.
shoreline

Fig. 7-8 b)

For tests characterised by large $F_M > 0.1$ the calculated trajectory indicates the plume rapidly approaches the ambient current direction. The calculations are discontinued at a point where $u(x) \simeq u_a \cos \theta$. As the induced velocity in these cases (with impaired near field dilution) is usually small, this occurs at a distance from the diffuser that is small compared with the scale of the isotherm plot (1000 ft.). Consequently it is judged sufficient to illustrate only several comparisons of this type (Runs in Fig. 7-8 b); the agreement in other tests belonging to this category is similar.

7.3.3 Sensitivity of results to C_D

The sensitivity of the theoretical predictions to the blocking coefficient C_D is illustrated in Fig. 7-9. The major determinant of the plume trajectory, C_D, is varied $\pm$ 40% from the assumed value in all the previous calculations for a typical run with $F_M < 0.1$. The results show that a larger assumed value of C_D leads to more pronounced plume deflection; the ultimate lateral position of the plume is changed by only about 10 % from the $C_D = 4$ prediction.

7.4 Summary

This chapter concerns the induced temperature field of a unidirectional diffuser in a perpendicular crossflow.

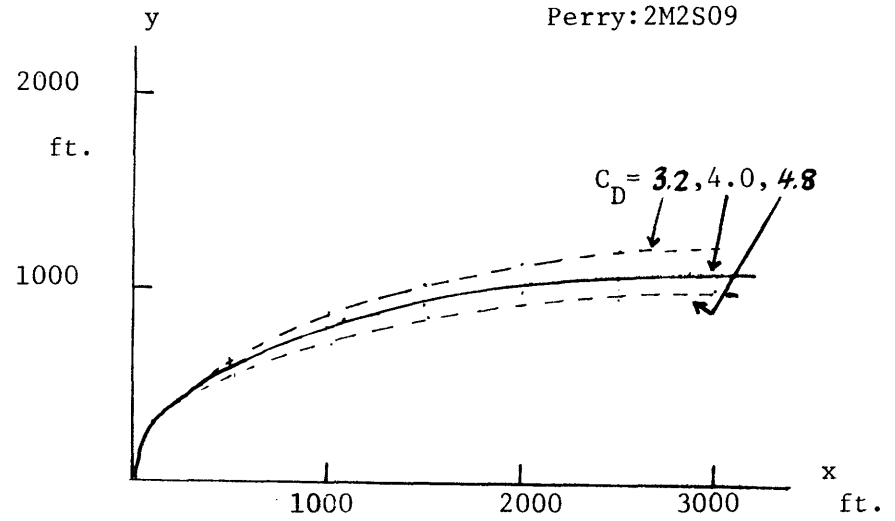

Fig. 7-9 Sensitivity of predicted plume trajectory to blocking coefficient C_D

Based on a vertically fully mixed assumption, a theory is developed for calculating the near field dilution and plume trajectory.

Data analysis of tests in this study and the Perry model study shows that for a low momentum input in a strong cross-flow, characterised by $F_M = \frac{u_a^2}{Q_o} \frac{L_D H}{u_o} > 0.1$, the near field temperature rise can be considerably higher than predicted. An empirical correlation of near field temperature rise for a Tee-diffuser is given. The correlation also suggests that a T-diffuser can be designed in the $F_M < 0.1$ range to prevent adverse effect of the crossflow.

The computed plume trajectory is compared with observed plume boundaries in this study and surface isotherm plots in the Perry Study. Satisfactory agreement is obtained in all cases. Eq. 7.13 can be used to estimate in a prototype situation the distance of the diffuser plume from the shore.

CHAPTER VIII

FAR FIELD RECIRCULATION

In the previous chapters a theoretical model for a unidirectional diffuser in shallow water has been formulated, solved, and validated against experimental data. In this chapter we investigate a phenomenon that has hiterto been set aside; the potential heat build-up in the vicinity of the diffuser. Because of its large entrainment demand, a diffuser represents a strong sink. The question of interest is, therefore, under what conditions will the diffuser mixed flow recirculate, carrying heat back into the near field?

In the following sections an experimental confirmation for far field recirculation is given. The effect of the return flow on the temperature field will be discussed and semi-empirical correlations are presented.

8.1 Conceptual framework of heat recirculation

The conceptual basis upon which the experimental investigation of far field recirculation has been conducted can be schematized in Fig. 8-1. Under slack water conditions, we have seen from eq. 4.50 that the momentum of the diffuser plume is dissipated exponentially as $e^{-f_o x/8H}$; thus at a characteristic distance of $L_{rec} = \frac{8H}{f_o}$ away, the diffuser plume will have lost most of its initial momentum; a stagnant pool of water at this distance would, by flow continuity, serve

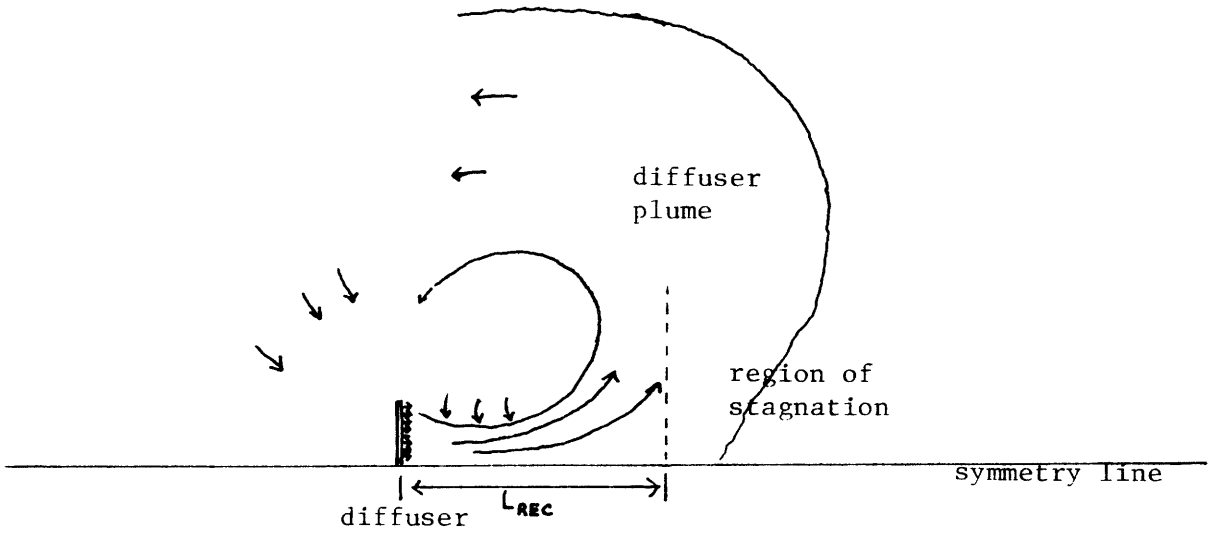

Fig. 8-1: Schematic of diffuser induced recirculation

as a source for the back entrainment demand of the diffuser, thus creating a far field recirculation resembling a source-sink type of flow.

Fig. 8-2 illustrates the recirculation pattern observed in an experiment. Twenty minutes after the start of the experiment, a 30 sec. dye injection is made; Fig. 8-2a shows the diffuser plume immediately following dye injection, the plume edge being blurred by dye diffusion. Fig. 8-2b is a snapshot taken five minutes after the dye injection has stopped. The clear discharge water and the dyed recirculation patterns reveal clearly the shape of the diffuser plume. The blue streak lines indicate the flow is laminar.

Fig. 8-2a. Recirculation demonstrated in a full diffuser test (MJ 23) : immediately following dye injection

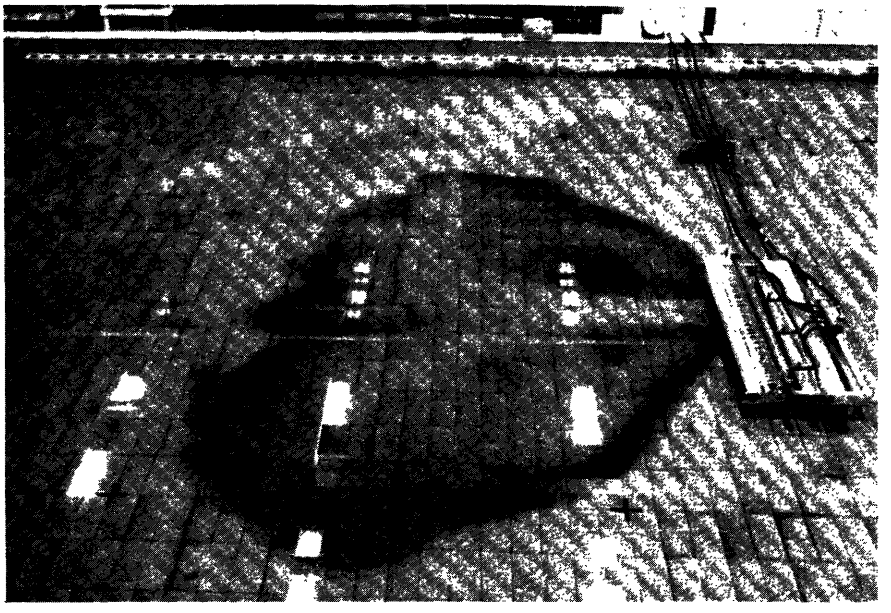

Fig. 8-2b. Run MJ 23 : 5 minutes after dye injection
$\frac{t}{T_{REC}} \approx 2.1$

8.1.1 Characteristic scales of recirculation

From the discussion of the previous section, we see that an estimate of the characteristic scale of recirculation, L_{REC} is

$$L_{REC} = \frac{8H}{f_o} \tag{8.1}$$

The sink strength (per unit depth) of the diffuser is measured by $\frac{SQ_o}{H}$. Thus the time scale of recirculation is characterised by a parameter

$$T_{REC} = \frac{HL^2_{REC}}{SQ_o} \tag{8.2}$$

In the laboratory, for runs that exhibit strong far field reciculation, the flow beyond the near field would be laminar Using a pipe flow analogy, the friction factor f_o can be estimated as

$$f_o = \frac{64}{R_e} \tag{8.3}$$

where

R_e = characteristic Reynolds number of mixed flow

$$= \frac{u_N(4H)}{\nu}$$

u_N = induced velocity in the near field

Thus the scale of recirculation, L_{REC}, for the laboratory experiments carried out in this study can be estimated as

$$L_{REC} \sim \frac{1}{2} \frac{u_N H^2}{\nu} \tag{8.4}$$

From eq. 3.41 we see that $u_N = u_o/s$

$$L_{REC} \sim \frac{1}{2} \frac{u_o H^2}{\nu S} \tag{8.5}$$

Thus L_{REC} is dependent on a characteristic parameter $\frac{u_o H^2}{\nu S}$. The constant of proportionality can be expected to be considerable less than unity as the actual jet velocity rapidly decreases below the characteristic velocity u_N as the diffuser plume spreads in the lateral direction

8.1.2 A dimensionless formulation of heat recirculation

As heat gets recirculated into the near field due to diffuser induced recirculation, the maximum temperature rise in the near field would be higher than ΔT_N, as part of the entrained flow is at a temperature higher than the ambient temperature T_a. The transient temperature build-up in the near field can be correlated with the diffuser design variables. The previous considerations suggest it is reasonable to assume a physical dependence of the following form for the far field recirculation effects.

$$\Delta T_{MAX} = f\ (\Delta T_N,\ \frac{SQ_o}{H},\ L_{REC},\ L_D, t) \qquad (8.6)$$

Thus the maximum temperature rise ΔT_{max} in the diffuser induced temperature field is assumed to depend on ΔT_N, the near field temperature rise in the absence of heat recirculation; $\frac{SQ_o}{H}$, the 'sink strength' of the diffuser; L_{REC}, the scale of recirculation; L_D, the diffuser length; and t, the time from the start of the experiment.

Choosing $\Delta T_N, L_{REC}$, t as the fundamental variables, the following dimensionless grouping can be obtained:

$$\frac{\Delta T_{MAX}}{\Delta T_N} = f\left(\frac{SQ_o t}{HL^2_{REC}}, \frac{L_D}{L_{REC}}\right) \qquad (8.7)$$

The correlation 8.7 can be obtained from the experimental results of this study, as shown in a later section.

8.2 Experimental Investigation

All the slack tide runs in Series MJ and FF are performed to test the phenomenon of far field recirculation. Most of these tests were done with a half-diffuser; a few full diffuer tests in series MJ were made to corroborate the findings of the half diffuser tests. The phenomenon of recirculation was confirmed in these runs. It was possible to produce a scale of recirculation that is significantly less than the basin extent, thus minimizing model boundary effects. The experiments in the MJ series were designed to investigate how the scale of recirculation varies as the diffuser design parameters; no heat is introduced. Each run lasted about 45 minutes. In the FF series the slack tide runs were performed to confirm the phenomenon of recirculation in the presence of heat input and investigate how the recirculation changes the temperature configuration in the near field of the diffuser. Each run usually lasted a little over two hours, when it was judged the model boundaries have significantly distorted the results. For these runs a steady state is not approached as heat is continually accumulating in the basin. It was found that small scales of recirculation (strong far field recirculation) are in general

characterised by long diffusers, low discharge velocities, and shallow water depths (cf. eq. 8.5).

8.2.1 Experimental Results

Fig. 8-3 (Run FF04) illustrates the dye pattern at various times after the beginning of an experiment. Also shown is a surface pathline which indicates a scale of recirculation that is significantly smaller than the basin size. The effect of the far field recirculation on the temperature field is illustrated in Fig. 8-4. The excess temperature field normalized by ΔT_N, $\overline{\Delta T}(x,y) = \frac{\Delta T(x,y)}{\Delta T_N}$, is plotted near the beginning and an hour from the start of the experiment. Any value of $\overline{\Delta T}$ greater than 1.0 is then indicative of heat recirculation effects. Characterised by a small time scale of recirculation (T_{REC}= 3.9 min), the run shows strong heat recirculation leading to temperatures much higher than ΔT_N within 60 minutes from the start of the experiment, $\frac{t}{T_{REC}} = 15.4$.

As a contrasting example, Fig. 8-5 (Run FF13) illustrates the surface flow field of a run that is characterised by a large scale of recirculation; thus the recirculation is clearly influenced by the presence of the model boundaries. Because T_{Rec} is large for this run (T_{REC} = 51 min.), we see from Fig.8-6 that no heat recirculation in the near field is visible even after 70 minutes from the start of the experiment, $\frac{t}{T_{Rec}} = 1.4$.

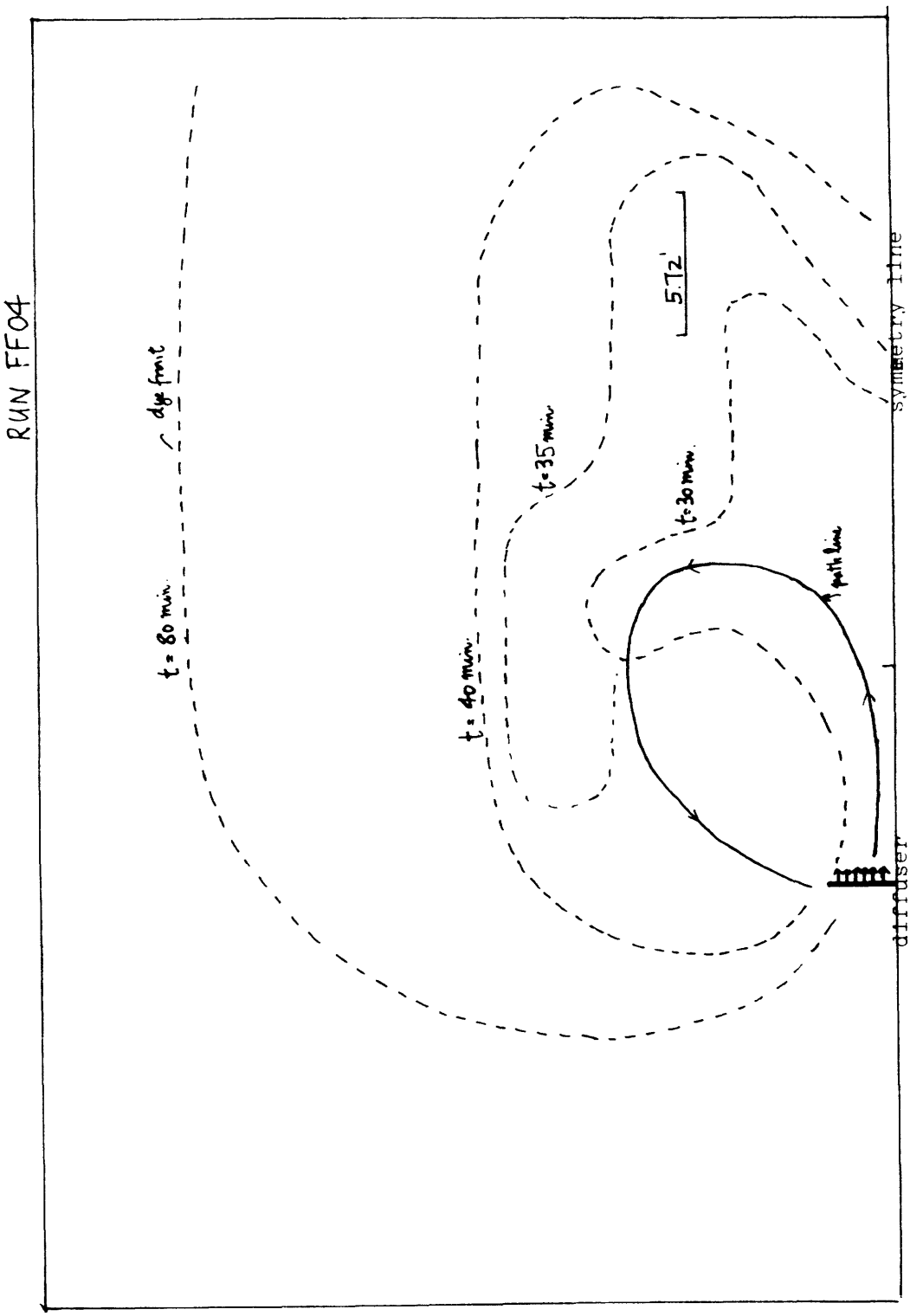

Fig. 8-3 Recirculation illustrated by movement of dye front

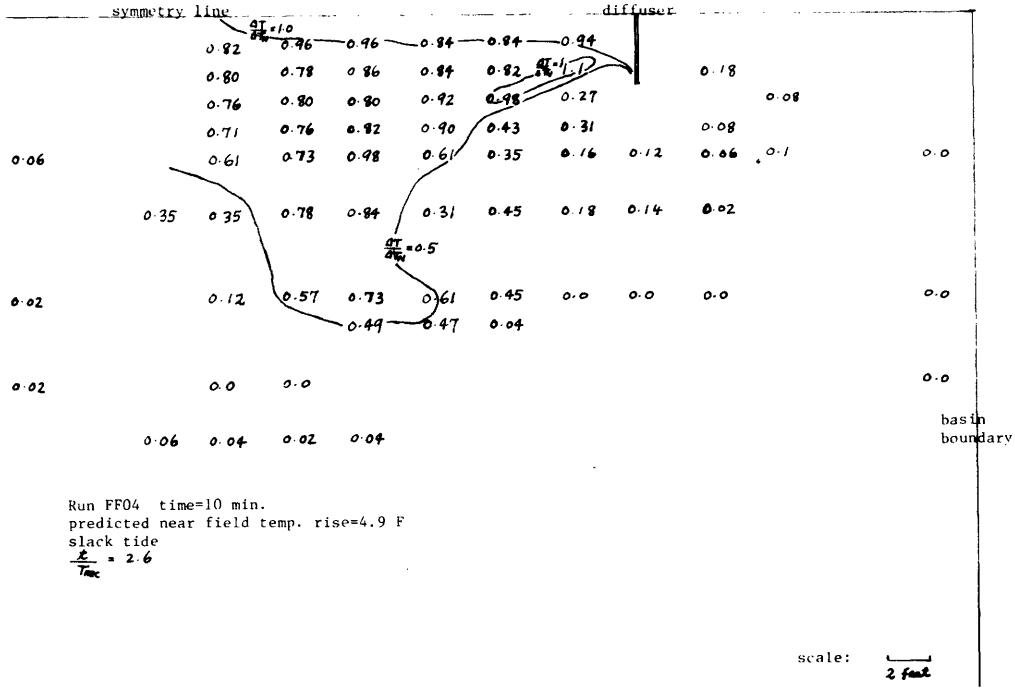

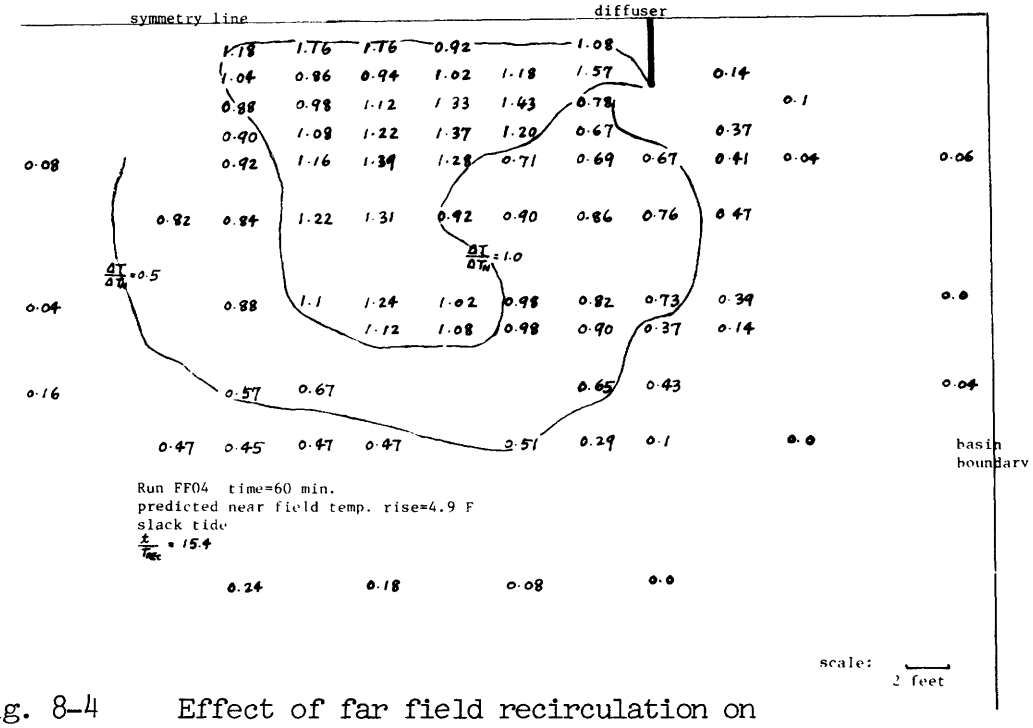

Fig. 8-4 Effect of far field recirculation on the normalised excess temperature field: strong recirculation $\overline{\Delta T} = \frac{\Delta T}{\Delta T_N}$

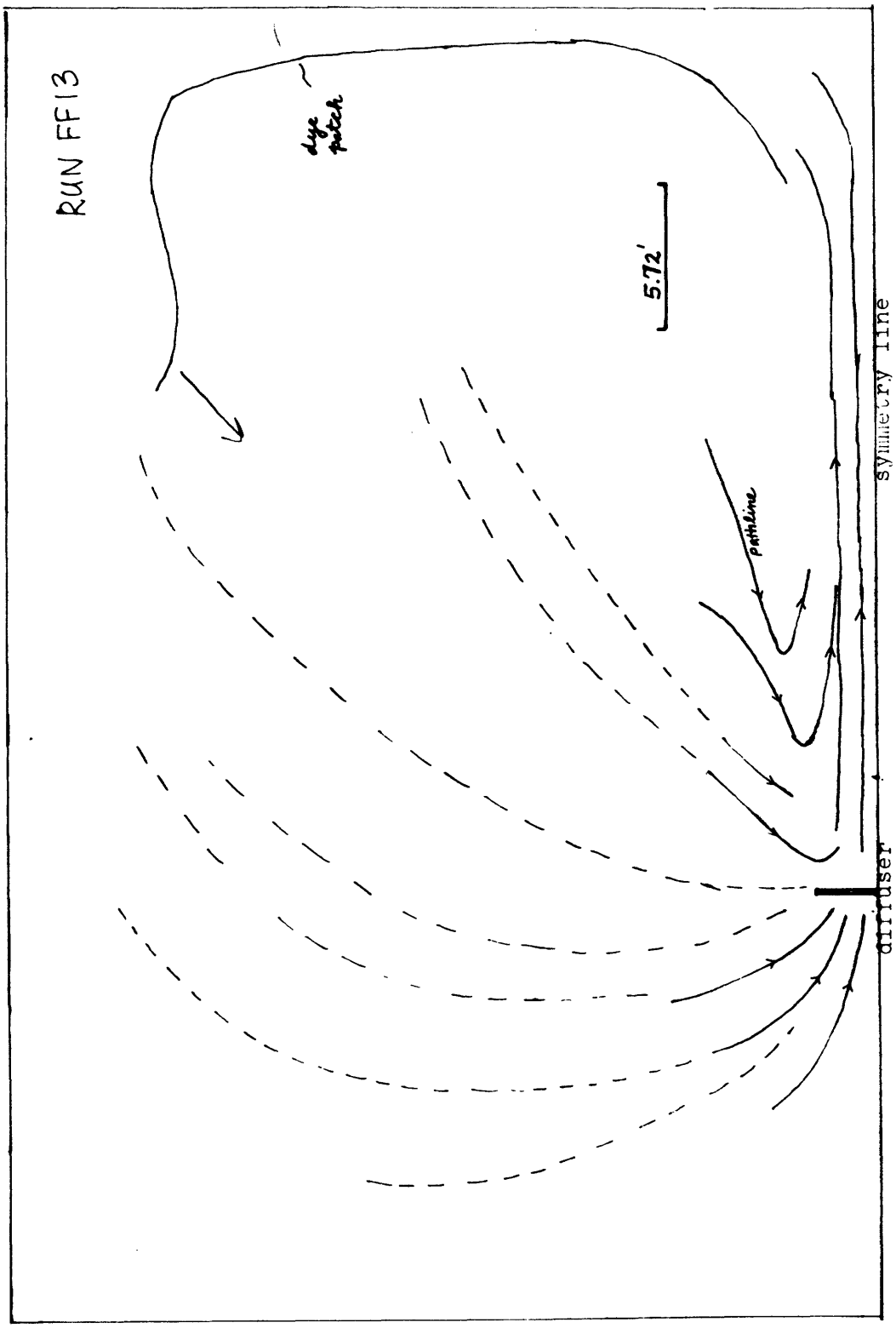

Fig. 8-5 Surface flow field of an experiment characterised by weak recirculation effects: $L_{REC} \sim$ model dimension

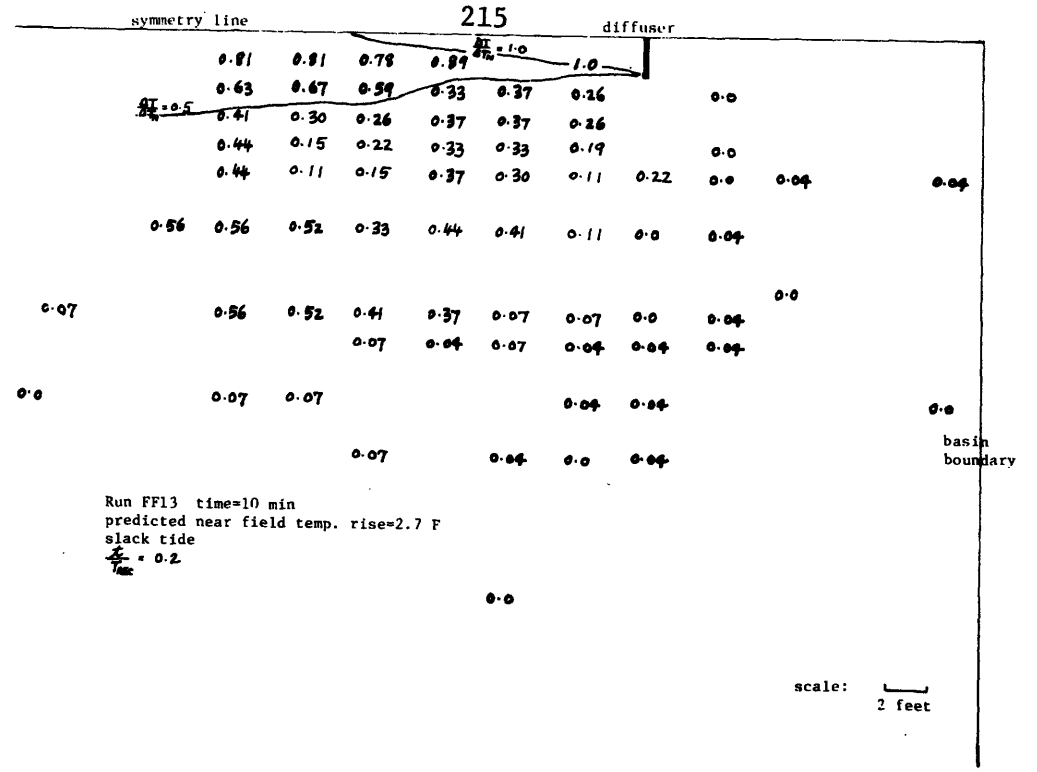

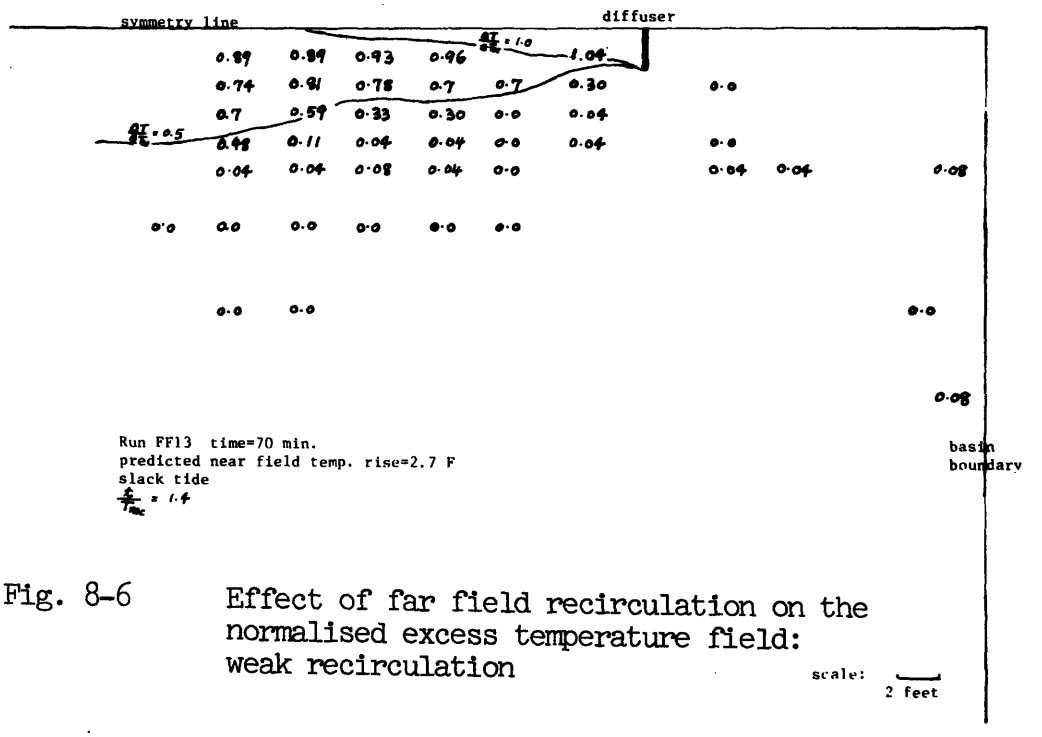

Fig. 8-6 Effect of far field recirculation on the normalised excess temperature field: weak recirculation

8.2.2 Empirical Correlation

A. The scale of recirculation, L_{REC}

In the experiment L_{REC} is taken to be the distance from the diffuser to the point where the center of the diffuser plume begins to recirculate (as indicated in Fig. 8-1 and Fig. 8-2). By defining the scale of recirculation in this manner, L_{REC} can be measured to within about 2 feet. In Fig. 8-7 the experimentally observed values for L_{REC} in the MJ and FF series are plotted against the characteristic parameter $\frac{u_o H^2}{\nu S}$. Rough as it is, the theoretical consideration in section 8.1 seems to be well borne out by the experimental data. The empirical correlation is:

$$L_{REC} = 0.088 \frac{u_o H^2}{\nu S} \qquad (8.8)$$

B. Maximum temperature rise

In Fig. 8-8 the normalised maximum temperature rise in the diffuser induced temperature field recorded at any time during an experiment, $\frac{\Delta T_{MAX}(t)}{\Delta T_N(\text{observed})}$, is plotted against a dimensionless time $\frac{t}{T_{REC}}$, where

$$T_{REC} = \text{characteristic time of recirculation} = \frac{HL^2_{REC}(\text{Obs.})}{SQ_o}$$

In general it can be seen that for small values of L_D/L_{REC}; i.e. large scale of recirculation, the heat build up is much more gradual whereas for large values of L_D/L_{REC}, the maximum temperature rise in the near field can be as high as two to

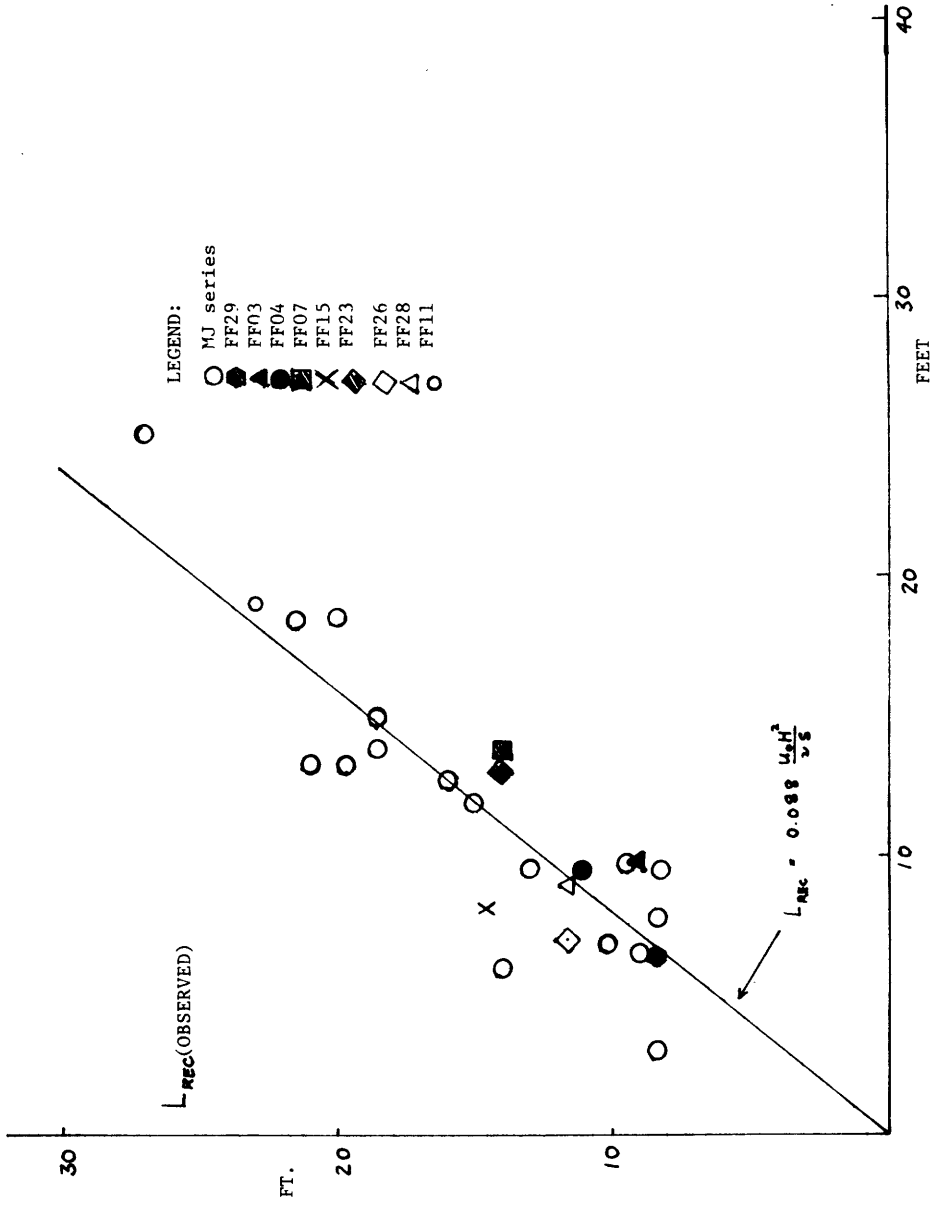

Fig. 8-7 Empirical correlation of scale of recirculation

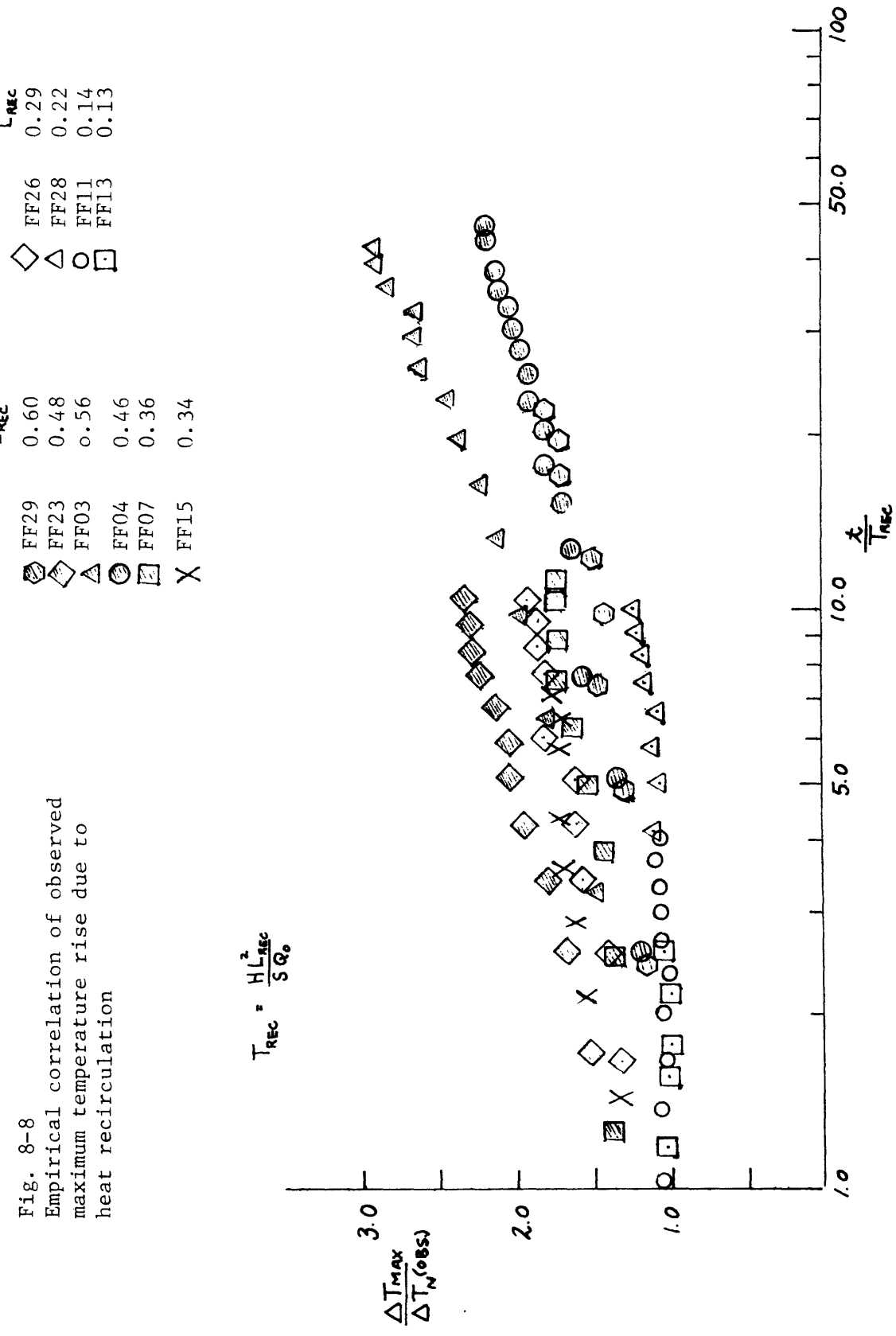

Fig. 8-8
Empirical correlation of observed maximum temperature rise due to heat recirculation

three times ΔT_N, the near field temperature rise without heat recirculation as given in section 4.1.1.

The temperature data of three FF slack tide runs have been excluded in these correlations for experimental reasons; Runs FF09 and FF25 are characterised by low jet Reynolds numbers, $R_D \sim 1500$, so that potential jet laminarity may affect the jet mixing. The diffuser length L_D of Run FF27 is short compared with the sensor spacing, so that the measurements are not sufficiently close to resolve ΔT_{MAX}.

8.2.3 Short vs. long diffuser

All the previous discussion and experimental results have suggested the far field heat recirculation is dependent on two parameters - the sink strength SQ_o/H, and the scale of recirculation L_{REC}. With this notion in mind we can compare the effect of diffuser length on far field recirculation.

Let us consider two diffuser designs. The design parameters are indicated below:

Design A	Design B
$Q_o, L_D, s, u_o, H, a_o, N$	$Q_o, 2L_D, 2s, u_o, H, a_o, N$

Thus design B differs from design A in that only the port spacing (and hence the diffuser length) is doubled, everything else being kept the same. From Eq. 3.41 we see that for the slack tide case the near field dilution S is proportional to $\sqrt{\frac{L_D H}{N a_o}}$; thus design B would have a near field dilution $\sqrt{2}$ times

that of A. For these two cases the sink strength and L_{REC} are compared:

$$SQ_o/H \qquad\qquad (\sqrt{2}\ S)Q_o/H$$

$$L_{REC} \sim \frac{u_o H^2}{\nu S} \qquad\qquad L_{REC} \sim \frac{u_o H^2}{\nu(\sqrt{2}\ S)}$$

The sink strength of design B is $\sqrt{2}$ times that of design A, with a scale of recirculation $1/\sqrt{2}$ times.

These elementary considerations are demonstrated by Runs FF28, 29. Fig. 8-9 compares the surface flow field recorded for the two runs; it can be seen that a longer diffuser has a smaller scale of recirculation. The movement of the dyed diffuser plume at various stages after dye injection for these two runs is also shown in Fig. 8-10. Fig. 8-11 compares the normalised excess temperature field for the same two runs; a longer diffuser induces more far field heat recirculation in the same real time t (cf. t= 120 minutes) after the beginning of the experiment, which corresponds to different normalised times t/T_{REC} = 10.2 (short) vs. 30(long diffuser).

8.3 Design Application

8.3.1 Prototype Considerations

In the prototype flow is turbulent; characteristic scales of recirculation are hence given by eq. 8.1, 8.2. Using typical values of

H = 20 feet

f_o = 0.02

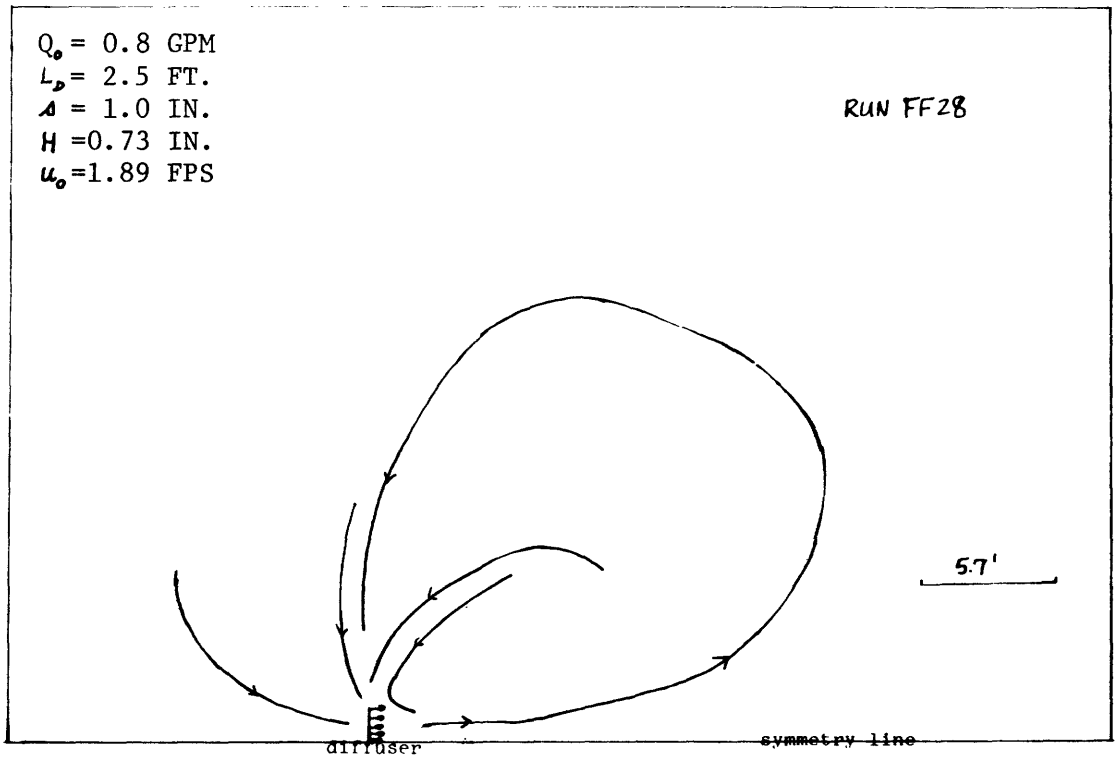

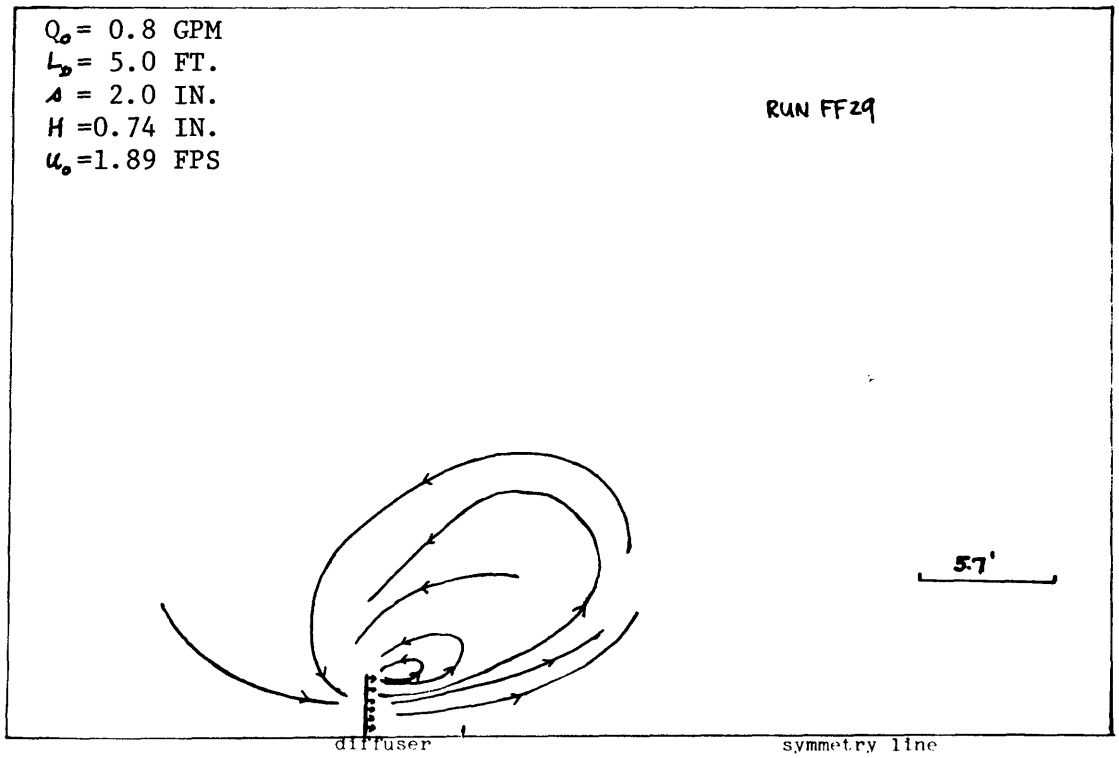

Fig. 8-9 Recorded surface flow field
(short vs long diffuser)

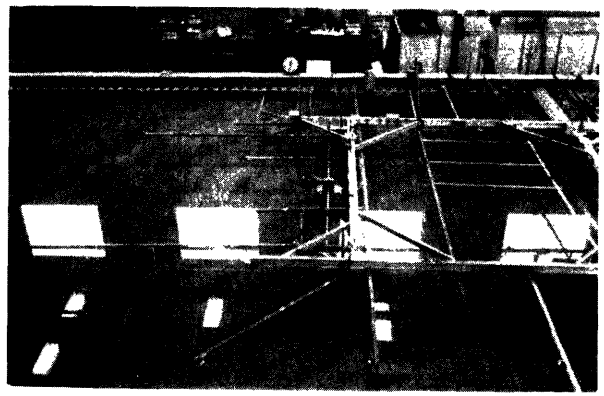

time after dye injection= 1 min.

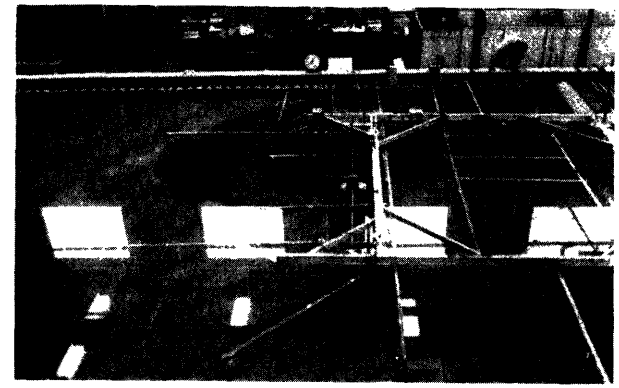

time= 10 min.

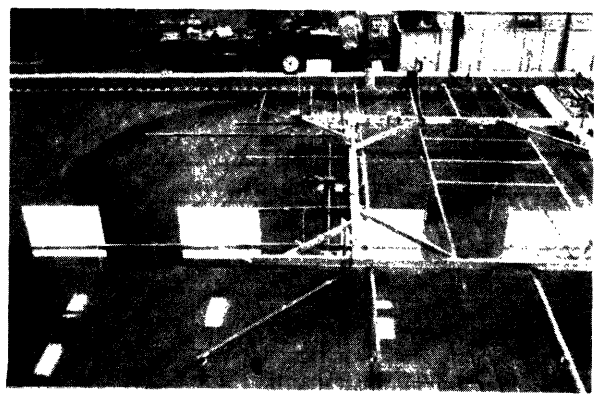

time= 20 min.

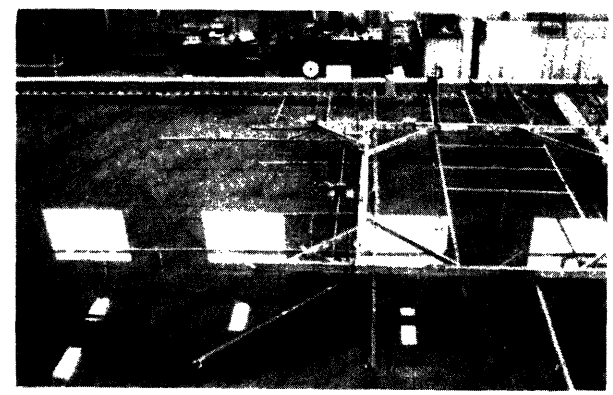

time= 50 min.

Fig. 8-10 a) Recorded dye patterns (short diffuser: Run FF23)

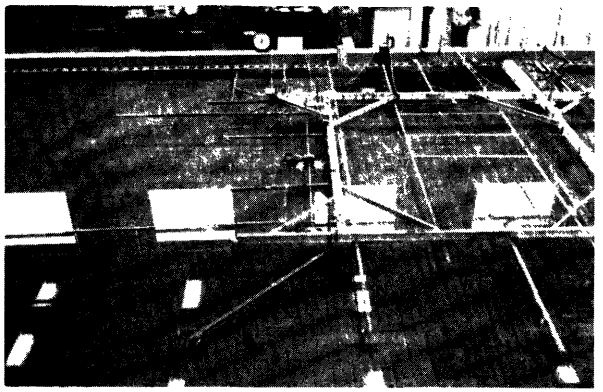

time after dye injection= 1 min.

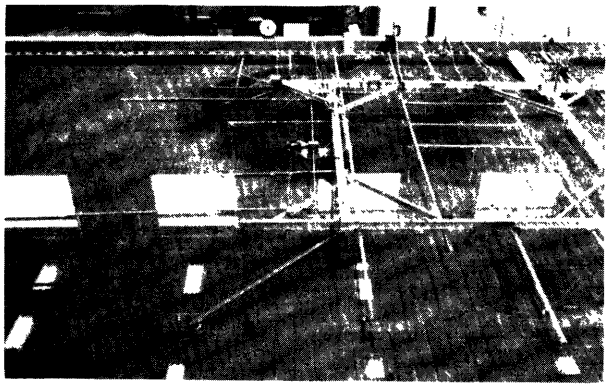

time= 10 min.

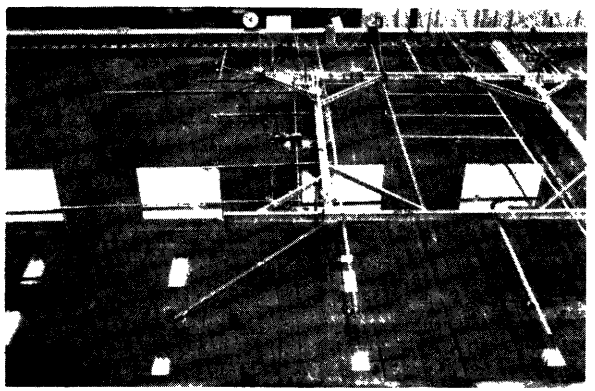

time= 20 min.

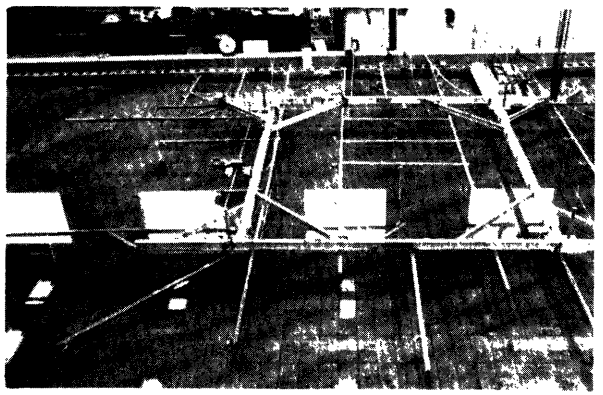

time= 50 min.

Fig. 8-10 b) Recorded dye patterns (long diffuser: Run FF29)

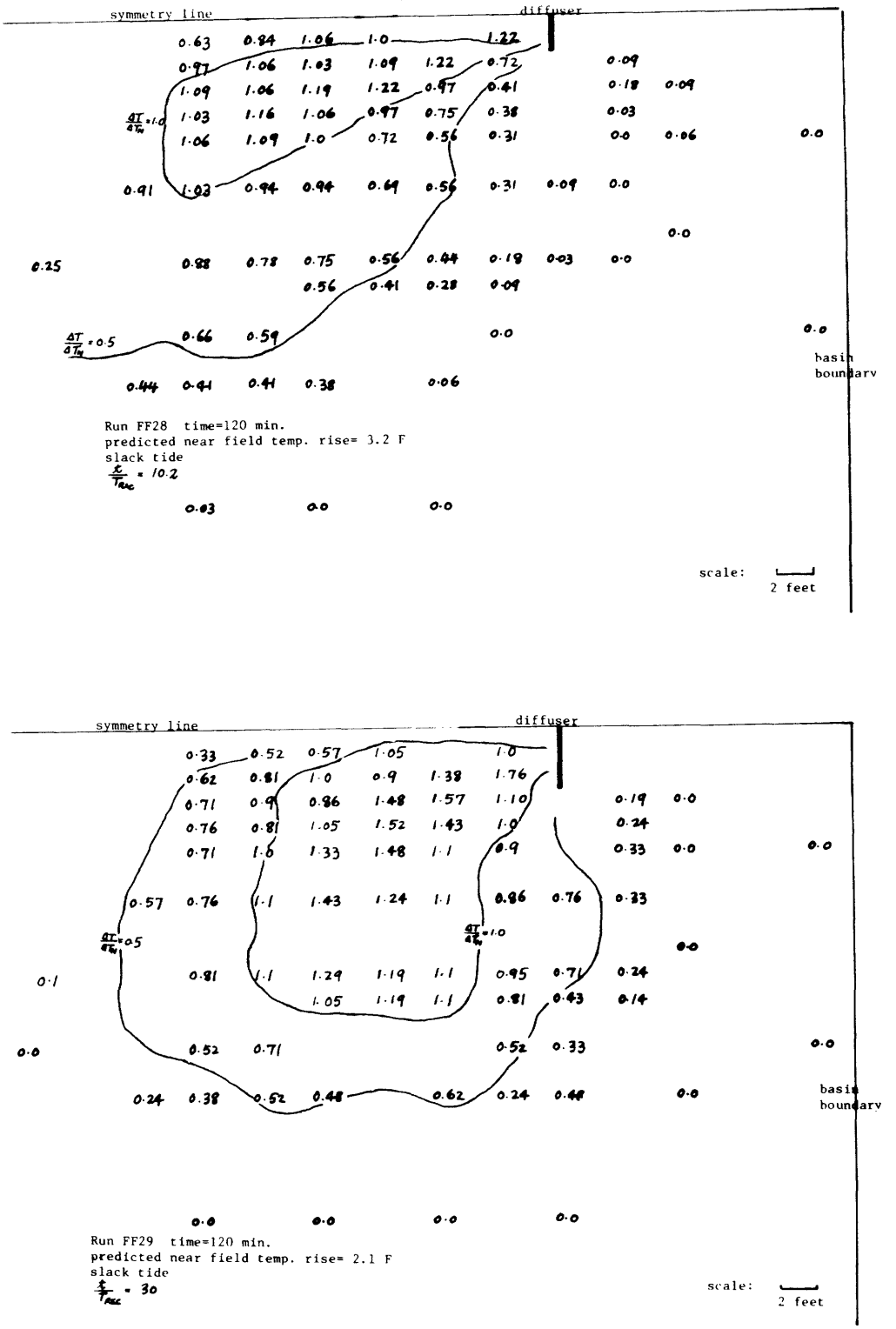

Fig. 8-11 Recorded normalised excess temperature field, (short vs long diffuser)

we have

$$L_{REC} = 1.5 \text{ miles}$$

Also the time scale of recirculation, T_{REC}, can be computed by eq. 8.2. For small diffuser flows and small initial near field dilution, for example.

$$S = 5$$

$$Q_o = 1000 \text{ cfs}$$

we have

$$T_{REC} = 71 \text{ hour}$$

For large diffuser flows and large initial near field dilution, for example,

$$S = 10$$

$$Q_o = 3000 \text{ cfs}$$

we have

$$T_{REC} = 11.8 \text{ hr.}$$

Thus at a given site, a larger diffuser flow and larger initial back entrainment is characterised by a smaller time scale of recirculation i.e. relatively stronger heat recirculation effects. Also for a given discharge flow, a longer diffuser (everything else kept constant) would have a shorter time scale of recirculation as

$$T_{REC} \sim \frac{1}{S} \sim \frac{1}{\sqrt{L_D}} \qquad \text{(cf. eq.8.2, 3.41);}$$

these considerations were demonstrated with relation to the laborabory tests as discussed in section 8.2.3.

In general, for any given situation, L_{REC} and T_{REC} can be estimated using eq. 8.1, 8.2 respectively. Based upon the frequency and duration of slack in a prototype situation, the importance of heat recirculation can then be assessed. Fig. 8-8 can also be used to estimate the heat build-up in the near field.

8.3.2 Design of Models

In the laboratory, for undistorted models that preserve dynamic similitude of the near field, the friction factor is not scaled properly. Laminarity of flow in the model tends to pronounce frictional effects. Thus stronger recirculation is observed in the physical scale model than in the prototype,i.e.

$$\frac{(L_{REC})\ \text{prototype}}{(L_{REC})\ \text{model}} = \frac{\ell_r (f_o)\ \text{prototype}}{(f_o)\ \text{model}}$$

where ℓ_r; length scale ratio of prototype to model.

For example, using typical values of

(f_o) model = 0.035

(f_o) prototype = 0.02

the scale of recirulation L_{REC} is overestimated by 50% in the laboratory.

For a given site, if it is desired to test diffuser induced heat recirculation in a hydraulic scale model, eq. 8.8 can be used to establish the minimum model scale ratio to be used.

By preserving Froude similitude in the prototype and model we have

$$\frac{(V)\ \text{model}}{(v)\ \text{prototype}} = \frac{1}{\sqrt{\ell_r}}$$

where V: characteristic velocity

Then for the hydraulic scale model

$$L_{REC} = \frac{0.088\left(\frac{u_o}{\sqrt{\ell_r}}\right)\left(\frac{H}{\ell_r}\right)^2}{\nu S}$$

$$= 0.088\ \left(\frac{u_o H^2}{\nu S}\right)_{prototype} \ell_r^{-5/2} \qquad (8.9)$$

For any given diffuser design and L_{model}, the appropriate length scale ratio can be chosen using eq. 8.9.

Using typical values of

u_o = 20 fps

H = 20 ft.

S = 10

ℓ_r = 100

we have

L_{REC} = 70 ft.

At this ratio, only by using model basins 200 feet or longer can diffuser induced heat recirculation be tested.

CHAPTER IX

DESIGN APPLICATION

In this chapter, the theoretical results presented in the previous chapters are interpreted from the viewpoint of practical design of thermal diffusers for once through cooling systems. First, a brief overview of diffuser design is given. Second, general features of diffuser performance for various designs are discussed for two cases of fundamental interest. Finally, an ecological interpretation of the model predictions is advanced, and prototype considerations are made.

9.1 Diffuser design in shallow water: a general discussion

At a particular site and for a given plant capacity, the design objective is often to meet state or Federal thermal standards. These standards can be either quantitative (e.g., the allowable extent of an isotherm area) or qualitative (e.g., siting to locate the discharge away from fish spawning areas, making provisions for zones of passage for marine organisms) in nature. The final design is based on the evaluation of the impact of the complicated interaction of a multitude of factors--frequency, magnitude and direction of the prevailing currents, topography and hydrography of the site, the type of organisms that are to be protected, and economic considerations.

It was pointed out in Chapter II there are three basic types of multiport thermal diffusers: alternating diffusers, staged diffusers, and unidirectional diffusers. Depending on the plant design and the nature of the ambient current, one type of

diffuser may be preferable to the other. For example, in a tidal situation, it may be desirable to use an alternating diffuser with no directional momentum input, whereas in the case of currents predominantly in one direction, either a staged or unidirectional diffuser may be more preferable. The details of the general design philosophy can be found in Ref. 15

In many instances, and especially for well designed diffusers, the temperature reduction in the presence of an ambient current is greater than the case of no current. Thus the stagnant water condition is often chosen as the worst or design condition upon which general design principles and first estimates of design values can be drawn.

The comments in the ensuing discussion in this chapter are limited to unidirectional diffusers, which are particularly applicable in shallow coastal waters.

A unidirectional diffuser inputs large momentum in one direction; it is effective in minimizing the area of mixing zones of elevated temperatues, and directing the thermal effluent offshore.

9.1.1 Design Alternatives

For a given plant capacity, the heat rejection rate is fixed; thus $Q_o \Delta T$ is constant. The design variables are

Q_o condenser flow

ΔT_o condenser temperature rise

L_D diffuser length

u_o nozzle velocity

N number of nozzles

a_o port area

H water depth at discharge

Many design alternatives can be explored. We may reduce ΔT_o to increase Q_o. Increasing Q_o can mean either 1) increasing the number of ports and hence L_D, keeping s and u_o constant, or 2) increase u_o, keeping the same number of ports and hence L_D constant, increase the port area a_o so that the number of ports and hence the diffuser length L_D is decreased - the condenser flow Q_o being fixed.

In the next section two design cases of fundamental interest are discussed. Design alternatives can be understood in terms of these two cases.

9.2 Design interpretation of theoretical predictions

General features of diffuser plume characteristics can be extracted by examining the theoretical solution given in Chapter IV. It is possible to interpret eq. 4.52, 4.53 from a design point of view. We have seen from eq. 4.19-4.20, 4.28-4.29, that for $\gamma=0$, the solution is dependent on $\frac{L_D H}{N a_o}$ - a near field parameter, and $\frac{L_D}{H}$, the relative diffuser length. For a specific site, we can

think of Q_o, ΔT_o, H as fixed. The near field temperature rise ΔT_N is given by

$$\Delta T_N = \frac{\Delta T_o}{S} = \frac{\Delta T_o}{\sqrt{\frac{L_D H}{2Na_o}}} \qquad (9.1)$$

Since $Q_o = Na_o u_o$, by definition, eq. 9.1 can be written as

$$\Delta T_N = \frac{\Delta T_o}{\sqrt{L_D u_o (\frac{H}{Q_o}) 0.5}} \qquad (9.2)$$

Thus for a specific site and plant design, ΔT_N is dependent only on the diffuser length L_D and the nozzle velocity u_o.

Given L_D, u_o, the details of the design - s,N,a_o can be determined by

$$(N-1)\ s = L_D \qquad (9.3)$$

$$N\ a_o = \frac{Q_o}{u_o} \qquad (9.4)$$

Given eq. 9.3 and 9.4, an arbitrary choice can be made for any of the three variables s,N, and a_o. Thus in principle we can choose s sufficiently small to approximate a line source of momentum, and then a_o and N are determined accordingly.

For purposes of discussion, the design values for a 2410 MWe power plant in shallow water - the Perry Nuclear Power Plant on Lake Erie are chosen

Q_o = 2780 cfs

H = 19 ft.

ΔT_o = 28 ^{o} F

f_o = 0.02

Two cases of fundamental interest are considered:

9.2.1 Case A: Effect of diffuser length for fixed discharge velocity

The nozzle velocity u_o is fixed and $\frac{L_D}{H}$ is varied. As shown by Eq. 9.2, a longer diffuser is more efficient in near field mixing. The intermediate field performance, however, can be contrasted to elucidate the tradeoff between a longer diffuser and a shorter one in the entirely fully mixed region.

Fig. 9-1 illustrates comparisons of variables of interest for four cases with

$$u_o = 20 \text{ fps}$$

$$\frac{L_D}{H} = 10,\ 20,\ 40,\ 60$$

The nozzle diameter D_o is fixed at 2 feet.

Fig. 9-1 a) illustrates the variation in centerline temperature rise with x. It can be inferred from the temperature drop that a longer diffuser induces more back entrainment, whereas the shorter diffuser entrains more flow in the intermediate field The ultimate ΔT at large distances is similar.

Fig. 9-1 b) shows the variation of centerline velocity $u_c(x)$ with distance from the diffuser. u_c increases in the near field due to inertial acceleration and then decreases due to side entrainment and momentum loss. A shorter diffuser induces less near field mixing and hence leads to a more pronounced velocity field.

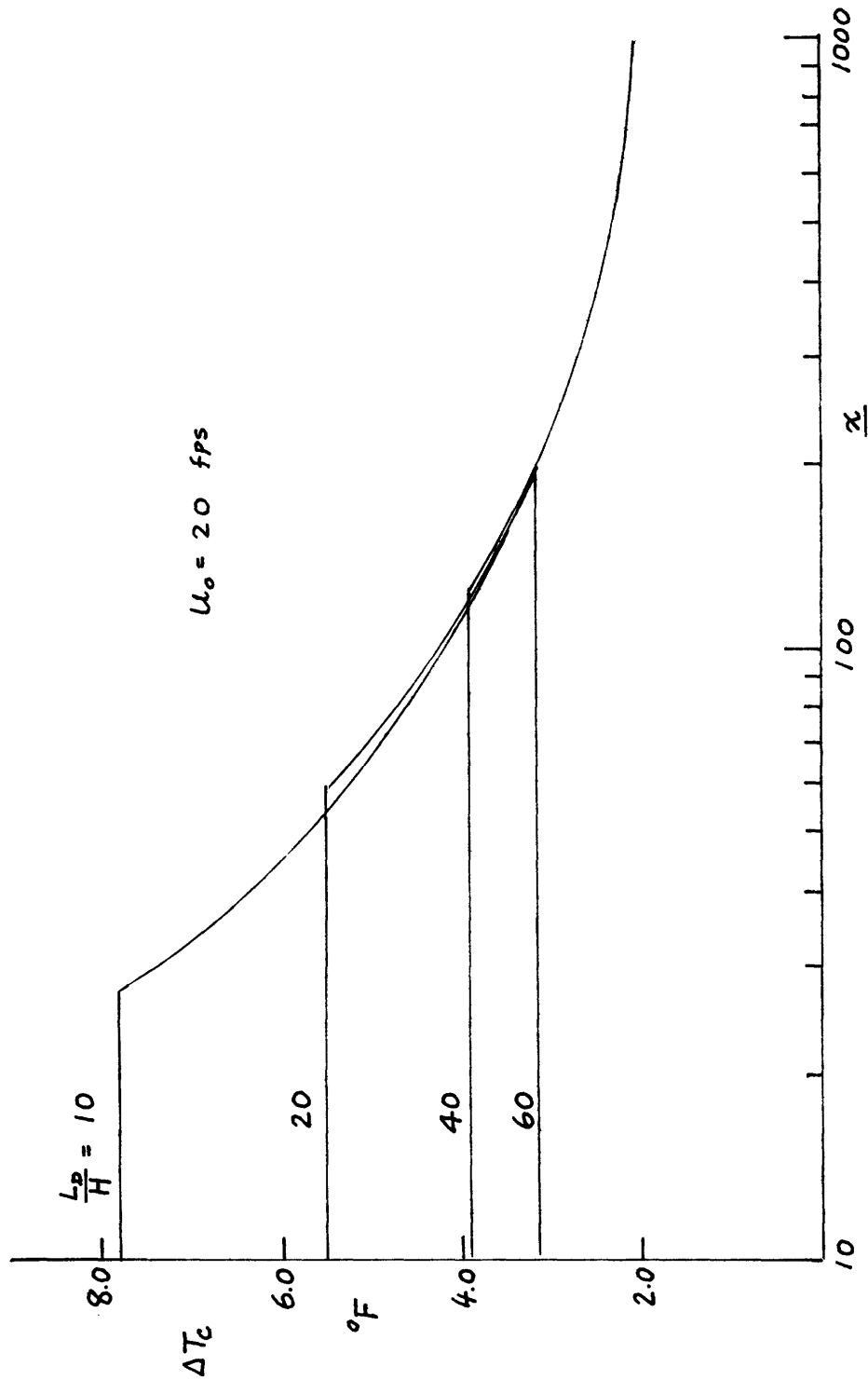

Fig. 9-1 a) Centerline temperature rise along the diffuser plume: Design comparisons (Case A)

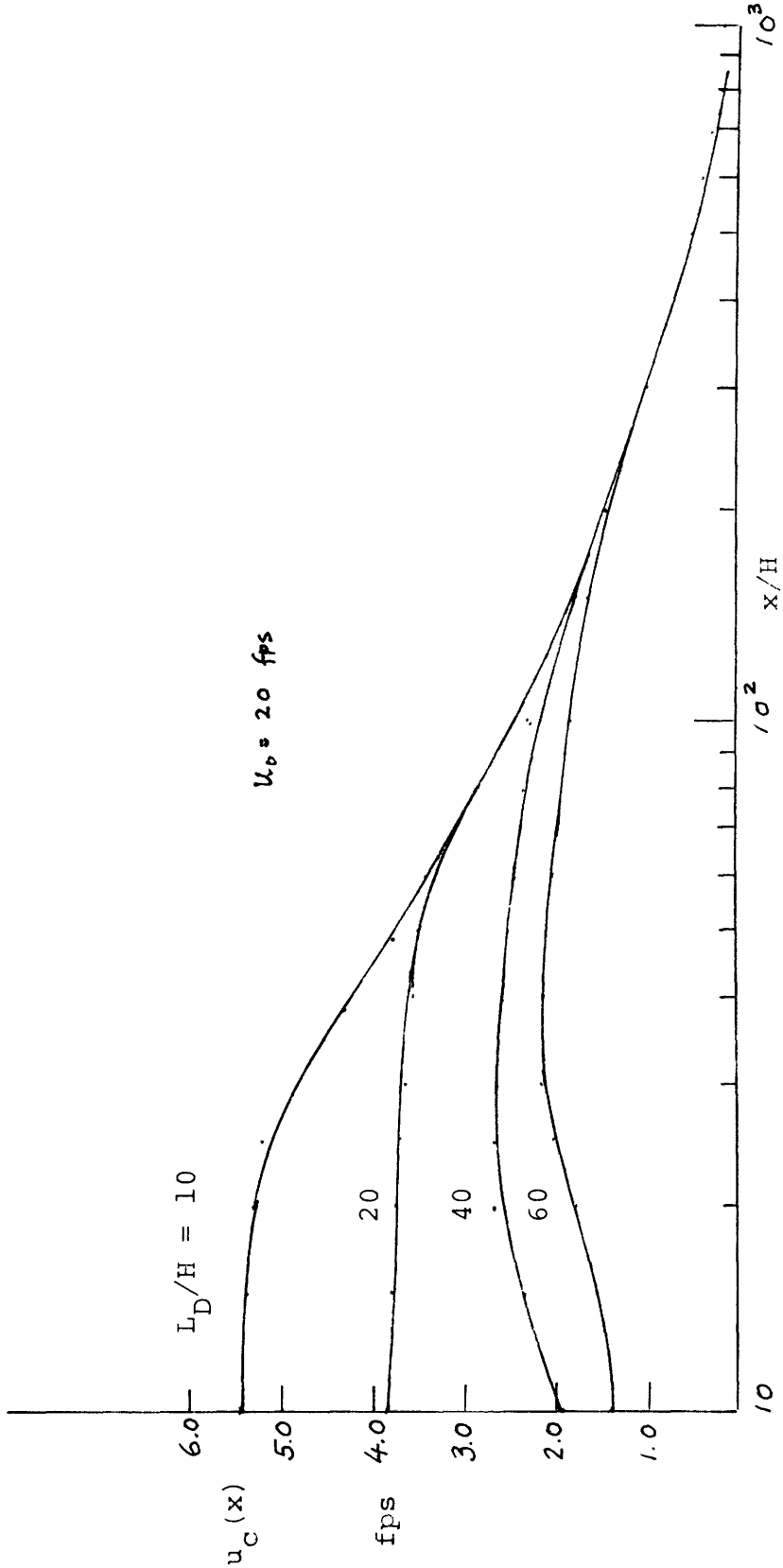

Fig. 9-1 b) Centerline velocity along the diffuser plume: Design comparisons (Case A)

Fig. 9-1 c) shows the shape of the diffuser plume. The longer diffuser starts out a wider plume, but the rate of increase of the shorter diffuser plume is greater by virture of its larger capacity to entrain.

Fig. 9-1 d) shows the areas within surface isotherms for different diffuser designs. For a given diffuser design the area within a ΔT^{o} F surface isotherm is meaningfully defined only for

$$\Delta T_{\infty} < \Delta T \leq \Delta T_{N}$$

where ΔT_N is the near field temperature rise as given in Section 4.1.1; $\Delta T_N = \frac{\Delta T_o}{S}$, S being given by Eq. 3.41. ΔT_∞ is the asymptotic temperature rise given by eq. 4.54. As pointed out in Section 4.3.2, this is a measure of the mixing capacity (total induced flow) of any unidirectional diffuser. For the range of temperatures when the different diffuser designs overlap, the A_s vs ΔT functions are virtually indistinguishable. This means that if the criterion of interest is a relatively low temperature isotherm (e.g. the 3^{o}F isotherm), a shorter diffuser might be as satisfactory as a diffuser twice as long.

Fig. 9-1 e) shows the travel time along the centerline as a function of ΔT_c; this is a characteristic measure of the time history of exposure to elevated temperatures for aquatic organisms entrained into the diffuser induced flow. It can be seen that the thermal impact of short vs long diffusers on an entrained organism is intimately related to the ability of the organism

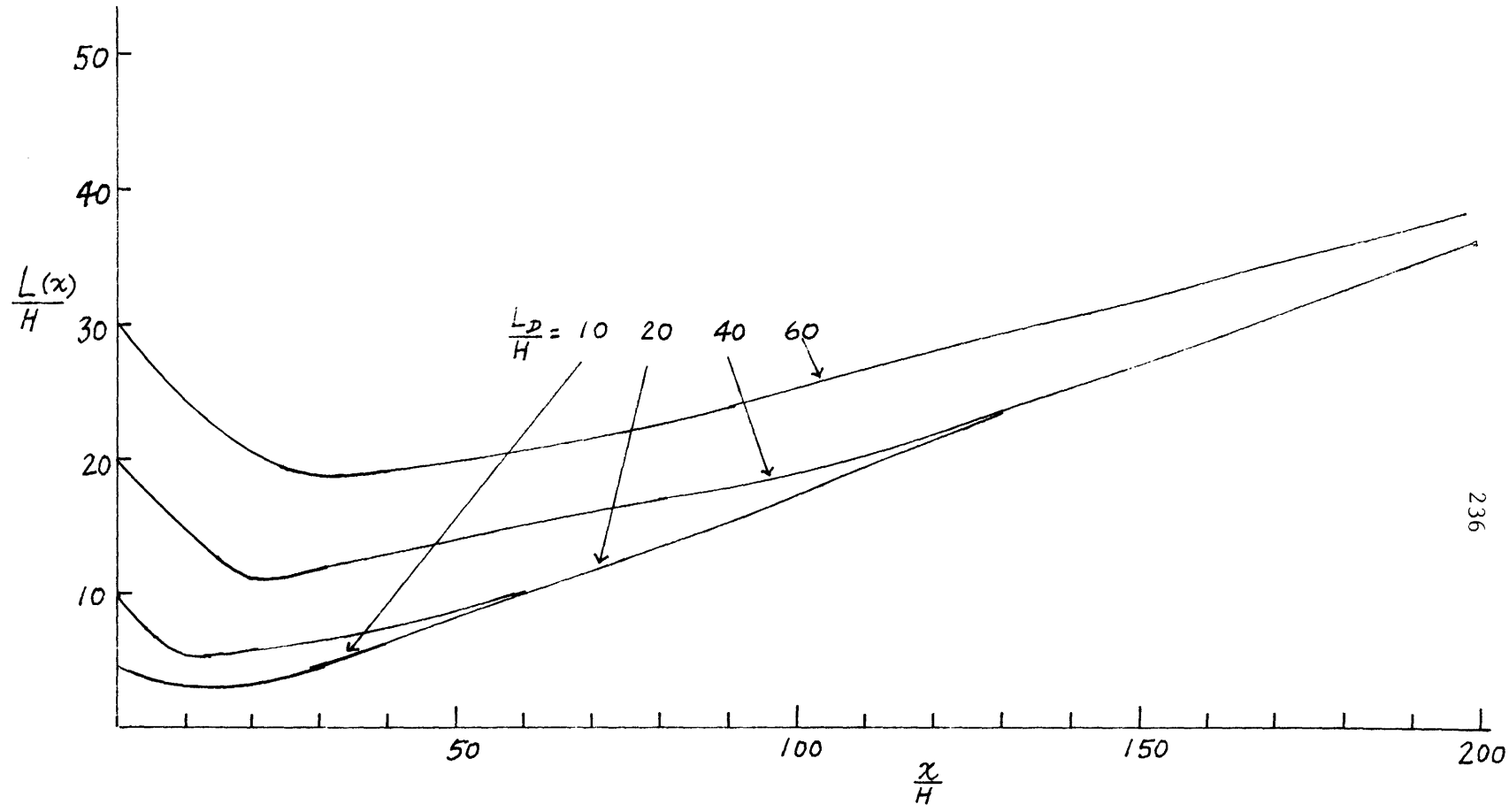

Fig. 9-1 c) Diffuser plume width:
Design comparisons (Case A)

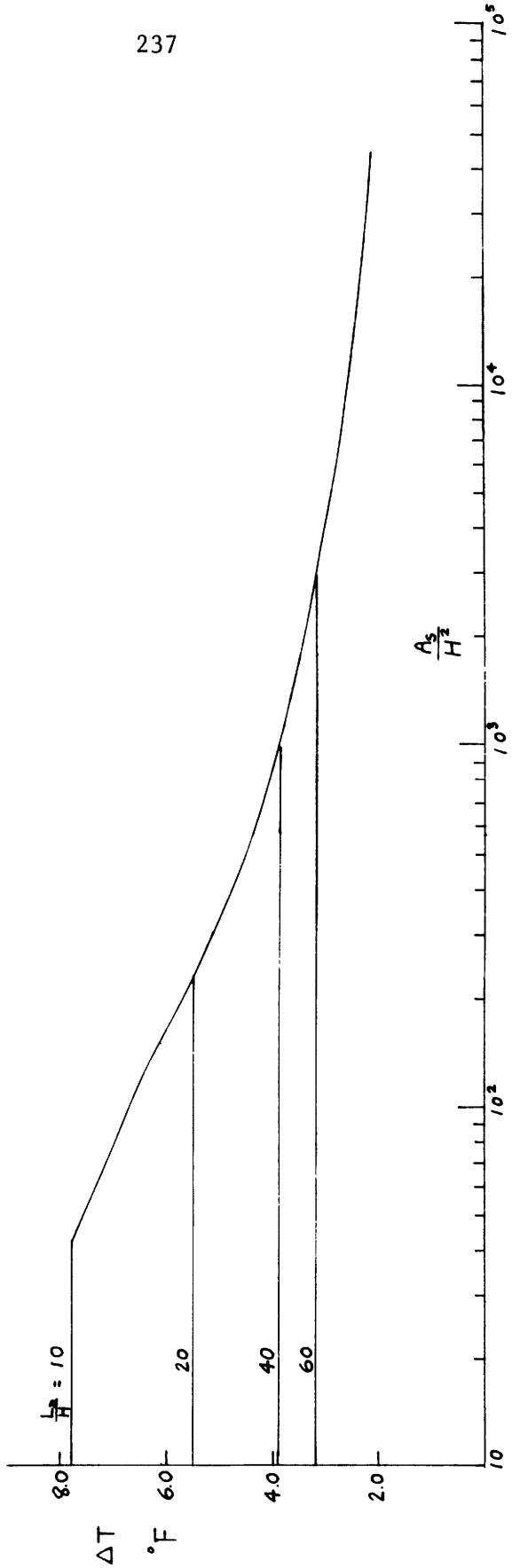

Fig. 9-1 d) Area within surface isotherms:
Design comparisons (Case A)

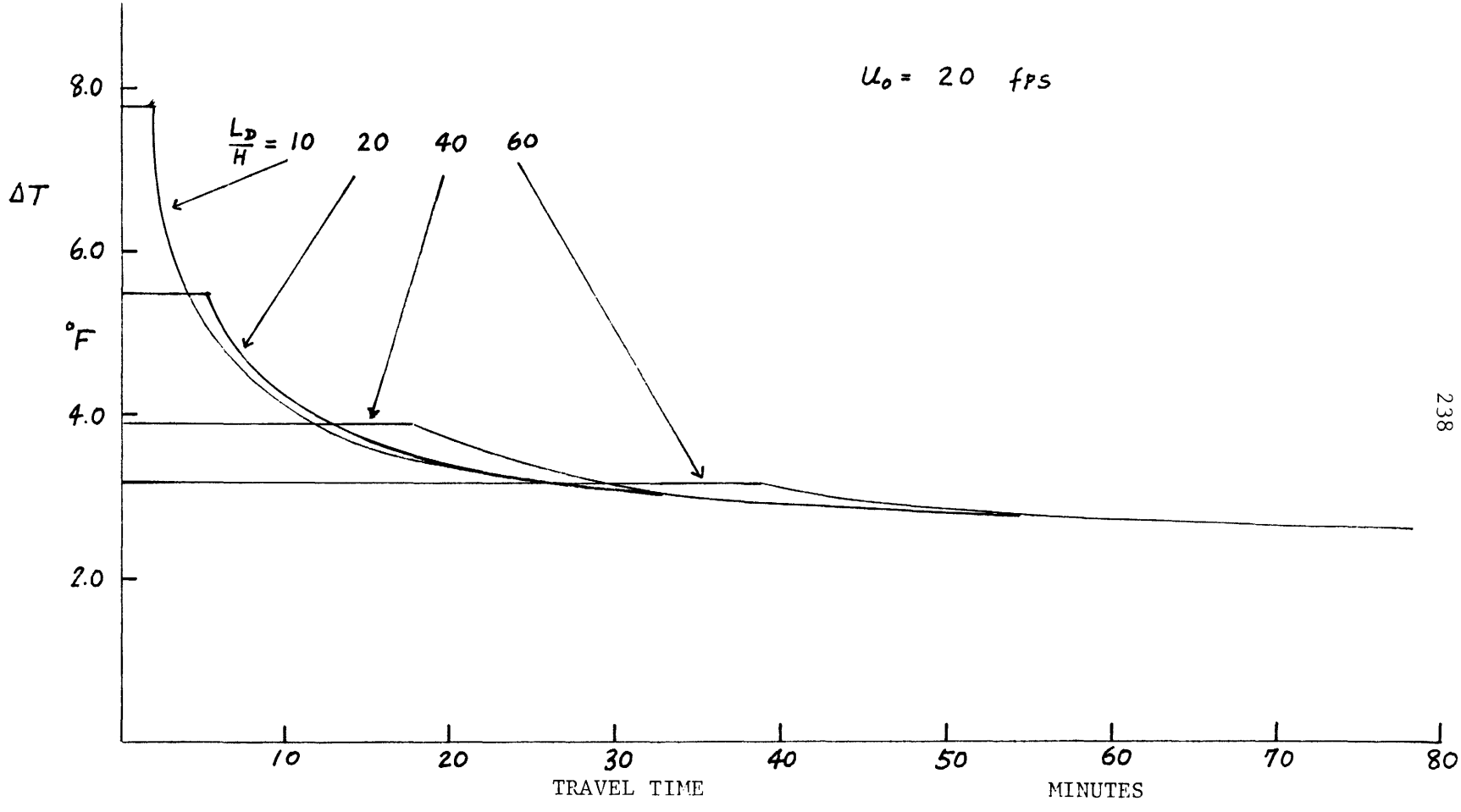

Fig. 9-1 e) Time History of exposure to elevated temperatures for entrained organisms: Design comparisons (Case A)

to withstand high temperature rises for small durations. This is discussed in greater detail in the next section.

As a check against the assumption of a two dimensional friction jet, the densimetric Froude number based on the water depth $F_H = \frac{u_x(x)}{\sqrt{g\beta_2 \Delta T_c H}}$ is plotted vs x/H in Fig. 9-1 f). It can be seen $F_H > 1$ up to x/H = 600. The essential features revealed by this model are thus consistent with the exclusion of buoyancy effects. (see section 4.3.2).

In summary, one striking feature that is common to all the physical variables of interest is that <u>beyond a distance of $\sim 10^2 H$ the effect of the diffuser length is no longer felt.</u> Short diffusers with its more concentrated momentum flux, make up for its lesser near field mixing capacity by entraining more ambient flow in the intermediate field. The results also support the two dimensional boundary layer type approximation for a region large enough to reveal the essential characteristics of the diffuser plume.

9.2.2 Case B: Variable discharge velocity and diffuser length with constant near field dilution

In this case we study the tradeoff between increasing u_o and decreasing L_D. Fig. 9-2 compares the thermal impact of five diffuser designs in which u_o varies from 15 fps to 45 fps. L_D/H is proportionally decreased from $\frac{L_D}{H} = 60$ to $\frac{L_D}{H} = 20$ so that $L_D u_o$ stays constant. Thus the near field dilution is not changed (cf. eq. 9.2) and the global performance can be compared.

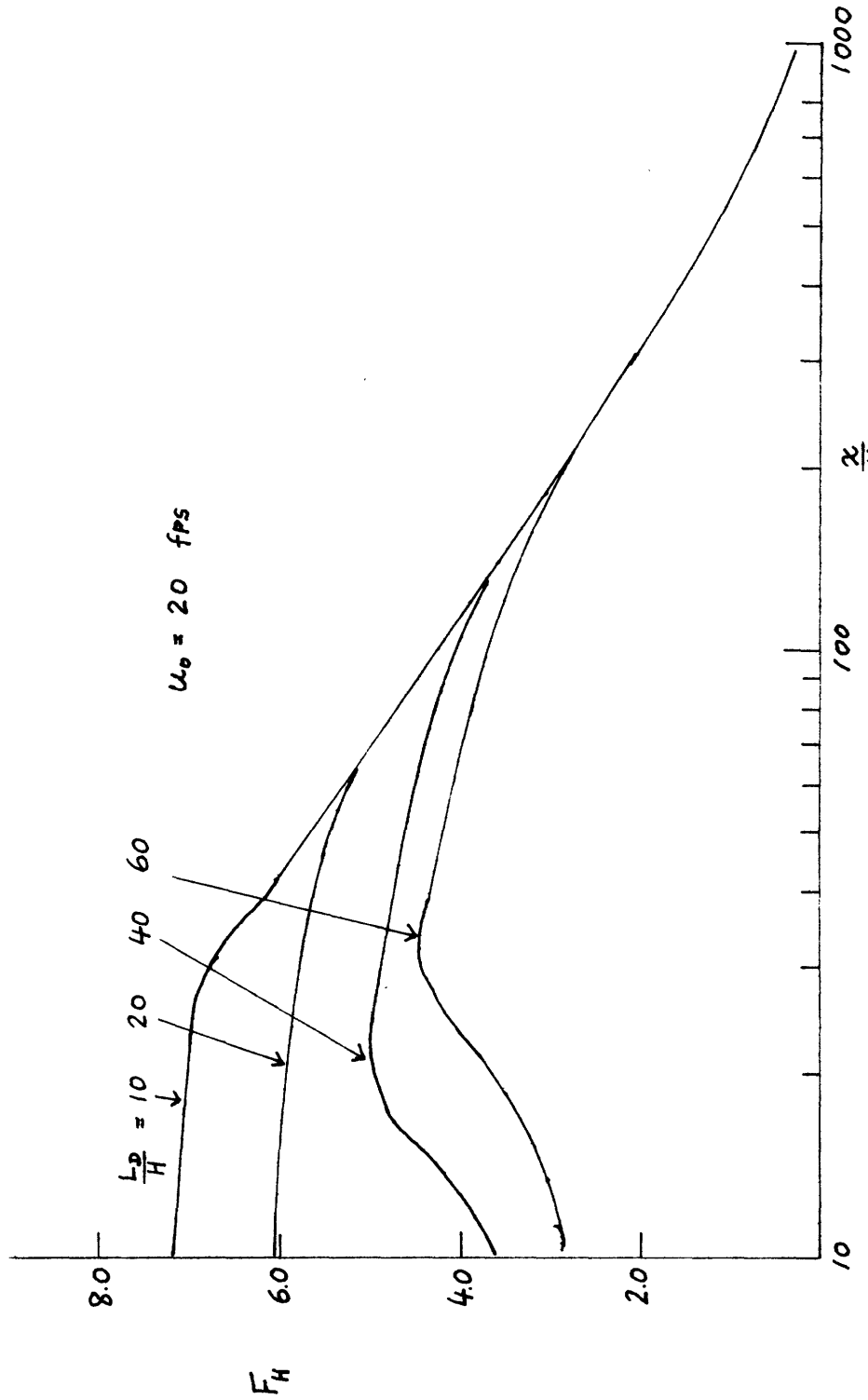

Fig. 9-1 f) Densimetric Froude number along the diffuser plume: Design comparisons (Case A)

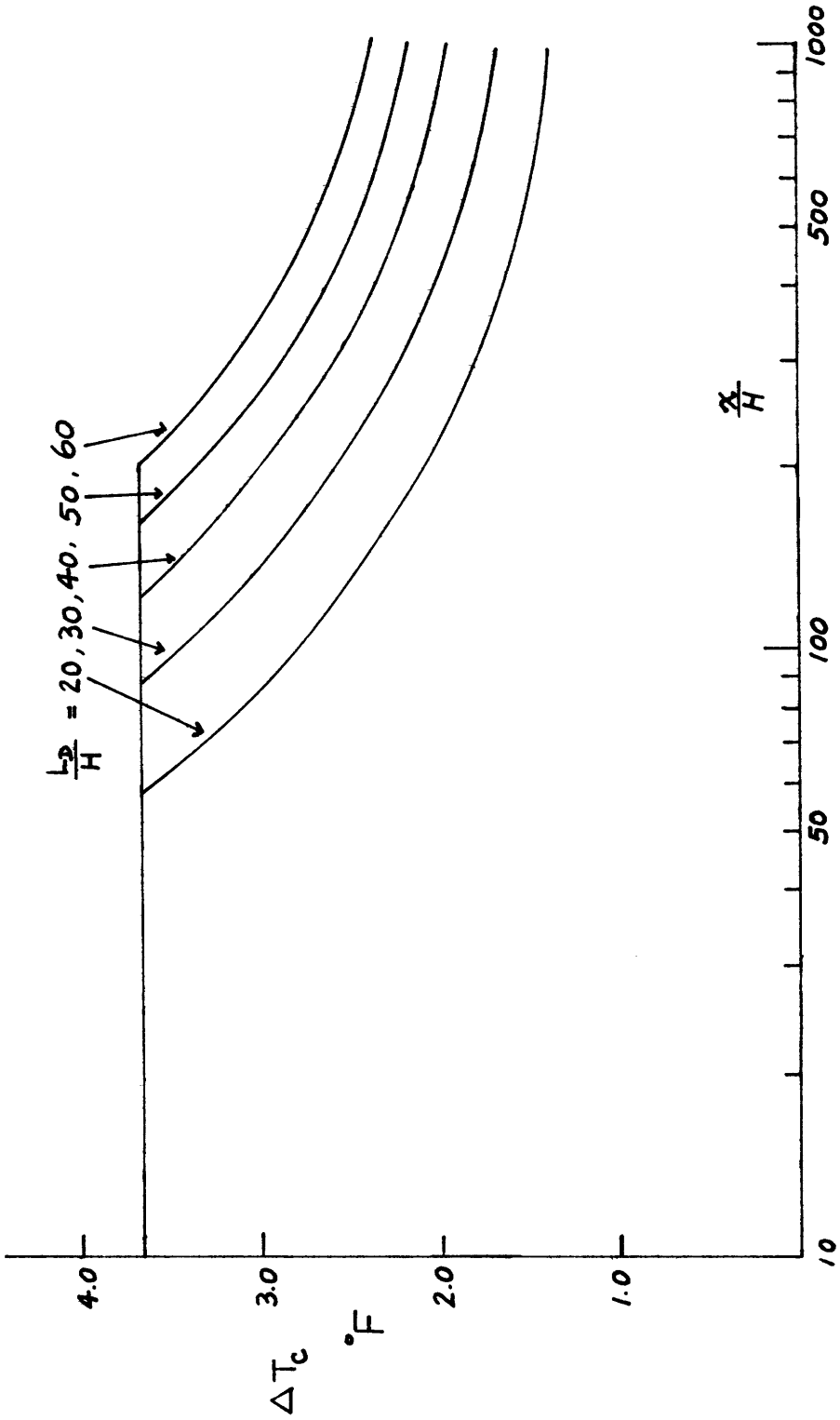

Fig. 9-2 a) Centerline temperature rise along the diffuser plume: Design comparisons (Case B)

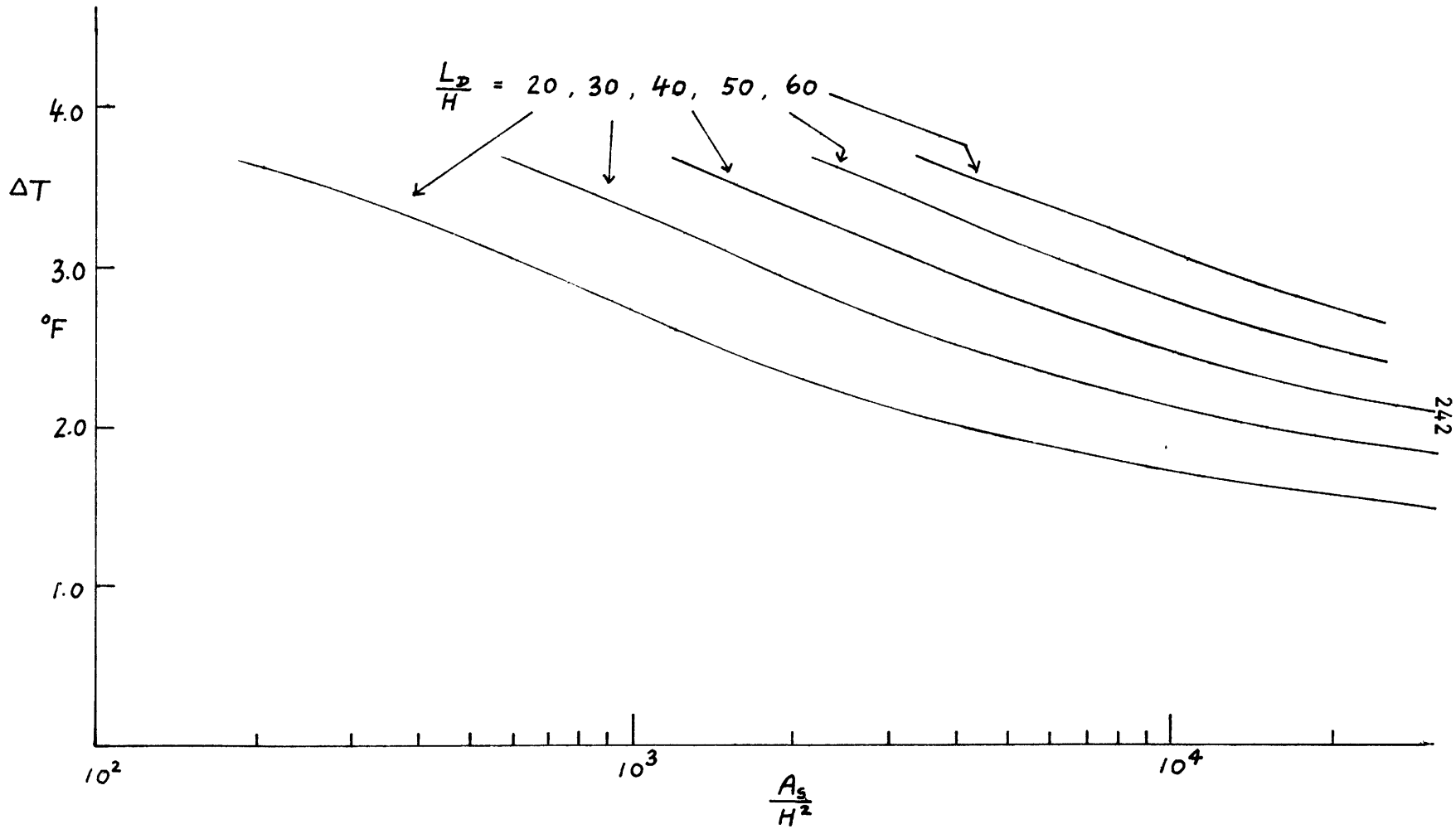

Fig. 9-2 b) Area within surface isotherms:
Design comparisons (Case B)

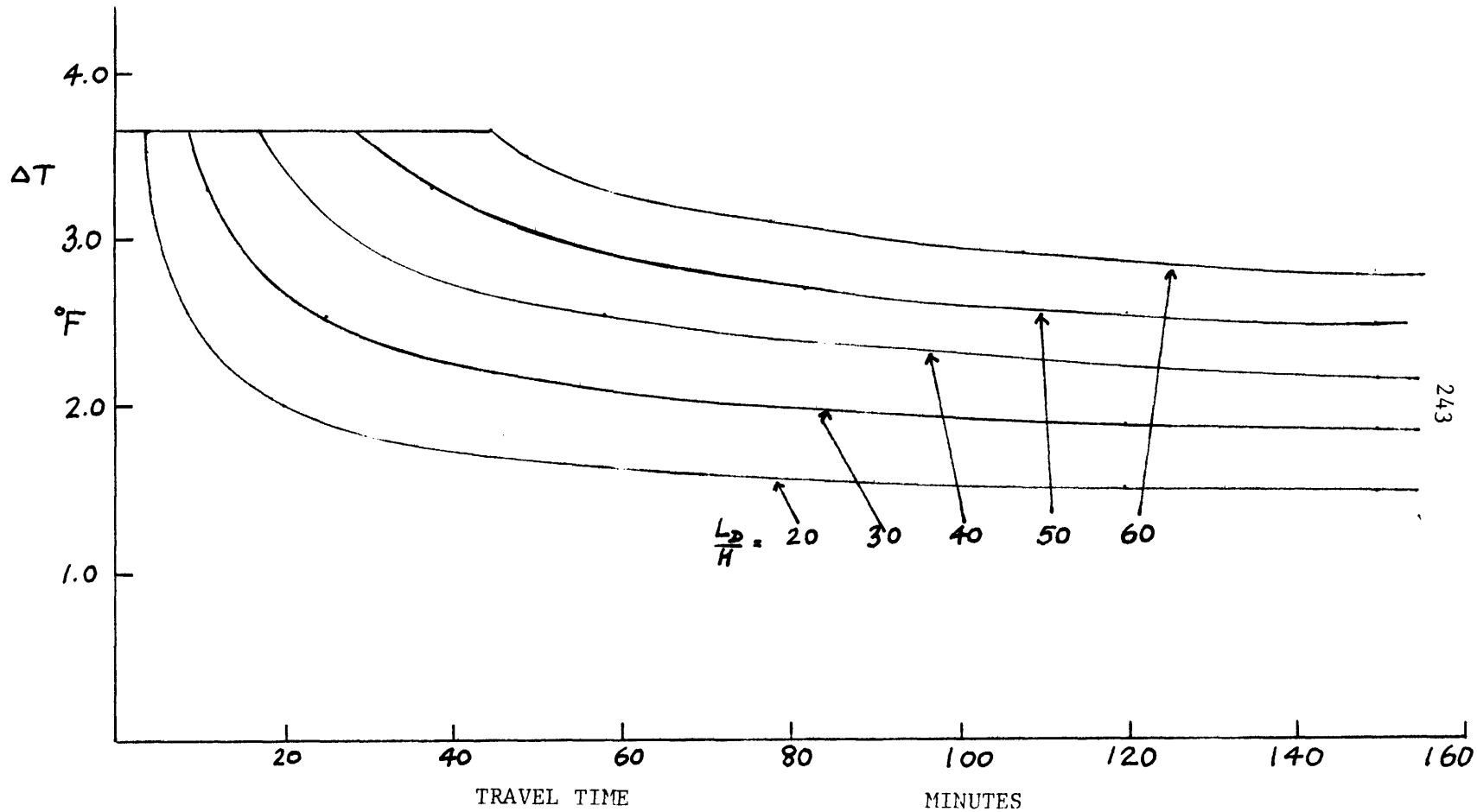

Fig. 9-2 c) Time History of exposure to elevated temperatures for entrained organisms: Design comparisons (Case B)

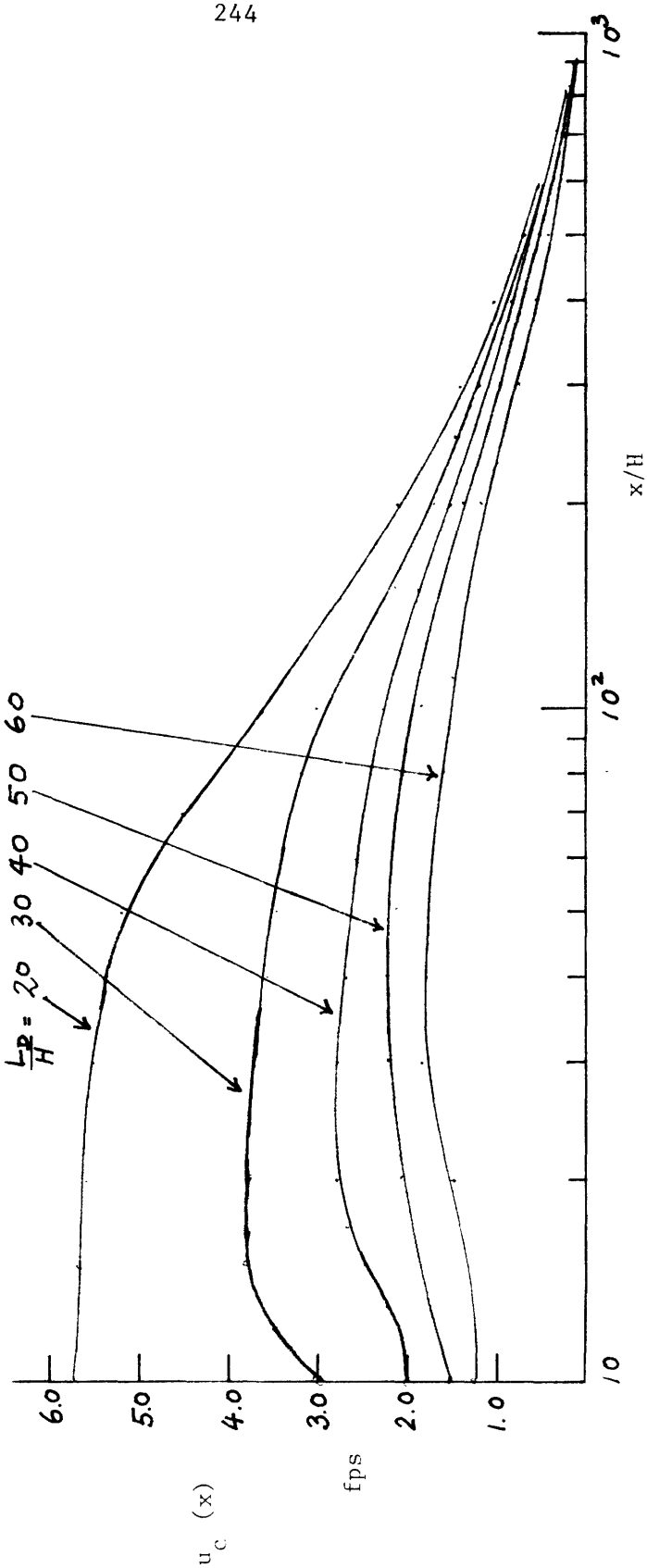

Fig. 9-2 d) Centerline velocity along the diffuser plume: Design comparisons (Case B)

The five designs correspond to

$\frac{L_D}{H}$	u_o fps
60	15
50	18
40	22.5
30	30
20	45

It can be seen from Fig. 9-2 a,b,c,d that by increasing the discharge velocity (keeping a_o constant and just decreasing N and hence L_D), a significant decrease is obtained both in terms of centerline temperature rises and areas of different surface isotherms. Comparing the $\frac{L_D}{H} = 60$ case and the $\frac{L_D}{H} = 30$ case, for example, an order of magnitude decrease in the area within the 3F isotherm is achieved by increasing u_o from 15 fps to 30 fps.

Fig. 9-2 d. shows, on the other hand, the increasing velocities which are induced by the shorter diffusers with higher discharge velocities.

9.3 Diffuser performance and aquatic environmental impact

Thus far, the comparison of diffuser designs have been presented in terms of centerline temperature rises, centerline velocities, and different isotherm areas in the previous sections. In addition to this type of Eulerian description, it may be desirable for purposes of quantifying the environmental impacts

of different diffuser designs to display the model predictions in an alternative manner that may provide more direct answers to questions of interest to the aquatic biologist, such as: What do these results mean in terms of the organisms that are entrained into the diffuser plume? Is there a quantitative measure for the total number of organisms that will be affected? What is the distribution of heat to which various portions of the aquatic population will be exposed, and for how long? (Fig. 9-3)

In this section we attempt to translate the model results to a form that could be of more potential use for biologists and decision makers. Diffuser performance is compared on the basis of "ecological histograms" which capture information from both the temperature and velocity field on one diagram.

To fix ideas, the concept is illustrated with reference to the same two design cases presented in Section 9.2.

In the following the basic assumption is made that the number of aquatic organisms entrained into the diffuser plume is proportional to the induced flow.

9.3.1 Case A: Comparison of ecological performance: variable diffuser length at fixed discharge velocity

We recall in this case the nozzle velocity is fixed at u_o = 20 fps and only the diffuser length L_D is varied. Let us compare the $\frac{L_D}{H}$ = 60 and $\frac{L_D}{H}$ = 20 designs. The asymptotic dilution achieved for the two cases is about the same

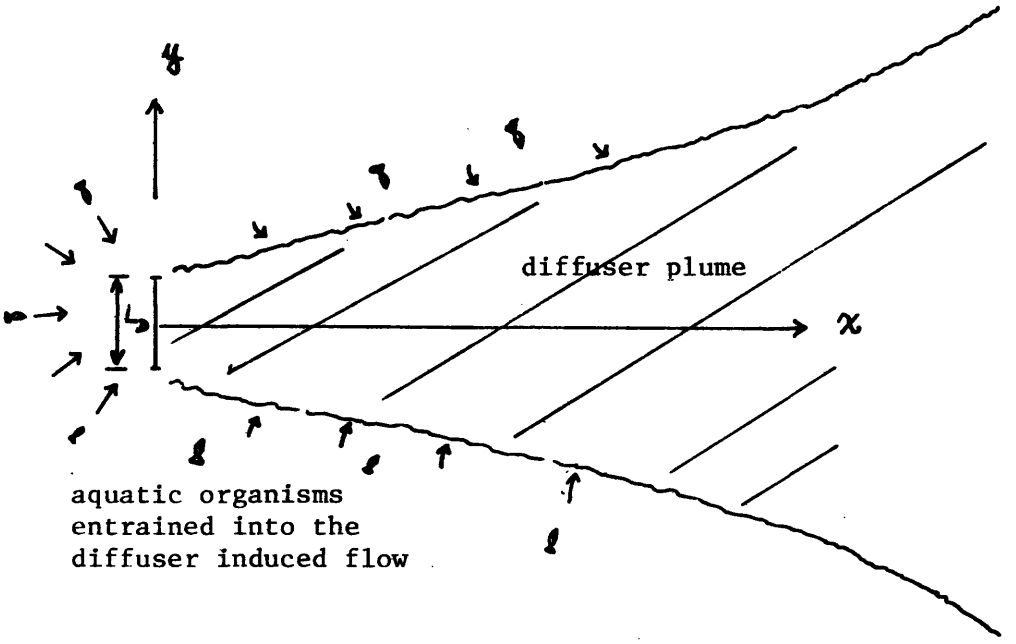

Fig. 9-3 An ecological interpretation of diffuser performance

(cf. Fig. 9-1 a): thus the total number of organisms that will be entrained into the diffuser plume will be the same. However, different proportions of this number of organisms will experience different temperature rises for different durations.

In Fig. 9-4 we plot a histogram of induced flow per unit distance/total induced flow (in increments of 50 H) for the two designs. It can be seen, as in section 9.1, the shorter diffuser produces a more distributed kind of flow pattern. The back entrainment is larger for the longer diffuser, whereas the shorter diffuser entrains more flow in the intermediate field.

In Fig. 9-5 we plot a histogram of the fraction of the total number of organisms experiencing a maximum temperature rise in a certain range and its duration. Thus for the design

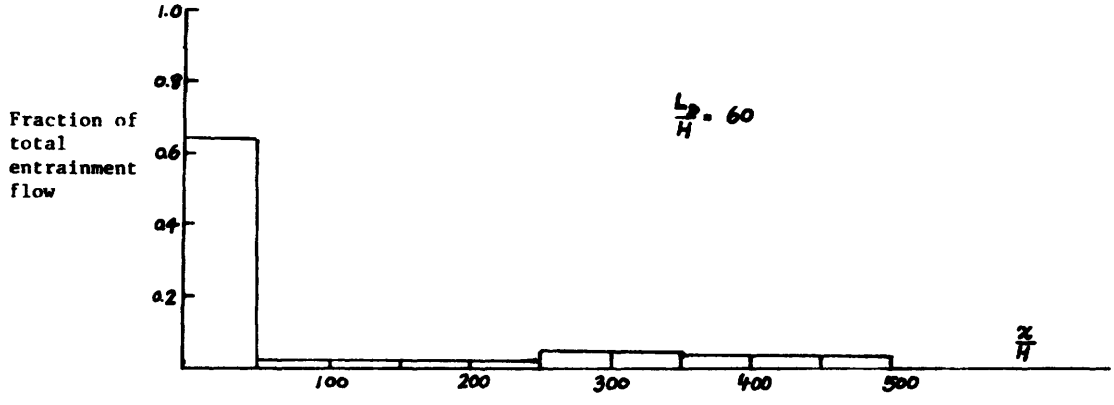

Fig. 9-4 Distribution of induced flow along diffuser plume

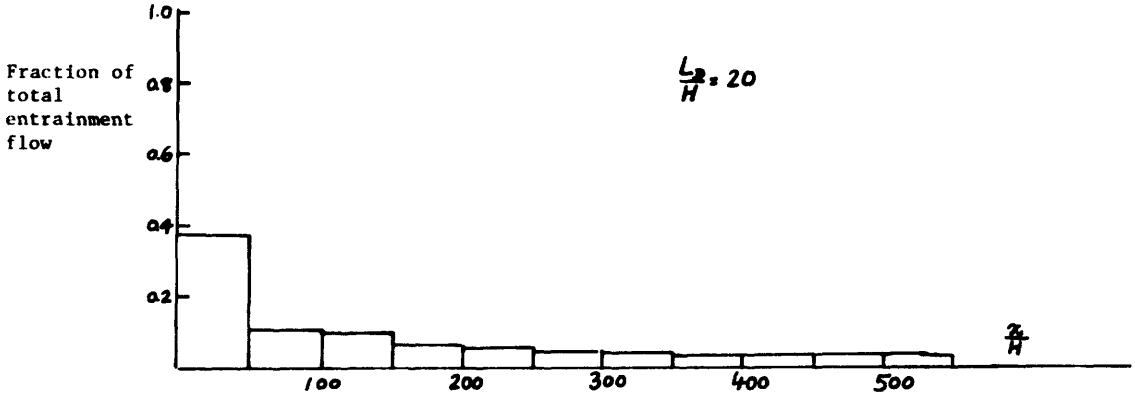

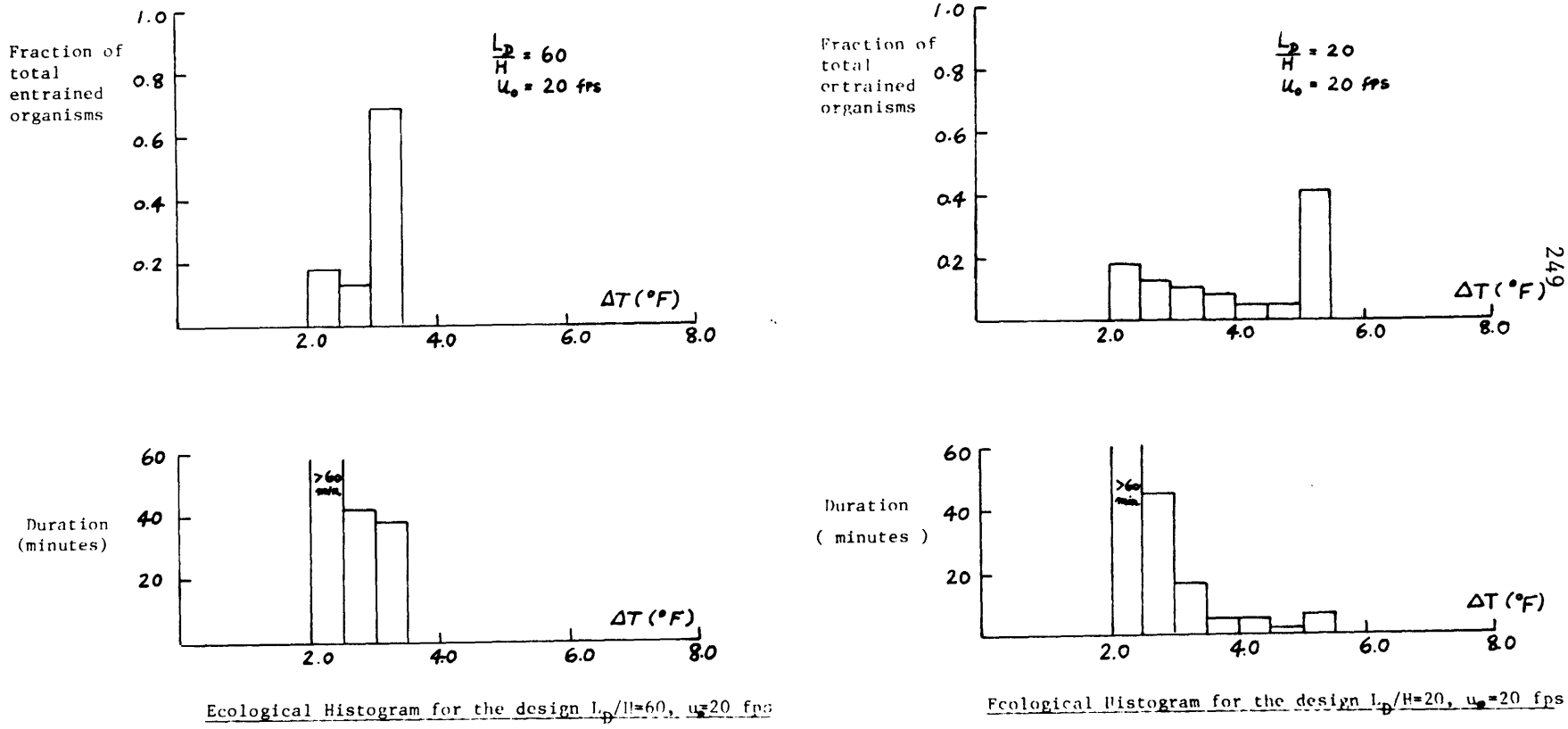

Fig. 9-5 Comparison of "ecological" performance of diffuser design: Case A

$\frac{L_D}{H}$ = 60, u_o = 20 fps, 70% of the entrained organisms will be exposed to a maximum temperature rise in the range of 3-3.5^oF for 38 minutes, 15% will experience a maximum temperature rise in the range 2.5-3^oF for 40 minutes, and the rest will experience a maximum temperature rise in the range 2-2.5^oF for longer than one hour. The "ecological tradeoff" of building a diffuser three times as short (and perhaps three times less costly) can then be interpreted as diverting a fraction of the entrained organisms (45%) to be exposed to higher maximum temperature rises (3.5-5.5F) for short durations (less than 10 minutes)

9.3.2 Case B: Variable diffuser length and discharge velocity at constant near field dilution

In this case when L_D is decreased u_o is increased to keep the near field dilution the same. We compare the two designs

i) $\frac{L_D}{H}$ = 60 u_o = 15 fps

ii) $\frac{L_D}{H}$ = 30 u_o = 30 fps

The total induced flow for these two designs is not the same as the asymptotic dilution is greater for the shorter diffuser (cf. Fig. 9-2a); thus the $\frac{L_D}{H}$ = 30, u_o = 30 fps design entrains a greater number of organisms. Using as base value the total number of entrained organisms for design i), we plot the same ecological histograms for the two designs. (Fig. 9-6). It can be seen for the higher velocity case the duration for the maximum temperature rise is reduced greatly (from e.g. 50 minutes to ten minutes for $3.5<\Delta T<4^oF$) at the expense of entraining a larger number of organisms at lower temperatures.

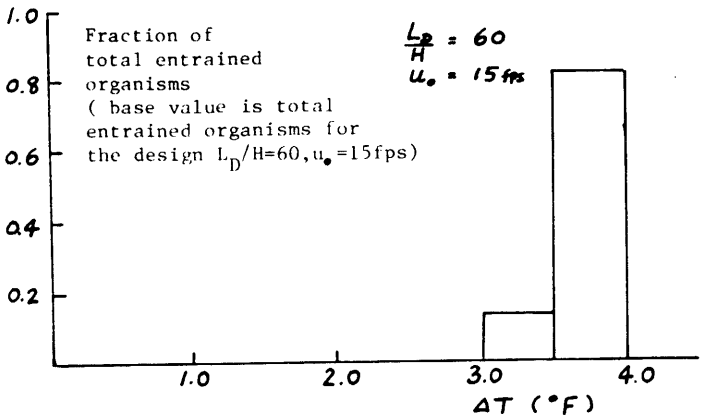

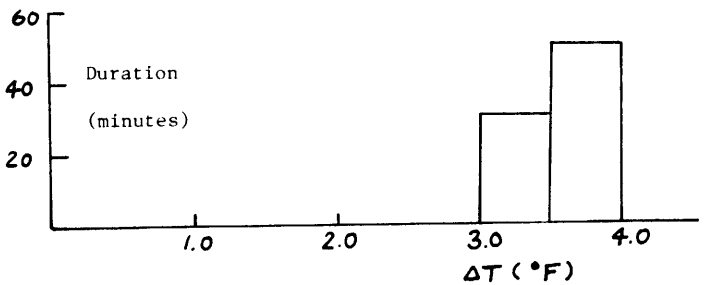

Ecological Histogram for the design $L_D/H=60$, $u_o=15$ fps

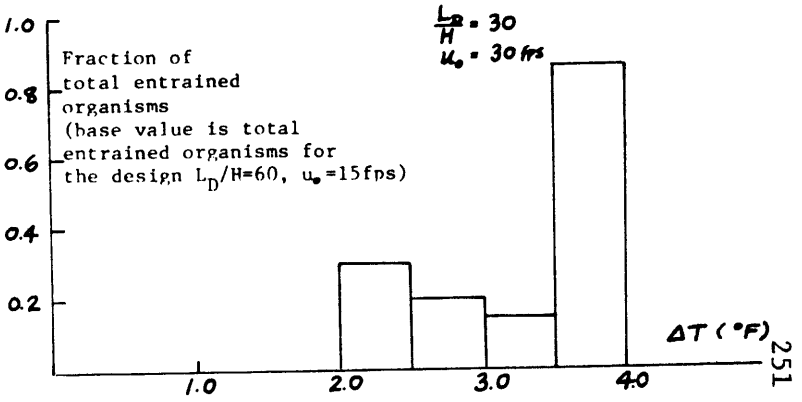

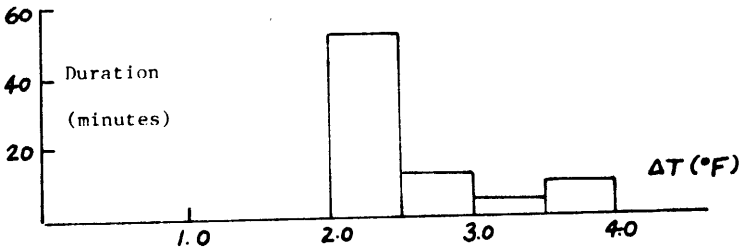

Ecological Histogram for the design $L_D/H=30$, $u_o=30$ fps

Fig. 9-6 Comparison of "ecological" performance of diffuser design (Case B)

9.3.3 Concluding Remarks

By presenting the results in this discretised fashion more information pertaining to possible ecological impact can be extracted in addition to other quantities previously adhered to: induced velocities, maximum temperature rise in the field, plume areas.

It should be pointed out the assumption of the quantity of entrained organisms being proportional to induced flow is only strictly valid for weak swimmers and drifting organisms, such as embryos and larvae of fish species. Aquatic organisms circulated through the power plant are not accounted for in the ecological histograms, as their inclusion would involve the consideration of many site specific conditions: intake design, condenser flow, length of connecting piping to the discharge structure, etc. Furthermore, the number of organisms actually pumped through the plant at much higher temperatures than ΔT_N is a small percentage of the total number of organisms affected, the ratio being characterised by $1/S_\infty$. In case A, for example, $S_\infty = 15$, and the ratio is 0.067.

The concept outlined in this section can be extended to other types of heat dissipation schemes (e.g. surface discharges) as well as other sources of pollutant (e.g. chlorine and copper), provided the initial concentration at the discharge point can be estimated.

9.4 Prototype Considerations: Short vs long diffusers

All the model interpretations in sections 9.2 and 9.3 point to say that in general by increasing the discharge velocity u_o (short diffusers), the diffuser performance is greatly enhanced by a large reduction in

i) isotherm areas

ii) the duration in the high temperature ranges for entrained organisms.

The advantages offered by a short diffuser discharging at relatively higher velocities than conventional designs can be further substantiated in a prototype setting:

a) In coastal regions, thermal diffusers are usually located close to the shoreline and oriented to direct the thermal effluent offshore, as shown in Fig. 9-7. The total piping required for a diffuser is then the sum of the diffuser length L_D and the length of piping connecting the discharge structure and the power plant, L_p.

Because of the two dimensional nature of the fluid motion induced by the shallow water discharge, the diffuser induced flow effectively blocks the oncoming current for some distance offshore. If the total induced back entrainment, SQ_o, is greater than $u_a L_p H$, the amount of flow that normally passes the region between the diffuser and the shoreline, possible local re-entrainment of warm mixed water can occur. Thus L_p, the length of connecting piping required to avoid local

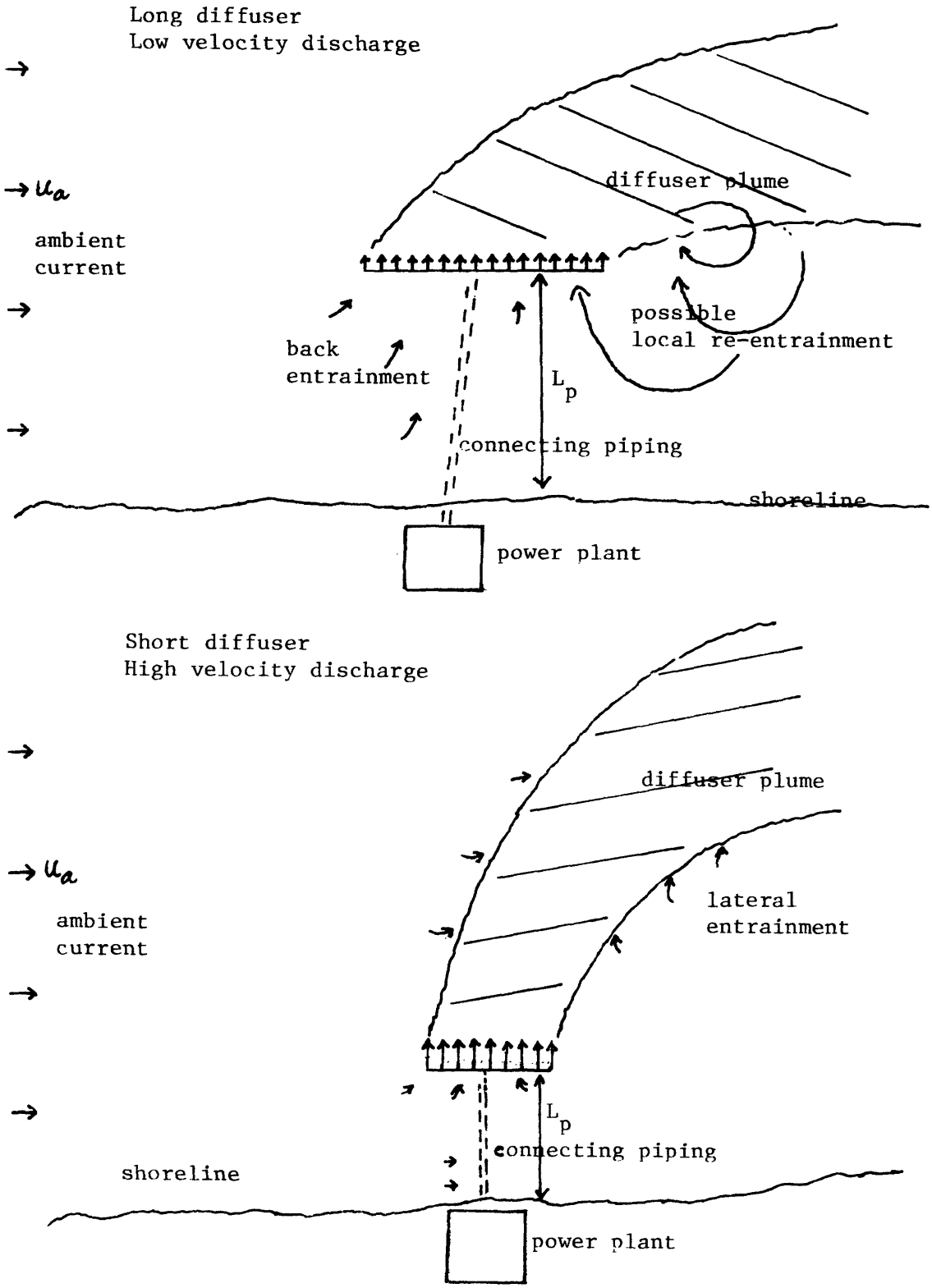

Fig. 9-7 Prototype considerations of diffuser design in coastal region: short vs long diffusers

re-entrainment is also a function of the diffuser length L_D. As $S \sim \sqrt{L_D}$, (for constant u_o cf e.g. Eq. 9.2) we would expect $L_p \sim \sqrt{L_D}$.

In order to avoid local recirculation leading to undersirable heat build-up, therefore, a longer diffuser has to be located further offshore. Assuming the cost of piping is proportional to its length, the economic tradeoff of two diffusers of length L_{D1}, L_{D2}, and connecting pipes of length L_{p1}, L_{p2}. would be characterised by

$$\frac{(\text{cost of piping})_1}{(\text{cost of piping})_2} = \frac{L_{D1} + L_{p1}}{L_{D2} + L_{p2}}$$

$$= \frac{(\frac{L_{D1}}{L_{D2}}) + (\frac{L_{p1}}{L_{p2}})(\frac{L_{p2}}{L_{D2}})}{1 + (\frac{L_{p2}}{L_{D2}})}$$

Supposing the connecting pipe is as long as the diffuser length for design 2; since $\frac{L_{p1}}{L_{p2}} = \sqrt{\frac{L_{D1}}{L_{D2}}}$ we have ratio of pipes cost

$$= (\frac{L_{D1}}{L_{D2}}) + \sqrt{\frac{L_{D1}}{L_{D2}}}$$

Thus building a diffuser twice as long would bear an economic cost $2 + \sqrt{2} \simeq 3.4$ times higher.

b) As pointed out in Chapter VII, for low values of the momentum flux ratio $F_M = \frac{u_a^2 L_D H}{Q_o U_o}$, (small L_D, large u_o), the near field mixing is not affected by the ambient current; whereas for $F_M > 0.1$ (large L_D, small u_o), plumes of temperature rises two or three times greater than ΔT_N are observed for

large distances downstream. The empirical correlations pointed out in Chapter VII can be used to design diffusers with sufficiently strong momentum flux, so that the temperature reduction is improved by the crossflow.

In periods of prolonged slack, long diffusers tend to induce stronger far field recirculation; this topic was discussed in detail in Chapter VIII.

In summary, it should be pointed out that depending on the geomorphological and hydrologic conditions at a specific site, the economic and ecological advantages offered by short diffusers have to be weighed against higher pumping costs, possible navigation hazards caused by higher induced velocities, and sedimentation problems. In general, the discharge velocity u_o should be set to the highest value that is acceptable by other considerations of importance.

CHAPTER X

SUMMARY AND CONCLUSIONS

10.1 Objectives

This study is concerned with the understanding and prediction of the velocity and excess temperature field induced by a unidirectional thermal diffuser in shallow water.

A unidirectional thermal diffuser is a submerged pipeline discharging waste heat from steam-electric power generation in the form of a line of high velocity turbulent heated jets. All the discharge ports are pointing in one direction. This type of once-through condenser cooling water discharge is effective in mixing the heat with the ambient water within a small area, and is hence capable of meeting stringent thermal standards. It provides large momentum in one direction, and can direct the thermal effluent offshore.

The objective is to understand induced flow and temperature patterns as a function of diffuser design and ambient conditions (discharge velocity, diffuser length,strength of ambient current) The ultimate goal is to establish a framework upon which the design of unidirectional thermal diffusers in coastal regions can be based. Three cases of fundamental interest are studied: 1) diffuser operating in stagnant conditions or a coflowing

current, 2) diffuser discharging into a perpendicular cross-flow, and 3) potential heat build-up due to recirculation induced by the pumping action of the diffuser.

Prior to this study, knowledge of a unidirectional diffuser in shallow water was primarily limited to a one-dimensional analysis of the total induced flow in the near field (Adams, 1972), and scattered experimental results of site specific hydraulic scale model studies of limited general value. No comprehensive treatment of the excess temperature field induced by the diffuser in an open water body had previously been attempted.

10.2 Theory

a) The theory for the diffuser operating in stagnant conditions or a coflowing current, as outlined in Chapters III and IV, forms the analytical foundation for the entire study. A vertically fully mixed condition is hypothesized downstream of the diffuser. Vertical variations of temperature are neglected and a two dimensional model is formulated and solved. The theory is based on the coupling of a potential flow model in the near field with a friction jet model in the intermediate field. The predictions do not involve any fitting of theory to experimental data; all physical coefficients are taken from well established data in the literature. As the travel time in the diffuser plume is of the order of an hour, surface heat loss effects are neglected.

By neglecting turbulent side entrainment and bottom friction, the total induced flow near the diffuser is first derived from a control volume analysis. This is then used as an integral boundary condition to obtain a potential flow solution of the near field. The near field solution is coupled into an intermediate field model that predicts the global temperature field, by incorporating lateral entrainment and bottom friction.

Scaling arguments show that Laplace's equation satisfies the equations of motion in the near field, where pressure and inertial effects dominate. A control volume analysis yields two gross parameters - the induced flow from behind SQ_o, and the contraction ratio σ of the mixed flow (Eq. 3.38, 3.40) These provide the integral boundary conditions for the potential flow model. By assuming uniform induced flow locally along the diffuser line, the complex potential plane and the hodograph plane corresponding to the flow can be derived. The existence of a slip streamline which models the locus of velocity discontinuity is hypothesized. The position of the slip streamline can be calculated using classical free streamline theory (eq. 3.62) by mapping the complex potential onto the hodograph plane. Once the slip streamline is known, the flow and pressure field can be calculated by solving Laplace's equation in a region with known boundaries and boundary conditions.

The near field model is a function of two parameters $\beta = \frac{L_D H}{N a_o}$, the ratio of the intercepted cross-sectional area to toal discharge port area, and $\gamma = \frac{u_a}{u_o}$, the ratio of the ambient current to discharge velocity. The theoretical results show that the extent of the near field is $0.5L_D$ and the computed slip streamlines always match asymptotically the contraction ratio predicted independently by the control volume analysis. The solution reveals a region of high pressure in front of the diffuser. The potential energy gained from the diffuser momentum is re-directed into longitudinal momentum as the flow contracts and accelerates downstream. The velocity distribution along the diffuser line can also be inferred as:

$$u = \frac{SQ_o}{L_D} \tag{10.1}$$

$$v(y) = \frac{u \sin\theta_A \; 2y}{\sigma \; L_D} \tag{10.2}$$

In the intermediate field, an integral friction jet model is formulated for the diffuser plume; inertia, turbulent side entrainment, and momentum dissipation due to bottom friction are included. Pressure variations are computed using the potential flow solution in the near field, and are neglected beyond the near field. The entrainment assumption relates the increase in volume flux across the plume to a characteristic centerline velocity excess. The global velocity and temperature

field is assumed to possess a boundary layer type structure (section 4.1) and is divided into two regions: The region of flow establishment refers to the zone where turbulent lateral entrainment has not penetrated to the core. The temperature rise in the core is assumed to be $\Delta T_o/S$. The unknowns in this region are u_c, the centerline velocity, $\delta(x)$ the core width, and $L(x)$ the diffuser layer thickness. The length of this region is obtained as a solution to the problem. In the region of established flow gaussian profiles are assumed for the velocity and temperature rise. The unknowns in this region are u_c, ΔT_c, and $L(x)$.

The entire model is a function of β, γ and an intermediate field parameter $\frac{f_o L_D}{H}$. Integrating the governing equations across the plume yields a system of first order ordinary differential equations in terms of the unknowns in each region.

An analytical solution of the friction jet model in the special case of no ambient current yields the following interesting features (eq. 4.52): In contrast to a 2D or 3D free turbulent jet, the momentum flux of a friction jet is dissipated exponentially as $e^{-\frac{f_o x}{8H}}$. The solution possesses an exponential type of behavior, leading to a divergent plume with rapid decrease in velocity. This suggests the possibility of heat recirculation into the near field. The model also predicts an asymptotic temperature rise ΔT_∞ (eq. 4.54) in the plume. This places a limit to the mixing capacity of any

unidirectional diffuser.

In the presence of a coflowing current, the numerically computed results indicate that the plume is much narrower and that the difference in ΔT_c from the stagnant case is small in the intermediate field.

b) For a <u>diffuser discharging into a perpendicular crossflow,</u> (Tee-Diffuser) a control volume analysis predicts that the near field dilution is independent of the current, $S = \sqrt{\frac{\beta}{2}}$ (eq. 7.8). Given the total induced flow from behind, a model for calculating the plume trajectory in a crossflow is formulated (eq. 7.13). The conservation equations are written in natural co-ordinates. The model uses top hat profiles and incorporates the same entrainment assumption and frictional dissipation as in the coflowing case. Pressure variations in the stream direction is neglected. The major factor in determining the plume trajectory is the dynamic pressure created by the blocking of the crossflow. The bending force is assumed to take on the form $F_b = \frac{1}{2} C_D \rho (u_a \sin\theta)^2$ where C_D is a blocking coefficient. The results show that the plume deflection is dependent on a parameter $F_M = \frac{u_a^2 L_D H}{Q_o u_o} = \beta\gamma^2$, measuring the ratio of ambient to diffuser momentum. The larger the value of F_M, the greater the plume deflection.

c) The phenomenon of <u>far field recirculation</u> is suggested by the analytical results of the coflowing current case. Under slack water conditions, the momentum flux of the diffuser plume

is dissipated at a characteristic distance of $\frac{\beta H}{f_o}$. A stagnant pool of water at this distance would, by flow continuity, serve as a source for the back entrainment demand of the diffuser, thus creating a far field recirculation resembling a source-sink type of flow. Characteristic length and time scale of recirculation can be estimated (eq. 8.1, 8.2). Heuristic arguments suggest that the heat recirculation can be regarded as a function of the 'sink strength' $\frac{SQ_o}{H}$ of the diffuser and the scale of recirculation L_{REC}. Semi-empirical correlations can be made based on these considerations.

10.3 Experiments

A comprehensive set of laboratory tests were carried out in a 60'x40'x1.5' model basin for a wide range of diffuser lengths ($\frac{L_D}{H}$ = 3 - $\frac{L_D}{H}$ = 100) and ambient conditions. Velocities are measured using time-of-travel method and detailed temperature measurements are made. Several series of experiments with different objectives were conducted as described in Chapter V.

10.4 Results and Comparison with Theory

For the case of a coflowing current the experimental data of this study validates the theory both qualitatively and quantitatively: surface pathlines always indicate a contraction of the diffuser induced flow at about $\sim 0.5\ L_D$ for a wide range of diffuser lengths. The observed flow patterns are in qualitative agreement with the predictions of the potential flow model. A core region of roughly constant temperature

is confirmed, and the predicted isotherms compare favorably with the observed temperature field. The centerline temperature rise, centerline velocities, and isotherm areas agree well with data. The theory is also compared with the results of an extensive set of tests carried out by Acres American Corp. (Ref. 3) Good agreement is obtained. The detailed thermal structure also demonstrates the validity of the 2D approxmiation in the discharge dominated regime. The results show the exact temperature distribution,as influenced by the detailed diffuser design, surface and bottom conditions, is very complicated. The good agreement of theory with data for all the parameters of interest, however, justifies the use of the model as a valid way of describing the essential features of the complicated phenomenon. The observed plume width is usually greater than predicted, due to stratification at the edge of the plume.

For Tee-diffuser tests it is found experimentally that for $F_M > .1$, the observed near field temperature rise can be considerably higher than $\Delta T_o/S$. The maximum temperature rise ΔT_{MAX} is correlated with F_M. The predicted plume trajectory compares favorably both with results of this study and the Perry tests. A $C_D = 4$ is assumed in all the calculations.

The phenomenon of far field recirculation is ascertained in the laboratory. It is found that for long diffusers and strong momentum dissipation, heat recirculation into the near field can cause temperature rises two to three times higher

than predicted. Empirical correlations of the scale of recirculation (Fig. 8-7) and maximum temperature rise (Fig. 8-8) are presented.

10.5 General Conclusions

This study provides a basis for comparing the effectiveness of different heat dissipation schemes. The model can be used to calculate induced velocities and temperature rises for a particular diffuser design. Simple, engineering formulae for estimating isotherm areas of interest are given in Appendix C The design implications of the model predictions are interpreted in Chapter IX. A novel interpretation of the results for purposes of environmental aquatic impact assessment is advanced. It is proposed to compare designs on the basis of 'ecological histograms' which embody information from both the velocity field and the temperature field. The general design implications are:

i) For fixed discharge velocity, a longer diffuser induces more back entrainment, but less lateral entrainment in the intermediate field. The striking feature is that beyond a certain distance (about 200 water depths) the effect of the diffuser length, as reflected in the field variables, is not felt. The results show that if the criterion of interest is the area within a low temperature isotherm, a short diffuser may be as satisfactory as one that is two or three times as long.

The 'ecological tradeoff' of building a shorter diffuser for this case can be interpreted as diverting a fraction of the entrained organisms to be exposed to higher maximum temperature rises for very short durations.

ii) For variable diffuser length and discharge velocity at constant near field dilution, it is shown that by increasing the discharge velocity while proportionally decreasing the diffuser length,a large reduction in centerline temperature rises and isotherm areas is obtained. The ecological interpretation for this case is that for the high velocity case the duration for the maximum temperature rise is reduced greatly at the expense of entraining a larger number of organisms at lower temperatues.

iii) The empirical correlation of Chapter VII shows that by designing diffusers with more concentrated momentum input (short diffusers with velocities higher than conventionally accepted values), so that $F_M<0.1$, the temperature reduction can be improved by the crossflow.

iv) The experimental results of Chapter VIII demonstrates that a longer diffuser is more prone to heat recirculation into the near field.

In summary, by designing shorter diffusers with higher velocities, the diffuser performance is greatly enhanced by a large reduction in isotherm areas and the duration of

high temperature ranges for entrained organisms. These advantages, however, have to be weighed against higher pumping costs, possible navigation hazards caused by higher induced velocities, and sedimentation problems.

10.6 Recommendations for Future Research

More studies, both experimental and theoretical, on the mechanics of a Tee-diffuser discharging into a perpendicular crossflow should be pursued. Based on the limited amount of available data, it is our speculation that for a low diffuser momentum input into a strong crossflow, $F_M > 0.1$, stratification is induced in the near field and the mixing capacity of the unidirectional diffuser is impaired. A more satisfactory explanation of more general applicability is needed.

Based on the insights gained in this study, numerical modelling of unidirectional diffusers can be attempted. Numerical models can offer more information in a specific prototype situation with complicated boundary geometries and conditions. Effects of a sloping bottom, ambient current, and distance from the shoreline can then be studied.

Our results indicate that beyond a large distance ($\sim$1000 water depths) the flow will be stratified for most designs without affecting the results in the discharge dominated fully mixed regime. More work should be directed to

investigate the coupling of this far field buoyant flow with the near and intermediate field model of this study .

BIBLIOGRAPHY

1. Abraham, G., "Jet Diffusion in Stagnant fluid", Delft Hydraulics Laboratory, Publication No. 29, (1963).

2. Abramovich, G.N., "The Theory of Turbulent Jets"., The M.I.T. Press, M.I.T. Cambridge, Massachusetts (1963).

3. Acres American Inc., "Perry Nuclear Power Plant, Thermal Hydraulic Model Study of Cooling Water Discharge', Buffalo, New York (1974).

4. Adams, E.E., "Submerged Multiport Diffusers In Shallow Water with Current", M.I.T., S.M. Thesis (Civil Engineering), June 1972.

5. Albertson, M.L., Dai, Y.B., Jensen, R.A., and Rouse, H., "Diffusion of Sumberged Jets", Trans. ASCE, 115 (1950).

6. Almquist, C.W., and Stolzenbach, K.D., "Staged Diffusers In Shallow Water", M.I.T. Parsons Laboratory for Water Resources and Hydrodynamics, Technical Report No. 213, June 1976.

7. Boericke, R.R., "Interaction of multiple Jets with Ambient Current", Journal of the Hydraulics Division, ASCE, Vol. 101, No. HY4, April 1975.

8. Brooks, N.H., "Dispersion in Hydrologic and Coastal Environments", Keck Laboratory of Hydraulics and Water Resources, California Institute of Technology, Report No. KH-R-29, Dec. 1972.

9. Carnahan, B., Luther, H., Wilkes, J., Applied Numerical Methods, John Wiley and Sons, 1969.

10. Cederwall, K., "Buoyant Slot Jets into Stagnant or Flowing Environments", Report No. KH-R-25, Keck Laboratory of Hydraulics and Water Resources, Caltech, April 1971.

11. Report of the Environmental studies Board, "Water Quality Criteria 1972", EPA. R3.73.033, March 1973.

12. Gurevich, M.I., Theory of Jets in Ideal Fluids, N.Y. Academic Press 1965.

13. Harleman, D.R.F., Hall, L.C., and Curtis, T.G., "Thermal Diffusion of Condenser Water in a River during Steady and Unsteady flows", Technical Report No. 111, Hydrodynamics Laboratory, Department of Civil Engineering M.I.T. September, 1968.

14. Harleman, D.R.F., Jirka, G. and Stolzenbach, K.D., "A Study of Submerged Multiport Diffusers for Condenser Water Discharge with Application to the Shoreham Nuclear Power Station", M.I.T. Parsons Laboratory for Water Resources and Hydrodynamics, Technical Report No. 139, June, 1971.

15. Harleman, D.R.F. et al, "Heat Disposal in the Water Environment", to be published by the M.I.T. Press, Cambridge, Massachusetts 1977.

16. Hoult, D.P., Fay, J.A., Forney, L.J., "A Theory of Plume Rise Compared with Field Observations", Journal of the Air Pollution Control, Vol.19, No. 8, August 1969.

17. Howe, C. et al, "Future Water Demands",Report prepared for the National Water Commission, NWC-EES-71-001, March 1971.

18. Jain, S.C., Sayre, W.W. et al, "Model Studies and Design of Thermal Outfall Structures, Quad-Cities Nuclear Plant", IIHR Report No. 135, University of Iowa, September 1971.

19. Jirka, G.H. and Harleman, D.R.F., "The Mechanics of Submerged Multiport Diffusers for Buoyant Discharges in Shallow Water", M.I.T. Parsons Laboratory for Water Resources and Hydrodynamics, Technical Report No. 169, March 1973.

20. Jirka, G., Abraham, G., and Harleman, D.R.F., "An Assessment of Techniques for Hydrothermal Prediction", M.I.T. Parsons Laboratory for Water Resources and Hydrodynamics, Technical Report No. 203, July 1975.

21. L.V. Kantorovich, and V.I. Krylov, "Approximate Methods of Higher Analysis", Interscience Publishers, Inc. N.Y.

22. Knystautas, R., "The Turbulent Jet from a Series of Holes in Line ", Aeronautical Quarterly, Vol. 15, No. 1, 1964.

23. Milne-Thomson, L.M. Theoretical Hydrodynamics, Mcmillan 1968.

24. Morton, B.R., Taylor, G.I. and Turner, J.S., "Turbulent Gravitational Convection from Maintained and Instantaneous Sources", Proc. Roy. Soc. London, A234 (1956).

25. Parr, D.A., "Prototype and Model Studies of the Diffuser Pipe System for Discharging Condenser Cooling Water at the Quad Cities Nuclear Power Station", Ph.D. Thesis, University of Iowa, May 1976.

26. Dr. Renfro, W., "Private Communication", Northeast Utilities Service Co., Harford, Connecticut, (1977)

27. Rouse, H., Yih, C.S., and Humphreys, H.W., "Gravitational Convection from a Boundary Source", Tellus, 4 (1952) pp. 201-10.

28. Special Summer Course Notes for 1.76S, "Engineering aspects of Heat Dissipation from Power Generation", M.I.T. Parsons Laboratory for Water Resources and Hydrodynamics, Dept. of Civil Engineering, June 1972.

29. Stone and Webster Co., "Hydrothermal Field Studies of the James A. Fitzpatrick Nuclear Power Plant", (1976).

LIST OF FIGURES AND TABLES

Figure

Table

LIST OF SYMBOLS

Superscripts

'	turbulent fluctuating quantities
-	time-mean quantity, or quantity normalised with ΔT_N, or depth averaged quantities
*	dimensionless quantity
+,-	in front of and behind the diffuser

Subscripts

a	ambient value
A	value at point of separation
o	initial or discharge value
c	centerline value
D	quantity at diffuser line
e	entrainment quantity
i,j	indices
∞	value at large distances from diffuser
r	ratio of prototype to model
1,2	indices
I, II	quantities in Region I and II
N	near field quantity
a_o	diffuser port area
a_1, a_2	constants determined by conformal mapping in slip streamline calculations
A, A_s, $A_{\Delta T}$	isotherm area

b	edge of plume
b_1, b_2	constant determined in conformal transformation in slip streamline calculations
B	slot jet width
b_o, B_o	initial jet width
c	concentration, clearance of diffuser port from bottom
c'	empirical coefficient relating mixing length to jet width
c_1, c_2	constants of integration
C_D	blocking coefficient
C_Q, C_W	scale factor in conformal mapping
D_o, D	port or nozzle diameter
E	index of dilution comparison of multiple jets with an equivalent slot jet
F	source densimetric Froude number of buoyant slot jet in confined flow
F_b	plume deflecting force
F_D	densimetric Froude number based on nozzle diameter $\dfrac{u_o}{\sqrt{g\dfrac{\Delta\rho_o}{\rho_a} D_o}}$
F_H	local densimetric Froude number based on water depth $\dfrac{u_c}{\sqrt{g\beta_e \Delta T_c H}}$

F_M — ratio of ambient to diffuser momentum $= \frac{u_a^2 L_D H}{Q_o u_o}$

F_s — densimetric Froude number of equivalent slot jet $\frac{u_o}{\sqrt{g \frac{\Delta\rho_o}{\rho_a} B}}$

f_o — friction factor

g — acceleration due to gravity

g_s — y coordinates of given isotherm at any x

$g(x)$ — y-coordinate of slip streamline at any x

H — water depth

ΔH — characteristic free surface deviation

h — local free surface elevation

h^+, h^- — free surface level in front of and behind diffuser

Δh — head rise across diffuser, free surface deviation

h_1, h_2 — steps towards convergence in the determination of a_1, a_2, b_1, b_2

I_1, I_2, I_3 — integrals in conformal mapping

$I_{\Delta T}$, I_1, I_2 — integrals in isotherm area computation

i, — imaginary number = $\sqrt{-1}$

i, j — indices

k — variable of integration

L	characteristic length scale
$L(x)$	diffusion thickness in diffuser plume
L_D	diffuser length
L_I	diffuser layer thickness at x_I
L_{REC}	scale of recirculation
L_p	length of piping connecting power plant and diffuser
ℓ	mixing length scale
ℓ_r	length cale ratio of prototype to model
M	momentum flux across plume
m	$= u_c^2 L$
N	number of diffuser ports
n	coordinate in direction normal to plume trajectory, index
p	pressure
P	pressure force over plume cross-section
Q_o	power plant condenser flow
Q	hodograph plane, volume flux across plume
Q_A, Q_1, Q_2, Q_B	points on Q plane
Q_N	diffuser induced flow from behind
$\vec{q}$	velocity vector
$\vec{q}_D$	induced velocity along diffuser line
q_D	magnitude of velocity = $\lvert\vec{q}_D\rvert$

R_a	Reynolds number of ambient current based on water depth $= \frac{u_a H}{\nu}$
R_D	discharge Reynolds number based on nozzle diameter $= \frac{u_o D_o}{\nu}$
S	near field dilution
s	port spacing, distance along plume centerline
T	temperature
ΔT	temperature excess = $T-T_a$
T_a	ambient temperature
T_o	discharge temperature
ΔT_{MAX}	maximum temperature rise
t	time, variable of integration
T_{REC}	time scale of recirculation
(u,v,w)	velocity components in (x,y,z) direction
U,V	characteristic velocities in x and y direction
u_a	ambient current velocity
u_o	discharge velocity
u_d	x-component of $\vec{q}_D$
u_A, v_A	velocity components at diffuser end
v_e	entrainment velocity
u_c	centerline velocity
u_N	velocity in induced near field

u_p	induced velocity given by potential flow solution
u_I	centerline velocity at x_I
u_i	mean plume velocity in the near field
W	complex potential plane
W_A, W_1, W_2, W_B	points on W plane
(x,y,z)	caresian co-ordinate directions
x_I	location of end of region I
u_M	velocity at point of merging of interacting jets
$x_{\Delta T}$	centerline position of isotherm

α_I, α_{II}	entrainment coefficients
$\alpha_A, \alpha_1, \alpha_2, \alpha_B$	interior angles of polygons approximating curvilinear
$\beta_A, \beta_1, \beta_2, \beta_B$	figures
β	near field parameter = $\frac{L_D H}{N a_o}$
β_1	= S/β
β_2	momentum dissipation parameter = $\frac{f_o L_D}{16H}$ = $\frac{-32\alpha_{II} H}{c_1 L_I f_o L_D}$
β_e	coefficient of thermal expansion of water
γ	ratio of ambient to discharge velocity = $\frac{u_a}{u_o}$
ρ	density
$\Delta\rho$	density difference
δ	potential core width, characteristic transverse length scale

θ	angle of inclination to x-axis
θ_A	angle of separation at diffuser end
λ_1, λ_2	ratio of sides of polygons
ε	small quantity in limits of integration, error of approximation
α_a	inclination of ambient current to diffuser
λ	jet spreading ratio between mass and momentum
ν	kinematic molecular viscosity
σ	contraction coefficient
τ	bottom shear
ϕ	velocity potential
ψ	stream function
ζ	upper half plane, variable of integration

APPENDIX A

CONTROL VOLUME ANALYSIS VALID FOR ALL DILUTIONS

Following the same general assumptions outlined in Chapter III, the more exact version of eq. 3.34-3.36 for the case of arbitrary values of the induced near field dilution S is

$$(S-1)\ Q_o u_a + Q_o u_o = S Q_o u_N$$

$$\Delta h = \frac{u_N^2 - u_a^2}{2g}$$

$$(S-1)\ Q_o u_d + Q_o u_o = S Q_o u_d + g H L_D \Delta h$$

where u_d = x component of $q_D = \frac{(S-1)Q_o}{L_D H}$

Combining and rearranging, a cubic equation in S can be obtained:

$$S^3 - (\beta+1)S^2 + \beta^2\gamma(1-\gamma)S + \frac{\beta^2(1-\gamma)^2}{2} = 0 \qquad (A.1)$$

$$\beta = \frac{L_D H}{N a_o} \qquad \gamma = \frac{u_a}{u_o}$$

The predictions of A.1 are compared with that of eq. 3.38 for a range of dilutions; the comparisons in Table A-1 show that even for dilutions as small as 3, the error involved in using the thory for high dilutions is only a few percent.

β	Predicted dilution assuming S>>1 Eq. 3.38	Predicted dilution using Eq. A.1	Ratio of predicted values
10.0	2.24	2.41	1.08
15.0	2.74	2.93	1.07
20.0	3.16	3.37	1.07
25.0	3.54	3.75	1.06
40.0	4.47	4.69	1.05
50.0	5.00	5.22	1.05
60.0	5.48	5.71	1.04
85.0	6.52	6.75	1.04
100.0	7.07	7.31	1.03

$\gamma = 0$

Table A-1: Comparison of theory assuming high dilutions with exact theory

APPENDIX B

SCHWARTZ-CHRISTOFFEL TRANSFORMATION FOR AN ARBITRARY POLYGON WITH SIX VERTICES

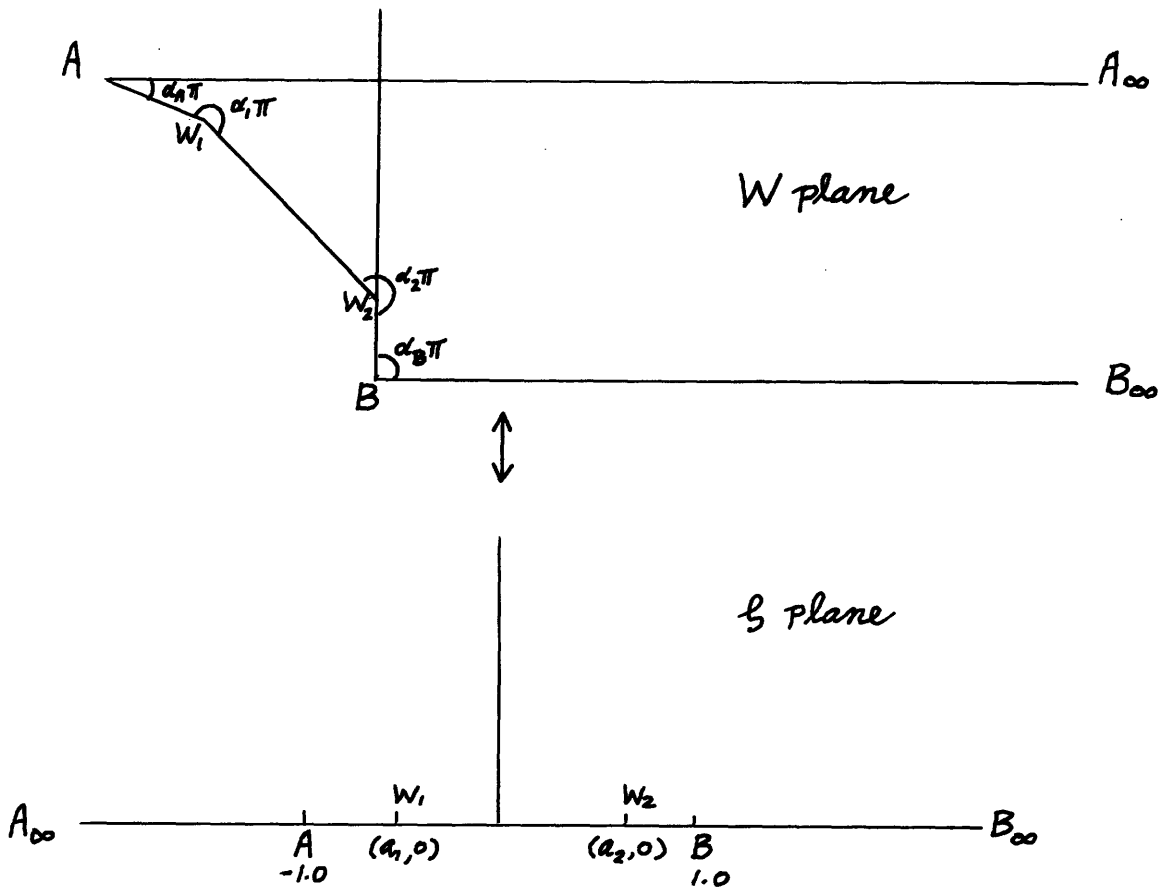

The W-ζ transformation is illustrated below. The Q-ζ transformation is entirely analogous .

$$W(\zeta) = C_W \int_{-1}^{\zeta} (\zeta+1)^{\alpha_A-1} (\zeta-a_1)^{\alpha_1-1} (\zeta-a_2)^{\alpha_2-1} (\zeta-1)^{\alpha_B-1} \, d\zeta + W_A$$

$$W(1) = W_B$$

$$\Longrightarrow C_W = \frac{W_B - W_A}{\int_{-1}^{1} (\zeta+1)^{\alpha_A-1} (\zeta-a_1)^{\alpha_1-1} (\zeta-a_2)^{\alpha_2-1} (\zeta-1)^{\alpha_B-1} \, d\zeta}$$

To find a_1, a_2:

preserve ratio of sides, for 'conformal' transformation;

$$\frac{|W_2 W_1|}{|A\ W_1|} = \lambda_1 \qquad \frac{|BW_2|}{|A\ W_1|} = \lambda_2$$

Let

$$I_1(a_1,a_2) = \int_{1}^{a_1} (\zeta+1)^{\alpha_A-1} (a_1-\zeta)^{\alpha_1-1} (a_2-\zeta)^{\alpha_2-1} (1-\zeta)^{\alpha_B-1} \, d\zeta$$

$$I_2(a_1,a_2) = \int_{a_1}^{a_2} (\zeta+1)^{\alpha_A-1} (\zeta-a_1)^{\alpha_1-1} (a_2-\zeta)^{\alpha_2-1} (1-\zeta)^{\alpha_B-1} \, d\zeta$$

$$I_3(a_1,a_2) = \int_{a_2}^{1} (\zeta+1)^{\alpha_A-1} (\zeta-a_1)^{\alpha_1-1} (\zeta-a_2)^{\alpha_2-1} (1-\zeta)^{\alpha_B-1} \, d\zeta$$

Then

$$I_2 = \lambda_1 I_1 \qquad (*)$$

$$I_3 = \lambda_2 I_1$$

(a_1, a_2) is the solution that satisfies (*)

Solution for a_1 a_2: Newton-Fourier Method

Start with an initial guess $\underline{a}^{(o)} = (a_1^{(o)}, a_2^{(o)})$

Then, a Taylor's series expansion gives

$$I_1(\underline{a}) = I_1(\underline{a}^{(o)}) + h_1 \frac{\partial}{\partial a_1} I_1(\underline{a}^{(o)}) + h_2 \frac{\partial}{\partial a_2} I_1(\underline{a}^{(o)}) + \ldots$$

$$I_2(\underline{a}) = I_2(\underline{a}^{(o)}) + h_1 \frac{\partial}{\partial a_1} I_2(\underline{a}^{(o)}) + h_2 \frac{\partial}{\partial a_2} I_2(\underline{a}^{(o)}) + \ldots$$

$$I_3(\underline{a}) = I_3(\underline{a}^{(o)}) + h_1 \frac{\partial}{\partial a_1} I_3(\underline{a}^{(o)}) + h_2 \frac{\partial}{\partial a_2} I_3(\underline{a}^{(o)}) + \ldots$$

Substituting these expressions into (*)

$$I_2(\underline{a}^{(o)}) + h_1 \frac{\partial}{\partial a_1} I_2(\underline{a}^{(o)}) + h_2 \frac{\partial}{\partial a_2} I_2(\underline{a}^{(o)}) = \lambda_1 [\, I_1(\underline{a}^{(o)}) + h_1 \frac{\partial}{\partial a_1} I_1(\underline{a}^{(o)}) + h_2 \frac{\partial}{\partial a_2} I_1(\underline{a}^{(o)}) \,]$$

$$I_3(\underline{a}^{(o)}) + h_1 \frac{\partial}{\partial a_1} I_3(\underline{a}^{(o)}) + h_2 \frac{\partial}{\partial a_2} I_3(\underline{a}^{(o)}) = \lambda_2 [\, I_1(\underline{a}^{(o)}) + h_1 \frac{\partial}{\partial a_1} I_1(\underline{a}^{(o)}) + h_2 \frac{\partial}{\partial a_2} I_1(\underline{a}^{(o)}) \,]$$

$$\Longrightarrow h_1 \left[\frac{\partial I_2}{\partial a_1} - \lambda_1 \frac{\partial I_1}{\partial a_1} \right] + h_2 \left[\frac{\partial I_2}{\partial a_2} - \lambda_1 \frac{\partial I_1}{\partial a_2} \right] = \lambda_1 I_1 - I_2$$

$$h_1 \left[\frac{\partial I_3}{\partial a_1} - \lambda_2 \frac{\partial I_1}{\partial a_1} \right] + h_2 \left[\frac{\partial I_3}{\partial a_2} - \lambda_2 \frac{\partial I_1}{\partial a_2} \right] = \lambda_2 I_1 - I_3 \qquad \text{(B.1)}$$

Solve B.1 for (h_1, h_2)

set $\underline{a}^{(1)} = \underline{a}^{(o)} + \begin{pmatrix} h_1 \\ h_2 \end{pmatrix}$

and iterate until convergence i.e. $h_1 = h_2 = 0$

The partial derivatives in B.1 have to be evaluated at each iteration: Their expressions are given below

$$\frac{\partial I_1}{\partial a_2} = (\alpha_2-1)\int_{-1}^{a_1}(\zeta+1)^{\alpha_a-1}(a_1-\zeta)^{\alpha_1-1}(a_2-\zeta)^{\alpha_2-2}(1-\zeta)^{\alpha_B-1}\,d\zeta$$

$$\frac{\partial I_1}{\partial a_1} = \frac{\alpha_1+\alpha_A-1}{1+a_1} I_1 - \frac{(\alpha_B-1)}{1+a_1}\int_{-1}^{a_1}(\zeta+1)^{\alpha_A}(a_1-\zeta)^{\alpha_1-1}(a_2-\zeta)^{\alpha_2-1}(1-\zeta)^{\alpha_B-2}d\zeta$$
$$- \frac{(\alpha_2-1)}{(1+a_1)}\int_{-1}^{a_1}(\zeta+1)^{\alpha_A}(a_1-\zeta)^{\alpha_1-1}(a_2-\zeta)^{\alpha_2-2}(1-\zeta)^{\alpha_B-1}\,d\zeta \qquad \text{(B.2)}$$

I_1 is defined previously

$$\frac{\partial I_2}{\partial a_1} = \frac{1-\alpha_1-\alpha_2}{a_2-a_1} I_2 - \frac{(\alpha_B-1)}{a_2-a_1}\int_{a_1}^{a_2}(\zeta+1)^{\alpha_A-1}(\zeta-a_1)^{\alpha_1-1}(a_2-\zeta)^{\alpha_2}(1-\zeta)^{\alpha_B-2}d\zeta$$
$$+ \frac{(\alpha_A-1)}{(a_2-a_1)}\int_{a_1}^{a_2}(\zeta+1)^{\alpha_A-2}(\zeta-a_1)^{\alpha_1-1}(a_2-\zeta)^{\alpha_2}(1-\zeta)^{\alpha_B-1}\,d\zeta$$

$$\frac{\partial I_2}{\partial a_2} = \frac{\alpha_1+\alpha_2-1}{a_2-a_1} I_2 - \frac{(\alpha_B-1)}{a_2-a_1}\int_{a_1}^{a_2}(\zeta+1)^{\alpha_A-1}(\zeta-a_1)^{\alpha_1}(a_2-\zeta)^{\alpha_2-1}(1-\zeta)^{\alpha_B-2}d\zeta$$
$$+ \frac{(\alpha_A-1)}{(a_2-a_1)}\int_{a_1}^{a_2}(\zeta+1)^{\alpha_A-2}(\zeta-a_1)^{\alpha_1}(a_2-\zeta)^{\alpha_2-1}(1-\zeta)^{\alpha_B-1}\,d\zeta \qquad \text{(B.3)}$$

I_2 is defined previously

$$\frac{\partial I_3}{\partial a_1} = -(\alpha_1-1)\int_{a_2}^{1}(1+\zeta)^{\alpha_A-1}(\zeta-a_1)^{\alpha_1-2}(\zeta-a_2)^{\alpha_2-1}(1-\zeta)^{\alpha_B-1}\,d\zeta$$

$$\frac{\partial I_3}{\partial a_2} = \frac{1-\alpha_2-\alpha_B}{1-a_2} I_3 + \frac{(\alpha_1-1)}{1-a_2} \int_{a_2}^{1} (1+\zeta)^{\alpha_A-1} (\zeta-a_1)^{\alpha_1-2} (\zeta-a_2)^{\alpha_2-1} (1-\zeta)^{\alpha_B} d\zeta$$

$$+ \frac{(\alpha_A-1)}{1-a_2} \int_{a_2}^{1} (1+\zeta)^{\alpha_A-2} (\zeta-a_1)^{\alpha_1-1} (\zeta-a_2)^{\alpha_2-1} (1-\zeta)^{\alpha_B} d\zeta \quad . \quad (B.4)$$

I_3 is defined previously

Remarks

a) In carrying out the partial differentiation of some of the integrals, the variable itself appears in the limits of integration

e.g. $$\frac{\partial I_2}{\partial a_1} = \frac{\partial}{\partial a_1} \int_{a_1}^{a_2} (\zeta+1)^{\alpha_A-1} (\zeta-a_1)^{\alpha_1-1} (a_2-\zeta)^{\alpha_2-1} (1-\zeta)^{\alpha_B-1} d\zeta$$

in such cases a change of variable is needed. We present the details for this derivative as an example. The others follow similarly. As the integrand does not exist at the limits of intergration, Leibtnitz rule cannot be used.

Let $t = \frac{\zeta - a_1}{a_2 - a_1}$, $\zeta = a_1(1-t) + a_2 t$

$$d\zeta = (a_2-a_1)\, dt$$

This transforms (a_1, a_2) to $(0,1)$

Let the integrand be $I_2^*(\zeta)$

Then it can be shown by rearranging,

$$I_2^*(t) = [1+a_2 t+a_1(1-t)]^{\alpha_A-1} [t(a_2-a_1)]^{\alpha_1-1} [(a_2-a_1)(1-t)]^{\alpha_2-1}$$

$$[1-a_2 t-a_1(1-t)]^{\alpha_B-1}$$

Then $$\frac{\partial I_2}{\partial a_1} - \frac{\partial}{\partial a_1}\int_o^1 I_2^*(t)\,dt\,(a_2-a_1)$$

$$= \int_o^1 \{\frac{(\alpha_1-1)}{(a_2-a_1)} + \frac{(\alpha_2-1)}{(a_2-a_1)} + \frac{(\alpha_B-1)(t-1)}{[1-a_2t-a_1(1-t)]}$$

$$+ \frac{(\alpha_A-1)(1-t)}{[1+a_2t+a_1(1-t)]}\}I_2^*(t)(a_2-a_1)dt$$

from this we have what is given in B.3

b) Every integral in these computations has an integrand that does not exist at the limits of integration.

As such the singularity has to be subtracted off first before the integrals can be evaluated numerically. The subtracted off part is evaluated analytically.

As an example, consider

$$I_1 = \int_{-1}^{a_1} (\zeta+1)^{\alpha_A-1}(a_1-\zeta)^{\alpha_1-1}(a_2-\zeta)^{\alpha_2-1}(1-\zeta)^{\alpha_B-1}\,d\zeta$$

Near a_1, the integrand behaves like

$$F_1(\zeta) = (1+a_1)^{\alpha_A-1}(a_1-\zeta)^{\alpha_1-1}(a_2-a_1)^{\alpha_2-1}(1-a_1)^{\alpha_B-1}$$

Near -1, the integrand behaves like

$$F_2(\zeta) = (1+\zeta)^{\alpha_A-1}(1+a_1)^{\alpha_1-1}(1+a_2)^{\alpha_2-1}2^{\alpha_B-1}$$

Therefore

$$I_1(\zeta) = \int_{-+\varepsilon}^{a_1-\varepsilon}[I_1-F_1(\zeta) - F_2(\zeta)]d\zeta + \int_{-1}^{a_1}F_1(\zeta)d\zeta + \int_{-1}^{a_1}F_2(\zeta)d\zeta$$

↖ well behaved: evaluated numerically

$$= \int_{-1}^{a_1} [I_1 - F_1 - F_2]\, d\zeta + (1+a_1)^{\alpha_1+\alpha_A-1} (1+a_2)^{\alpha_2-1}{}_2{}^{\alpha_B-1}/\alpha_a$$

$$+ (1+a_1)^{\alpha_1+\alpha_A-1} (a_2-a_1)^{\alpha_2-1} (1-a_1)^{\alpha_B-1}/\alpha_1$$

APPENDIX C

COMPUTATION OF ISOTHERM AREAS

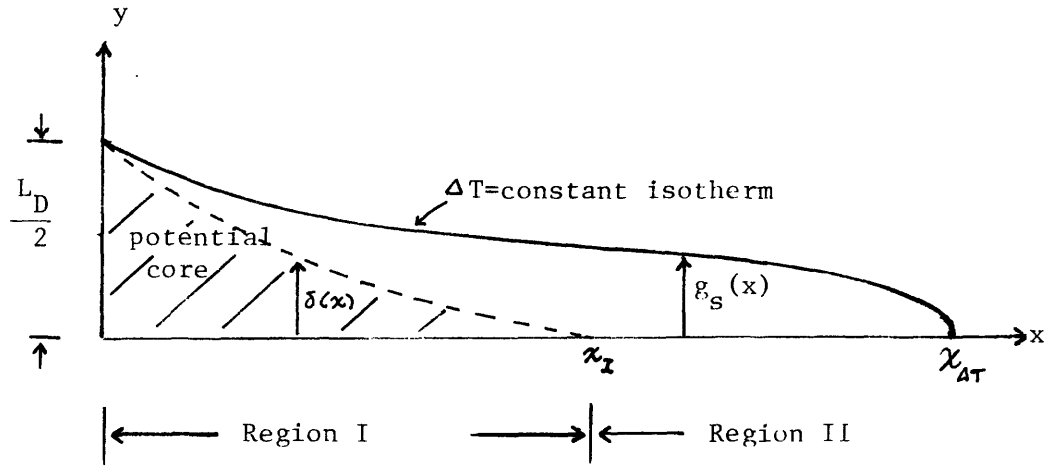

$g_s(x)$: lateral position of isotherm

$\delta(x)$: potential core width

L_D : diffuser length

x_I : length of Region I

$x_{\Delta T}$: centerline position of given isotherm

Fig. C-1 Computation of isotherm area

In the absence of heat recirculation, the two dimensional model outlined in Chapter III and IV predicts the excess temperature field $\Delta T(x,y)$ induced by a unidirectional thermal diffuser such that

$$\Delta T_\infty \leq \Delta T \leq \frac{\Delta T_o}{S} \qquad (C.1)$$

For any diffuser design it is only meaningful to calculate isotherms in this range using this model.

S is the near field dilution given by Eq. 3.41

ΔT_∞ is given by Eq. 4.54; it characterises the ulitimate temperature reduction in the discharge dominated region.

A typical isotherm ΔT = constant is illustrated in Fig. C-1. The notations are the same as used in section 4.1. Thus the figure shows the area within the isotherm, $\Delta T = \Delta T_N = \frac{\Delta T_o}{S}$, is given by

$$A_{\Delta T_N} = 2 \int_o^{x_I} \delta(x)\, dx \qquad (C.2)$$

$x_I, \delta(x)$ are given by the Region I solution in section 4.3.1.

In general, the area within a given ΔT isotherm, $A_{\Delta T}$, is given by

$$A_{\Delta T} = \int_o^{x_{\Delta T}} g_s(x)\, dx \qquad (C.3)$$

where $g_s(x)$ is the y-co-ordinate of the isotherm at any x, $x_{\Delta T}$, the position of the isotherm along the centerline, is given by rearranging eq. 4.52.

$$x_{\Delta T} = x_I + \frac{1}{\beta_2} \ell n \left\{ \frac{1}{\beta_3} \left[\frac{1}{(\frac{S\Delta T}{\Delta T_o})^2} - (1 - \beta_3) \right] \right. \qquad (C.4)$$

where

$$\beta_2 = \frac{f_o L_D}{16H} \quad \beta_3 = \frac{-32\alpha_{II} H}{C_1 L_I f_o L_D} \quad \text{as given by eq. 4.53}$$

The computation of $A_{\Delta T}$ has to be split into two parts- the contributions from region I and II respectively.

$$A_{\Delta T} = 2 \left[\int_o^{x_I} g_s(x)\, dx + \int_{x_I}^{x_{\Delta T}} g_s(x)\, dx \right] \qquad (C.5)$$

The contribution from region I is

$$I_1 = \int_o^{x_I} g_s(x)\, dx = \int_o^{x_I} \delta(x)\, dx + \int_o^{x_I} [\, g_s(x) - \delta(x)\,]\, dx \qquad (C.6)$$

By virtue of the profile assumptions stated in section 4.3.1 we have

$$I_1 = \int_o^{x_I} \delta(x)\, dx + \int_o^{x_I} \delta(x) \sqrt{\ell n \left(\frac{\Delta T_o}{\Delta T_S}\right)}\, dx \qquad (C.7)$$

Similarly, the contribution from Region II is

$$I_2 = \int_{x_I}^{x_{\Delta T}} g_s(s)\, dx = \int_{x_I}^{x_{\Delta T}} L(x) \sqrt{\ell n \left(\frac{\Delta T_c(x)}{\Delta T}\right)}\, dx \qquad (C.8)$$

where $\Delta T_c(x)$ is given by eq. 4.52.

The isotherm area can then be obtained by performing the necessary numerical integrations in Eq. C.7 and C.8.

Design formula for isotherm areas

For estimating isotherm areas of interest it is desirable to derive simple, engineering formulae that can give close approximations very quickly instead of performing numerical computations for the solution given in section 4.3.1.

From numerical experience it is found that the isotherm areas corresponding to $\frac{\Delta T}{\Delta T_N} = 0.8$ and $\frac{\Delta T}{\Delta T_N} = 0.5$ can be well approximated by

$$\left(\frac{A_s}{L_D^2}\right)_{\frac{\Delta T}{\Delta T_N} = 0.8} = 1.8 \exp\left[\, 0.534 \left(\frac{f_o L_D}{H}\right)^{1.437} \,\right]$$

and

$$\left(\frac{A_s}{L_D^2}\right)_{\frac{\Delta T}{\Delta T_N} = 0.5} = 9.5 \exp\left[\, 3.22 \left(\frac{f_o L_D}{H}\right)^{1.83} \,\right]$$

Appendix D

Numerical Results of Slip Streamline Computations

The numerical values used in the computations of the slip streamlines (Eq. 3.62) and an abridged version of the results are given for the five cases illustrated in Fig. 3-8. The integrations for Eq. 3.62 are carried out using Simpson's rule with step sizes $\Delta\zeta = 0.0001$ close to $\zeta = (-1, 0)$ and $\Delta\zeta = 0.01$ further away.

1. $\sigma = 0.5$ $\qquad \theta_A = -60^o = -1.0472$

$W_A = (-0.866, 1.0)$, $W_1 = (-0.4, 0.73)$, $W_2 = (0.0, 0.23)$, $W_B = (0,0)$

$\alpha_A = 0.167$, $\alpha_1 = 1.118$, $\alpha_2 = 1.125$, $\alpha_B = 0.5$

$$\frac{|W_2W_1|}{|A\ W_1|} = \lambda_1 = 1.187 \quad , \quad \frac{|BW_2|}{|AW_1|} = \lambda_2 = 0.427$$

$a_1 = -0.9693$, $a_2 = 0.487$, $C_W = 0.323$

$Q_A = (0,-1.0472)$, $Q_1 = (0.4,-0.77)$, $Q_2 = (0.693,-0.16)$,

$Q_B = (0.693,0)$

$\beta_A = 0.3071$, $\beta_1 = 0.8354$, $\beta_2 = 0.8575$, $\beta_B = 0.5$

$$\frac{|Q_1Q_2|}{|A\ Q_1|} = \lambda_1 = 1.39 \quad , \quad \frac{|BQ_2|}{|AQ_1|} = \lambda_2 = 0.3285$$

$b_1 = -0.818$, $b_2 = 0.8769$, $C_Q = 0.268$

$\frac{x}{0.5L_D}$	$\frac{y}{0.5L_D}$	θ
0.0000	1.0000	-1.0472
0.0605	0.8977	-0.9927
0.0686	0.8855	-0.9798
0.0738	0.8777	-0.9709
0.0778	0.8719	-0.9638
0.0811	0.8673	-0.9579
0.0863	0.8599	-0.9482
0.0905	0.8542	-0.9403
0.0956	0.8473	-0.9305
0.1010	0.8402	-0.9197
0.1054	0.8344	-0.9107
0.1101	0.8285	-0.9010
0.1141	0.8235	-0.8927
0.1202	0.8160	-0.8798
0.1247	0.8105	-0.8700
0.1860	0.7468	-0.7376
0.2149	0.7221	-0.6786
0.2529	0.6937	-0.6069
0.3016	0.6629	-0.5248
0.3430	0.6406	-0.4634
0.3845	0.6207	-0.4070
0.4628	0.5911	-0.3206
0.5141	0.5754	-0.2739
0.5526	0.5652	-0.2433
0.6095	0.5523	-0.2041
0.6514	0.5442	-0.1793
0.6989	0.5362	-0.1548
0.7560	0.5280	-0.1296
0.8053	0.5221	-0.1112
0.8485	0.5176	-0.0972
0.9029	0.5124	-0.0800
0.9524	0.5087	-0.0682
1.0011	0.5056	-0.0583
1.0299	0.5040	-0.0530
1.0466	0.5032	-0.0502

2. $\sigma = 0.5907$, $\theta_A = -53.8^o = -0.9389$

$W_A = (-0.683, 1.0)$, $W_1 = (-0.31, 0.70)$, $W_2 = (0.0, 0.15)$, $W_B = (0,0)$

$\alpha_A = 0.2156$, $\alpha_1 = 1.121$, $\alpha_2 = 1.1634$, $\alpha_B = 0.5$

$\lambda_1 = 1.318$, $\lambda_2 = 0.3134$

$a_1 = -0.919$, $a_2 = 0.7498$, $C_W = 0.319$

$Q_A = (0, -0.9389)$, $Q_1 = (0.23, -0.75)$, $Q_2 = (0.526, 0.2)$, $Q_B = (0.526, 0)$

$\beta_A = 0.2811$, $\beta_1 = 0.8761$, $\beta_2 = 0.8428$, $\beta_B = 0.5$

$\lambda_1 = 2.099$, $\lambda_2 = 0.672$

$b_1 = -0.9739$, $b_2 = 0.672$, $C_Q = 0.2143$

$\frac{x}{0.5L_D}$	$\frac{y}{0.5L_D}$	θ
0.0000	1.0000	-0.9389
0.0481	0.9366	-0.8676
0.0621	0.9206	-0.8418
0.0700	0.9119	-0.8269
0.0804	0.9008	-0.8069
0.0909	0.8901	-0.7867
0.1008	0.8804	-0.7675
0.1100	0.8716	-0.7496
0.1201	0.8625	-0.7303
0.1932	0.8053	-0.5992
0.2277	0.7831	-0.5454
0.2727	0.7578	-0.4825
0.3047	0.7418	-0.4425
0.3415	0.7253	-0.4027
0.3951	0.7043	-0.3468
0.4284	0.6922	-0.3153
0.5207	0.6658	-0.2450
0.5811	0.6519	-0.2073
0.6265	0.6430	-0.1826
0.6933	0.6317	-0.1511

2. (Continued)

$\frac{x}{0.5L_D}$	$\frac{y}{0.5L_D}$	θ
0.7424	0.6248	-0.1312
0.7981	0.6180	-0.1115
0.8533	0.6123	-0.0946
0.9053	0.6077	-0.0808
0.9460	0.6047	-0.0712
0.9602	0.6037	-0.0681
0.9854	0.6015	-0.0611
1.0370	0.5986	-0.0514

3. $\sigma = 0.6428$, $\theta_A = -50^{\circ} = -0.8727$

$W_A = (-0.5959, 1.0)$, $W_1 = (-0.28, 0.7)$, $W_2 = (0, 0.2)$, $W_B = (0,0)$

$\alpha_A = 0.2418$, $\alpha_1 = 1.096$, $\alpha_2 = 1.163$, $\alpha_B = 0.5$

$\lambda_1 = 1.3154$, $\lambda_2 = 0.4591$

$a_1 = -0.9105$, $a_2 = 0.6227$, $C_W = 0.3193$

$Q_A = (0,-0.8727)$, $Q_1 = (0.2,-0.69)$, $Q_2 = (0.442,-0.2)$, $Q_B = (0.442,0)$

$\beta_A = 0.2644$, $\beta_1 = 0.8816$, $\beta_2 = 0.854$, $\beta_B = 0.5$

$\lambda_1 = 2.017$, $\lambda_2 = 0.738$

$b_1 = -0.9836$, $b_2 = 0.4626$, $C_Q = 0.1875$

$\frac{x}{0.5L_D}$	$\frac{y}{0.5L_D}$	θ
0.0000	1.0000	-0.8727
0.0432	0.9507	-0.7917
0.0517	0.9423	-0.7755
0.0574	0.9367	-0.7645
0.0656	0.9290	-0.7489
0.0742	0.9212	-0.7327

3. (Continued)

$\frac{x}{0.5L_D}$	$\frac{y}{0.5L_D}$	θ
0.0844	0.9122	-0.7137
0.0906	0.9069	-0.7022
0.0982	0.9006	-0.6884
0.1073	0.8932	-0.6720
0.1177	0.8852	-0.6538
0.1210	0.8825	-0.6479
0.1995	0.8307	-0.5255
0.2375	0.8099	-0.4754
0.2872	0.7862	-0.4176
0.3225	0.7713	-0.3810
0.3506	0.7605	-0.3543
0.3743	0.7520	-0.3332
0.4043	0.7420	-0.3082
0.4297	0.7342	-0.2885
0.4582	0.7254	-0.2664
0.5590	0.7013	-0.2037
0.6250	0.6889	-0.1703
0.7141	0.6753	-0.1327
0.7758	0.6678	-0.1111
0.8616	0.6594	-0.0859
0.9219	0.6546	-0.0710
0.9883	0.6504	-0.0570
1.0064	0.6494	-0.0536
1.0309	0.6481	-0.0491

4. $\sigma = 0.7068$, $\theta_A = -45^\circ = -0.7859$

$W_A = (-0.5, 1.0)$, $W_1 = (-0.2, 0.65)$, $W_2 = (0.0, 0.15)$, $W_B = (0, 0)$

$\alpha_A = 0.2744$, $\alpha_1 = 1.1045$, $\alpha_2 = 1.121$, $\alpha_B = 0.5$

$\lambda_1 = 1.168$, $\lambda_2 = 0.3254$

$a_1 = -0.804$, $a_2 = 0.7857$, $C_W = 0.3185$

$Q_A = (0, -0.7859)$, $Q_1 = (0.19, -0.57)$, $Q_2 = (0.347, 0.15)$,

$Q_B = (0.347, 0)$

4. (Continued)

$\beta_A = 0.2298$, $\beta_1 = 0.8841$, $\beta_2 = 0.8861$, $\beta_B = 0.5$

$\lambda_1 = 1.559$, $\lambda_2 = 0.5216$

$b_1 = -0.9844$, $b_2 = 0.4763$, $C_Q = 0.1499$

$\frac{x}{0.5L_D}$	$\frac{y}{0.5L_D}$	θ
0.0000	1.0000	-0.7859
0.0368	0.9654	-0.6851
0.0451	0.9587	-0.6678
0.0552	0.9509	-0.6475
0.0622	0.9457	-0.6340
0.0701	0.9400	-0.6194
0.0763	0.9356	-0.6081
0.0846	0.9300	-0.5936
0.0901	0.9263	-0.5842
0.0992	0.9204	-0.5691
0.1067	0.9157	-0.5570
0.1146	0.9109	-0.5447
0.2011	0.8654	-0.4296
0.2423	0.8476	-0.3855
0.2962	0.8274	-0.3357
0.3344	0.8147	-0.3046
0.3906	0.7983	-0.2644
0.4231	0.7899	-0.2437
0.4420	0.7853	-0.2324
0.4591	0.7813	-0.2226
0.4818	0.7755	-0.2091
0.5916	0.7553	-0.1579
0.6635	0.7448	-0.1308
0.7175	0.7382	-0.1132
0.7609	0.7336	-0.1005
0.8556	0.7252	-0.0767
0.9020	0.7219	-0.0668
0.9220	0.7206	-0.0628
0.9574	0.7185	-0.0562
0.9731	0.7176	-0.0534
0.9879	0.7169	-0.0509
1.0017	0.7168	-0.0486

5. $\sigma = 0.766$, $\theta_A = -40^o = -0.6981$

$W_A = (-0.4195, 1.0)$, $W_1 = (-0.19, 0.7)$, $W_2 = (0, 0.2)$, $W_B = (0, 0)$

$\alpha_A = 0.2921$, $\alpha_1 = 1.0923$, $\alpha_2 = 1.1156$, $\alpha_B = 0.5$

$\lambda_1 = 1.416$, $\lambda_2 = 0.5295$

$a_1 = -0.8558$, $a_2 = 0.6747$, $C_W = 0.3185$

$Q_A = (0,-0.6981)$, $Q_1 = (0.15, -0.49)$, $Q_2 = (0.2666, -0.1)$,

$Q_B = (0.2666, 0)$

$\beta_A = 0.1988$, $\beta_1 = 0.8937$, $\beta_2 = 0.9075$, $\beta_B = 0.5$

$\lambda_1 = 1.587$, $\lambda_2 = 0.3899$

$b_1 = -0.995$, $b_2 = 0.5356$, $C_Q = 0.1113$

$\frac{x}{0.5L_D}$	$\frac{y}{0.5L_D}$	θ
0.0000	1.0000	-0.6981
0.0343	0.9735	-0.5755
0.0426	0.9682	-0.5575
0.0483	0.9647	-0.5457
0.0528	0.9620	-0.5369
0.0628	0.9562	-0.5183
0.0723	0.9510	-0.5018
0.0827	0.9453	-0.4848
0.0842	0.9446	-0.4825
0.0897	0.9418	-0.4741
0.0977	0.9377	-0.4623
0.1097	0.9319	-0.4456
0.1158	0.9289	-0.4375
0.2040	0.8930	-0.3438
0.2475	0.8783	-0.3085
0.2791	0.8687	-0.2860
0.3263	0.8556	-0.2562

5.

$\frac{x}{0.5L_D}$	$\frac{y}{0.5L_D}$	θ
0.3624	0.8465	-0.2361
0.3922	0.8396	-0.2209
0.4403	0.8294	-0.1987
0.4957	0.8189	-0.1761
0.6214	0.7987	-0.1338
0.6988	0.7891	-0.1135
0.8038	0.7783	-0.0908
0.9325	0.7681	-0.0691
0.9779	0.7651	-0.0627
1.0333	0.7618	-0.0557
1.0642	0.7601	-0.0522

Copies of a listing of computer programs can be obtained by request to the R.M. Parsons Laboratory.